Encapsulation of Iron(III) Protoporphyrin IX and Tetraphenylporphyrin in Metal-Organic Frameworks for Application as Heterogeneous Oxidation Catalysts

BY

Nicola A. Dare

BSc. Hons (University of Cape Town)

University of Cape Town

Thesis Presented for the Degree of

DOCTOR OF PHILOSOPHY

In the Department of Chemistry

UNIVERSITY OF CAPE TOWN

February 2018

SUPERVISORS: PROFESSORS TIMOTHY EGAN AND SUSAN BOURNE

The copyright of this thesis vests in the author. No quotation from it or information derived from it is to be published without full acknowledgement of the source. The thesis is to be used for private study or non-commercial research purposes only.

Published by the University of Cape Town (UCT) in terms of the non-exclusive license granted to UCT by the author.

University of Cape Town

Declaration

I, Nicola A. Dare declare the following,

1. That the above-titled report is my own work, both in concept and execution, apart from the normal guidance of my supervisors;
2. That in cases where others' work has been cited, this has been acknowledged and referenced;
3. That no part of this work has been, is being, or is to be submitted for another degree at this or any other university;
4. That I grant the University of Cape Town free license to reproduce this work, in whole or in part, for the purpose of research.

I hereby present this report in fulfilment of the requirements for the degree of Doctor of Philosophy in the Department of Chemistry at the University of Cape Town.

Signature: Signed by candidate

Date: February 2018

Abstract

Two MOFs, $[H_2N(CH_3)_2][Zn_3(TATB_2(HCOO)]\cdot HN(CH_3)_2\cdot DMF\cdot 6H_2O$ (**1**) and Zn-HKUST-1 (**2**) (TATB = 4,4′,4″-*s*-triazine-2,4,6-triyl-tribenzoate) were investigated as potential hosts to encapsulate Fe(III) protoporphyrin IX (ferrihaem = Fe(III)PPIX) and Fe(III) tetraphenylporphyrin (Fe(III)TPP). Methyl orange (MO) adsorption was used as an initial model for substrate uptake in MOFs **1** and **2**. MOF **1** showed good adsorption of MO (10.3 ± 0.8 $mg.g^{-1}$) which could undergo in situ protonation upon exposure to aqueous HCl vapour. By contrast MO uptake by **2** was much lower (2 ± 1 $mg.g^{-1}$) and PXRD indicated structural instability on exposure to water was the likely cause. Two methods for Fe(III)PPIX incorporation into **1** were investigated: soaking and encapsulation. Encapsulation was verified by SEM-EDS and showed comparable concentrations of Fe(III)PPIX on exposed interior surfaces and on the original surface of fractured crystals. SEM EDS results were consistent with ICP-OES data on bulk material (1.2 ± 0.1 mass % Fe). PXRD data showed that the framework in **1** was unchanged after encapsulation of Fe(III)PPIX. MO adsorption (6 ± 1 $mg.g^{-1}$) by Fe(III)PPIX-**1** confirmed there is space for substrate diffusion into the framework, while the UV-visible spectrum of solubilized crystals confirmed that Fe(III)PPIX retained its integrity. A solid-state UV-visible spectrum of Fe(III)PPIX-**1** indicated that Fe(III)PPIX was not in a μ-oxo dimeric form. Although single-crystal XRD data did not allow for full refinement of the encapsulated Fe(III)PPIX molecule owing to disorder of the metalloporphyrin, the Fe atom and pyrrole N atoms were located, enabling rigid-body modelling of the porphine core. For comparison, Fe(III)PPIX was further encapsulated in **2**, forming Fe(III)PPIX-**2**. Reaction of 2,2'-azino-bis(3-ethylbenzothiazoline)-6-sulphonic acid (ABTS) with H_2O_2, catalysed by Fe(III)PPIX-**1** and -**2** showed that Fe(III)PPIX-**1** is significantly more efficient than Fe(III)PPIX-**2** and is superior to solid Fe(III)PPIX-Cl due to the faster initial rate of reaction as well as the greater conversion of ABTS to $ABTS^{\bullet+}$.

Both frameworks **1** and **2** were also investigated as potential hosts to encapsulate Fe(III) tetraphenylporphyrin (Fe(III)TPP). Attempts to encapsulate Fe(III)TPP into **1** were unsuccessful, but Fe(III)TPP was successfully encapsulated into **2**, forming Fe(III)TPP-**2**. The framework was characterised by PXRD and SEM-EDS confirmed uniform distribution of Fe(III)TPP through the framework. The loading of Fe(III)TPP determined using ICP-OES (0.604 ± 0.008 Fe mass %) agreed well with SEM-EDS data. Single crystals of Fe(III)TPP-**2** were obtained and structure determination showed that the Fe(III) porphyrin was positionally disordered over three positions. The instability of Fe(III)TPP-**2** in the presence of H_2O resulted in it being an inappropriate choice as an oxidation catalyst. The kinetics of ABTS oxidation by H_2O_2 catalysed by Fe(III)PPIX-**1** were further investigated. The peroxidatic activity of this heterogeneous system conforms to a rate law identical to that observed in solution with no discernible influence of particle size, suggesting that the MOF system closely mimics the solution state. The proposed rate law indicates a reaction mechanism with two possible pathways, as suggested for the same reaction in solution. The major pathway describes the coordination of H_2O_2 to the Fe(III) centre and subsequent formation of a high valent intermediate, while the minor pathway describes the same process preceded by ABTS coordination to the Fe(III) centre forming a six-coordinate complex. The further application of Fe(III)PPIX-**1** as an oxidation catalyst was probed by investigating the catalytic oxidation of hydroquinone, thymol, benzyl alcohol and phenyl ethanol by *tert*-butyl-hydroperoxide (^{t}BuOOH). Reactions were successful and showed $t_{1/2}$ values that increase with increasing substrate molecular volume.

Publications and Conference Proceedings

Publications

Parts of this thesis have been published in the following publication:

N. A. Dare, L. Brammer, S. A. Bourne and T. J. Egan, Fe(III) Protoporphyrin IX Encapsulated in a Zinc Metal−Organic Framework Shows Dramatically Enhanced Peroxidatic Activity, *Inorg. Chem.*, 2018, DOI: 10.1021/acs.inorgchem.7b02612

Conference Proceedings

1. **SACI Inorganic Chemistry Conference** (June 2017) - Arabella, South Africa
   Poster and Flash presentation (First prize- flash presentation): N. A. Dare, S. A. Bourne and T. J. Egan, Using metal-organic frameworks to investigate Fe(III) porphyrins.
2. **SACI Young Chemists Symposium** (December 2016) – Stellenbosch, South Africa
   Poster: N. A. Dare, S. A. Bourne and T. J. Egan, Using metal-organic frameworks to investigate ferrihaem.
3. **Gordon Research Conference, The Chemistry and Biology of Tetrapyrroles** (July 2016) – Newport, RI, U.S.A.
   Poster: N. A. Dare, S. A. Bourne and T. J. Egan, Using metal-organic frameworks to investigate ferrihaem.
4. **SACI Inorganic Chemistry Conference** (July 2015) – Grahamstown, South Africa
   Poster and Flash presentation (First prize- poster presentation): N. A. Dare, S. A. Bourne and T. J. Egan, Using MOFs as a ‘crystalline sponge’ to investigate properties of haem.
5. **Meeting on Porous Molecular Solids** (April 2015) – Stellenbosch, South Africa
   Poster: N. A. Dare, S. A. Bourne and T. J. Egan, Using metal-organic frameworks to investigate the properties of ferrihaem.

Acknowledgements

While there are many people who have made essential contributions to this work, I particularly would like to express my gratitude to the people below.

Professor Timothy Egan, thank you for teaching how to ask the right questions, for your patience, guidance and time throughout the project, and to always remember 'don't speculate, calculate!'. I would not be half the researcher I am now without your guidance.

Professor Susan Bourne, thank you for being an amazing supervisor, for the interesting discussions and for always finding time to talk crystallography with me, no matter how busy you were.

To **Professor Lee Brammer,** thank you for inviting me to spend some time in your laboratory and generously allowing me to use some of your valuable synchrotron beamtime. **Professor Neil Ravenscroft**, thank you for your NMR expertise and always being willing to answer any questions that I had. **Christel Tinguely**, thank you for all the help obtaining ICP data on material that just would not go into solution. You are truly a lifesaver. **Dr Hong Su**, thank you for all your help and expertise using the diffractometers. **Dr Clive Oliver** for your help with the gas sorption equipment and **Pete Roberts** for NMR, **Miranda Waldron**, for the SEM expertise and for allowing me to see the beauty of my crystals close up. **The Analytical Workshop at the Department of Chemical Engineering** for running my ICP-OES samples and to **Diamond Light Source** for the beamtime.

The 'Haem' Team members (Past and present): Thank you for group meetings, helping with lab clean-ups and general chats/advice: **Dr Aneesa Omar, Dr John Woodland, Fabrizio, Dr Jill Combrink, Roxanne O, Dr John Okombo, Dr Ana De Sousa** and to **Roxanne M**, thank you for the long chats, advice and for always being present with a smile. Your positive attitude makes Level 6 a much brighter place.

The Supramolecular Group (Past and present): **Laurelle, Terence, Alexios**, **Nicole**, **Nolwazi**, **Razan**, **Nabanita**, **Francoise**, **Jacky**, **Christelle**, **Khadijah**, **Dr Lee Hunt**. In particular to **Dr Vaughn Maurel**, for help with any questions related to thermal techniques **Richard** for help with the gas sorption apparatus and for the chats about gas sorption, rugby and everything in between. To **Savannah**, thank you for bringing the outside in with your (many!) pot-plants, the countless cups of tea and for your continuous support and encouragement.

To the admin wizards, **Karin**, **Deirdre, Zaeem, Jo** and **Leeta**, thank you for all your help over the years.

To my friends, **Giselle**, **Guy**, **Erik** and **Rudelee**, thank you for keeping me sane and for reminding me that I don't need to always talk about Chemistry. A particular thank you to **Rudelee,** for allowing me to come and work at your co-working space, for the movie nights and reminding me to always enjoy the little things.

To my **family**, and particular my **parents** for all your love and support, and for always showing an interest in what I am doing. I appreciate it more than you will ever know.

And finally, to **David Kuter**: there are too many things to count to thank you for. Mostly, thank you for believing in me when I did not believe in myself. I could not have done this without you.

List of Abbreviations

AA	Atomic absorption	**MOM**	Metal-organic material
ABTS	2,2'-azino-bis(3-ethylbenzothiazoline)-6-sulphonic acid	**MP-11**	Microperoxidase 11
BET	Brunauer–Emmett–Teller	**MP-8**	Microperoxidase 8
BTC	benzene-1,3,5-tricarbxylic acid, trimesic acid	**NMR**	Nuclear magnetic resonance
DMF	*N, N*-dimethylformamide	**PDB**	Protein data bank
DTBC	3,5-di-tert-butylcatechol	**PhIO**	Iodosobenzene
EDS, EDX	Energy-dispersive X-ray spectroscopy	**porph**	Porphyrin
ee	Enantiomeric excess	**PXRD**	Powder X-ray diffraction
Fe(III)PPIX	Fe(III) protoporphyrin IX	**SEM**	Scanning electron microscopy
Fe(III)TPP	Fe(III) tetraphenyl porphyrin	**^{t}BuOOH**	*tert*-Butyl hydroperoxide
FT-IR	Fourier-transform infrared spectroscopy	**TDCPP**	Tetra-2,6-dichlorophenylporphyrin
GCE	Glassy carbon electrode	**TEM**	Transmission electron microscopy
GOx	Glucose oxidase	**TGA**	Thermal gravimetric analysis
H_3TATB	4,4′,4″-*s*-Triazine-2,4,6-triyl-tribenzoic acid	**TMB**	3,3’,5,5’-Tetramethylbenzidine
Haem	Fe(II) protoporphyrin IX	**TMPyP**	5,10,15,20-Tetrakis(1-methyl-4-pyridinio)porphyrin
Haemin	Cl- Fe(III) protoporphyrin IX	**TON**	Turnover number
hh-metMb	Horse heart metmyoglobin	**TPP**	Tetraphenyl porphyrin
		TPyP	5,10,15,20-tetra-(4-pyridyl)porphyrin
HRP	Horseradish Peroxidase	**TRIS**	tris(hydroxymethyl)aminomethane
ICP-OES	Inductively coupled plasma optical emission spectroscopy	**UV**	Ultraviolet
MO	Methyl Orange	**XRD**	X-ray diffraction
MOF	Metal-organic framework		

Table of Contents

Chapter Two: General Information and Instrumentation

Chapter Three: Encapsulation of Fe(III)PPIX into MOFs

Chapter One: Introduction and Literature Review

1.1 Oxidation reactions in biology

Oxidation of organic substrates, especially alcohols, is an important class of industrially relevant reactions[1] and therefore there has been much interest in developing heterogeneous catalysts for this purpose.[1–3] Heterogeneous catalysts provide many advantages in a synthetic environment, such as ease of separation, waste minimization and reusability.[4,5] It is for this reason that the development of such catalysts is a focus of green chemistry since they eliminate the need for distillation or extraction to separate products from the catalyst.[5,6]

The oxidation of organic substrates in nature is one of the well-known roles of the class of metalloproteins known as haemoproteins.[7] These proteins contain Fe(III) protoporphyrin IX (ferrihaem or FePPIX) as a cofactor (Fig. 1.1a).[8] They are crucial in organisms where they are responsible for a wide variety of metabolic functions such as gas binding (e.g. haemo- and myoglobin)[9], electron transport (e.g. cytochromes *a, b* and *c*)[10], ligand sensing (e.g. guanylyl cyclase)[11] and redox catalysis (e.g. cytochromes *P450* and peroxidases such as horseradish peroxidase) (Fig. 1.1b).[7,8,12] By making use of the FePPIX cofactor, haemoproteins have been shown to catalyse reactions with high stereo-, chemo- and regioselectivity.[13,14]

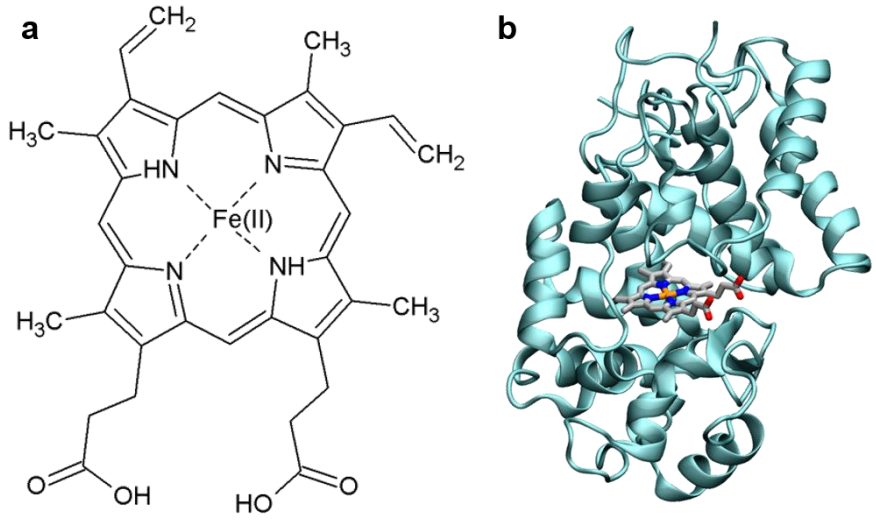

Figure 1.1: *(a) Structure of haem or iron protoporphyrin IX (FePPIX) and (b) horse-radish peroxidase with the haem cofactor highlighted. Possible axial ligands not shown for clarity. Protein structure generated using crystal structure data from the PDB.*[15]

The centre of reactivity of catalytic haemoproteins is the haem co-factor, where the resting state of haem typically consists of a six coordinate low-spin Fe(III) centre with an axial water and axial coordination to a protein residue.[16] While haemoproteins can catalyse both oxidative and reductive chemistry, the catalysis of oxidative reactions has been the focus of much of the research in this area. In this context, there are two broad classes of oxidative haem enzymes namely: (i) oxygenases which use O_2 to oxidise, and usually oxygenate, substrates and (ii) peroxidases which use H_2O_2 as an oxidant.[7]

While both oxidants are potent, they are not inherently reactive molecules and thus require activation before oxidation can proceed. This reactivity is particularly unusual in the case of O_2 since it has a large kinetic barrier to reactivity because of the spin-forbidden reaction between spin-paired biomolecules and its paramagnetic electron arrangement (triplet state, S = 1 compared to the typical singlet state, S = 0).[7,17] Lowering the barrier to reactivity is mediated by binding to the iron centre of the haem co-factor, where a one electron reduction occurs leading to the formation of an active oxidant.[17] For the reaction to occur, low spin

[Fe(III)porph] first undergoes a one electron reduction to form a reduced Fe(II) centre, to which O_2 can bind. This forms a complex best described as ferric-superoxide, [Fe(III)-O_2^-(porph)] (Scheme 1.1). Subsequent protonation to [Fe(III)-OOH(porph)] then occurs and, at this point, the mechanisms of oxygenases follows that of peroxidases.[7]

In the case of peroxidases, the reaction is typically a two-electron oxidation-reduction reaction.[18] The oxidant, H_2O_2, binds reversibly to the Fe(III) centre of the porphyrin (Fe(III)-OOH(porph)]) with a loss of a proton where the species subsequently undergoes irreversible O-O bond cleavage to form a high valent species, either with a two electron transfer to form [Fe(IV)=O(porph)$^{\bullet+}$], a π radical cation species, and H_2O (heterolytic cleavage) or a one electron transfer [Fe(IV)=O(porph)] and $^{\bullet}$OH species (homolytic cleavage).[19,20] The type of cleavage will depend on the specific enzyme, as well as the substrate. For example, peroxidases undergo heterolytic cleavage upon binding of the oxidant H_2O_2; whereas cytochromes *P450* have been shown to undergo homo- or heterolytic cleavage depending on the structure of the oxidant.[21]

Heterolytic cleavage of the O–O bond to form [Fe(IV)=O(porph)$^{\bullet+}$] is thought be promoted by simultaneous electron transfer from the porphyrin ring to the Fe–O bond as the porphyrin π-cation radical is generated, coupled with the delivery of a H^+ ion to the distal oxygen, promoting the release of H_2O and generation of an oxygen with 6 valence electrons, thereby forming [Fe(IV)=O(porph)$^{\bullet+}$], a species which is two oxidation states above the resting state, [Fe(III)porph].[16,22] Activation of the O-O bond is enhanced by the introduction of electron rich axial ligands, such as tyrosine.[22] This [Fe(IV)=O(porph)$^{\bullet+}$] species has been proposed to be the key reactive intermediate in oxidation reactions, and will rapidly react to oxidise electron rich substrates in two subsequent one electron oxidation steps (Scheme 1.1) or oxygenate a substrate (as seen in oxidases).[17] The precise structure of this high valent species and its subsequent

interaction with the substrate is highly dependent on the protein structure as well as protein substrate and many detailed catalytic cycles have been proposed to describe this process.[16]

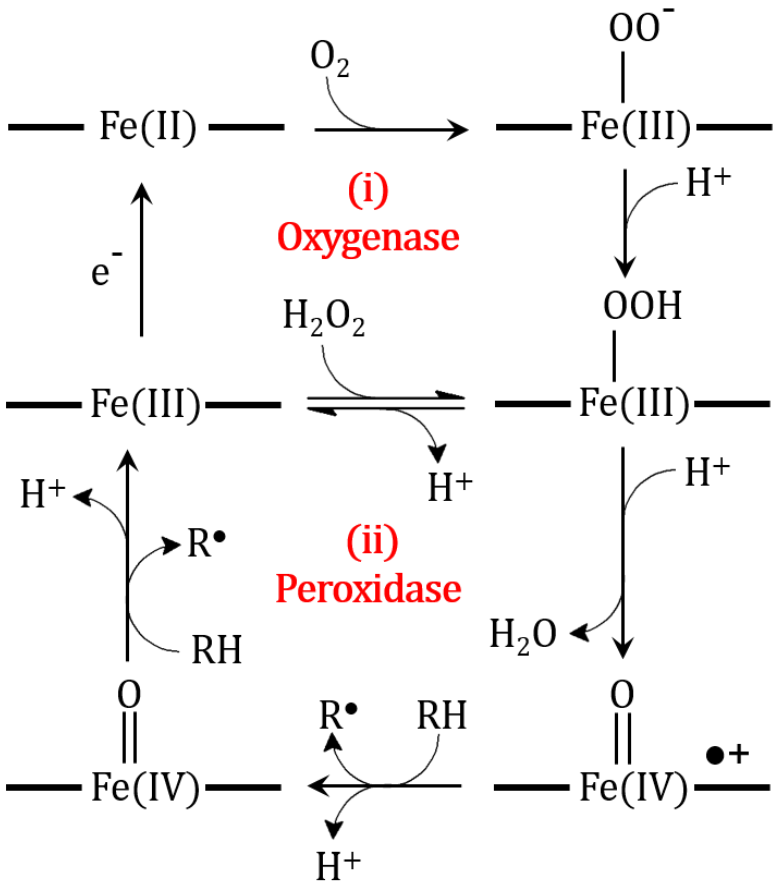

Scheme 1.1: *Typical catalytic cycle of (i) oxygenase and (ii) peroxidase haemoproteins showing the formation of the high valent [Fe(IV)=O(porph)•+] intermediate and subsequent one electron oxidation steps of an electron rich substrate RH to reform [Fe(III)porph]. In the diagram the thick black lines represent the plane of the porphyrin. Note that proximal ligands on the Fe centre have been omitted for clarity.*

The importance of these proteins in biology has prompted extensive experimental and theoretical investigations into using either haem or synthetic derivatives (e.g. tetraphenyl porphines) of this molecule as a catalyst outside of the protein environment.

1.2 Fe(III) porphyrin homogeneous catalysis

There have been numerous studies investigating the ability of Fe(III) porphyrins dissolved in an aqueous solutions to mimic the activity of enzymes such as cytochrome *P450* and horseradish peroxidase to catalyse the oxidation of organic substrates.[19,20,23–30] It is well known that FePPIX readily forms μ-oxo dimers in aqueous solutions; therefore there have been many strategies to prevent this, as well as aggregation of the porphyrin molecules in solution.

One method that has been utilized to circumvent these problems is the synthesis of synthetic tetraphenyl porphyrins (TPP).[31] These porphyrins contain a phenyl group at the *meso*- position on the porphyrin ring, a site which can be further functionalized to elicit desired properties of the porphyrin. An example of these synthetic porphyrins that have been designed to prevent aggregation and oxidation are 'picket fence' and "capped" porphyrins (Fig. 1.2).[32–36] These porphyrins contain bulky side chains attached at the *meso* position and will create steric bulk on one plane of the porphyrin therefore hindering the process of aggregation as well as formation of the μ-oxo dimeric form.[33] While this method has been used with varying degrees of success to prevent μ-oxo dimerization, problems of low solubility and aggregation still remain.

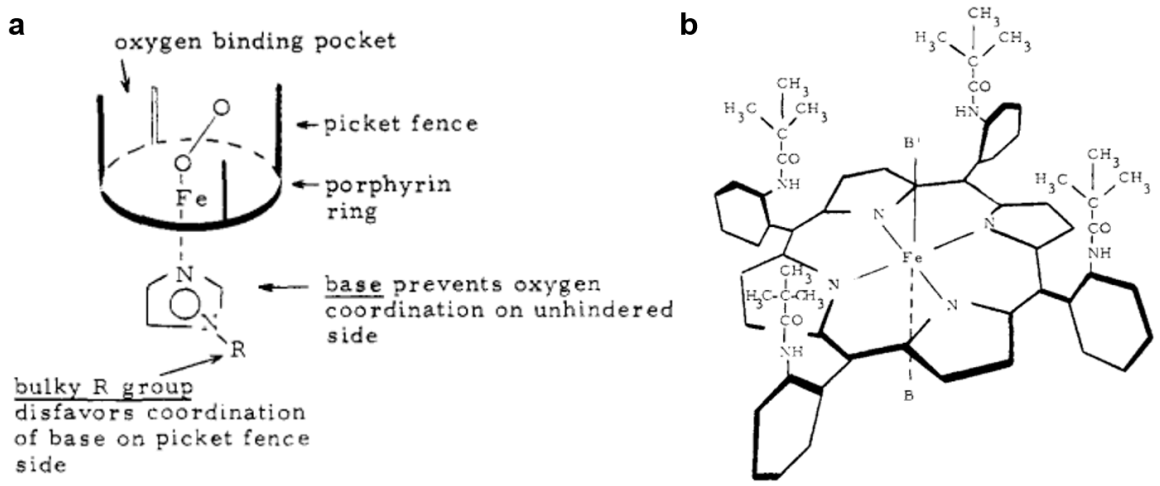

Figure 1.2: *Picket fence porphyrins. (a) The 'picket fence' concept as described by Collman et al.;*[35] *(b) Structure of picket fence porphyrins synthesised. B and B' refer to the two axial ligands used in the study. Reprinted with permission from Ref. [35]. Copyright © 1975, American Chemical Society.*

One such example of a study of the peroxidase activity of a tetraphenyl porphyrin designed to not aggregate or form µ-oxo dimers was conducted by Zipplies *et al.*[23] In this study a non-aggregating tetraphenyl porphyrin was synthesized [5,10,15,20-tetrakis(2,6-dimethyl-3-sulfonatophenyl)porphyrin] and the decomposition of H_2O_2 was studied resulting in the proposal of possible mechanisms.

More recently studies by Brausaum *et al.*[19] and Cunningham *et al.*[37] on tetraphenyl porphyrins designed to be non-aggregating and to not form µ-oxo dimers have investigated both the peroxidatic and oxidative ability of these catalysts by investigating the decomposition of H_2O_2 and subsequent oxidation of diammonium-2,2′-azinobis(3-ethylbenzothiazoline-6-sulfonate) (ABTS) and 3-hydroxy-2-cycloheptylnaphtho-1,4-quinone respectively. In both cases a hypothesized rate law was derived and the experimental evidence was used in support of this.

When studying the peroxidase activity of native FePPIX, different strategies need to be used due to the low aqueous solubility as well as the problems previously mentioned of this cofactor. Adams[29] conducted a study using an octapeptide derived from cytochrome *c*, microperoxidase 8 (MP-8). This prevents dimersation and aggregation. A study by Ribeiro *et al*. makes use of native haem in solution in order to determine its activity in solution, and while Fe(III)PPIX displays peroxidase activity, the effects of dimerization and haem degradation are significant.[38]

One of the major drawbacks of metalloporphyrin catalysts in solution is that they can be degraded by hydroxyl radicals produced during peroxidation reactions and thus suffer from low recyclability.[19,39] Furthermore, while haem is very active in a protein environment, once removed, the catalytic power decreases significantly. This is due to a variety of factors including poor aqueous solubility, aggregation and irreversible oxidation in aqueous solutions.[20,24] It is for this reason that encapsulation of FePPIX (and tetraphenyl porphyrins) in solid supports forming heterogeneous catalysts has garnered much interest in recent years.[40,41]

1.3 Encapsulation of FePPIX and other porphyrins on solid supports

While haem- containing enzymes are all homogeneous, heterogeneous catalysts provide many advantages in a synthetic environment such as ease of separation, waste minimization and reusability.[4,5] It is for this reason that the development of heterogeneous catalysts is a focus of green chemistry due to elimination the need for distillation or extraction to separates products and catalyst.[5,6] By immobilizing haem onto a solid support, problems which are prevalent in porphyrin homogeneous catalysts, can be circumvented. In recent years there has been a surge of interest in immobilizing haem and synthetic porphyrins onto materials using different strategies with the aim of synthesizing effective heterogeneous oxidation catalysts.

1.3.1 Encapsulation of porphyrins in layered double hydroxides and mineral clays

One of the first examples of immobilisation of porphyrins on mineral clays for application as heterogeneous catalysts was reported by Battioni and co-workers in 1990.[42] In this study Mn(III) 5,10,15,20-*tetrakis*(1-methyl-4-pyridinio)porphyrin (TMPyP) was immobilised on montmorillonite, a silica-based smectite clay. The immobilisation was conducted by stirring the porphyrin with the clay for 24 h. Successful immobilisation was confirmed by UV-visible spectroscopy and elemental analysis. The oxidation of alkanes (cyclo-octane, cyclohexane, adamantane, heptane and pentane) by iodosylbenzene (PhIO) was investigated. The supported porphyrin was found to have drastically improved activity relative to the porphyrin in solution and was shown to be particularly active for short linear alkanes.

Nakagaki and co-workers immobilised two Fe(III) anionic porphyrins, [5,10,15,20-*tetrakis*(2-fluoro-6-chlorophenyl-3-sulfonatophenyl)porphyrinate] Fe(III)Fe(III)TCFSPP)$^{3-}$) and [5,10,15,20-*tetrakis*(2,6-difluorphenyl-3-sulfonatophenyl) porphyrinate] Fe(III) (Fe(III)TDFSPP)$^{3-}$), onto exfoliated layered double hydroxides (LDH).[43] The porphyrins were immobilised by reaction with pre-formed Al-Mg layered hydroxides exfoliated with glycine under Ar and filtering off the resultant product (Fig. 1.3). Powder X-ray diffraction (PXRD) confirmed that the distance between the layers (7.8 Å) did not change after loading of the Fe(III) porphyrins therefore indicating that the porphyrin is localised on the external basal planes and edges of the material.

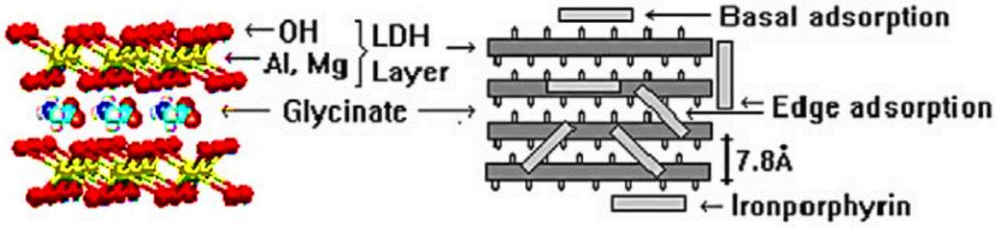

Figure 1.3: *Schematic representation of Fe(III) porphyrins immobilised on LDH clay, intercalated with glycine.*[43] *Reprinted with permission from Ref. [40]. Copyright © 2005, Elsevier.*

The epoxidation of cyclooctene and oxidation of cyclohexane by PhIO catalysed by both synthesized catalysts was investigated. It was found that both materials had a higher yield of epoxidation with Fe(TCFSPP) than the porphyrin in solution (87%). The oxidation of cyclohexane by Fe(TDFSPP)@GlyLDH showed a high alcohol vs. ketone selectivity, although the yield was low. It was interesting to note that the yield of the oxidation of cyclohexane increased from approximately 20% – 45% in the first cycle to 80% – 85% in the second and third cycles respectively.

While there are multiple examples of synthetic porphyrins being immobilised on a range of mineral clays and layered materials;[44–46] there are only two examples of FePPIX being immobilised on these materials.[47,48] Inada and co-workers immobilised haemin (Fe(III)PPIX-Cl) on hectorite, a synthetic smectite mineral, but the material was not used for catalysis and was found to be to be soluble after immobilisation of haemin and therefore homogeneous in nature.

Zhang *et al*. aimed to mimic the activity of horseradish peroxidase (HRP) by synthesizing a haemin-montmorillonite conjugate.[48] The surface of the montmorillonite clay was first histidine functionalised to facilitate coordination of haemin to the clay. This procedure aimed to increase the loading of haemin onto the montmorillonite which was determined using UV-visible spectroscopy. The peroxidatic capability of the synthesised material was investigated using the oxidation of guaiacol, a commonly used reaction to assay the acidity of HRP enzymes (Fig. 1.4a). It was found that the histidine functionalised material had far greater activity than both the non-functionalised haemin@clay material as well as native haematin (Fig. 1.4b).

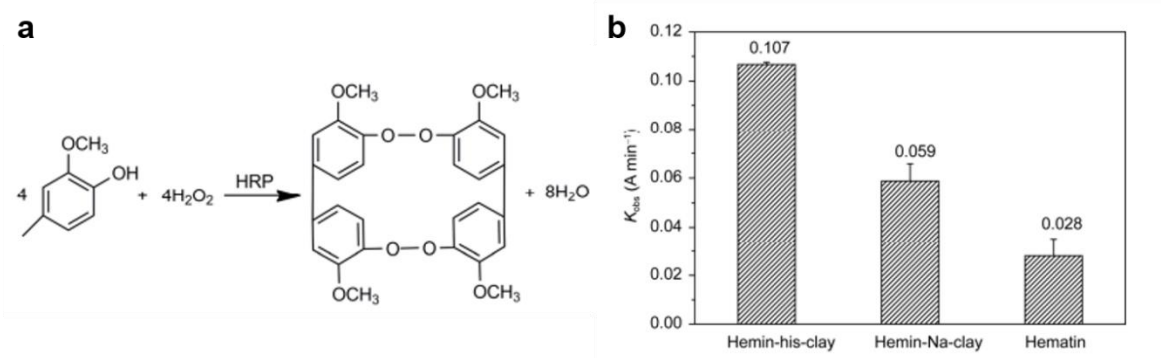

***Figure 1.4**: (a) Oxidation of guaiacol by H_2O_2 catalysed by HRP; (b) Observed rate constants of haemin@histidine-clay, haemin@clay and native haemin.*[48] *Reprinted with permission from Ref. [45]. Copyright © 2015, SpringerLink.*

1.3.2 Encapsulation of porphyrins in mesoporous molecular sieves

There has been major interest in porphyrin encapsulation in mesoporous silicate sieves such as MCM-41 (Fig. 1.5). These molecular sieves are comprised of a hexagonal array of rods with uniform mesopores and can be engineering to have a range of pore sizes from approximately 15 Å to greater than 100 Å and therefore have good potential for encapsulating catalysts such as porphyrins for heterogeneous catalysis.[49,50]

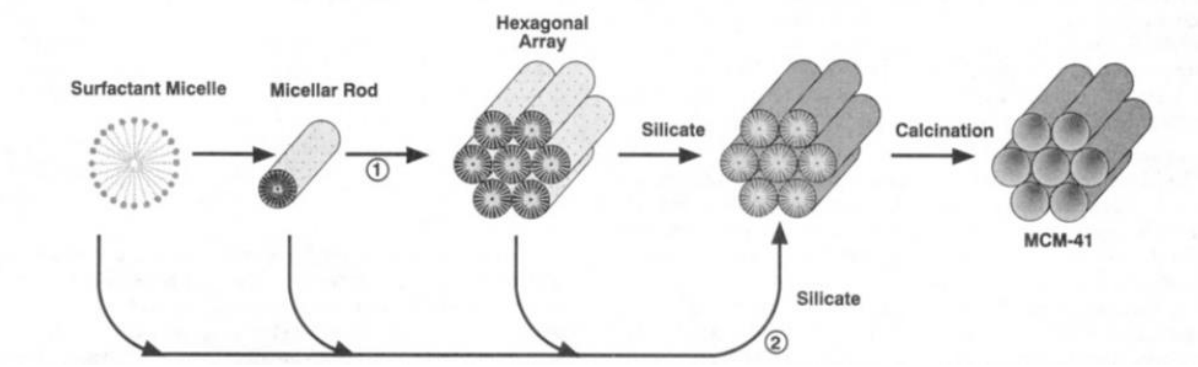

Figure 1.5: *Mechanism of formation and structure of MCM-41.*[49] *Reprinted with permission from Ref. [46]. Copyright © 1992, American Chemical Society.*

One of the first reports of porphyrin encapsulated catalysts in MCM-41 was by Stein and co-workers who reported the preparation of Mn(III) *meso*-tetrakis(5-trimethylammoniopentyl)porphyrin (TMAP) in MCM-41 in 1998.[51] The encapsulation was successful using two different methods, namely hydrothermal synthesis and surfactant-porphyrin ion exchange with previously synthesized MCM-41. Interestingly, using UV-visible spectroscopy, the authors found that when the ion exchange mechanism was used, the porphyrin molecules formed dimers or aggregates but when the porphyrin molecules were encapsulated during the synthesis procedure, monomers were obtained. The porphyrin could be metallated with Cu^{2+}, Ni^{2+} and Fe^{2+} ions and it was found that no leaching of the porphyrin out of the pores of MCM-41 occurred. The peroxidase activity of the material was examined by using the catalyst for the peroxidation of the azo dye β-naphthol violet. It was found that the

material synthesized by hydrothermal synthesis was more active than that synthesized by ion exchange. This was attributed to the monomeric form of the porphyrin being obtained during the hydrothermal synthetic procedure.

An example of an Fe(III) tetraphenyl porphyrin encapsulated by Al-MCM-41 was reported by Nur and co-workers.[52] In this study Fe(III)-5,10,15,20-tetra-(4-pyridyl)porphyrin (TPyP) was encapsulated in Al-MCM-41 with an Al/Si ratio of 20, where the porphyrin was metalled after inclusion of TPyP into the mesopores of Al-MCM-41. The same porphyrin was also encapsulated in poly(methacrylic acid) (PMAA) by polymerising the methacrylic acid with a cross-linker around the FeTPyP. Both catalysts were characterised using UV-visible, PXRD and FTIR spectroscopy which confirmed successful encapsulation. The oxidation capabilities of the synthesized catalysts were investigated using the oxidation of benzene to phenol by H_2O_2. It was found that both synthesized catalysts were more active than FeTPyP in solution, but FeTPyP@PMAA was more active than FeTPyP@Al-MCM-41. FeTPyP@Al-MCM-41, however, exhibited better recyclability and it was hypothesized that this was due to leaching of FeTPyP out of the polymer material.

There are several further examples of synthetic Fe(III), Co(II), Ru(II), Pd(II) and Mn(III) metalloporphyrins being encapsulated in molecular sieves such as MCM-41,[53–55] and more recently MCM-48[56] and SBA-15,[57,58] a mesoporous material in which the silica nanoparticles are arranged in a hexagonal array and have pores of 4.6 – 30 nm.[59] These materials were used to investigate a range of oxidation and epoxidation reactions, most commonly the oxidation of cyclohexene and styrene using H_2O_2 and PhIO as oxidants.

One interesting example was reported by Che and co-workers who synthesized a ruthenium chiral porphyrin immobilised on both MCM-41 and MCM-48 (which has a three-dimensional structure which can easily be functionalised).[60] In this study Ru(II) 5,10,15,20-tetrakis-(1S,4R,5R,8S)-1,2,3,4,5,6,7,8-octahydro-1,2,5,8-dimethanoanthracen-9-yl]porphyrin, $H_2(D_4$-Por*), was immobilised. This porphyrin had previously been shown to have excellent reactivity and enantioselectivity in solution but there were high costs involved in the separation of the catalyst from the reaction mixture.[61] The porphyrin was immobilised onto the surface of the molecular sieve or onto silica by modifying the respective surfaces with 3-aminopropyltriethoxysilane (Fig. 1.6). The porphyrin molecule was subsequently strongly coordinated to the amino group.

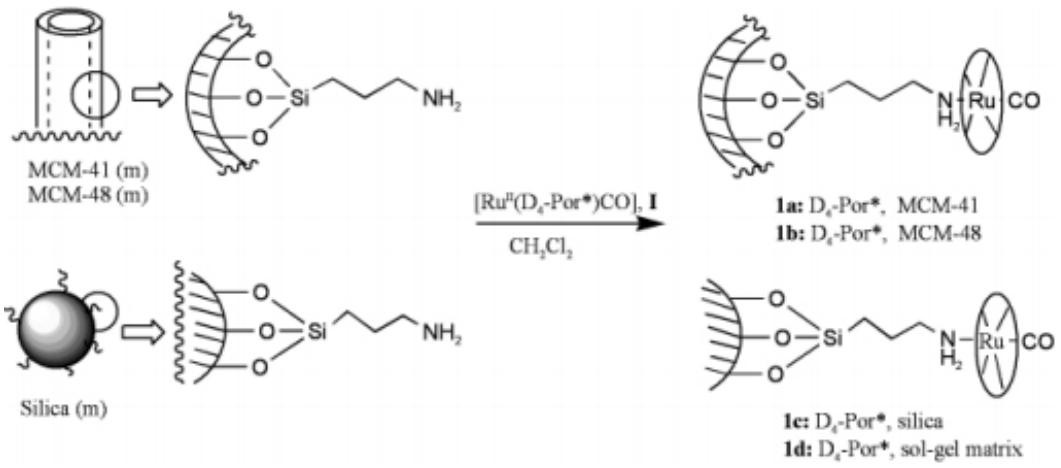

Figure 1.6: *Immobilisation of $H_2(D_4$-Por*) onto MCM-41 and MCM-48 (top) and silica surfaces (bottom).*[60] *Reprinted with permission from Ref. [57]. Copyright © 2002, Royal Society of Chemistry.*

The epoxidation of alkenes using 2,6,-dichloropyrine-*N*-oxide as oxidant was investigated. It was found that the porphyrin supported on both the molecular sieves and silica surfaces had very good conversions (72% - 99%) and excellent enantioselectivity (ee ≈ 70% for most substrates) with the exception of the porphyrin immobilised on the silica surface (ee 43%).

Furthermore, it was demonstrated that the catalyst could be reused through two cycles with only a slight drop in conversion percentage and a slight decrease in the enantioselectivity. This demonstrated that immobilisation of the porphyrin catalyst onto a silica surface or encapsulation within a molecular sieve was effective in converting a homogeneous catalyst to a heterogeneous one.

While there are multiple examples of molecular sieves being used for encapsulation of a variety of synthetic tetraphenyl porphyrins, there is, to date, only one reported example of FePPIX being encapsulated in a molecular sieve, MCM-41, published by Nazari *et al*. in 2005.[62] FePPIX was directly encapsulated into the pores of MCM-41 using micelles of cetyltrimethylammonium bromide both as a solvent for FePPIX and as a template for formation of MCM-41. Successful encapsulation was confirmed using N_2 adsorption isotherms, X-ray diffraction (XRD), Fourier transform infrared spectroscopy (FT-IR) and solid-state UV-visible spectroscopy techniques. The activity of FePPIX@MCM-41 was compared to the activity of MCM-41 impregnated with Fe(III) ions as well as horseradish peroxidase. The ability of FePPIX@MCM-41 to oxidise phenol and guaiacol as well as catalyse the synthesis of indophenol was investigated. It was found that the FePPIX@MCM-41 material was far more active than MCM-41 impregnated with Fe(III) ions with a 100-fold increase in relative initial rates. It was further observed that the FePPIX@MCM-41 material showed an increase in activity relative to FePPIX in solution, but, as expected, the activity was lower than that of horse radish peroxidase.

1.3.3 Encapsulation of porphyrins in zeolites

Zeolites are microporous aluminosilicate materials built from SiO_4 and AlO_4 tetrahedra which have attracted great interest in the field of heterogeneous catalysis in recent years.[2,63] Zeolites contain molecular sized channels and pores arranged in a three-dimensional network and can therefore exhibit both shape and size selectivity.[63] The most commonly used zeolites for porphyrin encapsulation are zeolites X (Z-X) and Y (Z-Y). Encapsulation of porphyrins into the cavity can be achieved using the method described by Balkus *et al*. for encapsulation of perfluorophthalocyanines, where the zeolite is built around the molecule.[64] Zeolite Y contains a three-dimensional, twelve-membered ring system and has been used with great success in the field of heterogeneous catalysis as the active component in catalysts for fluid catalytic cracking.[63]

One example of synthetic Fe(III) tetraphenylporphyrins being encapsulated in Z-X cavities in a zeolite X was reported by Rosa *et al*. who used the method described by Balkus *et al.*[64] to encapsulate Fe(III)TMPyP or Fe(III) 5-mono(2,6-dichloro-phenyl)10,15,20-tris(4-*N*-methylpyridyl)porphyrin (Fe(III)P2) (Fig. 1.7).[65] The epoxidation of cyclooctene and hydroxylation of adamantane and cyclohexane by PhIO were investigated. Cyclooctene was selectively oxidised to *cis*-epoxycyclooctane by both the free and encapsulated porphyrins and the yield of *cis*-epoxycyclooctane was increased from 50% and 60% to 86% and 95% for Fe(III)TMPyP and Fe(III)P2 respectively. The hydroxylation of adamantane gave lower yields of 52% and 45% for Fe(III)TMPyP and Fe(III)P2 respectively and was selective for carbon 1. The hydroxylation of cyclohexane was also less efficient, and gave a yield of 50% for Fe(III)TMPyP and an alcohol/ketone ratio of approximately 10. In both cases the encapsulated Fe(III)TMPyP and Fe(III)P2 were more active than the unencapsulated porphyrins in solution.

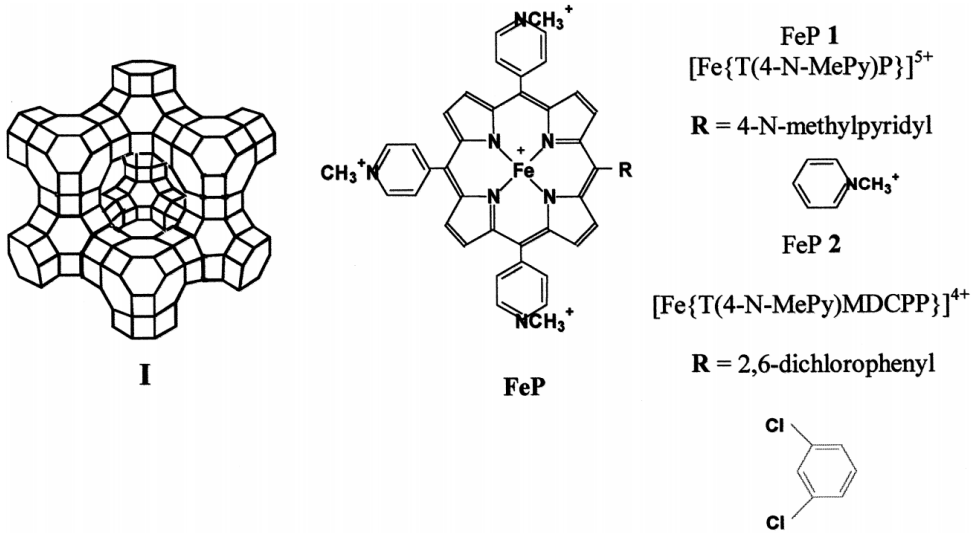

Figure 1.7: *Encapsulation of two Fe(III) tetraphenyl porphyrins into the cavities of zeolite NaX.*[65] *Reprinted with permission from Ref. [62]. Copyright © 2000, Elsevier.*

Moghadam *et al*. encapsulated Mn(III)TMPyP into zeolite X and Y (NaX and NaY) by synthesizing the zeolite around the porphyrin.[66] The materials obtained were characterised by UV-visible spectroscopy, PXRD, FT-IR and neutron activation analysis. Interestingly, PXRD analysis showed that encapsulation of the porphyrin has very little effect on the structure of both NaX and NaY. It was found that the loading of the porphyrin into NaY was almost double that in NaX and it was proposed that the difference was a result of the differing Si/Al ratios present in the two frameworks. The catalytic activity of both catalysts was investigated by oxidising a variety of linear and cyclic alkenes using sodium periodate ($NaIO_4$). Reactions were conducted either with mechanical stirring or microwave irradiation. A decrease in yield with increase in size of the linear alkenes was observed, indicating the possibility of the material being used for shape selective catalysis.

Xia and co-workers encapsulated Mn(III)TMPyP penta-acetate in both mesoporous MCM-41 and DMY (a NaY zeolite).[56] The porphyrin was encapsulated by soaking the zeolite in a solution containing the porphyrin. The potential of the porphyrin encapsulated materials as oxidation catalysts was investigated using the epoxidation of styrene and cyclohexene by PhIO (Scheme 1.2). It was found that the encapsulated porphyrin was more effective than the native porphyrin in solution and that the material could be reused through multiple cycles, although prolonged reuse resulted in a loss of activity.

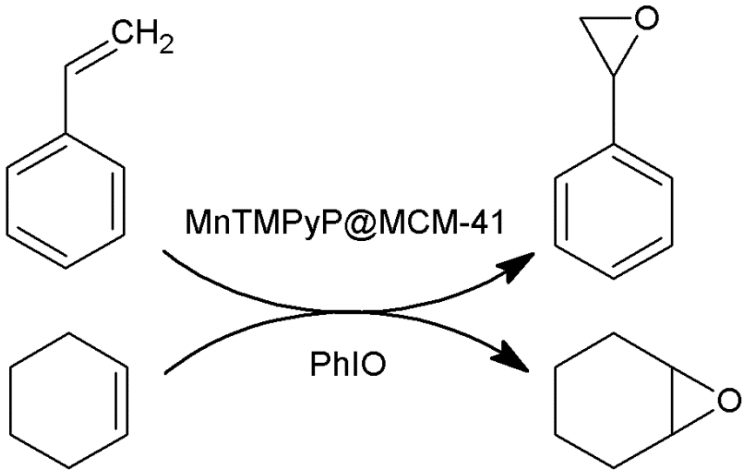

Scheme 1.2: *Epoxidation of styrene (top) and cyclohexene (bottom) by PhIO catalysed by Mn(III)TMPyP@MCM-41 and Mn(III)TMPyp@DMY,*

Another example of an Fe(III) synthetic porphyrin being encapsulated in a NaY zeolite was reported by Karimipour *et al.*[67] In this study [*meso*-tetrakis(3-pyridyl)porphyrinato]iron(III) chloride was encapsulated in NaY in the same manner as the previous examples and characterised using PXRD, UV-visible spectroscopy, FT-IR and atomic absorption (AA) spectroscopy and scanning electron microscopy (SEM). The epoxidation of cyclohexene and other alkenes by (diacetoxyiodo)benzene ($PhI(OAc)_2$) was used to probe the catalyst activity. It was found that the catalyst showed good activity (yields of 16% - 94%) and that it could be recovered and reused through multiple cycles. The oxidation of 4-nitrobenzyl alcohol as well

as a 1,4-dihydropyridine were investigated and very high yields were obtained in both cases (97% and 100% respectively).

To date, there are no examples of native FePPIX being encapsulated into zeolites reported in the literature.

1.3.4 Encapsulation of porphyrins in gels

The term gel is a broad description of any gelating species that uses non-covalent interactions when formed.[68,69] Gels are solid-like materials and do not flow like a liquid, and can therefore be used to encapsulate porphyrins to form a heterogeneous catalyst.[68]

In 1994 Iamamoto *et al*. reported the Fe(III) and Mn(III) *tetra*-2,6-dichlorophenylporphyrin (Fe(III)TDCPP and Mn(III)TDCPP) and Fe(III) and Mn(III) tetraphenylporphyrin encapsulated in an imidazole propyl gel and silica gel.[70] The porphyrin-containing material was synthesized by stirring the metalloporphyrin with the gel materials and filtering off the product. Characterisation was performed by UV-visible and electron paramagnetic resonance spectroscopies. The oxidation of cyclohexane to cyclohexanol by PhIO was studied and compared to the porphyrins in solution. It was found that the supported catalysts were more active than the catalysts in solution, and that Mn(III)TDCPP@imidazole propyl gel was the most active catalyst, giving the highest yield of cyclohexanol (67%). It was also found that the material could be recycled and reused up to five cycles.

Battioni and co-workers reported the synthesis of a silica based gel using the sol-gel process constructed by hydrolysis and polycondensation, or co-condensation of Fe(III) and Mn(III) meso-*tetrakis*-pentafluorophenylporphyrins derivatised with a trifluorosilyl functional group and tetraethoxysilane.[71] The oxidation of heptane, cyclohexane and adamantane using PhIO and epoxidation of cyclohexene using ^{t}BuOOH was investigated. It was found that these materials were efficient catalysts and showed a size selective oxidation of the larger substrate.

There are many examples of synthetic porphyrins being encapsulated in gels for a variety of applications; however, there are fewer examples of these materials being used as heterogeneous oxidation catalysts.[72–77] Most of these examples make use of silica-based gels as the support for the porphyrin. There are four examples of FePPIX being encapsulated in gel materials;[78–81] however, two of these examples are water-soluble nanogels and are therefore not heterogeneous catalysts.[78,81]

The first report of FePPIX immobilised in a supramolecular hydrogel for application in heterogeneous catalysis was published by Wang *et al*. in 2007.[80] Haemin was directly incorporated into the hydrogel (formed with two derivatised amino acids) by including it in the reaction mixture, which self-assembled to form a haemin@hydrogel material (Scheme 1.3). Transmission electron microscopy (TEM) with EDX was used to show that the haemin was localised along the surface of the nanofibers that made up the hydrogel, rather than being encapsulated in the nanofibers themselves. For comparison, the haemin@gel material was synthesized with and without a histidine residue, to investigate the effect of a potential axial ligand to coordinate to the iron centre of FePPIX. Importantly, it was found using UV-visible spectroscopy that haemin was in a monomeric form when encapsulated in the gel.

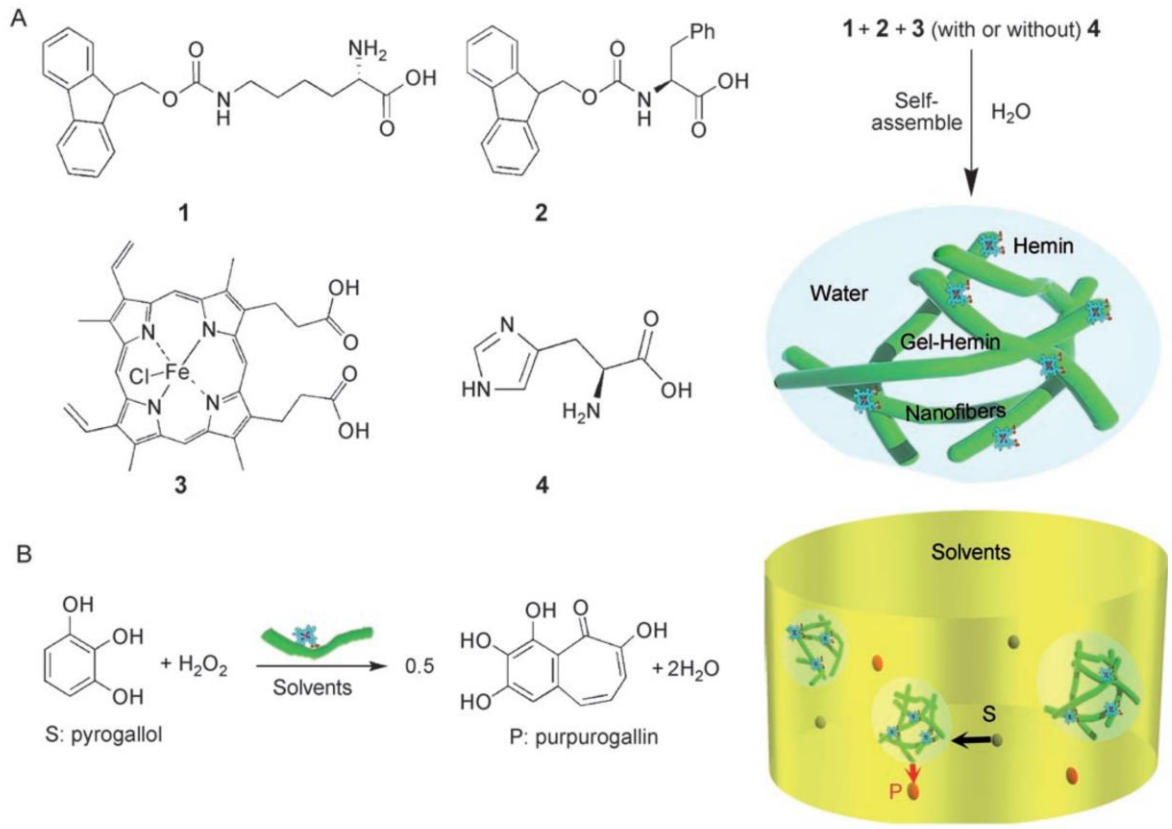

Scheme 1.3: *A) Derivatised amino acids (**1** and **2**), haemin (**3**) and histidine (**4**) used to synthesise supramolecular hydrogels; B) Peroxidation of pyrogallol to purpurogallin. In the figure, S = substrate (pyrogallol), P = product (purpurogallin), and solvent = aqueous buffer solution (0.01 M phosphate, pH 7.4,) or toluene.*[80] *Reprinted with permission from Ref. [77]. Copyright © 2007, John Wiley and Sons.*

The peroxidatic potential of the material was investigated by determining the ability of the haemin@gel material to catalyse the oxidation of pyrogallol to purpurogallin (Scheme 1.3B) in an aqueous solution and organic solvent (toluene). It was found that the encapsulated haemin was dramatically more active than native haemin in both aqueous and organic solutions. Interestingly, the haemin@gel prepared in the presentence of histidine was more active than that prepared in the absence of histidine and the increase in activity relative to haemin was greater in the organic solvent compared to aqueous solution. This study indicated that gel encapsulation is a viable method for preparing haem-based heterogeneous oxidation catalysts.

This work was extended during a study published in 2008, where the activities of synthetic derivatives of haem encapsulated in the same hydrogel were compared to that of native haemin (Fig. 1.8).[79] The activity was assayed using the same reaction, oxidation of pyrogallol to purpurogallin in an aqueous buffer as well as toluene, used in the initial study. It was found that the synthesized porphyrins were all far more active than native haemin, with the most active derivative (**6**) in toluene reaching 90% of the activity of horseradish peroxidase in aqueous buffer.

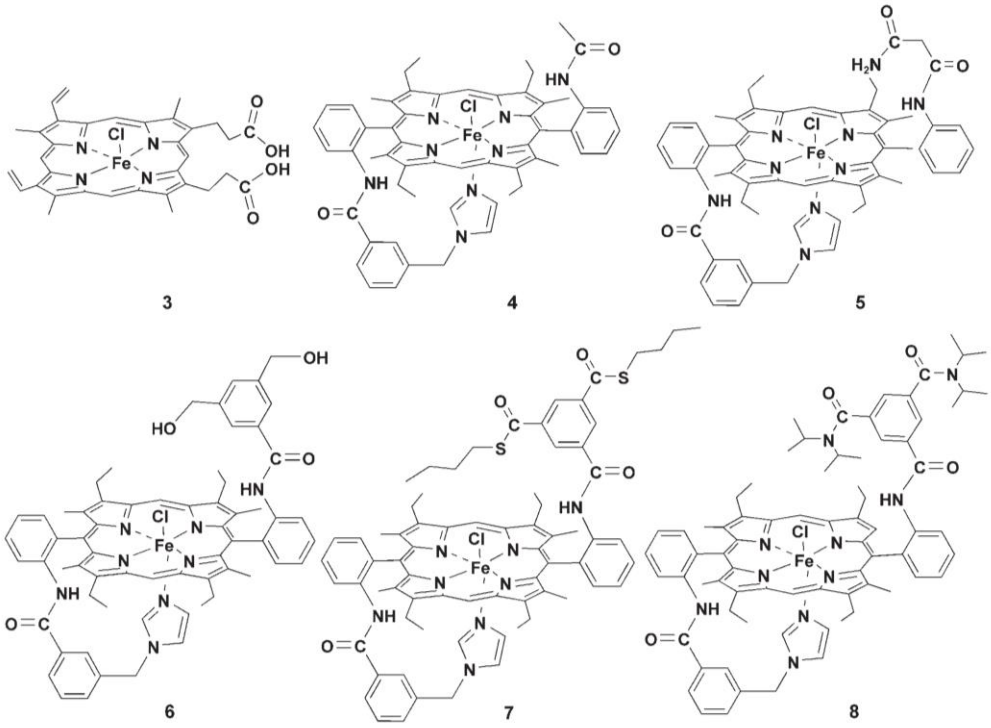

Figure 1.8: *Structures of haemin (**3**) and synthetic derivatives (**4** – **8**) used in the study by Wang et al.*[79,80] *Reprinted with permission from Ref. [76]. Copyright © 2008, John Wiley and Sons.*

While the above-mentioned solid supports have been successful in improving the catalytic activity of Fe(III)PPIX and its derivatives compared to the corresponding porphyrin in solution, these supports do not provide a well-defined active site as observed in haemoproteins. It is for this reason that metal-organic frameworks have gained much interest in recent years in the field of porphyrin heterogeneous catalysis.

1.4 Encapsulation of porphyrins in metal-organic frameworks

Metal organic materials (MOMs) are a broad class of materials which have, in their most basic form, metal centre(s) coordinated to organic linkers in order to create a material which has a variety of functionalities.[82–84] This class of materials can be sub-divided into four sub-classes, namely (i) coordination complexes, (ii) metal-organic polyhedra (MOPs), (iii) metal-organic frameworks (MOFs) and (iv) metal-organic gels (MOGs).[40] MOFs consist of metal-containing building blocks which serve as nodes that are connected into a two- or three-dimensional network by multitopic organic ligands.[85–88] These permanently porous materials afford a large degree of structural versatility and, by altering the ligand and metal combination, it is possible to tune the dimensions and chemical composition of the pores to design materials for specific applications.[89,90] MOFs have attracted a lot of interest in the field of porphyrin heterogeneous catalysis as they have the potential to overcome common problems identified with other solid supports by providing a well-defined environment for catalyst confinement in isolated active sites in which substrate access to the catalytic sites is also controlled, thereby creating robust and efficient catalysts.[1,91–93]

Encapsulation of metalloporphyrins into a MOF framework can either be done post-synthetically or *in situ* during the synthesis process.[40] When encapsulating the porphyrin *in situ*, a method commonly termed the 'ship-in-a-bottle process', the framework is built around the porphyrin in the reaction mixture, thereby locking the porphyrin in place and preventing it from leaching out of the framework through multiple catalytic cycles. The encapsulated porphyrin can either be pre-metallated, the porphyrin metallated *in situ* during the synthesis of the metalloporphyrin@MOF material or incorporation of the metal centre can be done post-synthetically by exposing the synthesized porphyrin@MOF material to a solution of the desired metal ions.

1.4.1 Encapsulation of synthetic porphyrins in MOFs

The first example of a metalloporphyrin being encapsulated in a metal-organic material (MOM) was reported by Hupp *et al*. in 1999 who encapsulated a Zn porphyrin in a Zn containing thin film material.[94] The first reported study of a synthetic tetraphenyl porphyrin being encapsulated in a MOF was reported by Eddaoudi and co-workers in 2008.[95] In this report, the sulfonate salt of TMPyP (Fig. 1.9a), was encapsulated in a zeolite-like MOF constructed from $In(NO_3)_3 \cdot xH_2O$ and 4,5-imidazoledicarboxylic acid (H_3ImDC) (rho-ZMOF) (Fig. 1.9b). This framework was negatively charged and therefore required a cationic porphyrin molecule for successful encapsulation. Attempts to encapsulate neutral and anionic porphyrins were unsuccessful. The material was characterised using solid-state UV-visible spectroscopy on washed crystals and the presence of the Soret band confirmed encapsulation of [H_2TMPyP] into the truncated octahedral cage of the MOF. Single crystal XRD of crystals obtained was not possible. This was attributed to the lowering of the inherent symmetry of TMPyP. The porphyrin was successfully post-metallated with Mn(III), Co(III), Cu(II) and Zn(II) ions and was confirmed using solid-state UV-visible spectroscopy.

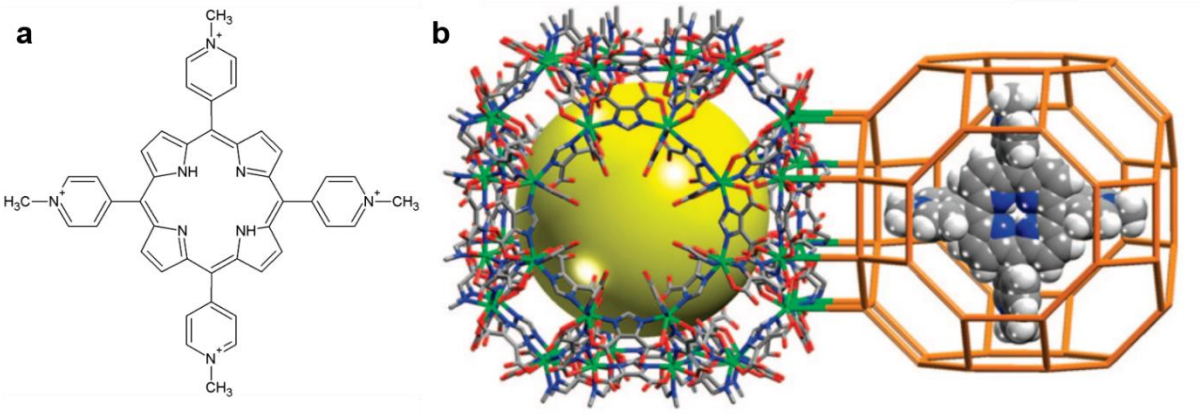

Figure 1.9: *(a) Structure of TMPyP; (b) Structural representation of rho-ZMOF encapsulating TMPyP.*[95] *Reprinted with permission from Ref. [93]. Copyright © 2008, American Chemical Society.*

The oxidation capability of the synthesized Mn(III)TMPyP@rho-ZMOF was investigated using the oxidation of cyclohexane to cyclohexanone via cyclohexanol. The oxidising agent ^{t}BuOOH was used in 2:1 ^{t}BuOOH to cyclohexane molar ratio. A conversion of reactants to a mixture of products of 91.5%, where the major product (approx. 60%) was cyclohexanone was reported. A turnover number of 23.5 was obtained after 24 h and the catalyst retained its activity through eleven consecutive cycles.

One of the most significant contributions to the field of metalloporphyrin@MOFs was published by Larsen *et al*. in 2011.[41] In this study a collection of metalloporphyrins were encapsulated in the HKUST-1 framework, a Cu/Zn framework constructed from three connected trimesic acid (benzene-1,3,5-tricarbxylic acid, BTC) ligands and four connected Cu/Zn carboxylate [Cu/Zn$_2$(-COO)$_4$] square paddlewheels which affords a framework with *tbo* topology. Frameworks with this topology have three distinct cages, namely rhombihexahedral, octahemioctahedral, and tetrahedral. The octahemioctahedral cage (diameter 13 Å), however, is the only cage suitable for porphyrin encapsulation owing to its larger size and volume relative to the other cages.

In this study Fe(III) and Mn(III) tetrakis(4-sulfonatophenyl)porphyrin (Fe(III)/Mn(III)TSPP) were encapsulated in Cu/Zn-HKUST-1 (Fig. 1.10). A loading of 66% of the available cavities was found using inductively coupled plasma optical emission spectroscopy (ICP-OES) when the material was synthesized in a saturated porphyrin solution, and the loading ranged from 33% - 66% when changing reaction conditions. Unlike the study by Eddaoudi and co-workers, in this study single crystal X-ray diffraction data were obtained. This allowed the exact position of the porphyrin in the MOF to be determined (Fig. 1.10 bottom). The phenyl rings extended into the adjacent cavities, thereby 'locking' the porphyrin into place and reducing the extent of disorder. The porphyrin molecule was, however, positionally disordered over the three equivalent orientations of the cavity. The loading calculated using the ICP-OES data was supported by the single crystal XRD data. Successful encapsulation was further confirmed using solid state UV-visible spectroscopy.

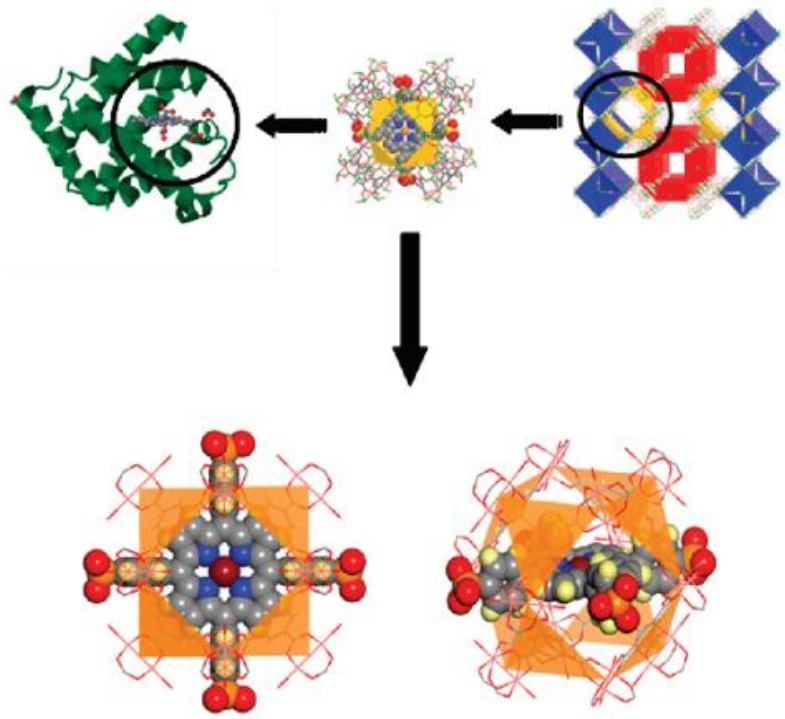

Figure 1.10: *(Top) Encapsulation of Fe(III)/Mn(III)TSPP into a octahemioctahedral cage of HKUST-1 framework and its resemblance to a haemoprotein; (bottom) two of the three equivalent orientations of Fe(III)/Mn(III)TSPP after encapsulation in HKUST-1.*[41] *Reprinted with permission from Ref. [94]. Copyright © 2011, American Chemical Society.*

The oxidation capabilities of FeTSPP@Cu-HKUST-1 were investigated using the oxidation of 2,2'-azino-bis(3-ethylbenzothiazoline)-6-sulphonic acid (ABTS) to $ABTS^{\bullet+}$ using H_2O_2 (Scheme 1.4). The activity was compared to horse heart metmyoglobin (hh-metMb), MP-11, homogeneous Fe(III)TSPP and Cu-HKUST-1. It was found that the initial rate of ABTS oxidation catalysed by the synthesised material was significantly lower than that of hh-metMb, MP-11 and homogeneous Fe(III)TSPP but the overall conversion was comparable to that of MP-11 and homogeneous Fe(III)TSPP. The recyclability was tested over three cycles and it was found that while the conversion percentage remained constant, there was a significant decrease in the rate of each successive reaction.

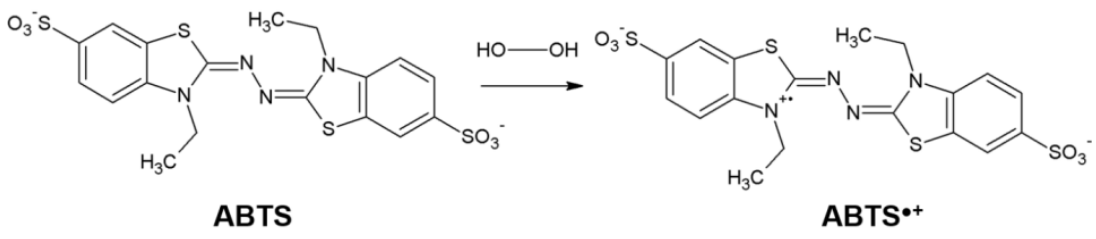

Scheme 1.4: *Fe(III) porphyrin catalysed oxidation of ABTS to ABTS$^{\bullet+}$ by H_2O_2.*

This group also further expanded the investigation to study the photophysical properties of Zn(II) TMPyP encapsulated in Zn-HKUST-1.[96] The structure of this porphyrin encapsulating complex was similar to that of Fe(III)/Mn(III)TSPP in CuHKUST-1 as reported by Larsen *et al*.[41] While no heterogeneous catalysis experiments were conducted with this material, it was interesting to note that the 'locking' of the porphyrin in place as observed in the previous study gave rise to a well resolved fluorescence emission spectrum as well as in increase in the emission lifetime of Zn(II)TMPyP.

In 2012, Zawarotko and co-workers published two significant studies on the encapsulation of metalloporphyrins in MOFs.[97,98] In the first study, Fe(II) (porph@MOF-4), Co(II) (porph@MOF-5), Mn(II) (porph@MOF-6), Ni(II) (porph@MOF-7), Mg(II) (porph@MOF-8) and Zn(II) (porph@MOF-9) M(II)TMPyP were encapsulated in MOFs constructed with BTC and the corresponding metal salt (namely chlorides in the case of Fe(III), Co(II), Mn(III), acetates in the case of Ni(II) and Mg(II) and nitrate in the case of Zn(II)).[97] Crystal structures were obtained for all metalloporphyrin@MOF materials obtained. While it was found that deviation from the ideal HKUST-1 structure occurred in some cases, the mode of encapsulation was retained throughout with the pyridyl rings of the porphyrin 'locked' in the adjacent cavities of the framework.

Porph@MOF-4,-5 and -6 displayed a structure isostructural with the HKUST-1 framework with similar cell dimensions to previously reported porphyrin encapsulating MOFs[41] and *tbo* topology (Fig. 1.11a). Porph@MOF-7 had a unit cell dimension that was larger than that reported for the previous frameworks (a = 27.478 Å, compared to a = 26.594 Å). The synthesis of porph@MOF-9 resulted in significant change to the structure of the previous porphyrin@MOFs synthesized, with a change in space group from *Fm*-3*m* to *Cmmm* and a novel 3,3,4,4,6-connected net (Fig. 1.11b).

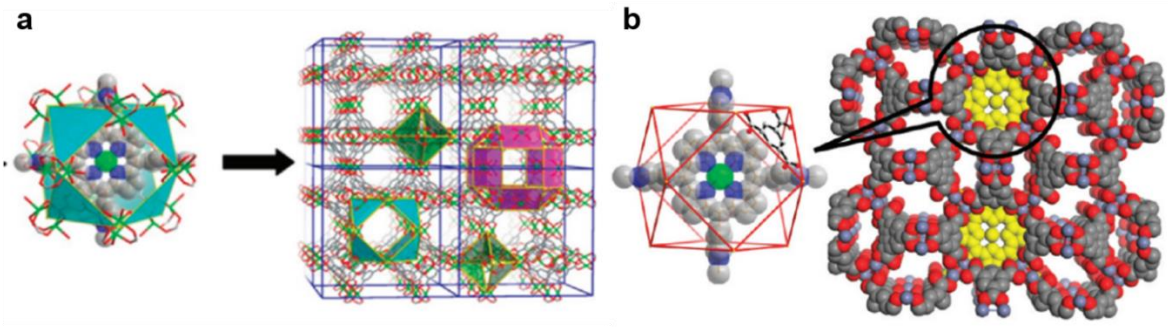

***Figure 1.11**: (a) TMPyP encapsulated in the octahemioctahedral cage of the HKUST-1 framework with pyridyl rings extending into the adjacent cages (left) and the structure of the framework in porph@MOF-4, -5, and -6 with three distinct cage types (right); (b) TMPyP located in an octahemioctahedral cage of porph@MOF-9 (left) and space-fill model of porph@MOM-9 (yellow) projected along the c-axis.*[97] *Reprinted with permission from Ref. [96]. Copyright © 2012, American Chemical Society.*

The epoxidation of alkenes using ^{t}BuOOH as an oxidant was used to investigate the catalytic activity of porph@MOF-4. The oxidation of styrene was completed to about ~85% after 10 h, with the major products identified as styrene oxide and benzaldehyde (30% and 57%, respectively) compared to only ~35% using the equivalent amount of Fe(III)TMPyP in solution. Porph@MOF-4 showed good size selectivity compared to Fe(III)TMPyP in solution (Fig. 1.12) and this was attributed to the increase in steric strain with the addition of bulky

groups. When the recyclability of this catalyst was tested, it was found that there was a drop in the conversion of substrate to products for cycles two and three (~70% and 60% respectively), but the conversion % remained constant for the following three cycles.

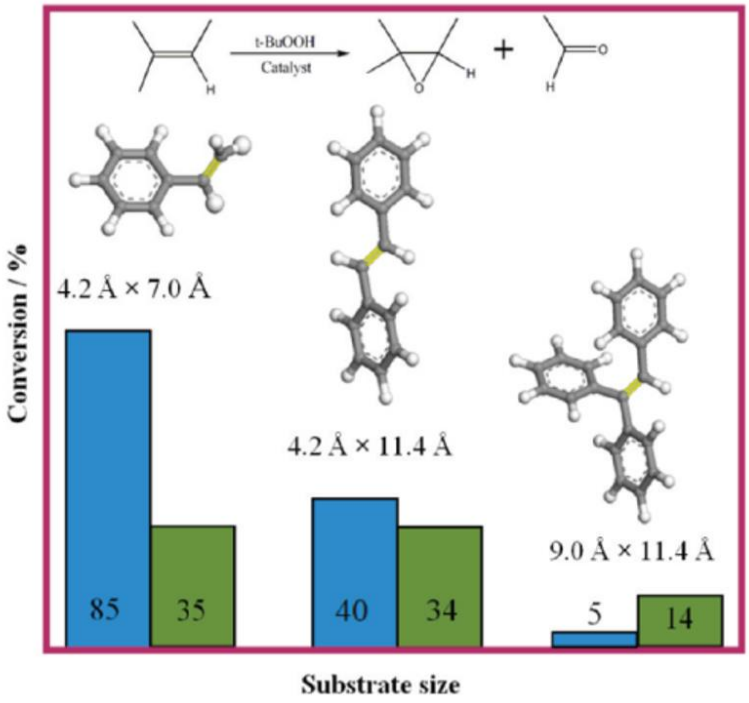

***Figure 1.12**: Epoxidation of alkenes by porph@MOF-4 (blue) and Fe(III)TMPyP (green) showing good size-selective catalytic activity by porph@MOF-4.* [97] *Reprinted with permission from Ref. [96]. Copyright © 2012, American Chemical Society.*

The second study published by Zawarotko and co-workers in 2012 involved the encapsulation of Cd(II)TMPyP cations in a MOF constructed from biphenyl-3,4,5-tricarboxylate (BPT) and $CdCl_3$; namely porph@MOF-10.[98] Single crystals of porph@MOF-10 were obtained and it was found that the framework itself was anionic, with cationic TMPyP and H_3O^+ ions encapsulated in the channels. The framework contained two square channels, with TMPyP being encapsulated exclusively in the larger channel (dimensions 12.6 x 12.6 $Å^2$) (Fig 1.13; channel B). Contrary to other examples of porphyrin encapsulation in MOFs, significant interactions between the porphyrin and the MOF framework were found. There were π···π interactions

between the pyridyl groups of porphyrin and phenyl rings of BPT as well as H-bond between methyl group of cationic pyridyl of the porphyrin and the μ-Cl ligands connected to the Cd ions of the framework.

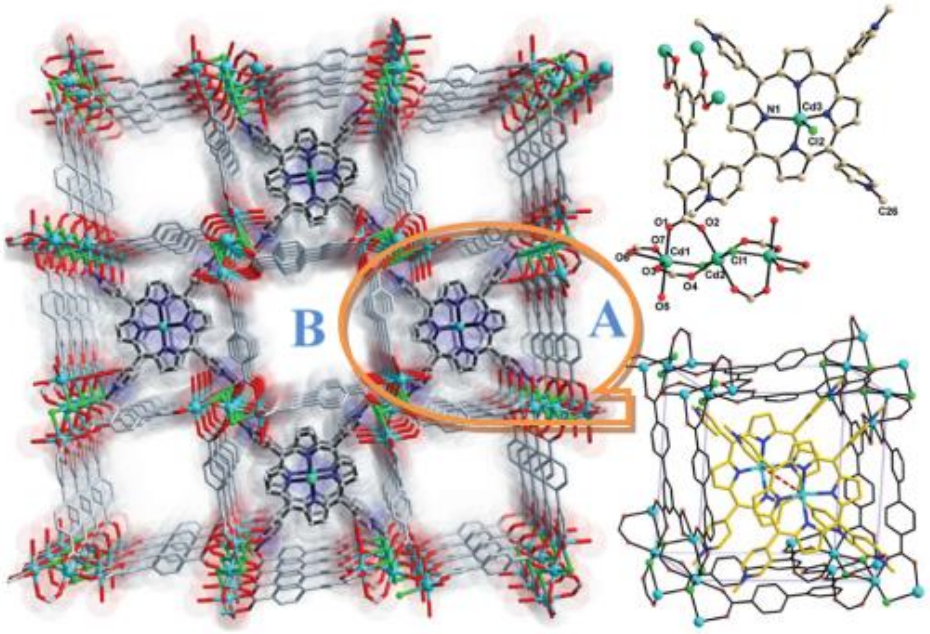

Figure 1.13: *Projection of the structure of porph@MOF-10 along the c axis showing Cd(II)TMPyP in channel B (orange circle); (upper right) Components of porph@MOF-10 showing the ligand and Cd(II)TMPyP cations; (lower right) Illustration of Cd(II)TMPyP cations trapped in square channels of porph@MOF-10.*[98] *Reprinted with permission from Ref. [97]. Copyright © 2012, American Chemical Society.*

It was found that crystals of porph@MOF-10 could undergo post-synthetic modification and the Cd ions in TMPyP as well as the framework (partially in the case of Cu) could be exchanged for Mn or Cu by soaking the crystal in a solution of $MnCl_2$ or $CuCl_2$ forming MnTMPyP@MOF-10-Mn and CuTMPyP@MOF-10-CdCu respectively. The catalytic activity of these materials was assessed using the oxidation of *trans*-stilbene with ^{t}BuOOH as an oxidant. It was found that the original porph@MOF-10 material had very poor activity with a conversion of only ~7%; however, both MnTMPyP@MOF-10-Mn and CuTMPyP@MOF-10-

CdCu showed good activities with conversions of 75% and 79% respectively with stilbene oxide and benzaldehyde as the major products. Both the catalysts showed good selectivity for stilbene oxide (56% and 61% respectively) and were recycled through six cycles with minimal loss in catalytic activity.

Zhang *et al.* further investigated the potential of Mn(III)TMPyP as an oxidation catalyst by encapsulating it in two further Cd MOFs, constructed from BTC and [1,1',3',1''-terphenyl]-4,4'',5'-tricarboxylate (TPT) respectively.[99] These structures were termed porph@MOF-12 and -13 respectively and the crystal structures of both materials were determined. The framework constructed from Cd and BTC did not give rise to the HKUST-1 type structure previously seen when this ligand was used, rather a framework which contained hexagonal channels with two different size channels which gave rise to a 3D honeycomb-like structure with a topology *mzz* (Fig. 1.14a). The porphyrin moiety was exclusively encapsulated in one channel with diameter 17.6 Å. Contrary to previous examples of Mn(III)TMPyP encapsulation, in the case of porph@MOF-13, the porphyrin was encapsulated in all the square channels formed by this framework (Fig. 1.14b) with *rtl* topology. Short range attractive forces similar to those described by Zawarotko and co-workers in 2012 were also found to be present.[98]

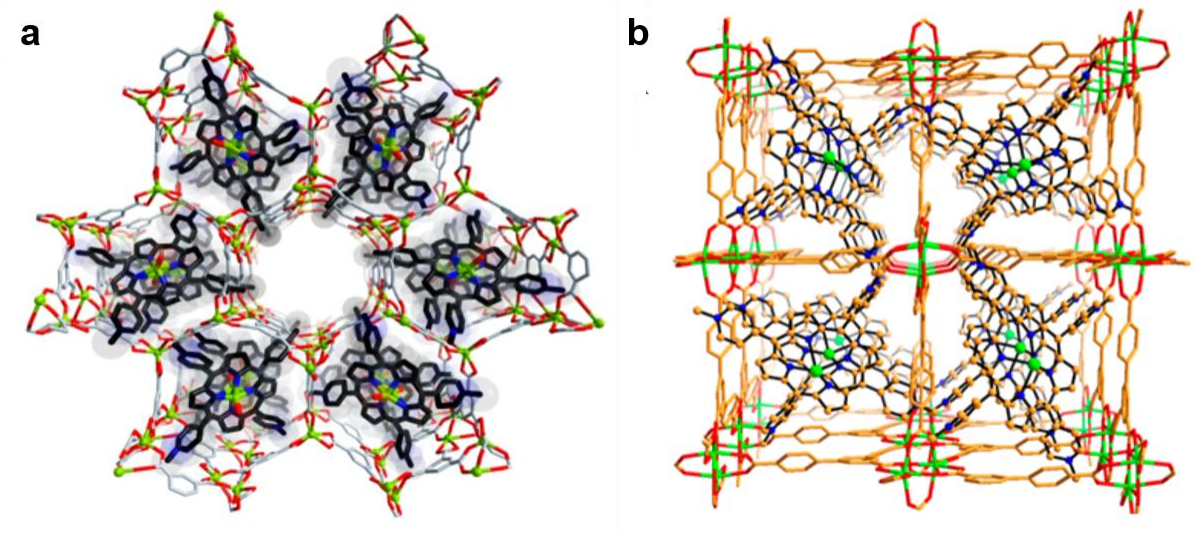

Figure 1.14: *(a) Porph@MOF-12 showing the hexagonal channels and mzz topology; (b) Porph@MOF-13 viewed along the a-axis showing Mn(III)TMPyP encapsulated in all the square channels.*[99] *Reprinted with permission from Ref. [98]. Copyright © 2014, American Chemical Society.*

It was found that porph@MOF-12 could undergo post-synthetic modification and the Cd ion could be exchanged for Mn by soaking the crystals in a solution on $MnCl_2$. The catalytic activities of both Mn- and Cd-porph@MOF-12 were investigated by studying the oxidation of styrene and comparing it to Mn(III)TMPyP. It was found that Mn(III)porphyrin@MOF was the most active catalyst, with a conversion of 61% compared to 45% and 5% conversion for Mn(III)TMPyP and Cd(II)-porph@MOF-12 respectively.

Qiu *et al*. encapsulated Cu(II) and Mn(II) *meso*-tetrakis[4-(nicotinoyloxy)phenyl] porphyrin (TNPP) in a Cu MOF with *pcu* topology containing paddlewheel nodes constructed from 1,1-*bis*-[3,5-bis(carboxy) phenyoxy]methane.[100] The same method of building the framework in a 'ship-in-a-bottle' fashion was employed in this study. Successful encapsulation was confirmed by ICP-AES, a marked colour change upon encapsulation of the porphyrin compared to the native MOF as well as a decrease in the BET surface area as obtained from N_2 gas sorption isotherms after encapsulation of the porphyrin. PXRD patterns confirmed retention of the

structure of the framework after encapsulation and while the porphyrin molecule could not be resolved in the single crystal X-ray diffraction data, it was hypothesized that the porphyrin molecule would reside in the largest cage in the framework.

The oxidation of 3,5-di-*tert*-butylcatechol (DTBC) to the corresponding quinone using H_2O_2 as the oxidant was investigated (Scheme 1.5). The activities of Cu(II)TNPP@MOF and Mn(III)TNPP@MOF were compared to the native MOF, as well as both porphyrins in solution. Cu(II)TNPP@MOF showed the highest activity, while Mn(III)TNPP@MOF displayed lower catalytic activity compared to the native MOF framework. Both Cu(II)TNPP@MOF and Mn(III)TNPP@MOF were more active than their homogeneous counterparts. Cu(II)TNPP@MOF was successfully recycled four times without loss of catalytic activity.

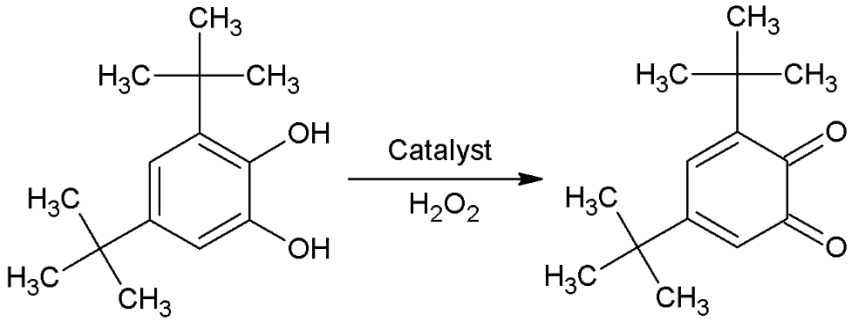

Scheme 1.5: *Oxidation of 3,5-di-tert-butylcatechol (DTBC) with H_2O_2 as an oxidant.*

In 2015 Ling *et al*. reported the encapsulation of Fe(III)TCPP in Cu-HKUST-1 which was then sequentially conjugated with streptavidin (SA), a nucleotide sequence recognizer, forming Fe(III)TCPP@Cu-HkUST-1-SA.[101] Successful synthesis of Fe(III)TCPP@Cu-HkUST-1 was confirmed using similar techniques previously used for metalloporphyrin@MOF catalysts, namely PXRD, UV-visible spectroscopy as well as gas sorption experiments.

This electrochemical sensor was designed to detect DNA using both the redox activity of Fe(III)TCPP@Cu-HKUST-1 as well as the allosteric switch of hair pin DNA. A hairpin DNA strand with a nucleotide sequence complementary to the target DNA and another sequence, which is suitable as a SA aptamer (small single-stranded nucleic acids that fold into a well-defined three-dimensional structure in the presence of the target),[102] were attached on a glassy carbon electrode (GCE) (Scheme 1.6). In the absence of the target, Fe(III)TCPP@CuHKUST-1-SA cannot bind to the DNA sequence on the electrode but, upon binding of the target to the allosteric centre of the DNA, a conformation change occurs and the aptameric sequence becomes available for binding of FeTCPP@Cu-HKUST-1-SA. The encapsulated porphyrin can catalyse the oxidation of phenylenediamine (*o*-PD) to 2,2′-diaminoazobenzene in the presence of H_2O_2 giving an electrochemical response. This sensor could detect DNA at 0.48 fM with the linear range of 10 fM to 10 nM. It was found that Fe(III)TCPP@Cu-HKUST-1-SA showed an enhancement of signal relative to native Fe(III)TCPP in solution.

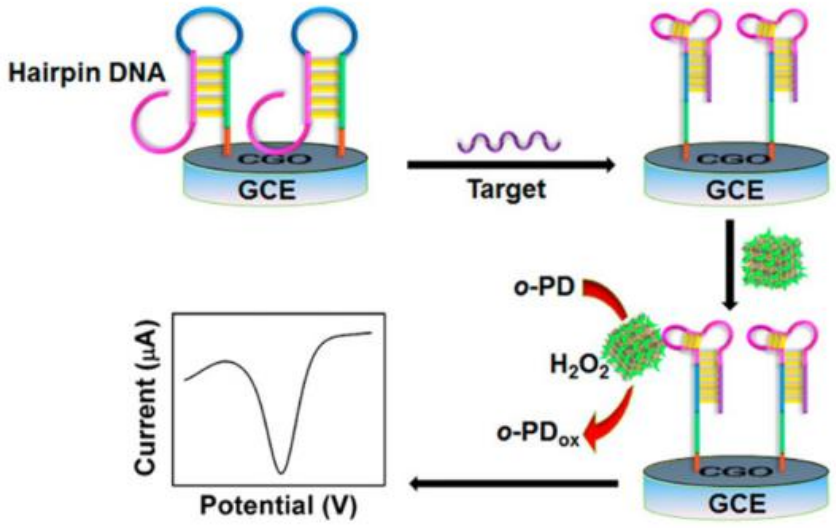

Scheme 1.6: *Schematic representation of electrochemical target DNA detection via Fe(III)TCPP catalysed oxidation of o-PDA by H_2O_2.*[101] *Reprinted with permission from Ref. [100]. Copyright © 2015, American Chemical Society.*

1.4.2 Fe(III)PPIX encapsulated in MOFs

In contrast to the many studies where synthetic tetraphenyl porphyrins have been encapsulated in MOFs, there are few reports of native FePPIX encapsulated in MOFs, in the form of Fe(III)PPIX. This natural porphyrin is responsible for the wide range of activity and high catalytic efficiency of haemoproteins and therefore harnessing its catalytic power is of great interest.

The first Fe(III)PPIX encapsulating MOF was reported by Liu and co-workers.[103] They encapsulated haemin (Cl-Fe(III)PPIX) into the well-known amino containing MIL-101(Al)-NH_2 framework.[103] The aim of using this material was for the amino group to anchor the haem within the framework by axial coordination. This study differs from others discussed so far in that encapsulation of haemin in the framework results in a structural change in the framework. It was shown that upon encapsulation of haemin the MIL-101(Al)-NH_2 framework transformed to MIL-53(Al)-NH_2 as seen by PXRD, SEM and the drastic reduction in BET surface area corresponding to the conversion from MIL-101(Al)-NH_2 to MIL-53(Al)-NH_2 (Fig. 1.15a). A crystallographic change of this nature has been previously reported in the literature upon exposing MIL-101(Al)-NH_2 to DMF for 12 h.[104] A loading of 1.02% of Fe into the framework was calculated using the Al to Fe ratio and a small decrease in BET surface area when comparing heamin@MIL-101(Al)-NH_2 to MIL-53(Al)-NH_2 (407.6 $m^2.g^{-1}$ compared to 464.5 $m^2.g^{-1}$) further confirmed successful loading (Fig. 1.15b).

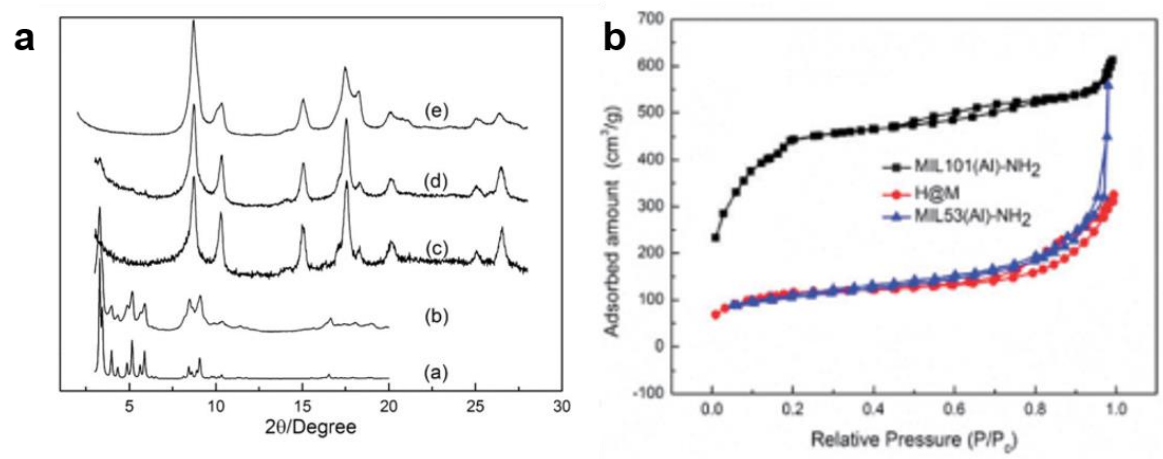

Figure 1.15: *(a) PXRD patterns of simulated (a) MIL–101(Cr),(b) MIL–101(Al)–NH_2, (c) synthesized haemin@MOF, (d) MIL–101(Al)–NH_2 soaked in DMF for 12 h and (e) pure MIL–53(Al)–NH_2; (b) N_2 adsorption and desorption isotherms of MIL-101(Al)-NH_2 (black), haemin@MOF (red) and MIL-53(Al)-NH_2 (blue).*[103] *Reprinted with permission from Ref. [102]. Copyright © 2013, Royal Society of Chemistry.*

The catalytic activity of this haemin@MIL-101(Al)-NH_2 MOF was investigated using the chromogenic substrate 3,3',5,5'-tetramethyl-4,4'-diaminebiphenyl (TMB) which is known to be active in the presence of Fe(III)PPIX catalysts (Scheme 1.7).[105,106] It was shown that haemin@MIL-101(Al)-NH_2 catalysed the oxidation of TMB, while the parent MOF brought about no reaction and haemin in solution only supported a slight reaction (Fig. 1.16). It was shown that pH 5 was the optimal pH for the reaction, and haemin@MIL-101(Al)-NH_2 was shown to be significantly more active than haemin, especially at higher H_2O_2 concentrations; therefore indicating that the MOF provides some protective effect against the degradation of haem. It was also shown that the optimum temperature was 10 °C higher for haemin@MIL-101(Al)-NH_2 than for native haemin, indicating that the MOF increased the thermal stability of haemin. It was also shown that the material loses its catalytic activity with each cycle and this was attributed to haemin being washed off the catalyst after being recovered. This could

indicate that the haemin was not in fact encapsulated, but rather coated the surface of the material.

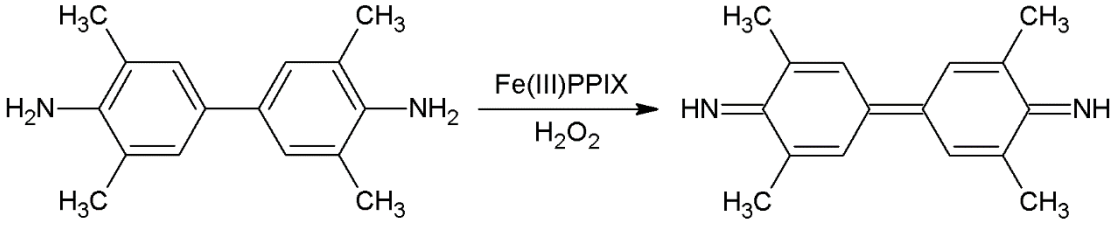

Scheme 1.7: *Fe(III)PPIX catalysed oxidation of TMB by H_2O_2.*

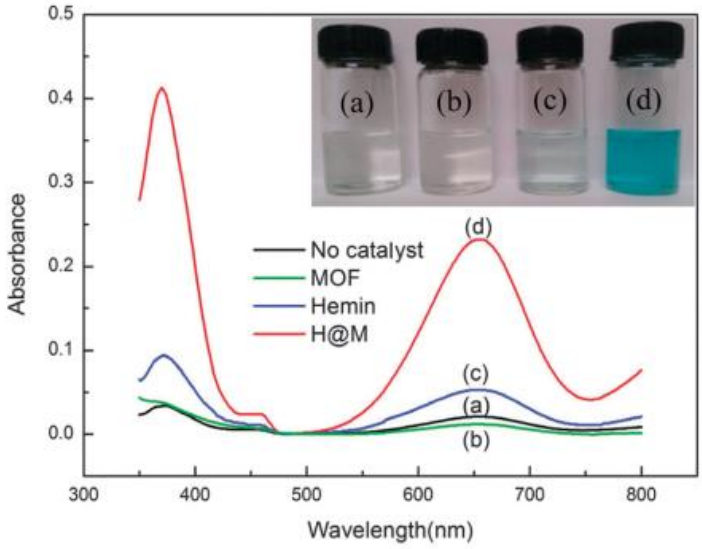

Figure 1.16*: Typical absorption spectra of reaction of 10 mM H_2O_2 with TMB (0.8 mM) in the presence of (a) no catalyst; (b) MIL–101(Al)–NH_2 (20 µg.mL^{-1}); (c) Cl-Fe(III)PPIX (20 µg.mL^{-1}) and (d) haemin@MIL–101(Al)–NH_2 (20 µg.mL^{-1}) at room temperature in sodium citrate buffer (50 mM, pH 5) after reaction for 5 min. Inset: photograph of each reaction product showing the characteristic blue colour.*[103] *Reprinted with permission from Ref. [102]. Copyright © 2013, Royal Society of Chemistry.*

The ability of the material to sense both H_2O_2 and glucose was probed. It was found that the material could detect H_2O_2 at concentrations starting at 2 µM and showed a linear response for H_2O_2 concentration against absorbance between 5 and 200 µM. Sensing of glucose was investigated by coupling the reaction of haemin@MIL-101(Al)-NH_2 and H_2O_2 with the enzyme glucose oxidase (GOx). It was found that glucose could be sensed between 10 and 300 µM and it was found that the sensing was substrate specific as no response was recorded when tested in the presence of fructose, lactose and maltose.

In a second report of a Fe(III)PPIX containing MOF by Luo *et al*.,[107] a similar strategy to that reported by Larsen *et al.*[41] was employed. Haemin (Cl-Fe(III)PPIX) was encapsulated into Cu-HKUST-1 for the application of sensing glucose and peroxide using chemiluminescence (Scheme 1.8).[107] The octahedral pores of the HKUST-1 framework have previously been shown to be suitable for tetraphenyl porphyrin oxidation;[41,97] however, this was the first reported study of HKUST-1 being used to encapsulate native haem. PXRD was used to confirm that Cu-HKUST-1 had indeed been formed, but contrary to previous reports of encapsulated Fe(III) tetraphenyl porphyrins in HKUST-1 frameworks, no significant colour change was observed. This could indicate that only a minimal amount of haem was in fact encapsulated. This was further reinforced by a very small reported change in BET surface area of haemin@HKUST-1 compared to Cu-HKUST-1 (1160.9 m^2g^{-1} vs. 1228.8 m^2g^{-1}).

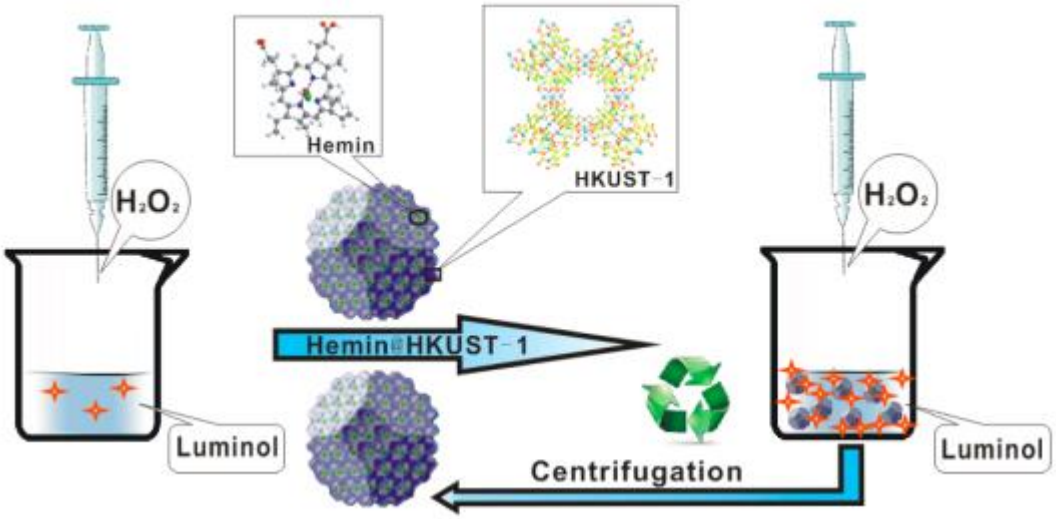

Scheme 1.8: *Schematic of process used by Luo et al. for use of haemin@HKUST as a H_2O_2 sensor using chemiluminescence.*[107] *Reprinted with permission from Ref. [106]. Copyright © 2015, American Chemical Society.*

The synthesised haemin@MOF was investigated for its use as a glucose and H_2O_2 sensor using chemiluminescence produced by the oxidation of luminol by H_2O_2 with can be catalysed by a redox active metal. This is a well-known reaction and the chemiluminescence of luminol in the presence of H_2O_2 and haemin has been previously reported in the literature (Scheme 1.9).[108,109] To this end, it was shown that in the presence of haemin@HKUST, H_2O_2 and luminol, a blue chemiluminescent glow was observed (Fig. 1.17a). A plot of the chemiluminescent intensity revealed that no reaction was observed without the catalyst or in the presence of CuHKUST-1. A moderate reaction was observed in the presence of haemin@HKUST and the largest reaction was observed in the presence of free haemin (Fig. 1.17b). It was also shown that the material retained its catalytic activity through eight catalytic cycles. The lack of chemiluminescence observed in the presence of Cu-HKUST-1 alone is contrary to the findings reported in a previous study which demonstrated that Cu-HKUST-1 can successfully catalyse the reaction between H_2O_2 and luminol.[110] This would be expected owing to the redox-active nature of Cu(II) ions present in the HKUST-1 framework.

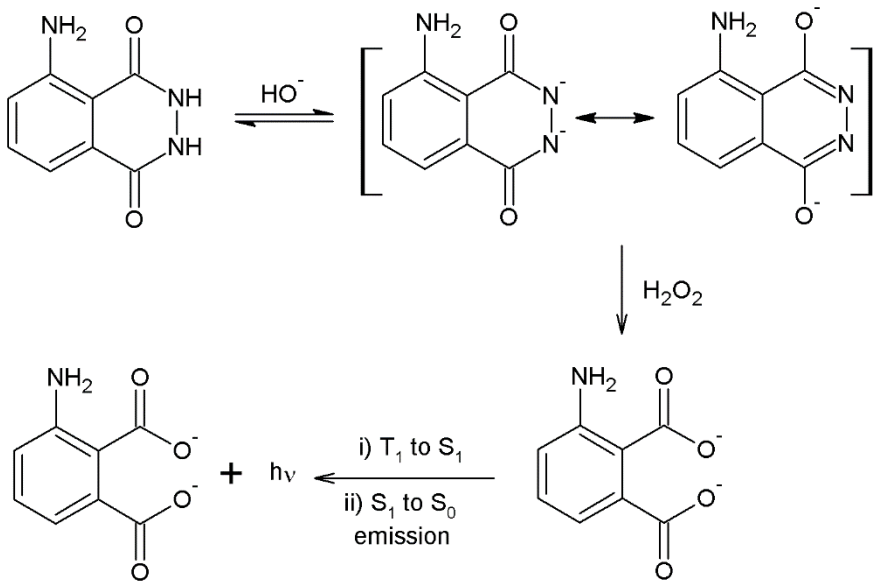

Scheme 1.9: *Mechanism of chemiluminescence observed from haemin catalysed oxidation of luminol by H_2O_2.*

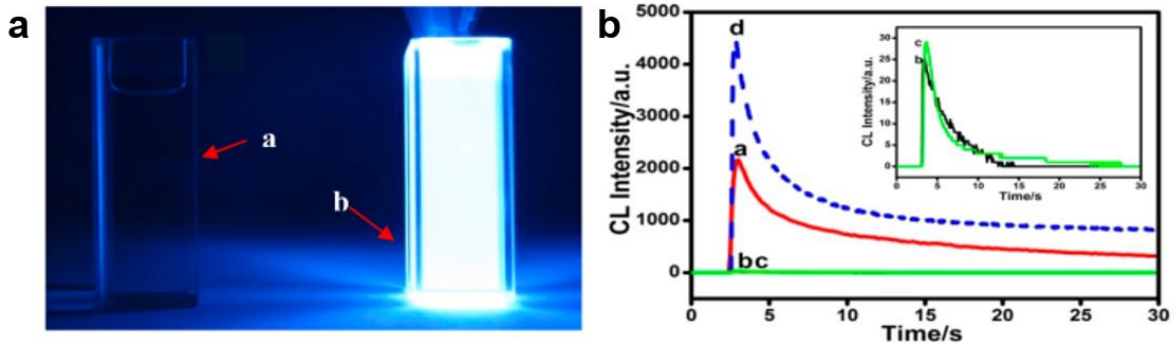

Figure 1.17: *(a) Luminol in soultion with H_2O_2 with and without haemin@HKUST (left and right respectively); (b) Chemiluminescence intensity observed in the presence of haemin@HKUST (red), with no catalyst (black), Cu-HKUST-1 (green) and free haemin (blue).*[107] *Reprinted with permission from Ref. [106]. Copyright © 2015, American Chemical Society.*

The sensing activity of haemin@HKUST was studied by also investigating the materials ability to detect H_2O_2 and glucose in a similar manner to the study conducted on haemin@MIL-101(Al)-NH_2 by coupling the oxidation reaction with the enzyme GOx. It was found that the material had a detection limit of 2 µM H_2O_2 and a plot of log(I_{CL}) vs. log[H_2O_2] showed a linear response between 5 and 1000 µM H_2O_2. In a similar manner, the detection limit for glucose was found to be 7.5 µM and had a linear range from 7.5 – 750 µM using the coupled reaction. The authors concluded that the material showed promise as a hydrogen peroxide and glucose sensor.

A study was reported by Cheng *et al*. where Fe(III)PPIX was encapsulated in a zeolitic imidazolate framework (ZIF-8) nanostructure for the design of integrated nanozymes (INAzymes) by co-encapsulating FePPIX and glucose oxidase (GOx) in the same framework.[111] This material was investigated for its use as a colorimetric glucose sensor. Both the FePPIX and FePPIX/GOx containing materials were synthesized in an aqueous solution at room temperature by adding the guests to be encapsulated as well as the components of the framework, yielding light green crystals with a rhombic dodecahedral shape with average sizes of approximately 210, 100, and 190 nm for ZIF-8, FePPIX@ZIF-8 and FePPIX/GOx@ZIF-8 (INAzyme) respectively (Scheme 1.10). The shape of the crystals became less regular with the inclusion of FePPIX and FePPIX/GOx. Element mapping with transmission electron microscopy (TEM) verified successful encapsulation of FePPIX which showed a uniform distribution of Fe throughout the crystals. Successful encapsulation of GOx was confirmed by conjugating GOx with fluorescein isothiocyanate (FITC), and producing GOx−FITC/FePPIX@ZIF-8. This demonstrated uniform fluorescence when the crystals were excited at 436 nm.

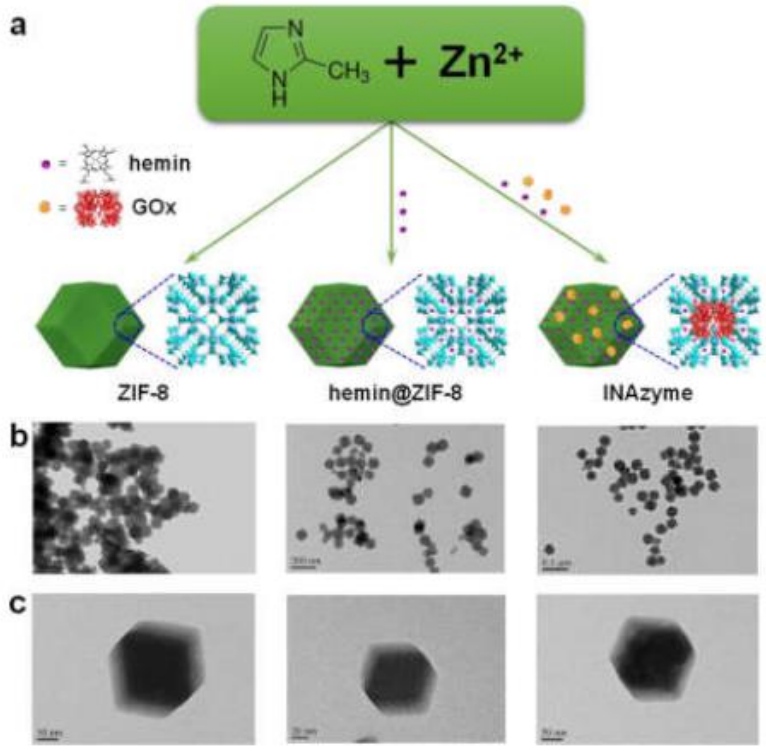

Scheme 1.10: *(a) Schematic synthesis of nanoscaled ZIF-8, haemin@ZIF-8 and GOx/haemin-ZIF-8 (INAzyme) from 2-methylimidazole and zinc acetate (Zn^{2+}) in a one-step synthesis and models of the structures of the obtained material (not drawn to scale); (b and c) TEM images of ZIF-8, haemin@ZIF-8 and GOx/haemin-ZIF-8 (INAzyme) from left to right at (b) low magnification and (c) high magnification).*[111] *Reprinted with permission from Ref. [110]. Copyright © 2016, American Chemical Society.*

The peroxidase mimicking ability of the synthesized haemin@ZIF-8 was evaluated by investigating the catalytic oxidation of ABTS by H_2O_2 (Scheme 1.4). It was found that haemin@ZIF-8 was peroxidatically active and showed an increase in activity relative to native haemin and demonstrated 90% retention of activity through multiple cycles. The catalytic activity of GOx/hemin@ZIF-8 in cascade reactions was also investigated (Fig 1.18). The encapsulated GOx first catalysed the oxidation of glucose to gluconic acid with O_2 to produce *in situ* H_2O_2 which subsequently oxidised ABTS, catalysed by the encapsulated haemin. The INAzyme material was found to be more active than a solution containing GOx and horseradish

peroxidase (HRP) and more active than the two components encapsulated separately (haemin@ZIF-8 and GOx@ZIF-8). Furthermore, the material demonstrated good recyclability through four cycles with approximately 80% of activity retained.

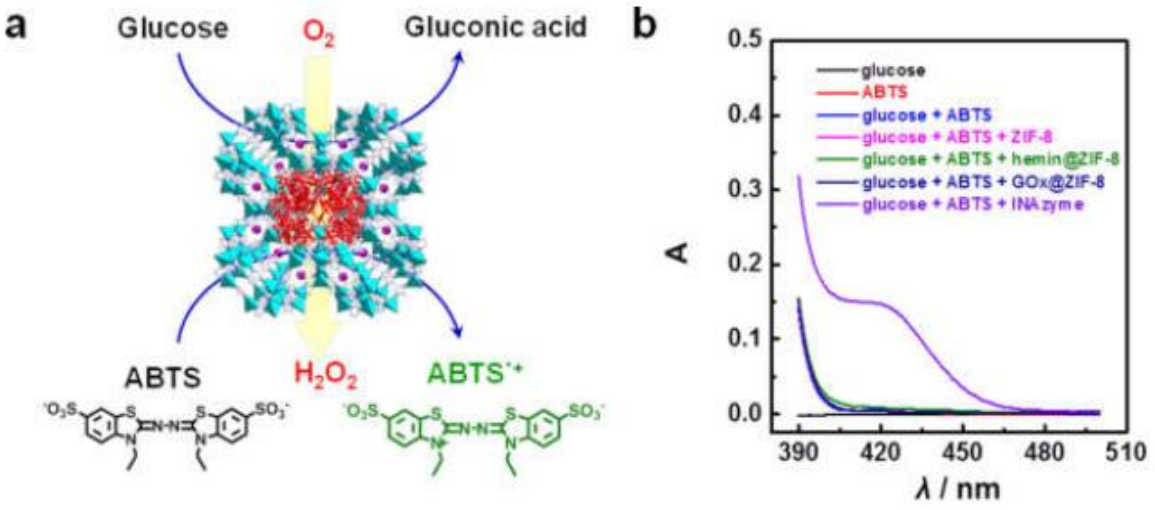

Figure 1.18: *(a) Schematic illustration of GOx/haemin@ZIF-8 (INAzyme) cascade oxidation of glucose and ABTS to produce ABTS$^{\bullet+}$; (b) Activity of GOx/haemin@ZIF-8 (INAzyme) and other components of the crystal system in 0.10 M Tris−HCl buffer (pH 7.0), respectively.*[111] *Reprinted with permission from Ref. [110]. Copyright © 2016, American Chemical Society.*

Due to the success seen in the initial experiments with GOx/haemin@ZIF-8, the material was evaluated for *in vivo* colorimetric detection of cerebral glucose in living mouse brains. It was found that the material could detect glucose in the range 0 to 250 μM which covers the range of physiological levels of glucose and it was found that this material could accurately determine the concentration of glucose in living mouse brains, before and after global cerebral ischemia. Furthermore, it was found that compounds such as ascorbic acid, lactate and dopamine, which are also present in significant levels in the mouse brain, did not interfere with the accurate detection of glucose at their physiological levels. Finally, the authors investigated the possibility of combining an INAzyme-modified microfluidic chip with microdialysis technology for the continuous online monitoring of cerebral glucose and the successful

monitoring of dynamic changes of cerebral glucose in living brains following ischemia/reperfusion was demonstrated.

There are four reports of FePPIX@MOFs being used in composite materials for the construction of electrochemical sensors.[112–115] In a study by Song and co-workers, Fe(III)PPIX and Cu(II)$(NO_3)_2$ were sonicated together to create a Fe(III)PPIX-Cu nanocomposite material (termed haemin-Cu MOF) which had a 3D ball-flower-like structure.[113] This haemin-Cu MOF was then adhered to a chitosan-reduced graphene oxide (CS-rGO) nanocomposite and the H_2O_2 sensing ability of this material investigated. It was found to have a linear range of 0.065 – 410 mM and detection limit of 0.019 mM.

The first reported example of a FePPIX@MOF composite material was reported in 2015 by Yuan and co-workers.[112] In this study, the encapsulation approach to incorporate haemin into a nano-sized Fe-MIL-88 MOF which was subsequently coated with Au nanoparticles and conjugated to glucose oxidase (GOx) for signal amplification and a thrombin (TB) binding aptamer in order to create an electrochemical aptasensor to detect thrombin (Scheme 1.11).[112] This sensor had a detection limit of 0.068 pM and a wide linear range of 0.0001 nM to 30 nM for TB detection. This low detection limit and wide linear range of detection was attributed to the multifunctional nature of the material synthesized as well as the enzyme-assisted amplification of the signal created by binding of TB to the aptamer.

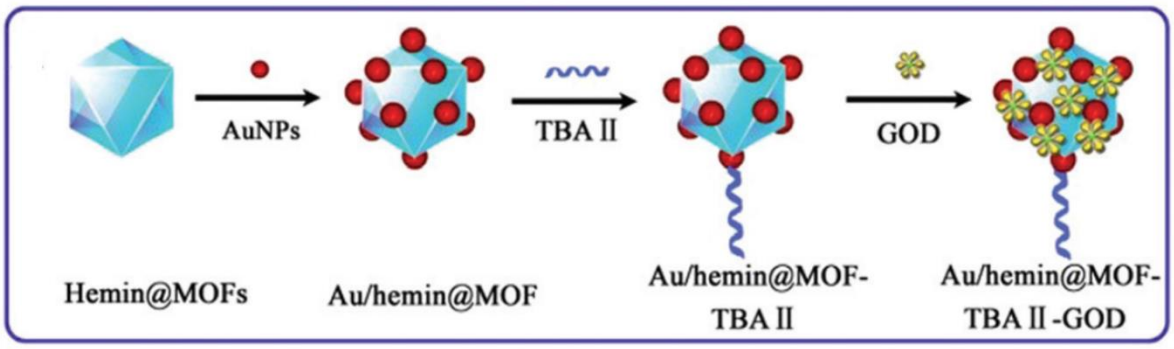

Scheme 1.11: *The preparation of Au/hemin@MOF–TBA II–GOx bioconjugates. In the figure GOD represents GOx and TBA refers to the thrombin aptamer.*[112] *Reprinted with permission from Ref. [111]. Copyright © 2015, Royal Society of Chemistry.*

A recent study published by Yuan *et al*. once again makes use of the Fe(III)-MIL-88 framework to encapsulate Fe(III)PPIX, forming FePPIX@Fe(III)-MIL-88-NH_2. The surface of the crystal was subsequently decorated with Pt nanoparticles and Cu^{2+} ions creating a nanocomposite material capable of detecting the hypertension-carrying adrenergic receptor gene (ADRB1) using the electrocatalytic oxidation of H_2O_2 by this nanocomposite material (Scheme 1.12).[114] The sensor was created by immobilising the nanocomposite material on a GCE which was further functionalised with a capture DNA probe for the target ADRB1 gene. In the presence of the target gene, an electrochemical response could be measured resulting from the oxidation of H_2O_2. It was found that the sensor had a very wide linear range of 1 fM to 10 nM and had a 0.21 fM detection limit.

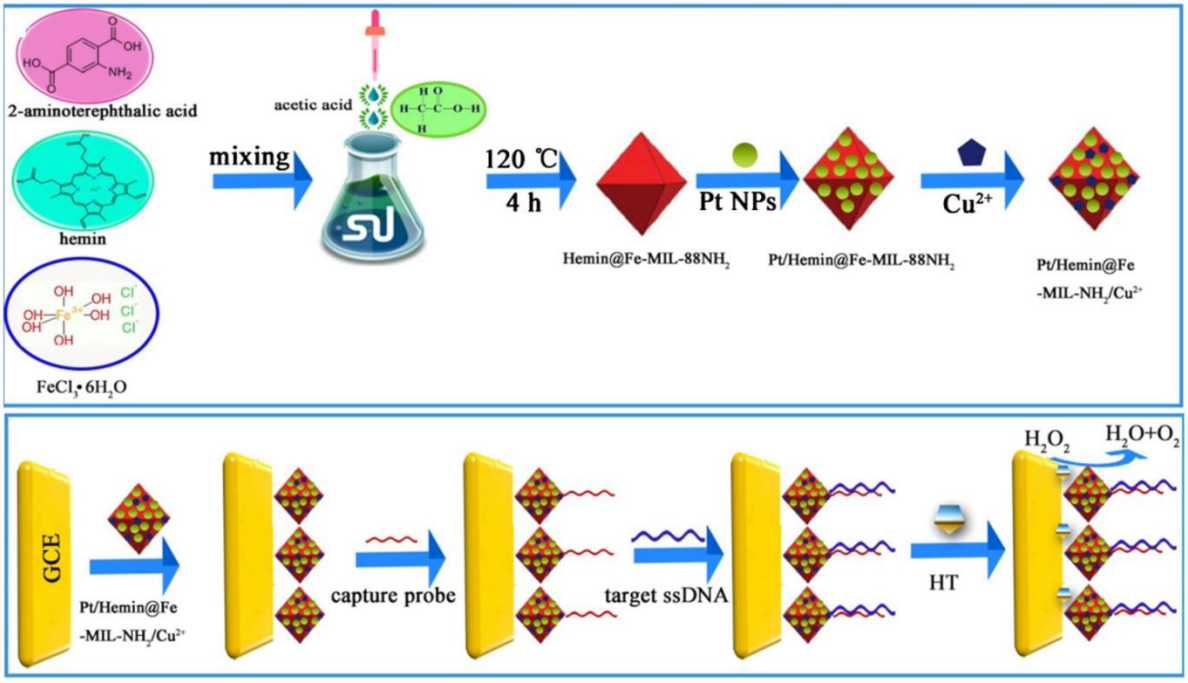

***Scheme 1.12**: The preparation process of Pt/Cu^{2+}/FePPIX@Fe-MIL-88NH_2 (top) and schematic representation of construction of the electrochemical ADRB1 gene sensor.*[114] *Reprinted with permission from Ref. [113]. Copyright © 2017, SpringerLink.*

A final example of FePPIX@FeMIL-88 being incorporated into a nanocomposite material was reported by Chen *et al.* in 2017 who designed a sensor to detect the FGFR3 gene mutation.[115] This group coated the FePPIX@FeMIL-88 material with Pt nanoparticles which was further coated with a thiol modified signal probe (SP) and bovine serum albumin. A GCE was modified with reduced graphene oxidetetraethylenepentamine (rGO-TEPA), gold nanoparticles and streptavidin for amplification of the signal and a biotin-modified capture probe immobilised. The sensor could detect FGFR3 with a linear range 0.1 fM to 1 nM with a detection limit of 0.033 fM. For comparison, FePPIX@FeMIL-88 was coated with Au nanoparticles as with the study by Yuan and co-workers.[112] It was found that the FePPIX@FeMIL-88 material coated with Pt nanoparticles showed a much greater electrochemical response than its Au counterpart.

In the majority of the reported studies, encapsulation of the porphyrin resulted in a significant increase in the catalytic activity of the porphyrin when compared to its homogeneous counterpart. This indicates that this method of encapsulating porphyrins in solid supports is feasible to overcome some of the problems associated with porphyrin catalysis in solution, most notably porphyrin degradation. While there are several reports of Fe(III)PPIX being encapsulated in MOFs, there are a few important considerations which have not been addressed. Despite the success of encapsulation of Fe(III)PPIX and other tetraphenylporphyrins in MOFs having been demonstrated; a serious drawback of this approach has been identified, namely poor access of substrates to the active site.[40] In order to be catalytically active, substrates require rapid access to the metalloporphyrin to allow for efficient interaction and for catalysis not to be limited to sites at the surface of the material.[89]

Furthermore, with the exception of the studies reported by Qin *et al*.[103] and Cheng *et al*.[111] all the catalytic activities of these systems are measured using metalloporphyrin@MOF systems constructed from redox active metals. This makes the contribution of catalytic activity stemming from the porphyrin unclear. Therefore, it is highly preferable to conduct studies on the catalysis of metalloporphyrin@MOF systems using MOFs constructed from redox inactive metals. It is also notable that there are no reported crystal structures of Fe(III)PPIX@MOF systems despite extensive examples of crystal structures of metallotetraphenyl porphyrin@MOF systems.

A thorough investigation into the encapsulation of Fe(III)PPIX and a Fe(III) tetraphenyl porphyrin into a redox-inactive MOF with suitable substrate diffusion properties is thus warranted in order to gain a better understanding of the catalytic activity of Fe(III)PPIX@MOF systems.

1.5 Aims and Objectives

1.5.1 Aims

The aim of this study was to synthesise and fully characterise a redox-inactive MOF which could encapsulate Fe(III)PPIX and probe its capabilities as an oxidation catalyst by investigating its peroxidatic activity as well as its ability to catalyse the oxidation of primary and secondary alcohols. To achieve this aim, the following objectives were proposed:

1.5.2 Objectives

i. Identify two suitable Zn(II) MOFs for Fe(III)PPIX encapsulation and encapsulate Fe(III)PPIX into both systems.

ii. Fully characterise the Fe(III)PPIX@MOF systems using thermal analysis, UV-visible spectroscopy, X-ray diffraction (powder and single crystal), scanning electron microscopy with energy-dispersive X-ray spectroscopy and inductively coupled plasma optical emission spectrometry.

iii. Synthesise and characterise synthetic Fe(III) tetraphenylporphyrin analogues of the Fe(III)PPIX@MOF systems using the same techniques.

iv. Investigate the peroxidatic activity of all Fe(III) metalloporphyrin@MOF systems synthesised using UV-visible spectroscopy.

v. Develop a full kinetic model for the most active Fe(III)PPIX@MOF system including the derivation of a rate law.

vi. Investigate the ability of the most active Fe(III)PPIX@MOF system to oxidise primary and secondary alcohols using UV-visible spectroscopy and ^{1}H NMR spectroscopy techniques.

Chapter Two: General Information and Instrumentation

2.1 General Information

With the exception of 4,4′,4″-*s*-triazine-2,4,6-triyl-tribenzoic acid (H_3TATB, CGene Tech. Inc.), all chemicals were purchased from Sigma Aldrich and used without further purification. Double-distilled deionized water was provided by a Millipore Direct-Q3 water purification system. The solvent used for synthesis was anhydrous *N*,*N*-dimethylformamide (DMF) 99.8% purity which was stored over activated molecular sieves (3 Å). All glassware, cuvettes and stirrer bars were scrupulously washed with 0.2 M NaOH and 1 M HNO_3 followed by rinsing with distilled H_2O and acetone as reported previously in order to prevent build-up of Fe(III)PPIX.[116] Details specific to each experiment are provided in the relevant chapters.

2.2 Instrumentation

2.2.1 pH Measurements

The pH of buffer solutions for kinetics measurements was determined using a Crison MicropH 2000 pH meter and Crison 52 03 glass electrode. Before pH determination the pH meter was calibrated at room temperature using standard solutions at pH 4.00 ± 0.01 (Buffer, reference standard, Sigma B5020) and 7.00 ± 0.01 (Buffer, reference standard, Sigma B4770). Electrodes were stored immersed in a 3 M KCl solution obtained from Sigma Aldrich.

2.2.2 UV-visible experiments

Solution-state UV-visible spectra were recorded on a Shimadzu UV-1800 spectrophotometer over the range 200 to 800 nm. Quartz cuvettes (Hellma, Suprasil®, 1 cm path length) were maintained at a constant temperature of 25.00 ± 0.02 °C by a TCC-100 thermoelectrically temperature-controlled cell holder accessory. Solid-state spectra were recorded at room temperature on a Cary 5000 UV-vis spectrophotometer with Harrick Praying Mantis diffuse reflectance accessory.

Kinetics experiments were recorded on a Shimadzu UV-1800 spectrophotometer using quartz cuvettes (Hellma, Suprasil®, 1 cm path length). All experiments were conducted at 37 °C with constant stirring unless otherwise stated. Data were analysed using the one-phase exponential function in GraphPad Prism in order to obtain maximal yield (Y_{max}) and a straight-line function to obtain initial rates.[117]

2.2.3 Inductively Coupled Optical Emission Spectroscopy (ICP-OES)

Samples were ashed in a furnace at 600 °C overnight before digestion with 4 mL of 4:1 conc. HF and HNO_3 at 130 °C for 48 h (Warning: HF is extremely dangerous and should be handled with caution). These samples were then dried and washed twice with 2 mL of conc. HNO_3 with drying between washes. The solid material remaining was diluted in a 5% HNO_3 solution before analysis by ICP-OES using a Varian 730-ES spectrometer. The mass % of Fe was calculated from the data obtained. All ICP-OES measurements of each sample were done on three preparations of the same material which were then combined to obtain an accurate mass % across differing preparations.

2.2.4 Thermal Gravimetric Analysis

TGA experiments were performed on a TA-Q500 TA Instrument. Data were analysed using the Universal Analysis 2000 software.[118] All experiments were performed with a 50 $cm^3.min^{-1}$ dry N_2 gas flow rate.

TGA experiments were used to accurately determine the solvent content of both the empty and Fe(III)PPIX- and Fe(III)TPP-loaded frameworks. Furthermore, it allowed the thermal stability of the host framework to be determined. Experiments were performed on material that had been surface dried on filter paper as well as the oven dried material used for kinetic studies. TGA was performed on all material prior to running kinetics to accurately determine the mass of material used without solvent content. All experiments were conducted with a heating rate of either 6 °C.min^{-1} or 10 °C.min^{-1}.

2.2.5 NMR experiments

Nuclear magnetic resonance (NMR) spectra were recorded on a Bruker 400 MHz Ultrashield 400 Plus NMR spectrometer and chemical shifts (δ) were recorded relative to residual acetonitrile in acetonitrile-d_3 (δ 1.94 in ^{1}H NMR, δ 118.26 in ^{13}C NMR) or D_2O (δ 4.79). All chemical shift values were reported in ppm.

2.2.6 Scanning electron microscopy (SEM)

A Leo 1450 LaB6 scanning electron microscope with a Bruker XFlash EDS Si Drift Detector was used to obtain micrographs of crystals. Quantification of the zinc and iron content on the exterior and exposed interior surfaces of all synthesized crystals (Fe(III)PPIX-**1**, Fe(III)PPIX-**2**, Fe(III)TPP-**1** and Fe(III)TPP-**2**) prepared using encapsulation methods was performed using energy dispersive X-ray spectroscopy (EDS). Prior to visualization samples were sputter-coated with carbon. Statistical significance was determined using an unpaired two-tailed t-test. In the case of Fe(III)PPIX-**1**, quantification experiments were performed on crystals prepared by both soaking and encapsulation methods.

2.2.7 Gas sorption

Both N_2 and water vapor sorption experiments were conducted using a Micromeritics 3Flex Surface Area Analyzer. Approximately 100 mg of oven dried **1** and Fe(III)PPIX-**1** were further dried under dynamic vacuum for 24 h at 80 °C prior to being treated in a Micromeritics Flowprep with a constant flow of nitrogen gas over the sample at 60 °C for 24 h. The samples were further heated at 60 °C under vacuum *in situ* on the Micromeritics 3Flex Surface Area Analyzer to ensure all solvent was evacuated from the pores of the MOF. Adsorption isotherms for N_2 were measured at -196 °C and water vapor at 25 °C. Data were analysed using 3Flex Version 3.01 to obtain the calculated Langmuir surface area.

2.2.8 Powder X-ray diffraction

Powder X-ray diffraction (PXRD) was used to confirm the structure of the bulk material. All patterns were collected at 25 °C on a Bruker D8 Advance diffractometer with a Lynxeye detector using Cu-Kα-radiation (λ = 1.5406 Å) and operating at 40 mA and 30 kV. A receiving slit of 0.6 mm and primary and secondary slits of 2.5 mm were used. All samples were measured using a zero-background sample holder and were lightly ground to a fine powder before collection of data. The samples were scanned over a 2θ range of 4° to 40° using a step size of 0.02° (1760 steps) with 2 s exposure time. Pawley fitting[119] was conducted using TOPAS (v 4.2) in order to determine unit cells from the PXRD patterns.[120]

2.2.9 Single crystal X-ray diffraction

Unless otherwise stated in the relevant chapter, the following equipment and procedure was used for single crystal X-ray diffraction data collection and analysis. Further details of collection and refinements are given where necessary in the relevant chapters.

Single crystals were removed from DMF and immediately placed under Paratone® oil to prevent solvent loss and crystal degradation. A suitable crystal was selected for single crystal X-ray diffraction. A full data collection was performed on a Bruker KAPPA APEX II Duo diffractometer using Mo-Kα radiation (λ = 0.71073 Å) with X-rays generated by a Bruker K780 generator powered at 50 kV and 30 mA. An Oxford Cryosystems Cryostream device was used to cool the crystal to 173(2) K using dry N_2 gas.

SAINT[121] was used for unit cell refinement and data reduction, while SADABS[122] was used to correct for absorption effects. XPREP[123] was used to determine the space group and input files were prepared using the same program. Structure solution was obtained using SHELXS[124] with direct methods and structure refinement was carried out using SHELXL[124] in the Olex2[125] interface. All non-hydrogen atoms of the framework were located in Olex2 and refined by full matrix least squares on F^2 with anisotropic thermal parameters. Hydrogen atoms were placed with geometric constraints and were refined with isotropic displacement parameters.

Chapter Three: Encapsulation of Fe(III)PPIX into MOFs

3.1 Introduction

The immobilisation of Fe(III)PPIX and other synthetic tetraphenyl porphyrins in MOFs for the application of heterogeneous catalysis has been widely studied in recent years.[40,126,127] MOFs have been identified as a potential support for heterogeneous porphyrin catalysis as these permanently porous materials afford a large degree of structural versatility and, by altering the ligand and metal combination, it is possible to tune the dimensions and chemical composition of the pores.[89,90] Thus MOFs have the potential to overcome the problems identified with other solid supports, such as gels and mesoporous molecular sieves, by providing a well-defined environment for catalyst confinement in isolated active sites in which substrate access to the catalytic sites is also controlled, thereby creating robust and efficient catalysts.[1,91–93]

Two main approaches have been used for this purpose. The first method is to synthesize a MOF that uses metalloporphyrins as linkers. For example, tetraphenyl porphyrins that contain coordinating substituents symmetrically arranged around the porphyrin can serve as multidentate ligands.[128–131] This approach, however, is not feasible for asymmetrically substituted porphyrins, such as the natural co-factor Fe(III)PPIX, and thus a second methodology has been developed to overcome this limitation whereby porphyrins are instead encapsulated within cavities of a MOF.[40,89,132] This latter methodology is thus the only valid approach that can be used for Fe(III)PPIX due to its asymmetrical nature.

As discussed in Chapter 1, there are several reports of Fe(III)PPIX-containing MOFs used in composite materials for the construction of electrochemical sensors,[112–114,133,134] and as oxidation catalysts.[103,107,111] Apart from two studies, these investigations made use of redox active metals to construct the framework. For example, the study by Luo *et al.*[107] made use of the Cu-HKUST-1 MOF, which is poorly suited for investigating the redox activity of metalloporphyrins as it has been independently shown that Cu-HKUST-1 itself exhibits inherent peroxidatic activity.[110,135] This makes it difficult to ascertain whether the catalytic activity observed stems from the encapsulated porphyrin or the framework itself. An additional point of interest is that none of the studies reporting FePPIX encapsulated in a MOF report a crystal structure for the material obtained despite crystal structures for the tetraphenyl porphyrins encapsulated within MOFs being extensively reported. Furthermore, in some cases the loading of the porphyrin has not been reported and uniform distributions of the porphyrin in the framework has not been confirmed in the majority of the studies.

In this chapter, the encapsulation of Fe(III)PPIX in two redox-inactive MOFs, namely $[H_2N(CH_3)_2][Zn_3(TATB)_2(HCOO)]\cdot HN(CH_3)_2\cdot DMF\cdot 6H_2O$ (**1**) and Zn(II)-HKUST-1 (**2**), was investigated. The material was fully characterised using a variety of analytical techniques and the suitability of each MOF system for application as a heterogeneous oxidation catalyst was also investigated.

3.2 Experimental

3.2.1 Synthesis of $[H_2N(CH_3)_2][Zn_3(TATB)_2(HCOO)]\cdot HN(CH_3)_2\cdot DMF\cdot 6H_2O$ (1)

Single crystals of **1** were prepared by dissolving 4,4′,4″-*s*-triazine-2,4,6-triyl-tribenzoic acid (H_3TATB) (5 mg, 0.0113 mmol) and $Zn(NO_3)_2.6H_2O$ (27 mg, 0.0907 mmol) in DMF (2 mL) with 30 µL 0.5 M HNO_3 in a glass vial. The vial was sealed with a lid (covered with Parafilm® for a tighter seal), sonicated to ensure the dissolution of all material, and placed in an oven at 105 ± 2 °C for 16 h. The oven was then allowed to cool to room temperature over 4 h, the crystals collected and washed extensively with fresh DMF. The product was identified and phase-purity confirmed by Pawley fitting of the PXRD pattern, elemental combustion analysis and TGA. The dimethylammonium ($[H_2N(CH_3)_2]^+$) counterion and formate ions present in the structure are produced by acid hydrolysis of DMF. Combustion analysis provided evidence for further uncoordinated dimethylamine, DMF and H_2O in the channels of the MOF. These solvent molecules were identified using a combination of TGA (Fig. A1a) and elemental analysis and the composition was in good agreement with previously reported results.[136] Anal. Calcd for $C_{56}H_{59}N_9O_{21}Zn_3$: C, 48.38%; H, 4.28%; N, 9.07%. Found: C, 48.65%; H, 4.12%; O, 9.10%. Solvent mass % from TGA: 21 ± 1%. Crystal structure data in Table A1.

3.2.2 Synthesis of Zn-HKUST-1 (2)

Single crystals of **2** were prepared by dissolving benzene-1,3,5-tricarboxylic acid (28 mg, 0.133 mmol) and $Zn(NO_3)_2.6H_2O$ (62 mg, 0.208 mmol) in DMF (2 mL) in a glass vial. The vial was sealed with a lid (covered with Parafilm®), sonicated to ensure all material was dissolved, and placed in an oven at 85 ± 2 °C for 20 h. The oven was then allowed to cool to room temperature over 3 h, the crystals collected and washed extensively with fresh DMF. The product was identified and phase-purity confirmed by Pawley fitting of the PXRD. TGA was used to determine the solvent content (Fig. A1b). Solvent mass % from TGA: 32.6 ± 0.6%.

3.2.3 Synthesis of Fe(III)PPIX-1 and Fe(III)PPIX-2

The same procedures used for synthesis of **1** and **2** were used for the synthesis of Fe(III)PPIX-**1** and Fe(III)PPIX-**2** respectively, with the exception that 5 mg (0.0079 mmol) haematin (Fe(III)PPIX-OH) was included in each reaction mixture. The crystals obtained from each mixture were washed extensively with fresh DMF to remove excess surface-adsorbed Fe(III)PPIX-OH. The products were identified and phase-purity confirmed by Pawley fitting of PXRD patterns of the bulk materials. TGA was used to determine the solvent content (Fig. A1c and A1d). The amount of Fe(III)PPIX encapsulated within the framework was determined using ICP-OES. Solvent mass % from TGA: Fe(III)PPIX-**1**, 18.2 ± 0.3%; Fe(III)PPIX-**2**, 27.2 ± 0.7%.

3.2.4 Methyl orange (MO) adsorption

Prior to methyl orange (MO, sodium 4-{[4-(dimethylamino)phenyl]diazenyl}benzene-1-sulfonate) adsorption experiments, single crystals of **1**, **2**, Fe(III)PPIX-**1** and Fe(III)PPIX-**2** were kept in an oven at 50 °C for 14 h. The remaining DMF mass was determined by TGA and accounted for to obtain an accurate mass of material used for MO adsorption experiments. All TGA experiments were performed with a dry N_2 gas flow rate of 50 $cm^3.min^{-1}$ and were monitored from room temperature to 400 °C at a heating rate of 10 °C.min^{-1}. A 40 µM aqueous MO solution was prepared by diluting a 1 mM aqueous stock solution of MO in 0.01 M TRIS buffer (pH 7.4). Approximately 2.5 mg of the appropriate dried MOF material was added and the decrease in concentration of MO was monitored at 465 nm using UV-visible spectroscopy over 3 h. All experiments were conducted with constant magnetic stirring until equilibrium was reached. The accurate mass of crystals without framework associated solvent was determined by TG analysis prior to the experiment being performed and this mass was used for the adsorption quotient calculation. Data were analysed using non-linear regression analysis in GraphPad Prism v6.05.[117] The adsorption quotient was calculated from the following equation:

$$q_t = \frac{(c_i - c_t)V}{m}$$

where q_t is the mass of dye adsorbed at time t ($mg.g^{-1}$), c_i and c_t are the initial and time t solution concentrations respectively ($mg.L^{-1}$), V is the volume of the aqueous dye solution added (L) and m is the mass of material studied (g).[137] Concentrations of MO were determined from its extinction coefficient (24350 $M^{-1}.cm^{-1}$), determined from a Beer's law plot.

3.2.5 Kinetics measurements

The ability of Fe(III)PPIX-**1** to oxidise substrates was initially investigated using MO (the same substrate used for the adsorption experiments) where 2.82 mg of Fe(III)PPIX-**1** (0.50 µmol Fe(III)PPIX-**1**) was added to 4.75 mL of a 2 mM aqueous MO solution (0.01 M TRIS, pH 7.4). The peroxidation reaction was initiated by adding 250 µL of 20 mM H_2O_2 (final concentration of 1 mM H_2O_2). The reaction was monitored by removing 100 µL aliquots of the reaction mixture at fixed time points. These aliquots were diluted in 2.5 ml 0.01 M TRIS buffer (pH 7.4) and the spectra were read on a Shimadzu UV-1800 spectrometer at 25.00 ± 0.02 °C. The decrease of the λ_{max} of MO at 465 nm was plotted as a function of reaction time and analysed using the one-phase exponential function in GraphPad Prism.[117] The % conversion was calculated using the concentration of the limiting reagent, H_2O_2, that can oxidize a maximum of 1 mM MO. Concentrations of MO were determined from its extinction coefficient (24350 $M^{-1}.cm^{-1}$), determined from a Beer's law plot.

The chromophoric substrate 2,2'-azino-bis(3-ethylbenzothiazoline)-6-sulphonic acid (ABTS) was used to monitor the progress of the peroxidatic reaction catalysed by Fe(III)PPIX-Cl or the Fe(III)PPIX-MOF systems. In a typical reaction, 1 mg of catalyst was added to 2.375 mL of a 5 mM aqueous ABTS solution (0.01 M TRIS, pH 7.4). The reaction was initiated by adding 125 µL of a 20 mM H_2O_2 solution to give a final concentration of 1 mM H_2O_2 and total volume of 2.5 mL. The rate of subsequent $ABTS^{\bullet+}$ formation was monitored by the intensity of its absorption band at 660 nm on a Shimadzu UV-1800 spectrometer at 37.00 ± 0.02 °C with constant magnetic stirring. Data were analysed using the one-phase exponential function in GraphPad Prism to obtain maximal yield (Y_{max}) and a linear function to obtain initial rates.[117] Concentrations of $ABTS^{\bullet+}$ were determined from its extinction coefficient (11946 $M^{-1}.cm^{-1}$), determined from a Beer's law plot.

The recycling experiments were conducted in the same manner as the previous kinetics measurements in triplicate (cycles four and five were single measurements). Crystals were collected and dried after each successive cycle. The solvent content was determined using TGA analysis before each cycle; and PXRD was conducted to ensure that crystallinity was retained.

3.2.6 Single crystal X-ray diffraction

The crystal structure of **1** was determined according to the procedure outlined in Chapter 2 (See Table A1 for crystallographic details). Single crystals of Fe(III)PPIX-**1** were removed from the mother liquor and immediately placed under Paratone® oil in order to prevent solvent loss and crystal degradation. Due to the dark colour of the crystals, light polarization could not be used to select a sample of suitable quality for data collection. Instead, crystals were screened on a Bruker KAPPA APEX II Duo diffractometer using Mo-Kα radiation (λ = 0.71073 Å) to find suitable crystals. Full data collection using synchrotron radiation was conducted at the I19 small-molecule single-crystal diffraction beamline at Diamond Light Source (λ = 0.6889 (3) Å), which is equipped with a Pilatus 2M detector.[138] An Oxford Cryosystems Cryostream device was used to cool the crystal to -173.15(2) °C using dry N_2 gas. Data were collected as a series of four sequences of frames with 0.1 s exposure time per frame with no beam attenuation. The best data obtained was of a crystal determined to be a three-component twin. Three-component twin data integration and reduction were performed using ChrysAlisPro and data were corrected for absorption using multi-scan empirical absorption correction.[139] Unit cell and space group were determined using ChrysAlisPro. Structure solution was conducted using direct methods with SHELXS-97 which located all non-hydrogen atoms of the MOF, while SHELXL-97 was used in a refinement by full matrix least-squares on F^2, with anisotropic displacement parameters.[124] Hydrogen atoms were placed with geometric constraints and were refined with isotropic displacement

parameters. All structure determination was completed using the Olex2 interface.[125] The iron centre of the porphyrin core was located using residual electron density and refined isotropically with a fixed site occupancy based on the calculated loading from the ICP-OES data. The nitrogen atoms forming the first coordination sphere of the porphyrin were also located and their positions refined using distance and angle restraints. These atoms were modelled with a lower site occupancy than the iron as a consequence of orientational disorder of the porphine core.[124] Crystal structure data are presented in Table A2.

3.3 Results and Discussion

3.3.1 Synthesis of two potential MOF host systems for Fe(III)PPIX encapsulation

Despite the previously reported success of encapsulating porphyrins in MOFs for the application of heterogeneous catalysis, a serious drawback of this approach has been identified, namely poor access of substrates to the active site.[40] In order to be catalytically active, substrates require rapid access to the metalloporphyrin to allow for efficient interaction and for catalysis not to be limited to sites at the surface of the material.[89] This is a problem that is yet to be addressed in the field of metalloporphyrin@MOF catalysis.

When designing a metalloporphyrin@MOF catalyst, this, together with other factors, needs to be taken into account. Thus, an ideal MOF for FePPIX encapsulation requires the following features: (i) cavities large enough to encapsulate the metalloporphyrin; (ii) enough space for diffusion of small molecules (reactants and products) through the framework; (iii) ability to withstand catalyst leaching; and (iv) a framework that maintains its structural and chemical integrity under catalytic conditions.[140] An additional criterion for investigation of redox catalysis is that the MOF itself should not be redox active. The two MOFs used in this study were chosen to satisfy these criteria with the aim of overcoming the potential problems identified in the field of metalloporphyrin@MOF catalysis.

The two MOFs **1** and **2** (Scheme 3.1) were selected as potential Fe(III)PPIX hosts based on their large pore sizes, solvent-accessible surface areas and redox inactive metal centres. Their key properties are given in Table 3.1. Framework **1** has good gas adsorption properties owing to its infinite 4_3 helical channels that permit permanent porosity[136] and has very large solvent accessible pores that can accommodate Fe(III)PPIX encapsulation with substrate accessibility. The second framework chosen for investigation was Zn-HKUST-1 (**2**). This was chosen as the

HKUST-1 one framework, particularly Cu-HKUST-1, has been extensively used as a host for metalloporphyrins but, although highly porous, is a poor choice for studying the role of the FePPIX guest in redox catalysis since the Cu(II) ions in the framework are redox active and have been shown to exert peroxidatic activity themselves.[110,135] Replacing Cu with redox-inactive Zn affords **2**, an isostructural analogue with the same (3,4)-connected *tbo* net topology and similar properties (Table 3.1). Frameworks **1** and **2** without Fe(III)PPIX were synthesized according to previously reported methods (Scheme 3.1) and both confirmed as phase-pure materials by Pawley fitting of powder X-ray diffraction patterns (Fig. 3.1). PXRD patterns matched the calculated patterns for the previously reported crystal structures.[136,141]

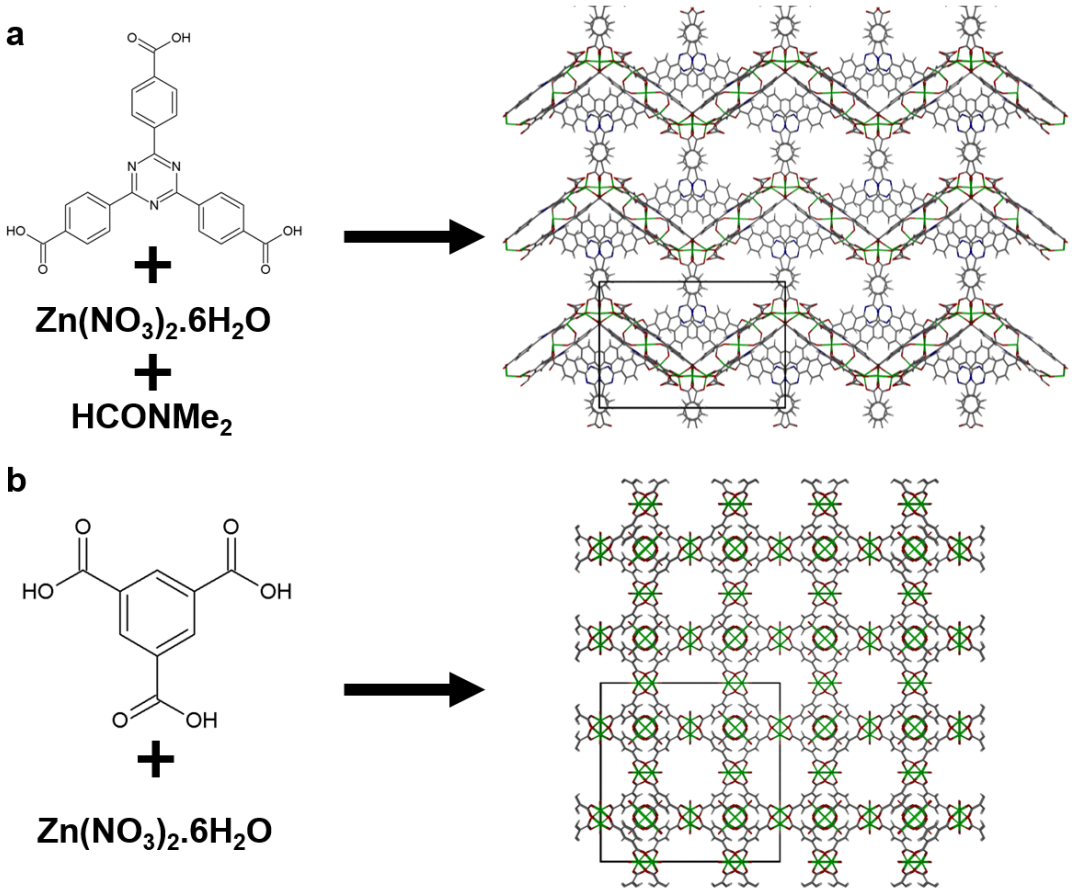

***Scheme 3.1**: Synthesis of (a) $[H_2N(CH_3)_2][Zn_3(TATB)_2(HCOO)]\cdot HN(CH_3)_2\cdot DMF\cdot 6H_2O$ (**1**) and (b) ZnHKUST-1 (**2**) from $Zn(NO_3)_2.6H_2O$ and their respective ligands in DMF. Crystal structures of **1** (from crystals obtained in this study) and **2** are shown viewed along the a-axis.*[136,141]

Table 3.1: Properties of frameworks **1** and **2** pertinent to substrate accessibility.

	$[H_2N(CH_3)_2][Zn_3(TATB)_2(HCOO)]$ (**1**)	Zn-HKUST-1 (**2**)
Pore diameter (Å)	21.9[a]	9.1[a]; 5.9[a]
Pore topology	4_3 infinite helical channels[c]	square channels[b]
% solvent accessible	50.7[d]	64.2[d]
Solvent accessible volume per channel ($Å^3$)	4245[d]	3002[d]

[a] Calculated with the Mercury software package, excluding van der Waals radii[142,143]; [b] Data from previously reported crystal structure;[141] [c] Data from previously reported crystal structure;[136] [d] Calculated using the Mercury software package with a probe radius of 1.2 Å.[142,143]

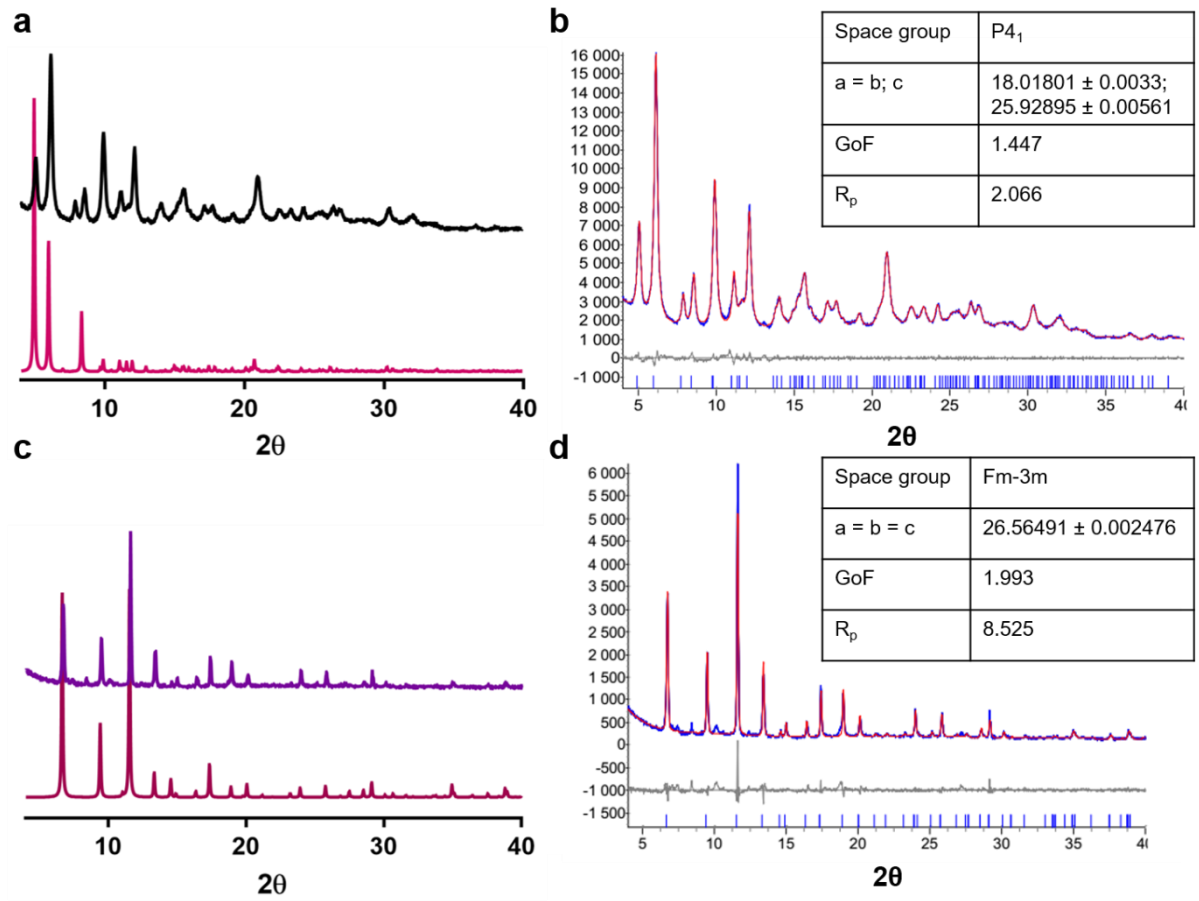

Figure 3.1: *(a) PXRD of **1** as synthesized (black) compared to calculated pattern (pink) of **1**;*[136] *(b) Pawley fitting of **1** as synthesized. Experimental pattern (blue), calculated pattern (red), difference pattern (expt-calc) (grey). Unit cell dimensions and agreement indices are shown in the inset and are in good agreement with the unit cell of the calculated pattern; (c) PXRD of **2** as synthesized (purple) compared to calculated pattern (pink);*[141] *(d) Pawley fitting of **2** as synthesized. Experimental pattern (blue), calculated pattern (red), difference pattern (expt-calc) (grey). Unit cell dimensions and agreement indices are shown in the inset and are in good agreement with the unit cell of the calculated pattern.*

Single crystals of **1** were obtained and it was confirmed that they had the same asymmetric unit as reported by Sun *et al.* (Fig. 3.2).[136] Location of solvent molecules in the channels was not possible due to extensive disorder. It is important to note that the addition of HNO_3 in the synthesis of **1** was essential for the *in situ* hydrolysis of solvent dimethylformamide molecules to form both the formate ions that terminally coordinate to the zinc oxygen clusters in the MOF and the dimethylammonium counterions. Formate coordination causes increased stability and results in the formation of infinite helical channels, producing chiral crystals that crystallize as a racemic mixture. Omission of HNO_3 results in the formation of a thermally unstable MOF which loses its crystallinity rapidly after removal from solvent.[136] The presence of the formate ion was observed in the single crystal structure of synthesized **1** and the high thermal stability was confirmed by TG analysis (Fig. 3.3). These findings agreed with those previously reported by Sun *et al*. The composition of the product was confirmed by combustion analysis.

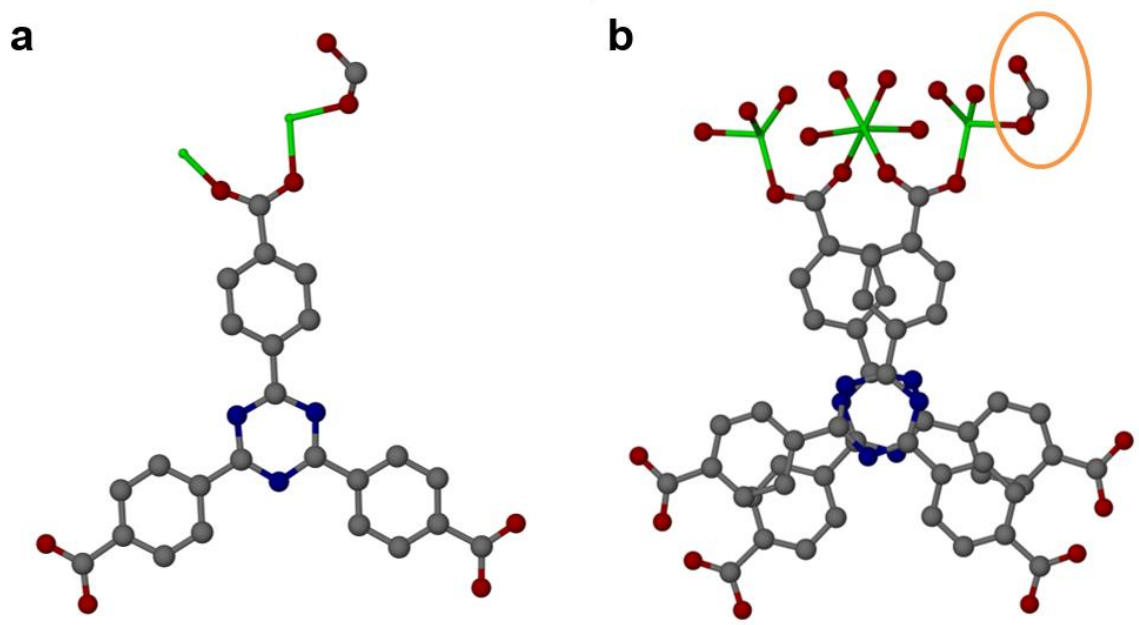

Figure 3.2: *Crystal structure of **1**. (a) Asymmetric unit of **1** with hydrogen atoms not shown for clarity; (b) Coordination environment of Zn ions in **1**. Bridging formate group is circled in orange. The structure of **1** is identical to the previously reported crystal structure of this framework.*[136]

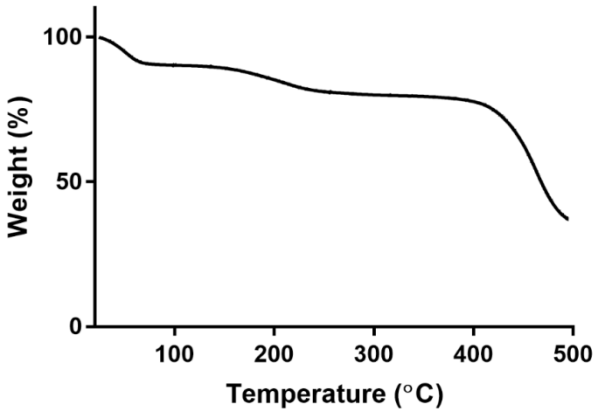

Figure 3.3: *TGA of **1** showing a 21 ± 1% mass loss due to the presence of solvent molecules. Degradation of the framework begins at approximately 400 ℃.*

The ability of substrate to diffuse into the two structures is essential for efficient MOF-assisted heterogeneous catalysis. Consequently, substrate diffusion within **1** and **2** was investigated by monitoring the uptake of methyl orange (MO) into the crystals. MO was chosen as a model substrate as it is of a similar size to typical organic substrates, is highly coloured (and thus amenable to detection via UV-visible spectroscopy) and it is stable under the conditions used to probe peroxidatic catalysis by FePPIX. Framework **1** showed a substantial uptake of MO (10.3 ± 0.8 mg.g^{-1} in 3 h; Fig. 3.4a) which follows a two-step process: (i) an initial rapid step that is attributed to the adsorption of the dye onto the crystal surface, followed by (ii) the slower step of MO diffusion into the framework until equilibrium is reached. This observed uptake is similar to that previously reported for the adsorption of MO by a Fe-HKUST-1 system.[91] The diffusion of MO into **1** is clearly evidenced by the dramatic colour change from colourless to orange (Fig. 3.4b-c). Interestingly, the colour of the crystals shifts to red when exposed to vapour emanating from concentrated HCl (Fig. 3.4d). This chromism occurs because of protonation of MO molecules and indicates that the substrate can readily undergo chemical changes while contained within the pores of the framework. In contrast to **1**, crystals of **2** displayed a low adsorption quotient (2 ± 1 mg.g^{-1}; Fig. 3.4a) which displayed only an initial fast step representative of surface adsorption. The lack of orange colour change in **2** when compared to **1** provided further evidence of the poor substrate uptake of this system. It has been reported that a densified layer forms on the surface of **2** which limits porosity and has been shown to result in very poor gas sorption properties.[141,144] This may account for the observed low adsorption of MO.

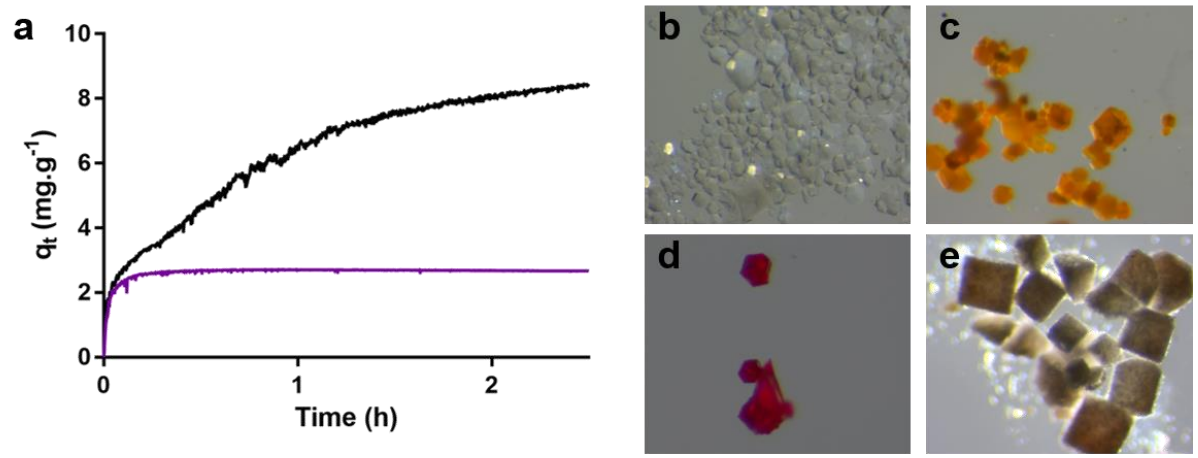

***Figure 3.4**: Adsorption of methyl orange (MO) by MOF crystals. (a) MO adsorption by **1** (black) and **2** (purple) shown as adsorption quotient (q_t) of MO adsorbed from a 40 μM MO solution in the presence of 2.5 mg of each respective MOF; (b) crystals of (**1**), (c) exposed to MO and then (d) HCl vapours; (e) crystals of (**2**) exposed to MO.*

While substrate uptake is an important consideration for MOF-mediated heterogeneous catalysis, a further vital concern is whether the framework maintains its crystallinity following adsorption and exposure to an aqueous solution. In the case of **1**, crystallinity was retained after MO uptake and Pawley fitting of the PXRD pattern demonstrated that the material did not undergo any phase changes upon exposure to water (Fig. 3.5). Crystals of **2**, on the other hand, immediately went opaque when exposed to water (Fig. 3.4e) and PXRD analysis revealed that a phase change also occurs (Fig. 3.6). Unfortunately, because the pattern could not be indexed, possibly due to a mixture of phases being present, this new phase(s) could not be identified and despite an extensive search of the literature, a match for this new phase could not be found. This change of phase upon exposure to aqueous solution may also account for the poor MO adsorption observed for **2**. Consequently, based on the MO uptake and framework stability findings, MOF **1** was considered more suitable for Fe(III)PPIX encapsulation, and therefore was prioritized for further investigation.

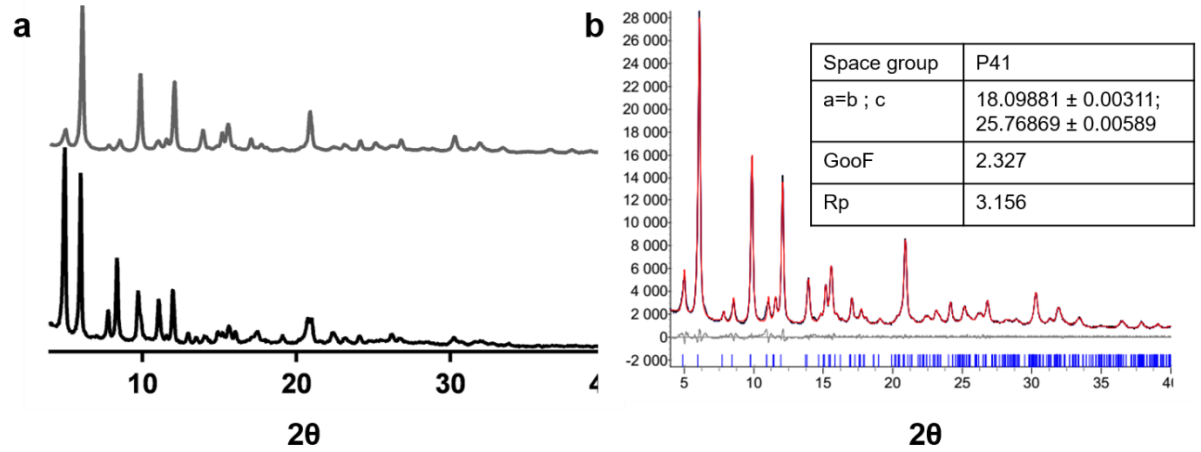

***Figure 3.5**: (a) PXRD of **1** before (black) and after (gray) exposure to an aqueous solution; (b) Pawley fitting of **1** exposed to water for 12 h. Experimental pattern (blue), calculated pattern (red), difference pattern (expt-calc) (grey). Unit cell dimensions and agreement indices are shown in the inset and are in good agreement with the unit cell of the calculated pattern.*

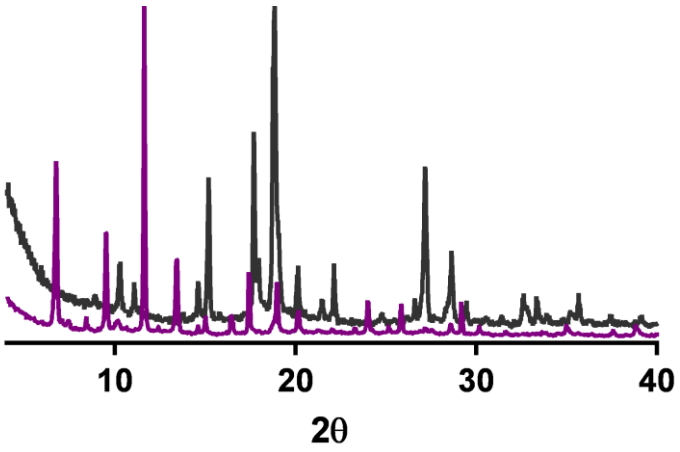

***Figure 3.6**: PXRD of **2** before (purple) and after (black) exposure to an aqueous solution showing the extensive changes to the PXRD trace indicating the presence of a new phase(s).*

3.3.2 Synthesis and characterization of Fe(III)PPIX-1

There are two main synthetic methodologies for non-covalent encapsulation of guests in MOFs: (i) diffusion by soaking the MOF in a solution of the guest,[145] and (ii) encapsulation by including the guest in the MOF reaction mixture and allowing the framework to form around it.[41] The latter method has been used with great success in the field of porphyrin MOF catalysis.

Both strategies were investigated to determine the optimal method of Fe(III)PPIX inclusion into the chosen MOF (**1**). Energy dispersive X-ray spectroscopy (EDS) analysis of the surface of intact crystals as well as of the exposed interior surface of fractured crystals prepared by both methods was used to determine the iron distribution in the crystals. Preparation of Fe(III)PPIX-**1** via soaking was found to be unsuitable as there was no detectable Fe on the newly exposed interior surface of crystals broken open after completion of the preparation (Fig. 3.7). Instead Fe was localized at the surface of the crystals, indicating that only surface adsorption of Fe(III)PPIX had occurred. The observation that very little, if any, Fe was present within the crystal core suggests that Fe(III)PPIX is likely to be too large to diffuse through the framework channels. By contrast, Fe(III)PPIX-**1** synthesized through encapsulation displayed a uniform distribution of Fe throughout the crystal as there was no statistically significant difference in the iron content between the crystal surface and newly exposed interior surface formed by crystal cleavage (Fig. 3.7). The smooth surfaces of Fe(III)PPIX-**1** prepared by encapsulation also show that there are no clumps of adsorbed Fe(III)PPIX on the crystal surface and therefore indicates that the washing process was sufficient to remove any excess Fe(III)PPIX. The loading of Fe(III)PPIX into framework **1** prepared by encapsulation was determined by ICP-OES on digested crystals (1.2 ± 0.1 mass % Fe) and was not significantly different from that determined using EDS analysis.

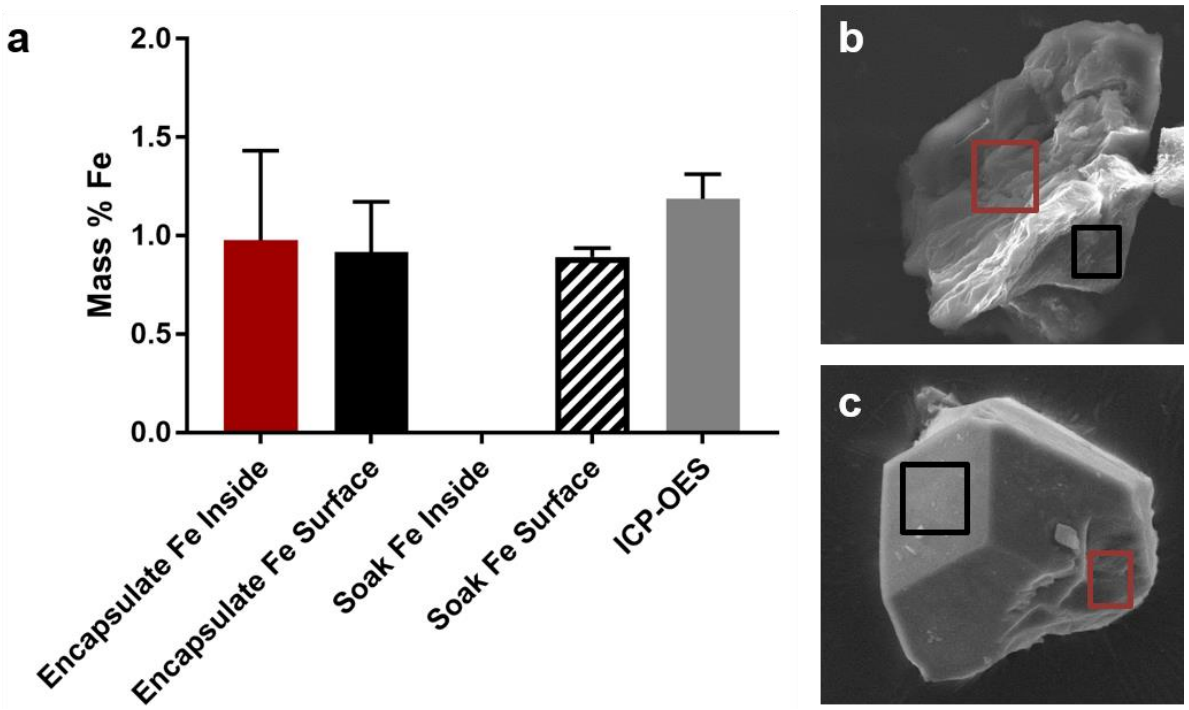

***Figure 3.7**: (a) Loading of Fe in crystals prepared via soaking and encapsulation. Representative SEM images of fractured crystals prepared via (b) soaking and (c) encapsulation. Red boxes indicate interior surfaces of the crystal exposed upon cleavage and black boxes indicate unbroken original surface areas that were analysed with EDS as presented in (a). ICP-OES refers to the ICP-OES measurement of bulk material prepared via the encapsulation method.*

The observation that Fe(III)PPIX uptake into **1** occurs through encapsulation but not diffusion suggests that, once included, catalyst leaching is not a concern. This was confirmed by UV-visible spectroscopy, which showed no evidence of the characteristically intense Soret band of Fe(III)PPIX present after soaking Fe(III)PPIX-**1** crystals in an aqueous solution for over 3 h (Fig. 3.8). Any leaching of Fe(III)PPIX from Fe(III)PPIX-**1** would result in an increase in absorbance at 405 nm. This observation indicates that potential reusability of the Fe(III)PPIX-**1** catalyst.

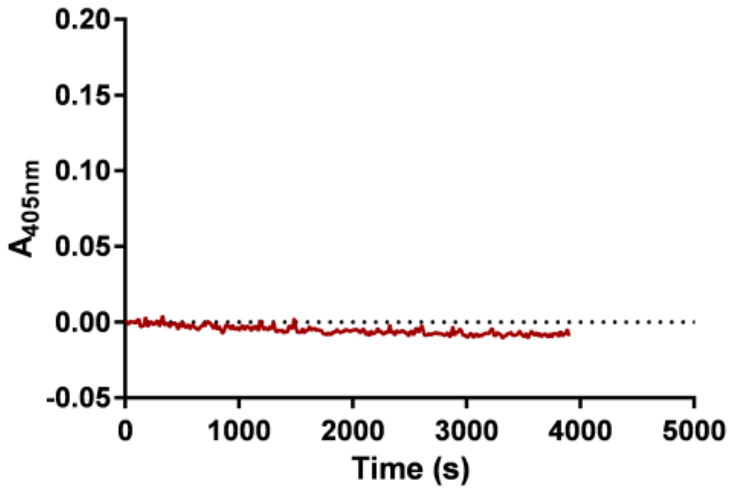

***Figure 3.8**: No evidence of catalyst leaching – no increase in absorbance at 405 nm (absorption of the Soret band of Fe(III)PPIX) was observed arising from Fe(III)PPIX leached out of the catalyst. ≈ 1 mg of Fe(III)PPIX-**1** was placed in 2.5 mL of 0.01 M TRIS (pH 7.4) in a cuvette with constant stirring.*

Once Fe(III)PPIX-**1** had been encapsulated, the material was fully characterised using a variety of techniques. Fe(III)PPIX encapsulation produced no change in crystal morphology as compared to the empty MOF **1**, although a dramatic colour change due to the presence of Fe(III)PPIX was observed (Fig. 3.9a). This dark colour persisted throughout as observed upon cleavage of crystals. The maximal loading of Fe(III)PPIX in Fe(III)PPIX-**1** was investigated by varying concentrations of Fe(III)PPIX in the reaction mixture. Using ICP-OES to quantify Fe content, a loading of 1.2 ± 0.1 mass % Fe was the maximum that could be achieved (Fig. 3.9b). Importantly, framework crystallinity and integrity were maintained upon encapsulation of Fe(III)PPIX as evidenced by the essentially identical powder X-ray diffraction patterns of Fe(III)PPIX-**1** and **1**. Pawley fitting of Fe(III)PPIX-**1** further indicated that the framework retained its unit cell, with only a slight decrease in the length of the *c*-axis when compared to **1** upon formation of Fe(III)PPIX-**1** (Fig. 3.10).

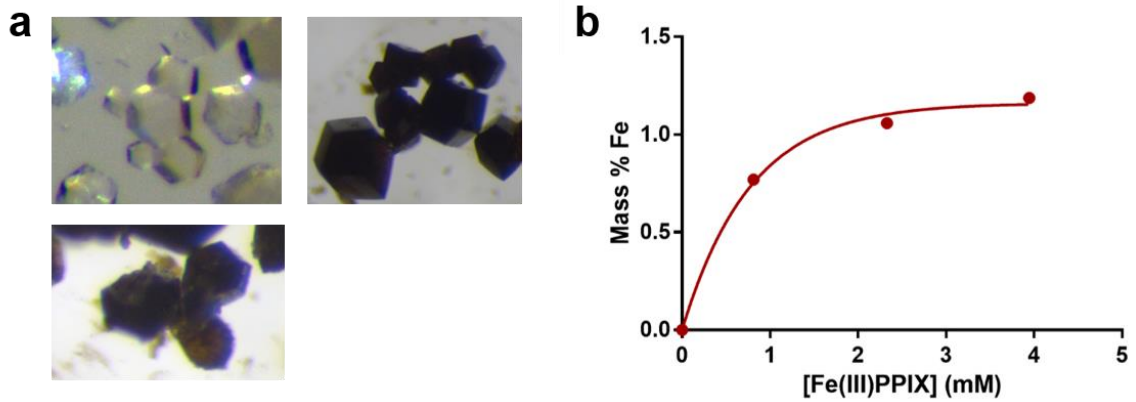

***Figure 3.9**: (a) Images of **1** (top left) and Fe(III)PPIX-**1** (top right) showing the dramatic colour change as well as the dark colour present (bottom) within cleaved crystals; (b) Dependence of loading of Fe(III)PPIX into **1** on concentration of Fe(III)PPIX in the reaction mixture.*

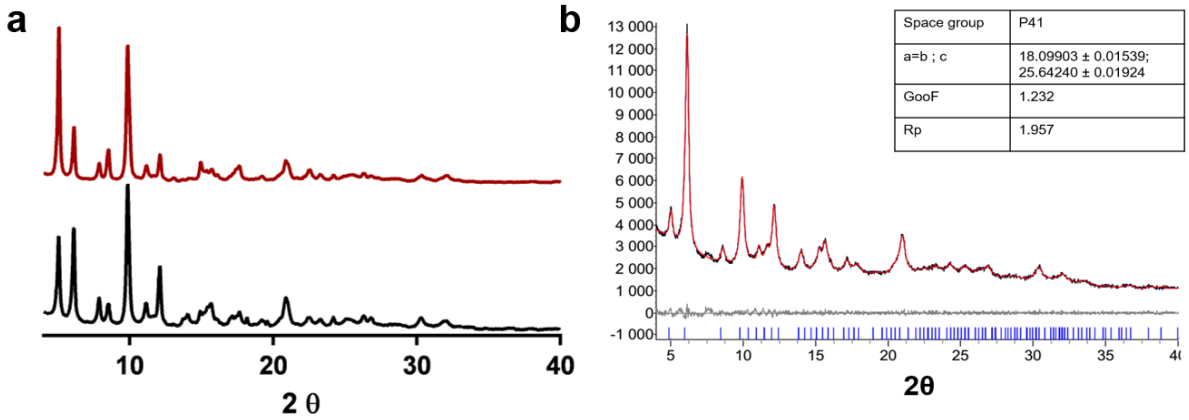

***Figure 3.10**: PXRD analysis of Fe(III)PPIX-**1**. (a) PXRD of 1 (black) and Fe(III)PPIX-1 (red) showing no significant change after encapsulation; (b) Pawley fitting of Fe(III)PPIX-**1** confirming that there were minimal changes to the unit cell upon encapsulation of Fe(III)PPIX into **1** compared to the fitted unit cell of **1** (a = b = 18.09881; c = 25.76869) (Fig. 3.1b). Experimental pattern (blue), calculated pattern (red), difference pattern (expt-calc) (grey). Unit cell dimensions and agreement indices are shown in the inset.*

Following the encapsulation of Fe(III)PPIX into cavities of **1**, it was important to establish whether the ability of the framework to take up substrate had been impeded. Adsorption experiments were thus conducted to ensure that Fe(III)PPIX-**1** retained porosity after inclusion of Fe(III)PPIX within the framework. MO uptake experiments confirmed that porosity was retained in the Fe(III)PPIX-**1** crystals, albeit to a lesser extent than the empty framework itself (Fig. 3.11a) with an adsorption quotient for MO of 6 ± 1 $mg.g^{-1}$ (56% of that observed for the empty framework). The reduced capacity for MO uptake is not unexpected, however, since some of the cavities have been filled by Fe(III)PPIX. Despite this reduction in adsorption capacity, the MO uptake by Fe(III)PPIX-**1** was still nearly three times greater than the uptake for the empty framework **2**. Further evidence for the retention of porosity of **1** after encapsulation of Fe(III)PPIX was obtained using N_2 adsorption isotherms. Findings from these experiments mirror those obtained for MO uptake where Fe(III)PPIX-1 is still able to adsorb substrate (in this case N_2) albeit to a lesser extent than the empty framework (Fig. 3.11b). The Langmuir surface areas calculated from these isotherms indicate a 30% reduction size between **1** (1398 $m^2.g^{-1}$) and Fe(III)PPIX-**1** (1015 $m^2.g^{-1}$). The former value is in agreement with the N_2 adsorption previously reported for **1** (1558 $m^2.g^{-1}$).[136] Importantly, Fe(III)PPIX-**1** could adsorb and desorb water vapor without loss of porosity (Fig. 3.11c) and thus highlights the stability of the material in the presence of water.

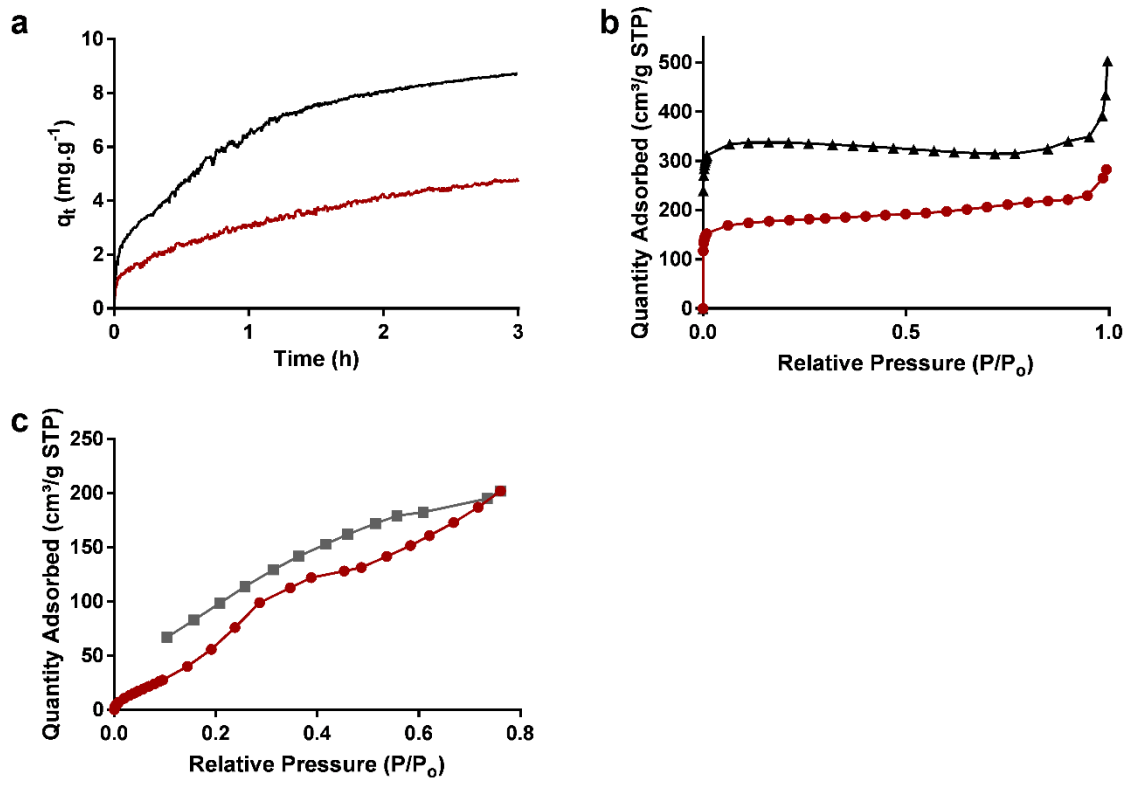

Figure 3.11: *Adsorption properties of Fe(III)PPIX-**1**. (a) Adsorption of MO into **1** (black) and Fe(III)PPIX-**1** (red); (b) N_2 sorption isotherms of **1** (black) and Fe(III)PPIX-**1** (red) at -196 °C; (c) Water sorption (red) and desorption (gray) isotherms of Fe(III)PPIX-**1** at 25 °C.*

Based on the above evidence, it is clear that Fe(III)PPIX successfully encapsulated within MOF **1** without disturbing crystal integrity or substrate adsorption capacity. It was important to establish, however, whether the Fe(III)PPIX structure had not degraded under the harsh crystallization conditions employed. This was investigated by solubilizing Fe(III)PPIX-**1** crystals in basic DMF and recording the resulting UV-visible spectrum. The characteristic Soret band of Fe(III)PPIX observed at 400 nm (Fig. 3.12a) confirmed no degradation had occurred. An important further consideration of Fe(III)PPIX structure is the form in which it exists within the framework. Fe(III)PPIX can readily form μ-oxo dimeric species which can affect the potential use of Fe(III)PPIX-**1** as a heterogeneous catalyst. To determine the speciation of Fe(III)PPIX within the framework, solid-state optical absorption spectroscopy

was employed. The absorption spectrum of Fe(III)PPIX in Fe(III)PPIX-**1** clearly shows that it does not exhibit the spectroscopic features of the μ-oxo dimer, since it lacks the characteristic feature near 600 nm. Instead, the broad envelope observed around 650 nm more closely resembles the predominantly charge-transfer band of H_2O-Fe(III)PPIX (Fig. 3.12b).[146,147] The lack of degradation and formation of H_2O-Fe(III)PPIX after encapsulation within the framework highlights the potential for catalytic activity of Fe(III)PPIX-**1**.

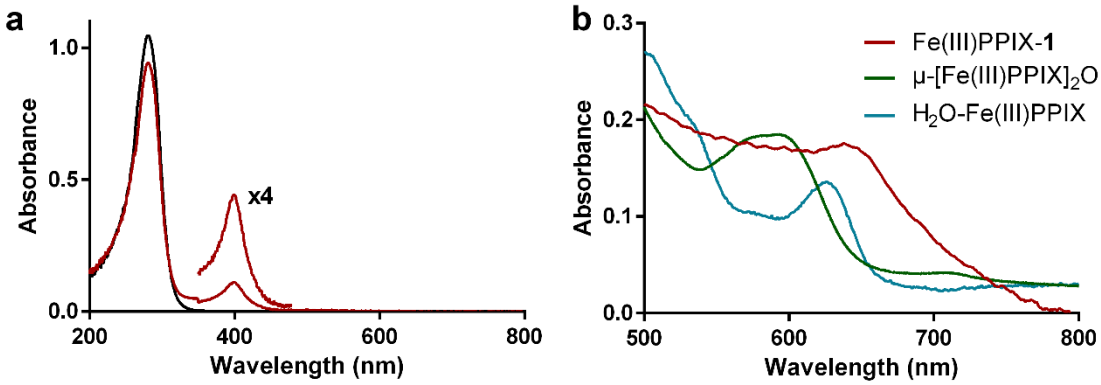

***Figure 3.12**: (a) UV-visible spectra of solubilized **1** (black) and Fe(III)PPIX-**1** (red) showing the presence of the Soret band at 403 nm in the latter; (b) Solution-state UV-visible spectra of μ-[Fe(III)PPIX]$_2$O (green) and H_2O-Fe(III)PPIX (blue) compared to the solid-state UV-visible spectrum of Fe(III)PPIX-**1** (red).*

3.3.3 Crystal structure of Fe(III)PPIX-1

Further insight into the structure of Fe(III)PPIX-**1** was obtained through single crystal X-ray diffraction analysis. The crystal studied was found to be a three-component twin with approximately equal contributions from each component and the framework was isostructural with the empty framework **1**. Interestingly, the bridging formate group present in the empty framework could not be located in the crystal structure of Fe(III)PPIX-**1** and only a bridging oxygen atom probably attributable to a hydroxide ion between the secondary building units (SBUs) was observed. The crystals form as a racemic mixture and therefore belong either to the space group $P4_3$ or $P4_1$. While previous studies of the host framework **1** reported crystals of higher symmetry ($P4_322$ or $P4_122$),[136] the presence of the asymmetric guest lowers the symmetry of the system.

The asymmetric unit contains an hourglass-shaped SBU, or pinwheel SBU, which consists of two tetrahedral terminal zinc ions and a central octahedral zinc ion (Fig. 3.13a). The central zinc is coordinated to six carboxylate oxygen atoms of the $TATB^{3-}$ ligand while both tetrahedral zinc ions are coordinated to three carboxylate oxygen atoms and a bridging oxygen atom, linking the SBUs. The $TATB^{3-}$ ligands π-stack with each other at a distance of 3.36 Å between the triazine rings and form a D_3 Piedfort unit ($\theta \approx 30°$).[136,148] The framework is a non-interpenetrated (10,3)-a network with chiral 4_1 (or 4_3) helical channels, creating a chiral environment within the channels. These channels are the hypothesized pathways through which substrates diffuse into the framework.

Despite exhaustive attempts to fully model the Fe(III)PPIX guest within the framework, this was not possible. This likely arose because of the extensive disorder within the channels and was exacerbated by the low loading of Fe(III)PPIX and the twinning of the crystal. Nonetheless, the central Fe(III) ion of Fe(III)PPIX could be located based on residual electron

density. This was refined isotropically and the site occupancy of the Fe ions was refined using a combination of the ICP-OES loading data and the magnitude of the observed electron density. The nitrogen atoms coordinated to the central iron ion could be located and were also refined isotropically using distance restraints (Fig. 3.13a). The occupancy of these nitrogen atoms was lower than that of the iron, as they represent one orientation of the disordered porphyrin centre. Further residual electron density in the vicinity of the iron centre could not be satisfactorily modelled. Location of the first coordination sphere of Fe(III)PPIX, however, did allow its position in the framework channels to be determined. Interestingly, it did not π stack with the $TATB^{3-}$ ligands along the walls of the channels, but rather was present in the centre of the channels. This channel-centre location of the Fe(III)PPIX could contribute to the orientational disorder observed, as the interactions between Fe(III)PPIX and the framework are likely weak. Due to the fact that the bridging formate groups could not be located in the structure, it could be hypothesized that the carboxylate groups on the Fe(III)PPIX propionate chains have exchanged for the formate groups in the framework itself. This has been observed by Yaghi and co-workers in a chiral MOF, MOF-520.[149]

Rigid-body modelling of the porphine core confirmed that there is sufficient space for this substructure of Fe(III)PPIX in the located position (Fig. 3.13b). The solvent-accessible volume after encapsulation is 3520 $Å^3$ (calculated using the Mercury software package with a probe radius of 1.2 Å).[143] which is approximately 40% of the unit cell volume. This confirms that typical organic substrates, such as MO,[142,143] have sufficient space to diffuse into the channels.

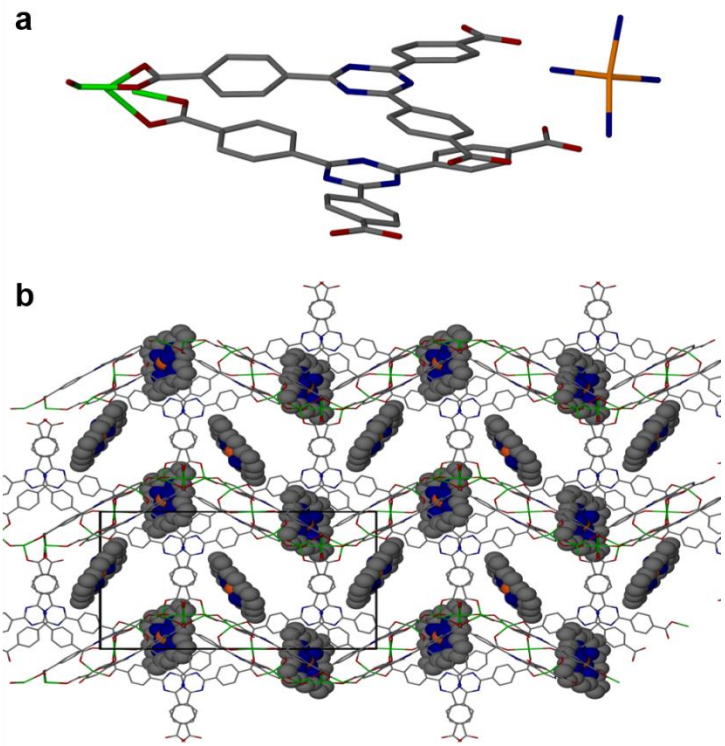

Figure 3.13: *Crystal structure of Fe(III)PPIX-**1**. (a): Coordination environment and Piedfort unit of the framework as seen in the asymmetric unit of Fe(III)PPIX-**1** showing the located Fe and N atoms of Fe(III)PPIX in **1** and (b) packing of Fe(III)PPIX-**1** viewed along the b-axis with a rigid-body model of the porphine core of Fe(III)PPIX in the channels of the framework (shown as space-fill; orange = Fe, blue = nitrogen).*

3.3.4 Synthesis and characterisation of Fe(III)PPIX-2

To compare the activity of Fe(III)PPIX encapsulated in frameworks with good and poor suitability for heterogeneous catalysis (**1** and **2** respectively), Fe(III)PPIX-**2** was synthesized analogously to Fe(III)PPIX-**1** using the encapsulation method. After successful encapsulation of Fe(III)PPIX into **2**, Fe(III)PPIX-**2** showed a similar dramatic colour change as observed for Fe(III)PPIX-**1** (Fig. 3.14). The cubic morphology of **2** was retained upon encapsulation of Fe(III)PPIX.

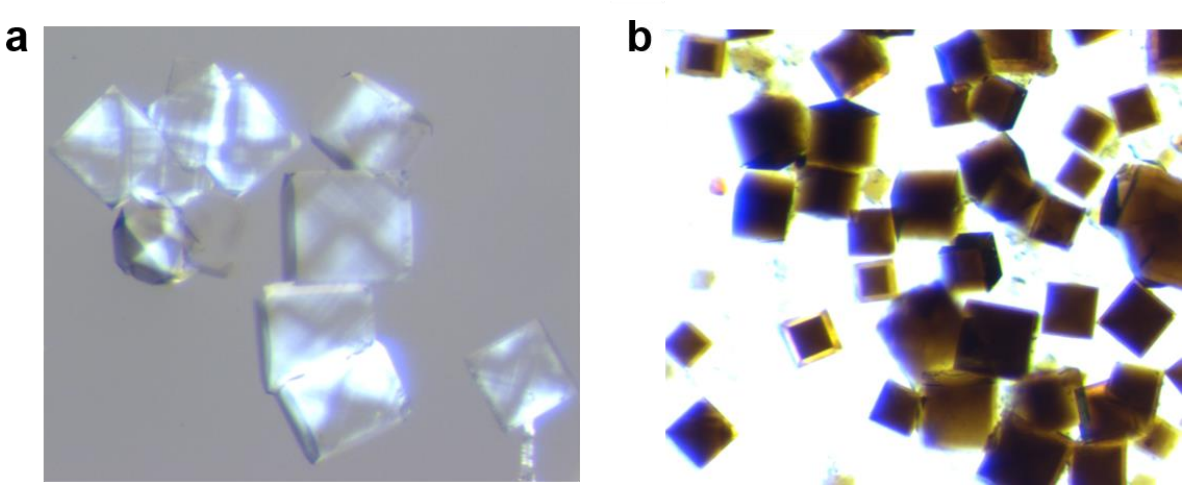

Figure 3.14: *(a) Images of **2** (left) and Fe(III)PPIX-**2** (right) showing the dramatic colour change and retention of morphology of **2** upon encapsulation of Fe(III)PPIX.*

Retention of the framework structure of **2** on forming Fe(III)PPIX-**2** was confirmed by PXRD and Pawley fitting (Fig. 3.15) which confirmed no major structural changes following Fe(III)PPIX encapsulation. It is important to note that it is possible to obtain multiple phases of Fe(III)PPIX-**2** depending on the reaction conditions and therefore the phase purity of the sample as confirmed by PXRD is crucial. The Fe loading in Fe(III)PPIX-**2** determined by ICP-OES was comparable to Fe(III)PPIX-**1** (1.039 ± 0.004 vs. 1.2 ± 0.1 mass % Fe respectively).

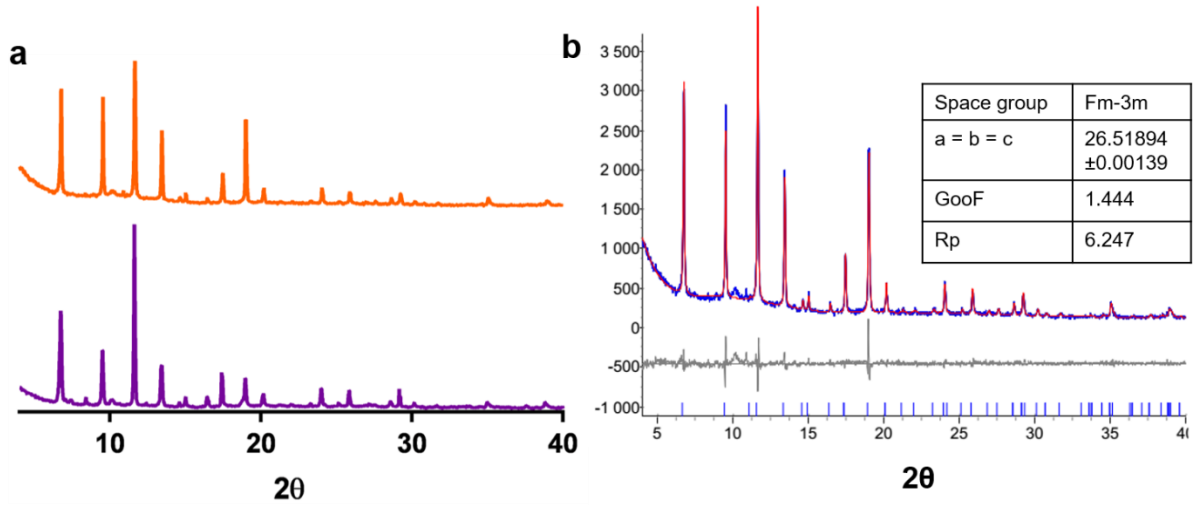

***Figure 3.15**: (a) PXRD of **2** (purple) compared to synthesized Fe(III)PPIX-**2** (orange); (b) Pawley fitting of Fe(III)PPIX-**2** as synthesized. Slight contamination is evident from the presence of small peaks at 6° and 9.5° resulting in a poor Pawley fit at these values of 2θ. Experimental pattern (blue), calculated pattern (red), difference pattern (expt-calc) (grey). Unit cell dimensions and agreement indices are shown in the inset and are in good agreement with the unit cell of **2**.*

As observed for Fe(III)PPIX-**1**, encapsulation of Fe(III)PPIX in **2** reduced the MO adsorption quotient by roughly half from 2 ± 1 $mg.g^{-1}$ for **2** to 1.0 ± 0.3 $mg.g^{-1}$, although the magnitude of the adsorption quotient for Fe(III)PPIX-**1** remains much larger than that for Fe(III)PPIX-**2**. This latter observation suggests that substrates would have better access to catalytic sites in Fe(III)PPIX-**1**, being able to access sites both on the surface and in the interior of the crystal. Based on the MO adsorption results for **2**, access of substrate to Fe(III)PPIX in Fe(III)PPIX-**2** is, by contrast, likely limited to only surface sites. This observation suggests once again that **1** is likely to be more suitable for MOF-encapsulated Fe(III)PPIX catalysis.

3.3.4 Catalytic activity of Fe(III)PPIX-1

To investigate whether the Fe(III)PPIX-**1** system is suitable as an efficient heterogeneous catalyst and whether it shows improved catalytic activity over solid-state Fe(III)PPIX itself, its peroxidatic activity was investigated. MO can undergo oxidation in the presence of peroxides and a suitable catalyst.[150] MO oxidation by H_2O_2 in the presence of Fe(III)PPIX-**1** was indeed possible and achieved a 86.6% conversion to its oxidized product (Fig. 3.16). It is not, however, a convenient substrate for kinetic studies owing to its intense colour which bleaches in this reaction. This necessitates either the use of very low concentrations of both MO and H_2O_2, resulting in slow reaction, or requiring an inconvenient out of cell reaction. Consequently, an alternate oxidation reaction more amenable to kinetic studies was required.

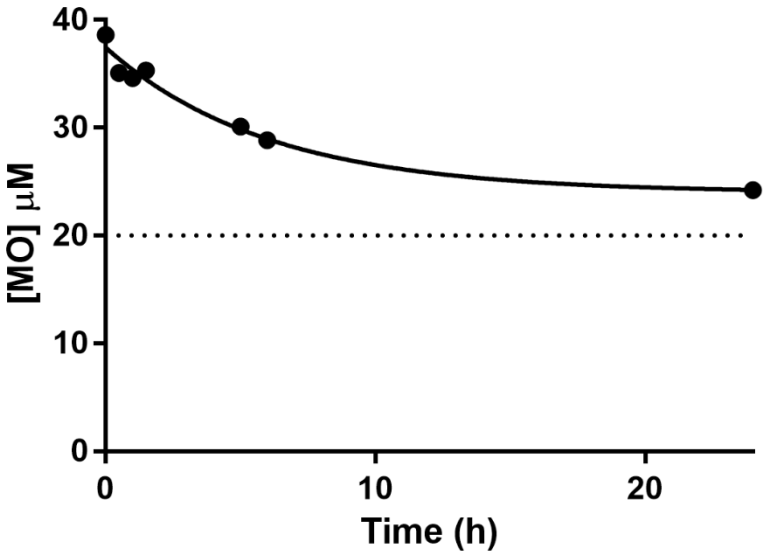

Figure 3.16: *Oxidation of MO by H_2O_2 in the presence of Fe(III)PPIX-**1**. Dotted line indicates theoretical concentration of MO after 100% oxidation by H_2O_2 catalyzed by Fe(III)PPIX-**1**.*

The chemically and structurally similar ABTS is as a good alternative substrate for kinetics investigation. Oxidation of this well-documented substrate results in an increased absorption of a band at 660 nm due to the formation of a radical cation ($ABTS^{\bullet+}$).[23,151–153] It was found that in the presence of **1**, no catalytic activity was observed (Fig. 3.17), confirming that **1** is not itself catalytically active. This confirms that all catalytic activity observed stems from the encapsulated porphyrin and not the framework itself. This result is expected due to the redox inactive nature of Zn(II) which is used to construct the framework.

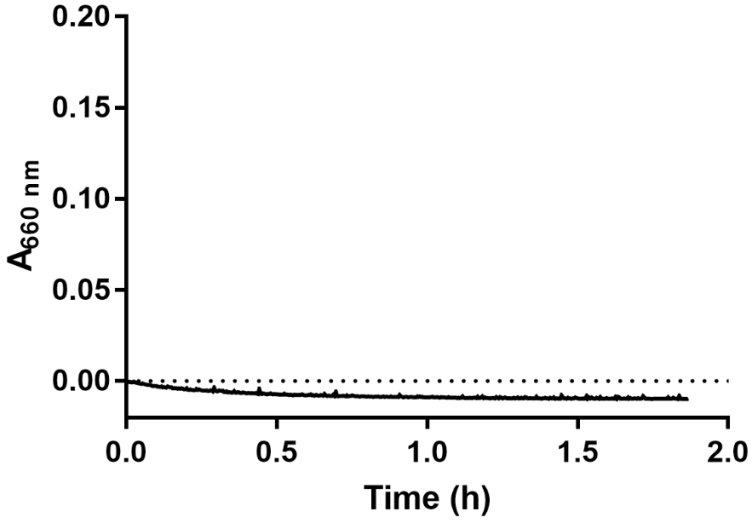

***Figure 3.17**: Lack of oxidation of ABTS by **1**. No increase in absorbance at 660 nm corresponding to the formation of $ABTS^{\bullet+}$ was observed under standard reaction conditions (≈1 mg **1** added as a "catalyst").*

The initial rates of the oxidation of ABTS to $ABTS^{\bullet+}$ by H_2O_2 catalysed by Fe(III)PPIX-**1** and Fe(III)PPIX-**2** were determined by monitoring the increase of absorption at 660 nm (Fig. 3.18). The catalytic activities of Fe(III)PPIX-**1** and Fe(III)PPIX-**2** were also further compared to solid Fe(III)PPIX-Cl (haemin). All reactions were conducted with [ABTS] ≫ [H_2O_2] ≫ [Fe(III)PPIX]. Under these reaction conditions one H_2O_2 molecule will oxidize two ABTS molecules to $ABTS^{\bullet+}$ through the formation of a high valent iron-oxo intermediate.[19,29] The

initial rates as well as the percentage conversion of ABTS in each system are presented in Table 3.2. It is important to note that the yield observed experimentally is not a true reflection of the number of ABTS molecules oxidized owing to disproportionation of $ABTS^{\bullet+}$.[151] The $ABTS^{\bullet+}$ cation exists in equilibrium with unreacted ABTS and an azodication. This reaction is slow and will therefore not affect initial rates; however, it will affect the experimentally observed yield of $ABTS^{\bullet+}$ and therefore the experimentally observed TON.[151] Consequently, reported values can be thought of as a lower limit to catalytic activity.

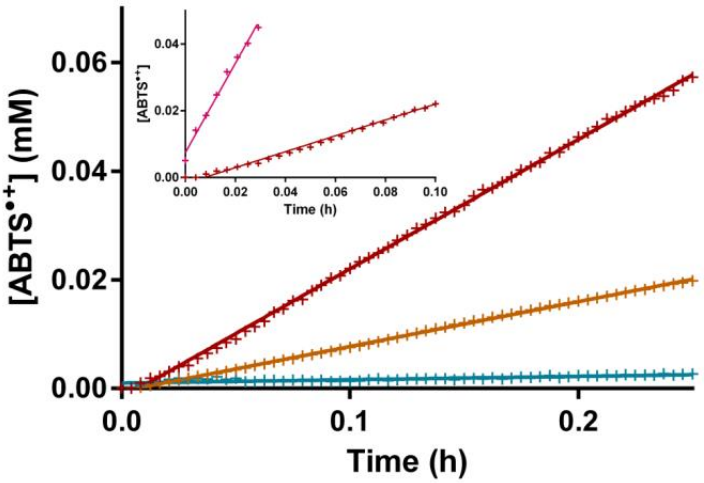

***Figure 3.18**: Initial rates of ABTS oxidation by H_2O_2 catalysed by Fe(III)PPIX-**1** (red), Fe(III)PPIX-**2** (orange) and solid Fe(III)PPIX-Cl (blue); Inset: Initial rate with Fe(III)PPIX-**1** (red) and solution state Fe(III)PPIX (pink). Reaction conditions are given in Table 3.2.*

Table 3.2: Summary of kinetic results for oxidation of ABTS by H_2O_2.

	Fe(III)PPIX-**1**[a]	Fe(III)PPIX-**2**[b]	Fe(III)PPIX-Cl[c]
Catalyst loading in reaction[d]	1.36 mol %	1.28 mol %	12.24 mol %
Initial rate (mM $ABTS^{\bullet+}.h^{-1}$)	0.2380 ± 0.0009	0.0826 ± 0.0003	0.0062 ± 0.0006
Yield [$ABTS^{\bullet+}$] (mM)	0.22 ± 0.02	0.075 ± 0.003	0.011 ± 0.001
Conversion %[e]	10.9 ± 1.2	1.86 ± 0.06	0.55 ± 0.09
TON[f]	3.4 ± 0.3	1.2 ± 0.1	0.0202 ± 0.0001

[a] ≈ 0.17 μmol Fe(III)PPIX in 2.5 mL TRIS reaction buffer; [b] ≈ 0.16 μmol Fe(III)PPIX in 2.5 mL TRIS reaction buffer; [c] ≈ 1.59 μmol Fe(III)PPIX; [d] Mol of Fe(III)PPIX per mol of H_2O_2; [e] Calculated using H_2O_2 as the limiting reagent with a maximum $ABTS^{\bullet+}$ yield of 2 mM: Conversion % = 100 × [$ABTS^{\bullet+}$] (mM)/2; [f] TON = [$ABTS^{\bullet+}$] (M)/[Fe(III)PPIX] (M). All reactions were conducted under the following conditions: 5 mM ABTS, 1 mM H_2O_2 in 0.01 M TRIS (pH 7.4), 37.00 °C, 2 h.

Both Fe(III)PPIX-**1** and Fe(III)PPIX-**2** showed a dramatic increase in yield and conversion of ABTS relative to solid Fe(III)PPIX-Cl despite of the fact that the quantity of Fe(III)PPIX was more than ten-fold higher in the Fe(III)PPIX-Cl experiments. This is a clear indication that the Fe(III)PPIX centres are more accessible in the metalloporphyrin@MOF materials compared to Fe(III)PPIX-Cl. Fe(III)PPIX-**1**, however, exhibited an approximately three-fold faster rate and six-fold higher conversion than Fe(III)PPIX-**2** confirming that the former is a more efficient catalyst than the latter. This is consistent with the ability of substrates to access the Fe(III)PPIX sites in the interior of **1** by diffusion and not only surface sites as seems to be the case for framework **2**. The structural stability of **1** but not **2**, in water likely also contributes to this finding.

Interestingly, when comparing the oxidation of ABTS catalysed by Fe(III)PPIX-**1** and a MOF constructed with metalloporphyrin linkers (MMPF-6) reported by Chen *et al*., the initial rates are comparable (0.2380 ± 0.0009 mM $ABTS^{\bullet+}.h^{-1}.mM^{-1}$ H_2O_2 for Fe(III)PPIX-**1** and 0.2945 mM $ABTS^{\bullet+}.h^{-1}.mM^{-1}$ H_2O_2 for MMPF-6).[128] This indicates that Fe(III)PPIX-**1** reaches the efficiency of catalysts in which the metalloporphyrin forms part of a highly ordered framework.

To compare the activity of Fe(III)PPIX encapsulated into the framework with Fe(III)PPIX in solution, the initial rates of heterogeneously catalysed ABTS oxidation were compared to the initial rate produced by homogeneous catalysis. This was investigated by dissolving Fe(III)PPIX-OH (0.125 μmol Fe(III)PPIX; 1 mol %) in aqueous solution and monitoring the production of $ABTS^{\bullet+}$ over time at 600 nm. At the same substrate concentration, the initial rate of this reaction was only about six times faster (1.34 ± 0.06 mM $ABTS.hr^{-1}$) than that for Fe(III)PPIX-**1** (Fig. 3.18 inset). This rapid reaction in solution, however, quickly dropped off so that the conversion of ABTS was only 5.67% compared to 10.91% for Fe(III)PPIX-**1** after reaction completion. This suggests the rate of the peroxidation reaction is limited by the diffusion of ABTS into the frameworks rather than the reaction between Fe(III)PPIX and H_2O_2. The increased yield observed when using the heterogeneous catalyst Fe(III)PPIX-**1** can probably be attributed to the framework preventing catalyst aggregation and protecting the metalloporphyrin from oxidative degradation, both of which contribute to limited FePPIX catalyst lifetime in solution.

The reusability of Fe(III)PPIX-**1** was investigated by conducting recycling experiments. The catalyst maintained its structural integrity through several cycles. PXRD analysis showed only changes in intensity of the peaks (Fig. 3.19a) and can be attributed to differing solvent content in the material as residual DMF leaves the pores and is replaced by water. Pawley fitting confirmed that the unit cell remained the same after three successive cycles of ABTS oxidation with a slight expansion along the *a* and *b* axes from 18.0993 Å to 18.15374 Å (Fig. 3.19b). Fe(III)PPIX-**1** showed no loss of catalytic activity through five successive cycles, demonstrating that this catalyst has excellent recyclability (Fig. 3.20). Thus, by encapsulating Fe(III)PPIX into the MOF, the catalytic centre becomes stable in an aqueous medium and, being heterogeneous, can be recovered and reused. This is in direct contrast to previously reported recyclability for a synthetic tetraphenyl porphyrin in Cu-HKUST-1[41] and for Fe(III)PPIX encapsulated in MIL-101-NH_2(Al)[103] which both showed a decrease in activity after each successive cycle.

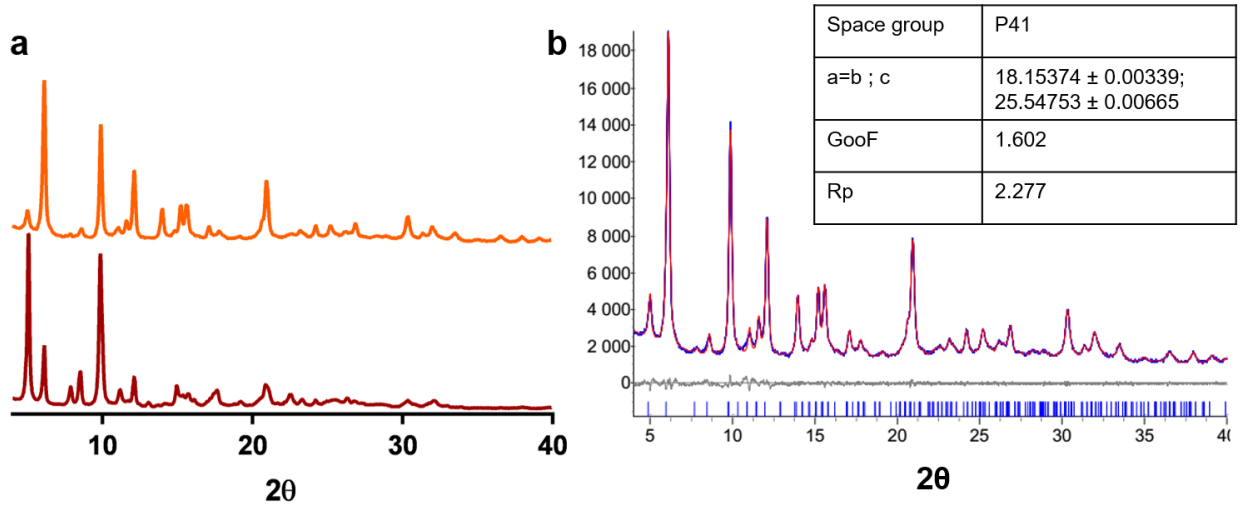

***Figure 3.19**: (a) PXRD comparison of Fe(III)PPIX-**1** (red) and the same material after five successive cycles of ABTS oxidation (orange) showing minimal changes and that Fe(III)PPIX-**1** retained its structural integrity; (b) Pawley fitting of Fe(III)PPIX-**1** after five cycles of ABTS oxidation. Experimental pattern (blue), calculated pattern (red), difference pattern (expt-calc) (grey). Unit cell dimensions and agreement indices are shown in the inset and are in good agreement with the unit cell of Fe(III)PPIX-**1**.*

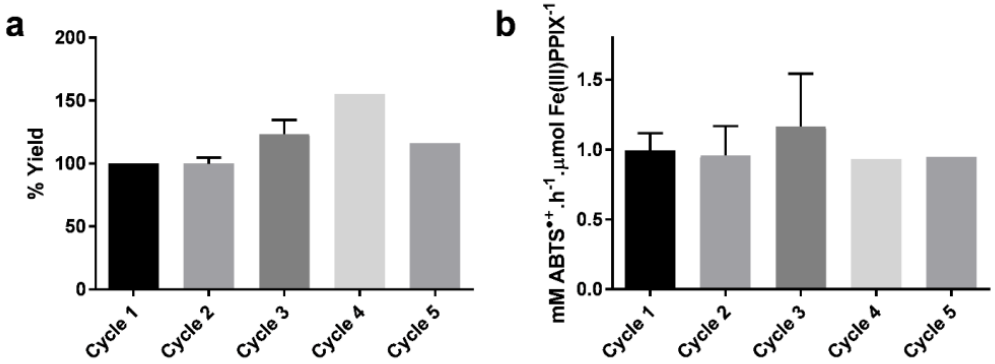

***Figure 3.20:** (a) Yield of $ABTS^{\bullet+}$ (relative to cycle 1) and (b) initial rate of ABTS oxidation represented as mM $ABTS^{\bullet+}.h^{-1}.\mu mol^{-1}$ of Fe(III)PPIX catalysed by Fe(III)PPIX-**1** through five successive cycles of catalyst recovery and reuse.*

3.4 Summary and Conclusion

Two redox inactive frameworks, **1** and **2**, were investigated for their potential use for encapsulating Fe(III)PPIX-**1** to synthesize a heterogeneous metalloporphyrin@MOF oxidation catalyst. It was found that framework **1** was more suitable for Fe(III)PPIX encapsulation owing to the direct access of substrates into the framework as well as its aqueous stability. By comparison, framework **2** showed a much lower adsorption quotient and evidence of aqueous instability.

Encapsulation of Fe(III)PPIX was confirmed using a variety of techniques, but importantly, the distribution and accessibility of catalytic sites in Fe(III)PPIX-**1** has been confirmed by synchrotron single-crystal X-ray diffraction and this is the first report of single crystal X-ray data for encapsulation of Fe(III)PPIX into a MOF. Furthermore, the retention of direct substrate access into the framework was confirmed using the same MO adsorption experiment conducted for the native framework (**1**). Substrate can most likely access the catalytic sites present within the MOF by diffusion through the infinite 4_3 helical channels. By contrast, Fe(III)PPIX-**2** showed poor substrate uptake and correspondingly poor catalytic activity. This, coupled with the observed aqueous instability of **2**, reinforces it unsuitability as a peroxidation catalyst in this system.

Inclusion of Fe(III)PPIX into **1** drastically increases both the initial rate of peroxidatic oxidation of ABTS compared to solid Fe(III)PPIX-Cl and dramatically increases the yield compared to both solid state Fe(III)PPIX-Cl and solution state Fe(III)PPIX. What is more, Fe(III)PPIX-**1** was shown to catalyse ABTS oxidation by H_2O_2 at an initial rate less than an order of magnitude slower than Fe(III)PPIX in solution and with almost double the yield of the native porphyrin in solution. This is most likely due to the MOF preventing aggregation and degradation of the porphyrin in solution. The catalyst can be readily recovered and recycled

without loss in catalytic activity, indicating that encapsulation of Fe(III)PPIX in **1** prevents degradation of Fe(III)PPIX in solution.

Further explorations of the mechanism of peroxidation and the potential use of Fe(III)PPIX-**1** as a heterogeneous oxidation catalyst are presented in Chapters 5 and 6 respectively. Development of synthetic metalloporphyrin@MOF systems using the same frameworks is presented in Chapter 4 for comparison with the nature Fe(III)PPIX molecule.

Chapter Four: Encapsulation of Fe(III)TPP into MOFs

4.1 Introduction

Synthetic tetraphenyl porphyrin (TPP) derivatives which contain a phenyl group at the *meso*- position on the porphyrin ring, a site which can be further functionalized to elicit desired properties of the porphyrin, have historically been extensively used and developed as mimics of Fe(III)PPIX. An example of these synthetic porphyrins that have been designed to prevent aggregation and oxidation are 'picket fence' and "capped" porphyrins.[32–36] These porphyrins contain bulky side chains attached at the *meso*- position and will create steric bulk on one plane of the porphyrin therefore hindering the process of aggregation as well as formation of the μ-oxo dimeric form.[33]

By manipulating the properties of the synthetic porphyrin, porphyrins can be designed to have better catalytic activities as they can be designed to circumvent some of the problems observed in FePPIX homogeneous catalysis. Given the success of synthesizing Fe(III)PPIX encapsulated MOFs demonstrated in the previous chapter, synthesizing Fe(III)TPP encapsulated MOFs was also considered to compare the catalytic activities.

Several authors have reported the encapsulation of various FeTPP derivatives in MOFs; however, the activity of the FeTPP group in these systems is unclear.[41,98,154–159] This is for two reasons: (i) a redox -active metal ion with intrinsic peroxidase activity has been used for the synthesis of the framework or; [41,98,154–157] (ii) in the case where inactive linkers such as Zn have been used, the activity has not been directly measured.[41,97,158,159] In order to determine the extent of the activity from the porphyrin moiety, it is crucial that Fe(III)TPP is encapsulated in a MOF with redox inactive metal ions such as Zn(II). Consequently, this chapter is devoted to the synthesis and evaluation of Fe(III)TPP encapsulated in the same redox-inactive Zn-containing MOFs used to encapsulate Fe(III)PPIX in Chapter 3.

4.2 Experimental methods and characterisation of products

4.2.1 Synthesis of Fe(III)TPP-1

Single crystals of Fe(III)TPP-**1** were prepared by dissolving 25 mg (0.113 mmol) of 4,4′,4″-*s*-triazine-2,4,6-triyl-tribenzoic acid (H_3TATB), 270 mg (0.907 mmol) of $Zn(NO_3)_2.6H_2O$ and 40 mg (0.057 mmol) 5,10,15,20-tetraphenyl-21H,23H-porphine iron(III) chloride (Fe(III)TPP-Cl) in 25 mL of DMF with 300 µL of 0.5 M HNO_3 in a 100 mL Schott bottle. The mixture was sonicated to ensure the dissolution of all material and placed in an oven at 105 ± 2 °C for 16 h. The oven was cooled to room temperature over 4 h, the crystals collected and washed extensively with fresh DMF to remove excess surface-adsorbed Fe(III)TPP-Cl. The product was confirmed by PXRD.

4.2.2 Synthesis of Fe(III)TPP-2

Single crystals of Fe(III)TPP-**2** were prepared by dissolving 28 mg (0.133 mmol) of benzene-1,3,5-tricarboxylic acid, 62 mg (0.208 mmol) of $Zn(NO_3)_2.6H_2O$ and 4 mg (0.0057 mmol) Fe(III)TPP-Cl in 3 mL of DMF in a Teflon-lined autoclave. The autoclave was placed in an oven at 85 ± 2 °C for 48 h. The oven was cooled to room temperature over 3 hours, the crystals collected and washed extensively with fresh DMF to remove excess surface-adsorbed Fe(III)TPP-Cl. The product was confirmed by PXRD and TGA was performed to determine the solvent content (Fig. 2b, Fig A2). The crystals were stored in fresh DMF and dried in an oven at 50 °C for 12 h prior to use in kinetics experiments. After drying, the crystals were stored under argon in a vial to limit decomposition. Solvent mass % from TGA: 35 ± 3%.

4.2.3 Single crystal X-ray diffraction

Single crystal X-ray diffraction data collection and analysis were conducted according to the method described in Chapter 2 with one addition. When refining the data obtained for Fe(III)TPP-**2**, the Fe(III)TPP molecule was located and refined isotropically with a fixed site occupancy. DFIX and DANG restraints were used due to the low site occupancy of the porphyrin moiety which was also statistically disordered over three positions. Crystallographic details for Fe(III)TPP-**2** and $(Fe(III)TPP)_2O$ are provided in Tables A3 and A4 respectively.

4.3 Results and Discussion

4.3.1 Synthesis and characterisation of Fe(III)TPP-1

Following the success of Fe(III)PPIX encapsulation by MOFs in Chapter 3, the same encapsulation methodology was employed. In the case of MOF **1**, red crystals were obtained when Fe(III)TPP-Cl was included in the reaction mixture for synthesis of Fe(III)TPP-**1**. PXRD of these crystals (Fig. 4.1) confirmed that no significant changes to the framework of **1** had occurred, with the exception of minor differences in intensity which can be attributed to variation in solvent content in the framework.

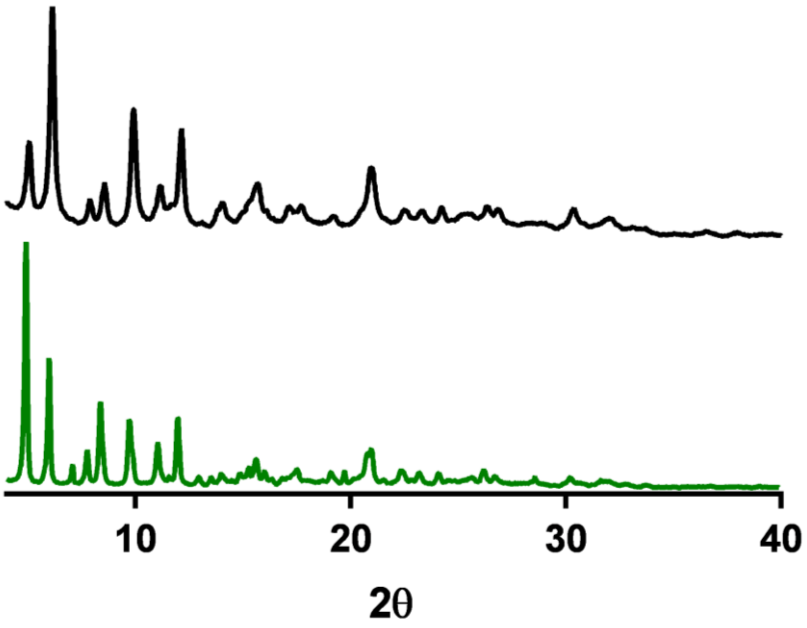

Figure 4.1: *PXRD of as synthesised Fe(III)TPP-**1** (green) and **1** (black).*

While the colour change from clear to red indicated that Fe(III)TPP had successfully been encapsulated to form Fe(III)TPP-**1**, closer analysis indicated that only surface adsorption had occurred. When crystals were broken open, the red colour did not persist throughout the crystal. Scanning electron microscopy (SEM) with energy dispersive X-ray spectroscopy (EDS) confirmed this observation by measuring the Fe content of Fe(III)TPP-**1** crystals, as described for Fe(III)PPIX-**1** in Chapter 3. Unlike the entirely smooth surface observed via SEM for Fe(III)PPIX-**1** (Fig. 4.2a), crystals of Fe(III)TPP-**1** displayed surface protrusions, even after extensive washing with fresh DMF. Fe was only detected on these surface protrusions of Fe(III)TPP-**1** (Fig. 4.2b, blue box) and was not present on smooth regions of the surface (Fig. 4.2b, black box), nor was it detectable inside a cleaved crystal (Fig. 4.2c). ICP-OES analysis of the Fe content in digested crystals of Fe(III)TPP-**1** further confirmed that Fe(III)TPP had a substantially lower loading in **1** than that measured for Fe(III)PPIX in the same MOF (0.36 ± 0.02 vs. 1.2 ± 0.1 mass % Fe respectively). Together, these findings reinforce the conclusion that Fe(III)TPP was not encapsulated into **1**, but rather adhered to the surface of the crystals.

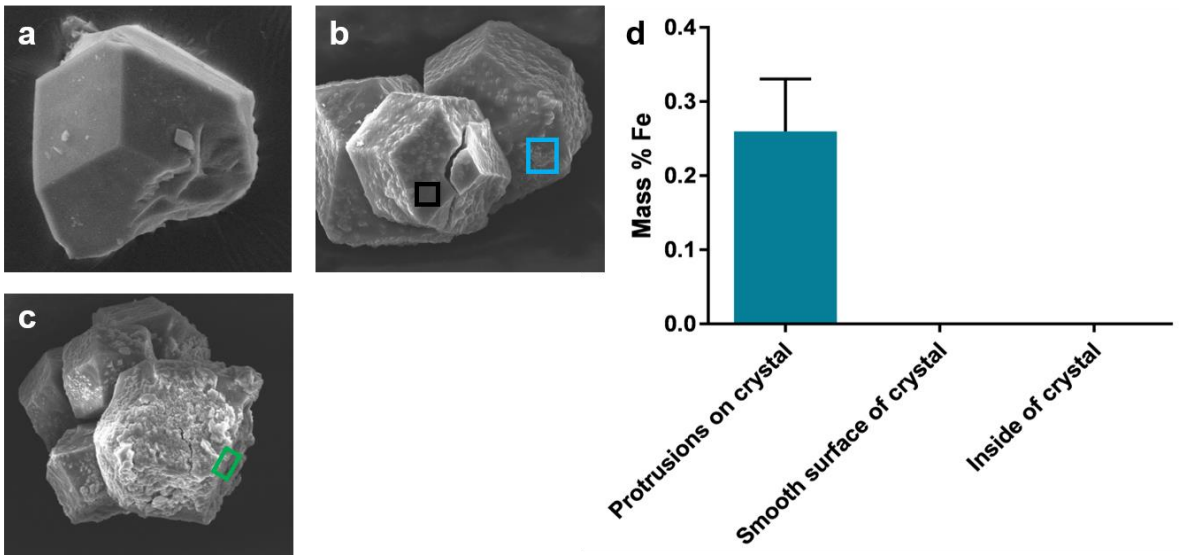

Figure 4.2: *SEM with EDS analysis of Fe(III)TPP-**1** crystals. (a) Representative SEM image of Fe(III)PPIX-**1** showing a smooth surface; (b) and (c) representative SEM images of crystals and (d) Fe content on the surface of intact crystals and on newly exposed surfaces of cleaved Fe(III)TPP-**1** crystals. Protrusions on the crystal surface (blue box) contained measurable iron content. No iron was detected on smooth areas of the crystal surface (black box) or the exposed surface of a cleaved crystal (green box).*

Attempts to alter the synthetic procedure were made in order to obtain Fe(III)TPP-**1** crystals in which Fe(III)TPP was distributed throughout the crystal. These included, (i) increasing and decreasing Fe(III)TPP concentration in the reaction mixture; (ii) using an autoclave as the reaction vessel; (iii) changing the temperature of the reaction; (iv) changing the length of the reaction time; (v) changing the solvent systems (namely DMA, DMF/EtOH mixture, EtOH); and finally (vi) altering the concentrations of Zn and H_3TATB in the reaction mixture. Despite these exhaustive efforts, when crystals were obtained under the modified conditions, no evidence of complete Fe(III)TPP encapsulation was observed. The failure to encapsulate Fe(III)TPP is thus likely due to structural incompatibilities between Fe(III)TPP and the cavities in **1**. The key structural differences between Fe(III)TPP (which does not encapsulate into **1**) and that of Fe(III)PPIX (which can be encapsulated by **1**) is the larger molecular size and

greater rigidity of substituent groups. In the case of Fe(III)PPIX, the propionate chains allow a degree of structural flexibility and therefore the ability to more easily accommodate shape changes necessary to fit into the 4_3 helical channels present in MOF **1**. By contrast, the phenyl substituents attached directly to the *meso*- position on the porphine core of Fe(III)TPP have limited conformational freedom and can only rotate around an axis parallel to the plane of the porphine core. Moreover, the helical nature of the channel produces varying widths along the channel itself, with the widest part being 19.8 Å. Since the measured width of Fe(III)TPP is 17.4 Å,[i] it is unlikely there is sufficient space for this porphyrin to be encapsulated and thus accounts for its surface adsorption on **1**.

[i] All measurements made in Mercury.[143]

4.3.2 Synthesis and characterisation of Fe(III)TPP-2

Fe(III)TPP was encapsulated into **2** using the same approach of including Fe(III)TPP in the reaction mixture as for Fe(III)PPIX-**2** and dark pink cubic crystals were obtained (Fig. 4.3a). The synthetic methodology was altered slightly to increase the yield of high quality crystals by making use of autoclaves rather than the reaction vials employed in the synthesis of Fe(III)PPIX-**2**. PXRD analysis of the crystalline Fe(III)TPP-**2** product indicated no major structural changes occurred upon encapsulation of Fe(III)TPP (Fig. 4.3b), although the variances in peak intensity suggest that there was a change in the solvent content in the framework.

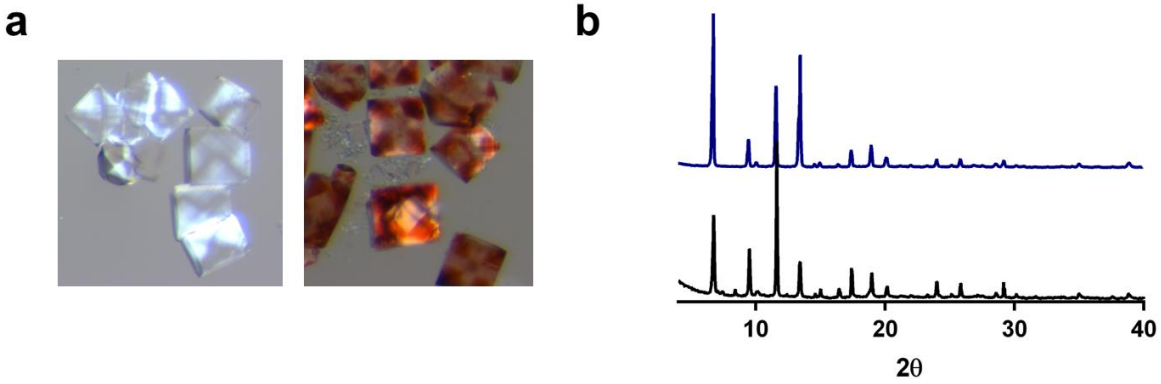

Figure 4.3: *(a) Images of **2** (left) and Fe(III)TPP-**2** (right) showing the pink colour of the crystals obtained when Fe(III)TPP is encapsulated; (b) PXRD patterns of **2** (black) and Fe(III)TPP-**2** (blue) confirm no structural change occurred upon encapsulation.*

It is important to note that the same findings were observed when attempts to encapsulated Fe(III)TPP in **1** were made, yet it was found that it was not possible to fully encapsulate Fe(III)TPP into **1**. Consequently, it was vital to conduct further analysis of the Fe(III)TPP-**2** crystals to determine whether Fe(III)TPP was uniformly distributed throughout the framework of **2**, and therefore that it was properly encapsulated, or if Fe(III)TPP was merely adsorbed onto the surface of the crystals.

To quantify the amount of Fe present in different regions of Fe(III)TPP-**2** crystals, specifically the outside surface as well as the surface of a crystal cleaved after the synthesis process, SEM-EDS was employed. Unlike for Fe(III)TPP-**1**, the measured Fe content was identical on the crystal surface and within cleaved crystals of Fe(III)TPP-**2** (Fig. 4.4a). A representative image of crystals examined by SEM-EDS is shown in Fig. 4.4b. Moreover, the Fe content measured by SEM-EDS was statistically consistent with the Fe loading determined by ICP-OES for Fe(III)TPP-**2** (0.604 ± 0.008 Fe mass %). This loading was lower than that of Fe(III)PPIX in **2** (1.039 ± 0.004 Fe mass %, see Chapter 3) and likely arises from the lower concentration of Fe(III)TPP compared to Fe(III)PPIX in the reaction mixture.[ii]

Attempts to increase the loading by increasing the concentration of Fe(III)TPP in the reaction mixture were unsuccessful and merely resulted in excess Fe(III)TPP co-crystallizing with Fe(III)TPP-**2** crystals. At the concentration of Fe(III)TPP in reaction mixture used in this study, however, homogeneous Fe(III)TPP-**2** crystals were obtained. Finally, to confirm that the structural integrity of Fe(III)TPP had not been compromised during the synthesis of Fe(III)TPP-**2**, the UV-visible spectrum of Fe(III)TPP-**2** crystals solubilised in acidic DMF was recorded (Fig. 4.4c). The presence of a characteristic peak at approximately 500 nm further confirmed that Fe(III)TPP had not degraded during the synthesis of Fe(III)TPP-**2**. The structural integrity of Fe(III)TPP in Fe(III)TPP-**2** was further confirmed by single crystal x-ray diffraction.

[ii] A lower concentration was used to minimise contamination of the bulk material with Fe(III)TPP crystals formed from unencapsulated Fe(III)TPP in the reaction mixture.

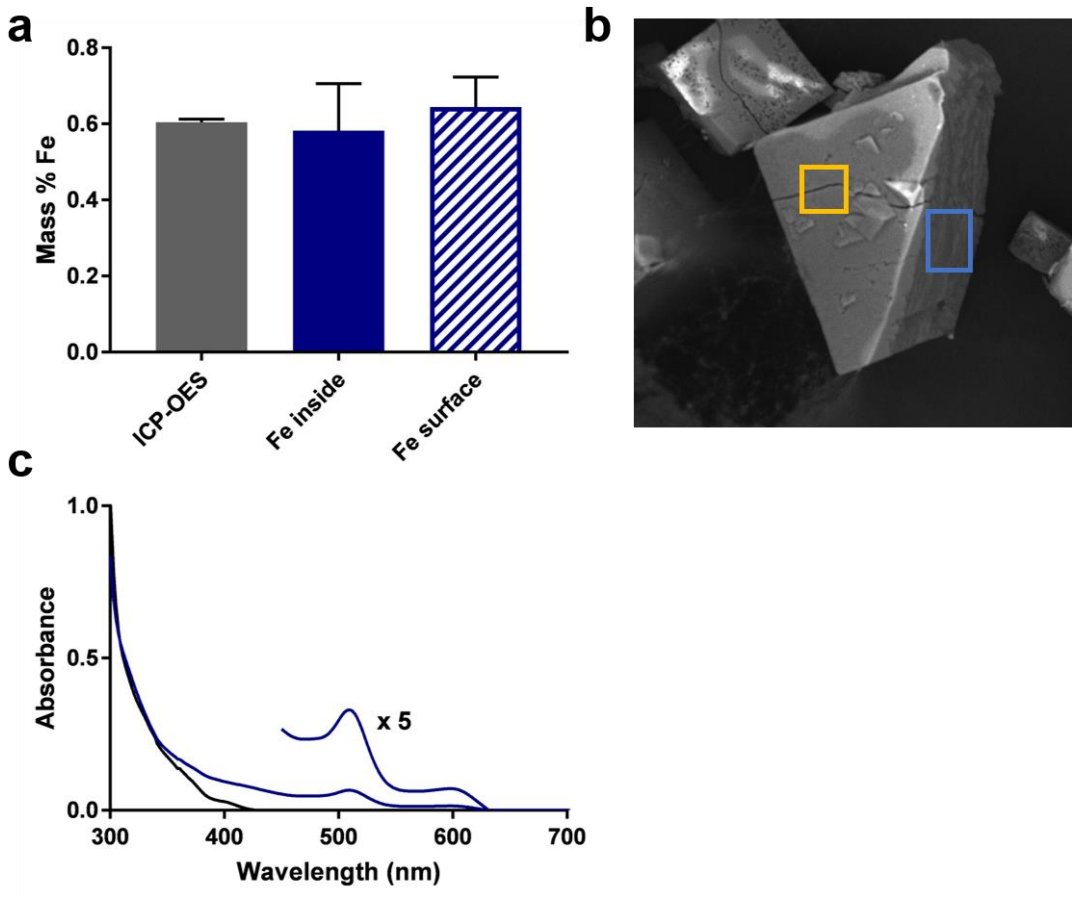

Figure 4.4: *(a) Loading of iron in Fe(III)TPP-**2** crystals. "Fe inside" refers to the iron content on the newly exposed surfaces of cleaved crystals, "Fe surface" refers to the iron content on the surfaces of intact crystals and ICP-OES refers to the iron content determined by ICP-OES analysis of the bulk material; (b) Representative image of cleaved Fe(III)TPP-**2** crystal used for SEM-EDS analysis. Yellow box indicates surface analysed for Fe and Zn content; blue box indicates newly exposed surface inside of Fe(III)TPP-**2**; (c) UV-visible spectra of solubilized **2** (black) and Fe(III)TPP-**2** (blue) showing an absorption maximum characteristic of Fe(III)TPP.*

4.3.3 Crystal structure of Fe(III)TPP-2

The crystal structure of Fe(III)TPP-**2** was determined of crystals obtained from autoclave reaction vessels. The framework of Fe(III)TPP-**2** was isostructural with that of the reported MOF **2**[141] and its Cu analogue, Cu-HKUST-1.[160] The large channels observed in **2** (and Cu-HKUST-1) stem from the formation of large secondary building units (SBUs).[160] The octahedral SBU is comprised of four BTC^{3-} ions in a tetrahedral arrangement along four of the eight faces of the octahedron (Fig. 4.5). Zn_2 dimers are present on six of the vertices and these dimers connect the SBUs forming a 3D network of pores throughout the framework.[160] Within the framework, there are three structurally distinct polyhedral pores that are available for guest encapsulation, the largest of which has a measured diameter of 8.5 Å (taking into account van der Waals radii and H atoms).[142]

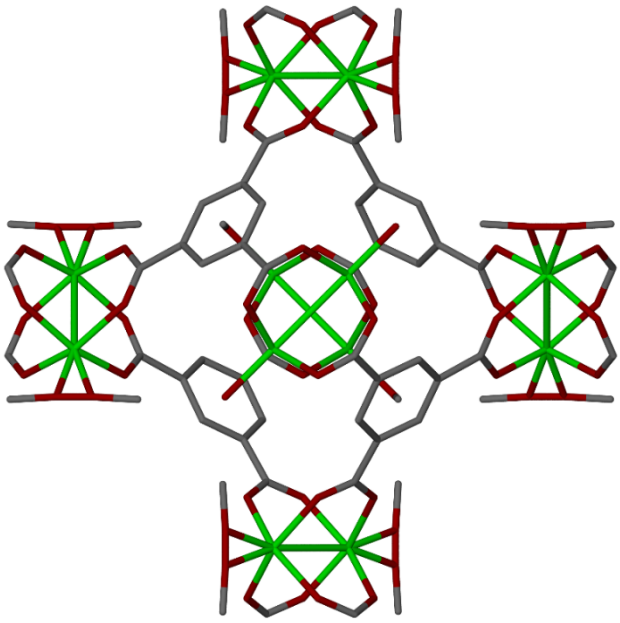

Figure 4.5: *Structural building unit (SBU) of ZnHKUST-1 framework of Fe(III)TPP-**2**. Porphyrin atoms omitted for clarity.*

The porphyrin core of Fe(III)TPP resides in the largest octahedral cavity of the framework with the phenyl rings extending into the adjacent cage (Fig. 4.6a). This has the effect of 'locking' the porphyrin into place and minimizes the extent of disorder observed. The octahedral cage possesses O_h symmetry while the porphyrin has D_{4h} symmetry; therefore the porphyrin is positionally disordered over three positions, all of which are equivalent.[96] This effect has been observed with other porphyrins encapsulated in MOF **2** and Cu-HKUST-1.[41,96]

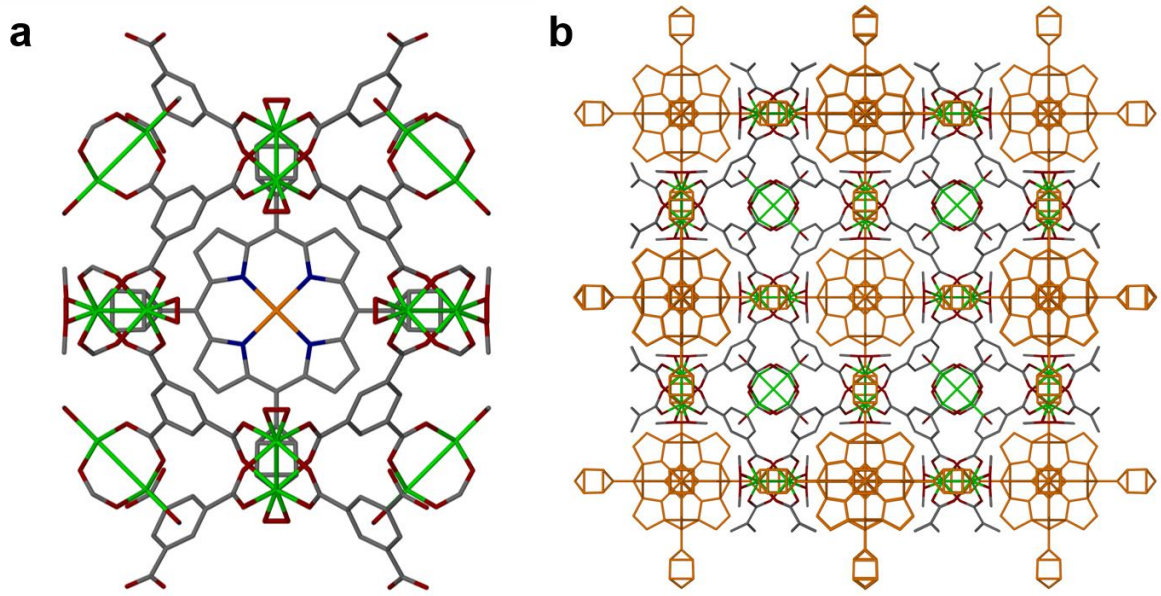

Figure 4.6: *Crystal structure of Fe(III)TPP-**2**. (a) Fe(III)TPP located in an octahedral cage of **2**. Only one position of the porphyrin is shown for clarity; (b) Packing of Fe(III)TPP-**2** viewed along the a-axis with Fe(III)TPP shown in all positions in orange.*

While encapsulation of Fe(III)TPP into **1** was unsuccessful, Fe(III)TPP was successfully encapsulated in **2** despite the pore diameter (8.5 Å) being significantly smaller than that in **1** (19.8 Å).[iii] This result is likely facilitated by the smaller adjacent pores in **2** which create "windows" for the phenyl rings to extend into. Larsen *et al.*[41] have reported that these pores serve the dual purpose of providing additional space for the Fe(III)TPP molecule as well 'locking' the porphyrin in place and thus reducing the extent of disorder (Fig. 4.7). This allowed the crystal structure of Fe(III)TPP-**2** to be determined without the use of a rigid body model, although the axial ligand could not be modelled due to the positional disorder of the porphyrin.

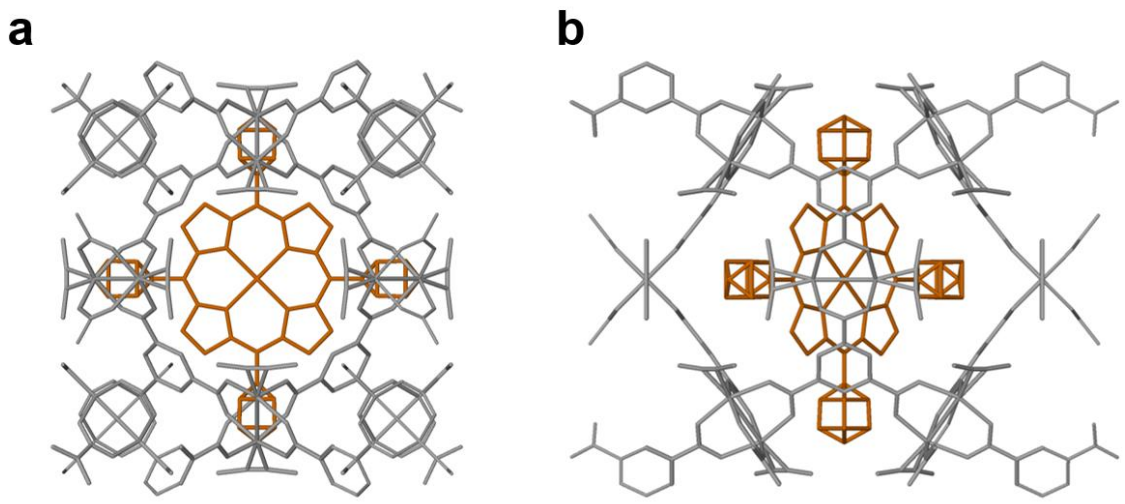

Figure 4.7: *Fe(III)TPP (orange) encapsulated in* ***2*** *(gray) viewed down (a) 0 0 1 and (b) 1 0 1 plane showing phenyl rings extending into adjacent cavities of the HKUST-1 framework and 'locking' the porphyrin in a fixed position within the cavity of HKUST-1.*

[iii] All measurements made in Mercury.[143]

Unsurprisingly, the crystal structure of Fe(III)TPP-**2** is structurally similar to previously reported metallotetraphenyl porphyrins encapsulated in HKUST-1 frameworks.[41,97,156,158] A search of the CCDC[161] yielded only two examples of crystal structures of a Fe(III) tetraphenyl porphyrin derivative encapsulated in a MOF.[41,162] Both encapsulated Fe(III) *meso*-tetra(N-methyl-4-pyridyl)porphine tetratosylate (TMPyP) into an Fe-HKUST-1 framework. When the crystal structures of these reported encapsulated porphyrins were compared to that of Fe(III)TPP in Fe(III)TPP-**2** it was found that the key Fe-N bond length was very similar (2.018(2) Å and 2.054(2) Å in the case of Fe(III)TMPyP and Fe(III)TPP respectively). Furthermore, all the crystal structures of metallotetraphenyl porphyrins encapsulated in HKUST-1 frameworks showed the same disorder over three positions as well as disorder due to rotation of the phenyl rings (Fig. 4.8).

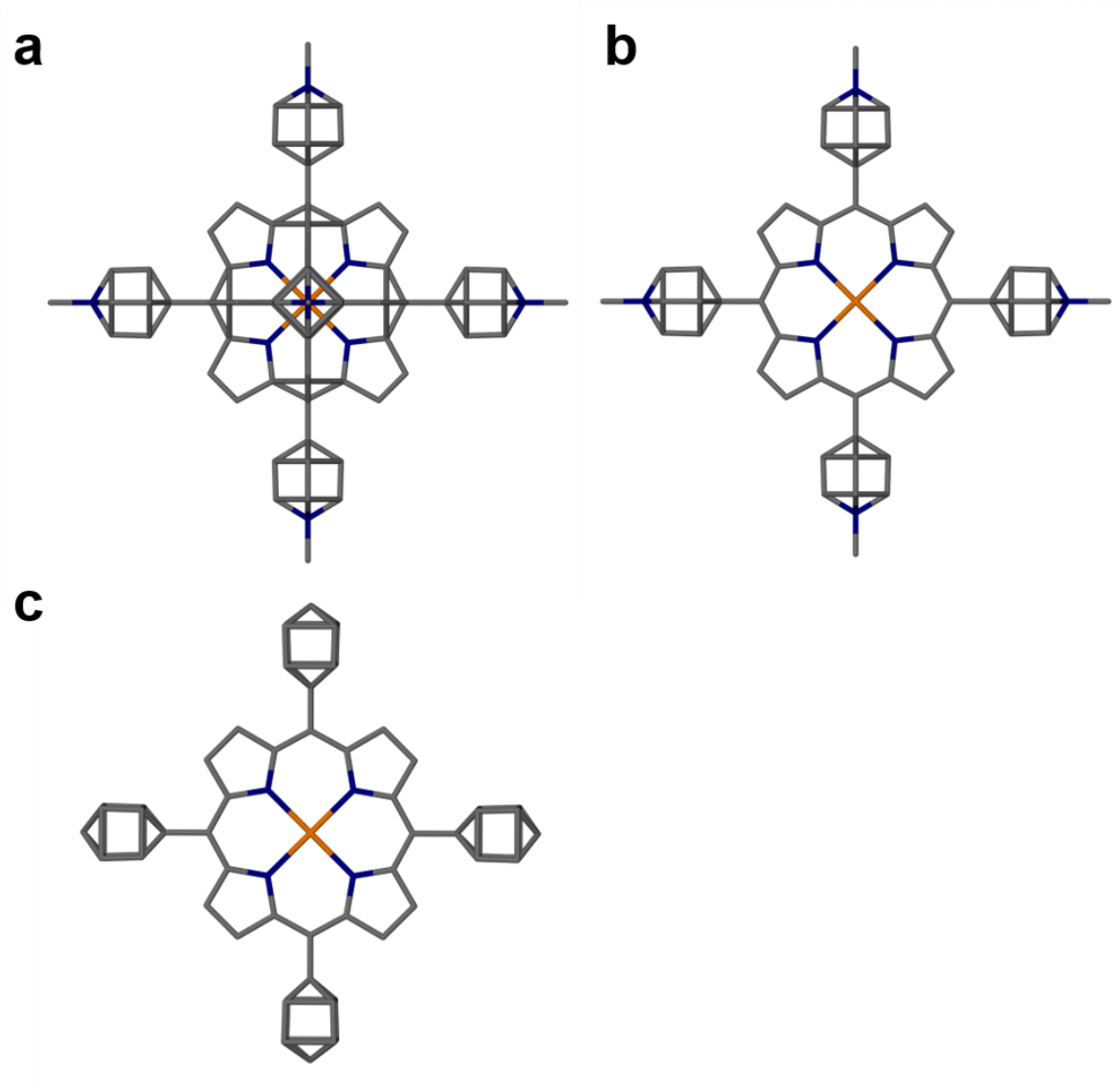

Figure 4.8: *Comparison of crystal structures of Fe(III) tetraphenyl porphyrins encapsulated in HKUST-1 frameworks. (a and b) Structure of Fe(III) TMPyP encapsulated in Fe-HKUST-1 as reported by Zhang et al.*[97] *shown disordered over three positions in the framework (a) and in one position (b) for clarity showing disorder of the phenyl rings;*[97] *(c) Structure of Fe(III)TPP encapsulated in* ***2*** *showing disorder of the phenyl rings in one position for clarity. In all cases the structure of the framework was omitted for clarity.*

It is important to note that the encapsulation of Fe(III)TPP into **2** involves the incorporation of Fe(III)TPP in its monomeric form. The ability of the framework to influence the speciation of the porphyrin is a crucial consideration for catalytic potential since porphyrin μ-oxo dimers can readily form which display substantially lower catalytic activity. Indeed, when higher concentrations of Fe(III)TPP were used in the reaction mixture in an attempt to increase loading of Fe(III)TPP in **2**, crystals of the μ-oxo dimer of Fe(III)TPP (Fig. 4.9) co-crystallised alongside Fe(III)TPP-**2** crystals which still specifically encapsulated monomeric Fe(III)TPP. The crystal structure of these crystals was very similar to a previously reported structure of the Fe(III)TPP μ-oxo dimer.[163] Both the Fe-N and Fe-O bond distances of the μ-oxo dimer crystals obtained from the reaction mixture are in good agreement with the previously reported crystal structure (Table 4.1). The ability of the MOF to specifically encapsulate the monomer of Fe(III)TPP illustrates an important advantage for their role as solid-state supports as the formation of μ-oxo dimers in solution is detrimental to the peroxidatic activity of the porphyrin.[164,165]

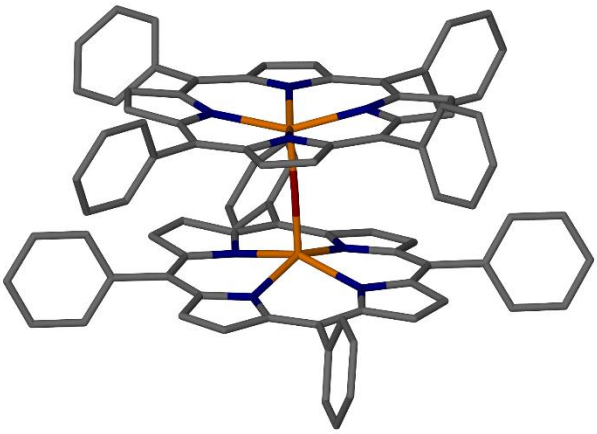

Figure 4.9: *Crystal structure of $(Fe(III)TPP)_2O$ from the reaction mixture. Excess Fe(III)TPP formed μ-oxo dimers alongside Fe(III)TPP-**2** during the crystallization experiments resulting in a physical mixture of both products. C, N, O and Fe atoms shown in grey, blue, red and orange respectively.*

Table 4.1: Comparison of bond lengths in μ-oxo dimers of Fe(III)TPP obtained and previously reported.

	This work	**Reported**[163]
Fe-O (Å)	1.760(2)	1.763(2)
Fe-N (Å)	2.078(2)	2.087(2)

4.3.4 Instability of Fe(III)TPP-2

Based on the above finding, Fe(III)TPP-**2** was thought to be a good system for heterogeneous catalysis. Upon further investigation, however, serious concerns over the stability of this system were discovered. When crystals were stored in air, changes to the crystal surface were observed. SEM images of crystals highlight the air sensitivity of Fe(III)TPP-**2** crystals (Fig. 4.10) as significant physical changes to the surface of the crystals were observed. Further confirmation was obtained via PXRD which showed significant phase change of crystals exposed to air after 72 h. This change is the same as that observed for the empty framework **2** when crystals were exposed to an aqueous solution (Fig. 4.11b, see Chapter 3 for details). On the basis of the observed moisture sensitivity, Fe(III)TPP-**2** is not suitable as a heterogeneous catalyst in aqueous solution.

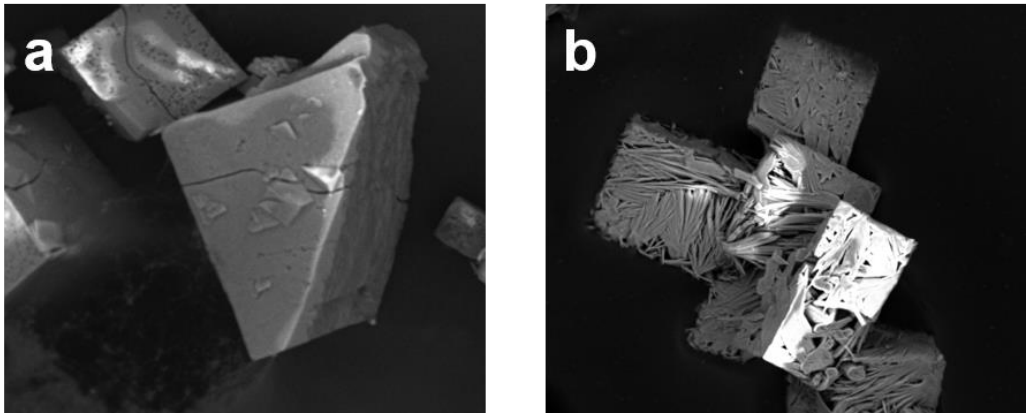

Figure 4.10: *(a) Cleaved Fe(III)TPP-**2** crystal after removal from solvent (DMF); (b) SEM image of Fe(III)TPP-**2** crystals stored open to air for 48 h.*

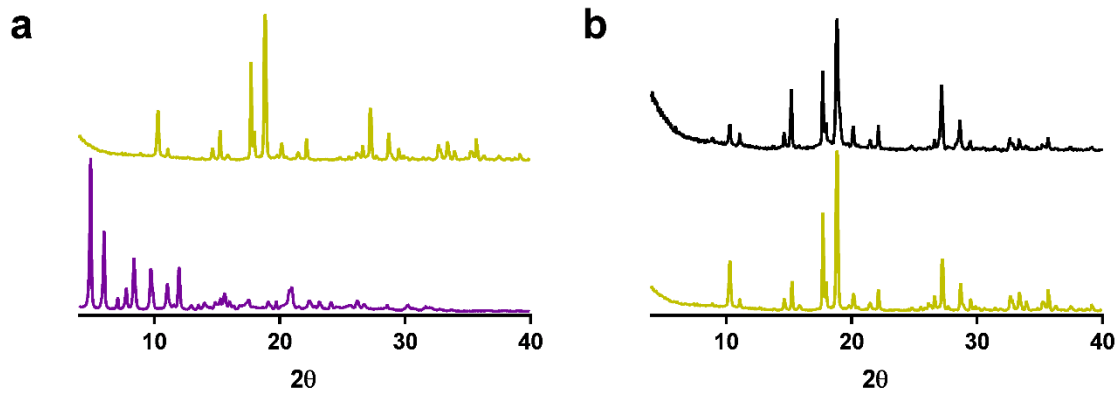

Figure 4.11: *(a) PXRD of dried Fe(III)TPP-**2** immediately after removal from oven (purple) and of dried Fe(III)TPP-**2** exposed to air after 72 h (green); (b) PXRD of dried Fe(III)TPP-**2** exposed to air after 72 h (green) and of **2** exposed to water (black).*

4.4 Summary and Conclusion

Encapsulation of the synthetic Fe(III)PPIX analogue, Fe(III)TPP, in the same two redox inactive frameworks previously used for the natural porphyrin was investigated. While MOF **1** failed to encapsulate Fe(III)TPP and instead lead to its surface adsorption, the encapsulation of Fe(III)TPP in MOF **2** (Zn-HKUST-1) was successful. This preferential encapsulation was based on better structural congruency between Fe(III)TPP and **2**, than with **1**, despite the latter having larger channels than the former. This finding highlights the importance of MOF cavity topology over simple size and provides strong support for its consideration when applying MOF as solid state supports for porphyrin encapsulation.

Crystals of sufficient quality for single crystal analysis were obtained and the crystal structure of Fe(III)TPP-**2** was determined. Fe(III)TPP was positionally disordered in three positions and it was confirmed that Fe(III)TPP was encapsulated in a monomeric form. Fe(III)TPP-**2** was found to be structurally similar to other metalloporphyrin@MOFs composed from synthetic tetraphenyl porphyrin encapsulated in HKUST-1 type frameworks. This indicates that the phenomenon of the phenyl rings 'locking' the porphyrin in place in the cavity is conserved when different synthetic tetraphenyl porphyrins are encapsulated in this framework.

Initial findings suggested Fe(III)TPP-**2** was a good candidate for heterogeneous catalysis. These included its uniform distribution of Fe(III)TPP throughout Fe(III)TPP-**2** crystals; no structural changes to the framework upon Fe(III)TPP encapsulation, and the selective incorporation of Fe(III)TPP in its monomeric form. However, Fe(III)TPP-**2** crystals were found to be unstable when exposed to moisture in the air and thus are not suitable as heterogeneous catalysts in aqueous environments. It may well, however, be better suited towards catalytic activity in non-aqueous media in an inert environment. Further exploration in this area is certainly warranted

Chapter Five: Kinetics of H_2O_2 oxidation of ABTS catalysed by Fe(III)PPIX-1

5.1 Introduction

In recent years there have been several reports of Fe(III)PPIX containing MOFs that mimic the peroxidatic activity of haemoproteins.[103,107,166] Encapsulation of Fe(III)PPIX into the MOF framework helps prevent catalyst degradation and aggregation, thereby facilitating greater turnover and overall better catalytic efficiency relative to free Fe(III)PPIX in solution.[1,41,91,92] This study has produced a further example of a Fe(III)PPIX@MOF catalyst, Fe(III)PPIX-**1**, which has displayed peroxidatic activity. This system therefore mimics the activity of a prominent class of haemoproteins called peroxidases which include horseradish peroxidase, cytochrome *c* peroxidase and lactoperoxidase[7,167]. These enzymes oxidize a wide variety of organic and inorganic substrates using H_2O_2 according to equation 1 (where RH represents a reducing substrate) and are essential in both non-mammalian and mammalian cells.[29,168,169]

$$2RH + H_2O_2 \rightarrow 2H_2O + 2R \qquad (\mathbf{1})$$

Initial studies of the peroxidatic activity of Fe(III)PPIX-**1** in Chapter 3 showed an increase in activity and yield as compared to solid Fe(III)PPIX and Fe(III)PPIX dissolved in solution, respectively. In this chapter, an in-depth study of the peroxidatic activity of Fe(III)PPIX-**1** is presented using the colourimetric oxidation of ABTS substrate by H_2O_2. The kinetics of such heterogeneous systems have been little studied, particularly when compared to aqueous

homogeneous catalysts. The findings provide insights into harnessing the peroxidatic activity of Fe(III)PPIX for heterogeneous catalysis using MOFs as solid-state supports.

5.2 Experimental methods

5.2.1 Synthesis and preparation of Fe(III)PPIX-1

Fe(III)PPIX-**1** was synthesized and characterised as described in Chapter 3. Before using Fe(III)PPIX-**1** in kinetics experiments, the following steps were followed to prepare the material: (i) PXRD analysis of bulk material was performed to confirm phase purity of the bulk material; (ii) material was dried in oven at 60 °C for 24 h; and (iii) TG analysis was conducted on the material to obtain an accurate solvent mass percentage (≈ 18%) such that mass of catalyst reported could be corrected for solvent contribution.

5.2.2 Kinetics measurements

ABTS was used to monitor the progress of the peroxidatic reaction catalysed by the Fe(III)PPIX-**1** system. In a typical reaction, ≈ 1 mg of catalyst was added to 2.35 mL of 5 mM aqueous ABTS solution (0.01 M TRIS, pH 7.4). The reaction was initiated by adding 125 µL of 20 mM H_2O_2 (final concentration of 1 mM H_2O_2) and the rate of $ABTS^{\bullet+}$ formation was monitored at 660 nm with constant magnetic stirring. All reactions were conducted with [ABTS] > [H_2O_2] ≫ [Fe(III)PPIX] to ensure that all available H_2O_2 was oxidized. Concentrations of ABTS, H_2O_2 and catalyst were altered as needed for specific experiments. All kinetics data were analysed using a one phase exponential function or linear regression in GraphPad Prism to obtain maximal yield (Y_{max}) or initial rates respectively.[117]

5.3 Results and Discussion

5.3.1 Approach to determine rate law

While a number of methods have been used to monitor the peroxidatic activity of Fe porphyrins,[105,109] the catalytic oxidation of the chromophoric substrate ABTS by H_2O_2 is regularly employed.[23,151–153] As described in Scheme 5.1, this approach relies on the reaction between H_2O_2 and a porphyrin catalyst which follows in a two-stage process: (i) reversible coordination of the peroxide to the Fe(III) centre of the porphyrin to give a Fe(III)-peroxo species [Fe(III)-OOH(porph)]; and (ii) a subsequent O-O bond cleavage to form a high valent species [Fe(IV)=O(porph)$^{\bullet+}$] + H_2O (heterolytic cleavage) or [Fe(IV)=O(porph)] + $^{\bullet}$OH (homolytic cleavage). The key reactive intermediate is thought to be a high valent iron oxo species [Fe(IV)=O(porph)$^{\bullet+}$], referred to as Compound I, which is responsible for the efficiency and versatility of these haemoproteins;[19,20,29,30,170] and can subsequently reduce two equivalents of ABTS to form a blue-green radical cation (ABTS$^{\bullet+}$, λ_{max} 660 nm)[19,20] that is readily measurable by UV-visible spectroscopy.[19,29,38] In the case of heterolytic cleavage, reduction occurs in two steps with one ABTS molecule reducing [Fe(IV)=O(porph)$^{\bullet+}$] to [Fe(IV)=O(porph)], which is subsequently reduced by a second ABTS molecule to reform the original Fe(III)PPIX-H_2O catalyst (Fe(III)H_2O, Scheme 5.2). This process is rapid and can be considered as a single step as shown in Scheme 5.1 to reduce complexity of the kinetic model.[29]

$$Fe(III)H_2O + H_2O_2 \underset{k_{-1}}{\overset{k_1}{\rightleftharpoons}} Fe(III)-OOH \xrightarrow{k_2} [Fe(IV)=O(porph^{\bullet+})] + 2ABTS$$

$$[Fe(IV)=O(porph^{\bullet+})] \xrightarrow{k_3} 2ABTS^{\bullet+} + Fe(III)H_2O$$

Scheme 5.1: *Reaction of Fe(III)PPIX with H_2O_2 and subsequent condensed reduction of two equivalents of ABTS. [Fe(IV)=O(porph$^{\bullet+}$)] is the key high-valent reaction intermediate in the cycle. Fe(III)H_2O and Fe(III)-OOH refer to Fe(III)PPIX ligated by water and peroxide, respectively. The first step (k_1) releases a H^+ ion and the second step (k_2) a H_2O molecule which have been omitted from the scheme.*

$$Fe(III)H_2O \underset{}{\overset{+H_2O_2}{\rightleftharpoons}} Fe(III)-OOH \longrightarrow [Fe(IV)=O(porph^{\bullet+})]$$

$$[Fe(IV)=O(porph^{\bullet+})] \xrightarrow{+ABTS} [Fe(IV)=O(porph)] + ABTS^{\bullet+}$$

$$ABTS^{\bullet+} + Fe(III)H_2O \xleftarrow{+ABTS} [Fe(IV)=O(porph)] + ABTS^{\bullet+}$$

Scheme 5.2: *Reaction of Fe(III)PPIX with H_2O_2 and subsequent expanded two step reduction of ABTS to ABTS$^{\bullet+}$ by [Fe(IV)=O(porph$^{\bullet+}$)] and [Fe(IV)=O(porph)] respectively.*

To probe the peroxidatic activity of Fe(III)PPIX-**1**, a fixed set of conditions to monitor ABTS$^{\bullet+}$ production was used. These conditions (unless otherwise specified) involved the addition of 125 µL of H_2O_2 (final concentration 1 mM) to 2.35 mL of ABTS solution (final concentration 5 mM) buffered at pH 7.4 (0.01 mM TRIS) in the presence of ≈ 1 mg Fe(III)PPIX-**1**, accurately determined, with constant stirring while monitoring the absorbance at 660 nm at 37 °C (Fig. 5.1). Under these conditions ABTS was successfully converted to ABTS$^{\bullet+}$ and appeared to follow pseudo-first order kinetics. It should be noted that when conducting experiments with heterogeneous catalysis the lower limit of catalyst concentration that can be used is determined by the mass of the catalyst that could be accurately weighed and it was for this reason that that

the above reaction conditions were chosen. When using ABTS as a substrate to monitor peroxidase activity, further considerations are possible processes which diminish the $ABTS^{\bullet+}$ radical cation stability, notably via the $ABTS^{\bullet+}$ disproportionation reaction (Scheme 5.3).[151,171] Previous reports have shown that $ABTS^{\bullet+}$ disproportionation to ABTS and the dication $ABTS^{2+}$ is minimized under conditions where [catalyst] ≪ [H_2O_2] ≪ [ABTS].[19,171,172] Under the conditions used in this work, there was an approximately 15-fold excess of H_2O_2 over Fe(III)PPIX and 5-fold excess of ABTS relative to H_2O_2 under the standard conditions used.

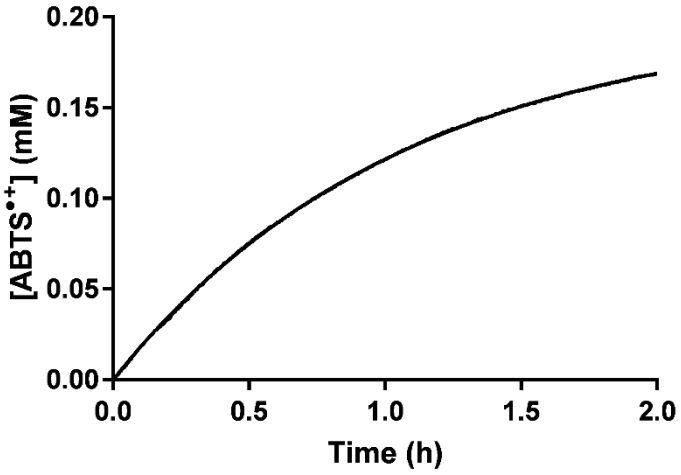

Figure 5.1: *Oxidation of ABTS to $ABTS^{\bullet+}$ by H_2O_2 catalysed by 1 mg Fe(III)PPIX-**1**. Reaction conditions: 5 mM ABTS, 1 mM H_2O_2, pH 7.4, 37.00 °C.*

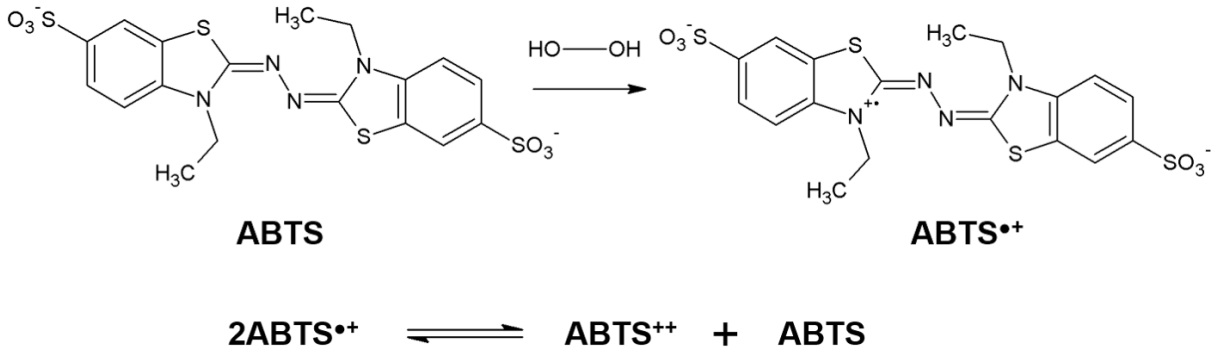

***Scheme 5.3**: Formation of ABTS$^{\bullet+}$ catalysed by Fe(III)PPIX-**1** and subsequent disproportionation of ABTS$^{\bullet+}$ to reform ABTS and ABTS^{2+}.*

To determine if disproportionation still contributed significantly to the reaction under the reaction conditions employed, the stability of the ABTS$^{\bullet+}$ cation in the reaction mixture was monitored at 660 nm following removal of Fe(III)PPIX-**1**. Removal of Fe(III)PPIX-**1** caused a decay in ABTS$^{\bullet+}$ concentration (Fig. 5.2) which can only be attributed to disproportionation. The kinetics of this decay follows pseudo-first order kinetics and, based on the rate of decay (k_{decay} = 0.38 ± 0.09 h^{-1}), can be expected to make a substantial negative contribution to the final concentration of ABTS$^{\bullet+}$ formed. Consequently, this process (which is often ignored for simplicity) had to be considered when establishing empirical and theoretical rate laws under these conditions. While it is possible to decrease the effect of the disproportionation reaction by increasing the concentration of ABTS in the system (i.e. driving the equilibrium in Scheme 5.3 towards the left), this was not practically possible since the absorbance of ABTS would then exceed the upper measurable limits of the spectrophotometer. Another strategy would be to decrease the concentration of catalyst, in this case Fe(III)PPIX-**1**, in order to reduce the concentration of ABTS$^{\bullet+}$ and drive the equilibrium to the left; however, this was not possible due to the limitation on the minimum amount of Fe(III)PPIX-**1** that could be accurately weighed.

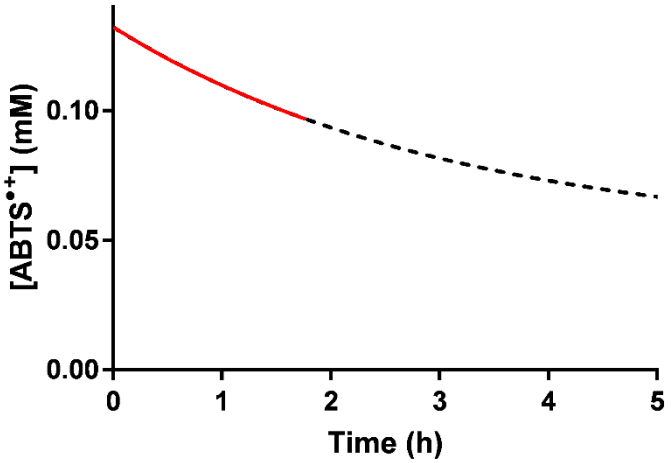

Figure 5.2: *Disproportionation of $ABTS^{\bullet+}$ after removal of Fe(III)PPIX-**1** (red) from the reaction mixture. Data were fitted with an exponential decay function (black). Reaction conditions: 5 mM ABTS, 1 mM H_2O_2, pH 7.4, 37.00 °C.*

Buffer choice is also crucial to the stability of the $ABTS^{\bullet+}$ radical. Good's buffers such as PIPES, MOPS and HEPES are particularly problematic since they can reduce the half-life of $ABTS^{\bullet+}$ to less than 2 min.[173] It was established that no such effects on the initial rate occurred when using TRIS buffered at pH 7.4 (Fig. 5.3a). There was no statistically significant effect of buffer concentration on the initial rate of the reaction ($p > 0.05$, determined using a one-way ANOVA with multiple comparisons).

A final consideration for development of the standard conditions for this study, was the effect of Fe(III)PPIX-**1** crystallite size on reaction kinetics since heterogeneous catalysis is usually dependent on surface area of the catalyst.[174,175] Crystals were sieved prior to the reaction and grouped into size ranges to determine the effect of crystallite size on the initial rate of the reaction. The size range explored, however, was fairly narrow since the size of the crystals obtained from the synthesis of Fe(III)PPIX-**1** were somewhat small and uniform. Over the range 63 – 250 µm, no significant effect ($p > 0.05$) on the initial rate was observed (Fig. 5.3b),

but for consistency, standard reaction conditions included crystals only in the size range 90 – 106 μm. Surprisingly, crystal size effects on heterogeneous catalyst activity have not been previously investigated with metalloporphyrin@MOF systems and it is impossible to know if the lack of size dependence (at least over the range investigated) is unique to this system, or a phenomenon conserved across all metalloporphyrin@MOF catalysts of this type.

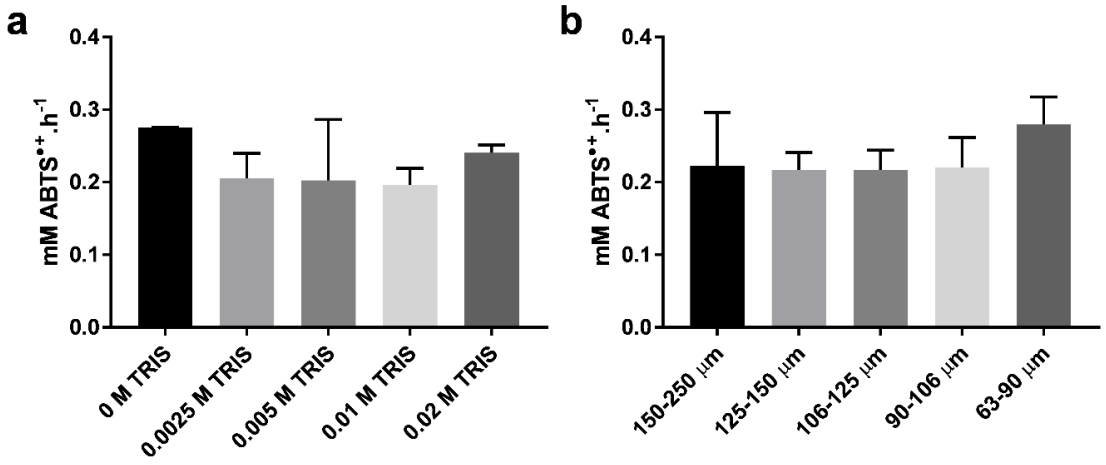

Figure 5.3: *(a) Effect of TRIS concentration on initial rate showing no significant effect of buffer on initial rate at any of the concentrations used. Reaction conditions: ≈1 mg Fe(III)PPIX-**1**, 5 mM ABTS, 1 mM H_2O_2, pH 7.4, 37.00 °C; (b) Effect of particle diameter on initial rate showing no significant effect on initial rate in the size range 63 – 250 μm (using a one-way ANOVA with multiple comparisons). All reactions were conducted under the following conditions: ≈1 mg Fe(III)PPIX-**1**, 5 mM ABTS, 1 mM H_2O_2, 0.01 M TRIS (pH 7.4), 37.00 °C. Error bars represent the standard error of mean (n=3).*

Owing to the impact of the disproportionation reaction on the reaction kinetics, data were analysed using only the first 15 minutes of the reaction, corresponding to the linear portion of the reaction curve shown in Fig. 5.1. This allowed determination of the initial rate of $ABTS^{\bullet+}$ formation (initial reaction rate; v_i – equation 2) which, based on the observed decay of the ABTS radical, is not strongly influenced by ABTS disproportionation. This approximation is valid since the disproportionation reaction is an equilibrium process which affects the final yield of $ABTS^{\bullet+}$ obtained and is not expected to significantly influence the rate of formation at shorter reaction times ($t < 0.5$ h).[151]

$$v_i = \left(\frac{d[ABTS^{\bullet+}]}{dt}\right)_{t=0} \quad (\mathbf{2})$$

5.3.2 Determination of empirical rate law

To determine the empirical rate law, the effects of concentration of each individual component on v_i were investigated. In the case of H_2O_2 and Fe(III)PPIX-**1**, the linear dependence of v_i on concentration (Fig. 5.4) indicates that there is a first order dependence of both components in this reaction. These findings mirror those reported by Ribeiro *et al.* for the homogeneous peroxidatic activity of Fe(III)PPIX dissolved in aqueous solution.[38] The linear dependence of v_i on Fe(III)PPIX concentration[iv] (Fig. 5.4b) can be described by an empirical rate law (eq. 3) in which the y-intercept is zero and *k'* is the slope of the graph. Since *k'* is also dependent on the H_2O_2 concentration, Fig. 5.4a can be used to further define this dependence. Eq. 4 thus expresses the dependence of v_i on Fe(III)PPIX and H_2O_2 concentrations with k_0 arising from the non-zero intercept in Fig. 4a and *k''* being the slope of this dependence.

$$v_i = k'[Fe(III)PPIX] \quad (\mathbf{3})$$

$$v_i = (k_0 + k''[H_2O_2])[Fe(III)PPIX] \quad (\mathbf{4})$$

[iv] Calculated by determining the number of mols of Fe(III)PPIX in ≈1 mg Fe(III)PPIX-**1** (accurately determined) and dividing through by the total volume (2.5 mL) of the suspension containing Fe(III)PPIX-**1**. This is treated as [Fe(III)PPIX] for the purposes of analysis.

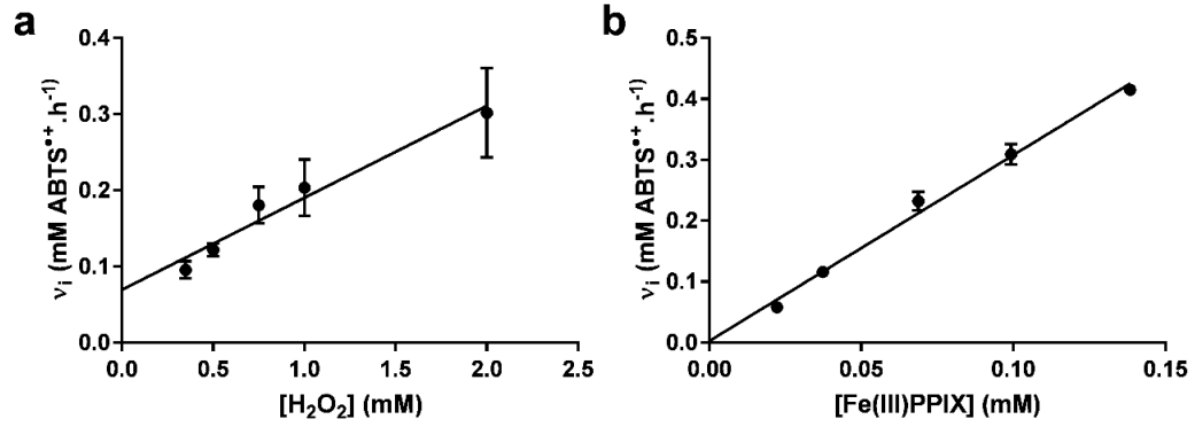

Figure 5.4: *Dependence of the initial rate of $ABTS^{\bullet+}$ formation (v_i) on (a) H_2O_2 at fixed Fe(III)PPIX-**1** concentration (66 ± 3 μM) and (b) Fe(III)PPIX concentration in the form of Fe(III)PPIX-**1** at fixed H_2O_2 concentration (1 mM). Reaction conditions: 5 mM ABTS, pH 7.4, 37.00 °C. Error bars represent the standard error of mean (n=3).*

When examining the effect of ABTS concentration on v_i, a linear dependence with a non-zero intercept was also observed (Fig. 5.5). This indicates that there is a further dependence of v_i on the concentration of ABTS. An equation to describe the observed dependence on ABTS and Fe(III)PPIX can be proposed (eqn. 5) and the empirical rate law describing the observed dependence on H_2O_2 and Fe(III)PPIX (eqn. 4) can be modified to incorporate the ABTS concentration dependence as well (eqn. 6). In this equation, the term *k'''[ABTS]* corresponds to k_0 in eqn. 3 and accounts for the non-zero intercept observed in Fig. 5.4a ([ABTS] = 5 mM) and *k''[H_2O_2]* accounts for the non-zero intercept observed in Fig. 5.5 ([H_2O_2] = 1 mM).

$$v_i = (k_0' + k'''[ABTS])[Fe(III)PPIX] \quad (\mathbf{5})$$

$$v_i = (k'''[ABTS] + k''[H_2O_2])[Fe(III)PPIX] \quad (\mathbf{6})$$

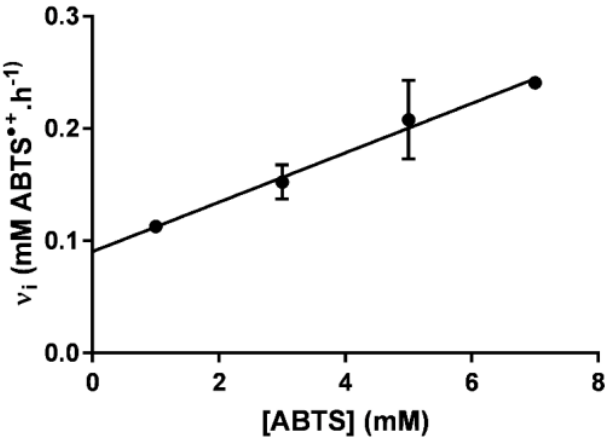

Figure 5.5: *Dependence of the initial rate of $ABTS^{\bullet+}$ formation (v_i) on ABTS concentration. Reaction conditions: 1 mg Fe(III)PPIX-**1**, 1 mM H_2O_2, pH 7.4, 37.00 °C. Error bars represent the standard error of mean (n=3).*

5.3.3 Determination and validation of theoretical rate law

To establish if the empirical rate law observed experimentally is consistent with the reaction proposed in Scheme 5.1, a theoretical rate law based on this scheme was derived. The derived rate law is shown in eqn. 7 (see Appendix B for full derivation).

$$\frac{d[ABTS^{\bullet+}]}{dt} = k_{obs}[Fe(III)H_2O][H_2O_2] \quad where \quad k_{obs} = \frac{k_2 k_1}{k_{-1} + k_2} \tag{7}$$

While this rate law is similar to a previously reported rate law for oxidation of ABTS by H_2O_2 catalysed by an Fe(III) metalloporphyrin[19] and correctly predicts a first order dependence on both Fe(III)PPIX and H_2O_2; it is unable account for the non-zero intercepts (k_0 and k_0'), nor does it account for the dependence on ABTS concentration observed in the experimental data. Consequently, an additional pathway was postulated. Coordination of ABTS to Fe(III)PPIX to form a six-coordinate Fe(III)H_2O-ABTS complex is possible,[29,38,151] and following ligation by H_2O_2, can proceed to form a high valent [ABTS···Fe(IV)=O(porph)$^{\bullet+}$] intermediate which will reduce two ABTS molecules (one of which is the coordinated ABTS), to reform the original Fe(III)H_2O catalyst (Scheme 5.4).

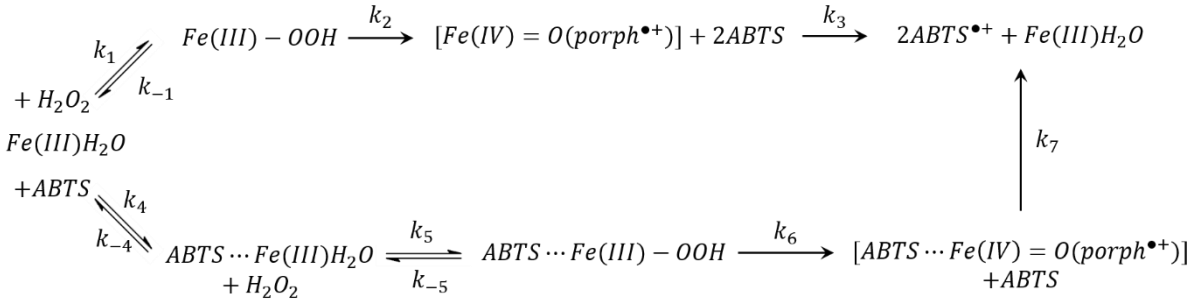

Scheme 5.4: *Proposed catalytic cycle accounting for the observed Fe(III)PPIX-**1** mediated ABTS reduction which incorporates a competing process where ABTS coordinates to Fe(III)PPIX (bottom branch).*

A new theoretical rate law (eq. 8) was derived to account for this competing process (Scheme 5.4) by applying steady state approximations for the intermediates in the reaction (full details given in Appendix B).

$$\frac{d[ABTS^{\bullet+}]}{dt} = k^1_{obs}[Fe(III)H_2O][H_2O_2] + k^2_{obs}[Fe(III)H_2O][ABTS] \quad (\mathbf{8})$$

$$where\ k^1_{obs} = \frac{k_1 k_2}{k_{-1} + k_2}\ and\ k^2_{obs} = k_4$$

At first glance this proposed rate law seems to correspond with the experimentally determined data by correctly accounting for the linear dependence on [ABTS], [H_2O_2] and [Fe(III)PPIX-**1**] as well as the two non-zero intercepts (k_0 and k_0') observed in the experimental data. To determine the validity of this proposed mechanism, equations (eqns. 9 - 14) to determine values for k^1_{obs} and k^2_{obs} were proposed using experimentally determined slopes and intercepts from Figures 5.4 and 5.5 (Table 5.1) and reaction conditions used in the study were used to calculate values for k^1_{obs} and k^2_{obs}. Equations used to calculate these values from Figures 5.4 and 5.5 are listed below.

Fig. 5.4a:

$$Slope = k^1_{obs}[Fe(III)H_2O] \quad (\mathbf{9})$$

$$Intercept = k^2_{obs}[Fe(III)H_2O][ABTS] \quad (\mathbf{10})$$

**Concentrations of each component used in relevant experiment
[Fe(III)H_2O] = 0.066 ± 0.003 mM; [ABTS] = 5 mM

Fig. 5.4b:

$$Slope = k^1_{obs}[H_2O_2] + k^2_{obs}[ABTS] \quad (\mathbf{11})$$

$$Intercept\ =\ 0 \quad (\mathbf{12})$$

** Concentrations of each component used in relevant experiment
[H_2O_2] = 1 mM; [ABTS] = 5 mM

Fig. 5.5:

$$Slope = k^2_{obs}[Fe(III)H_2O] \quad (\mathbf{13})$$

$$Intercept = k^1_{obs}[Fe(III)H_2O][H_2O_2] \quad (\mathbf{14})$$

** Concentrations of each component used in relevant experiment
[Fe(III)H_2O] = 0.065 ± 0.004 mM; [H_2O_2] = 1 mM

Table 5.1: Experimentally determined slopes and intercepts from Figures 5.4 and 5.5.

	Fig. 5.4a	**Fig. 5.5**	**Fig. 5.4b**
Slope (h^{-1})	0.12 ± 0.01	0.022 ± 0.001	3.1 ± 0.1
Intercept (mM $ABTS^{\bullet+}.h^{-1}$)	0.069 ± 0.015	0.091 ± 0.007	0.00 ± 0.01

Using these developed equations, along with the experimental data, values for k^1_{obs} and k^2_{obs} obtained from the plots of v_i against [H_2O_2] and [ABTS] respectively were calculated (Table 5.2). Each set of equations (from Fig. 5.4a and 5.5 respectively) allowed k^1_{obs} and k^2_{obs} to be determined independently from each other (i.e. k^1_{obs} was determined from the slope of Fig. 5.4a and the intercept of Fig. 5.5) and were found to be in good agreement with each other. There was no statistically significant difference at the 95% confidence interval between these values obtained from each of the graphs as calculated using an unpaired two-tailed t-test (p = 0.2592 and p = 0.1556 for k^1_{obs} and k^2_{obs} respectively).[117]

Table 5.2: Values of k^1_{obs} and k^2_{obs} calculated from v_i plots.

	v_i vs. [H_2O_2] (Fig. 4a)	**v_i vs.[ABTS] (Fig. 5)**
k^1_{obs} ($mM^{-1}h^{-1}$)	1.8 ± 0.2	1.4 ± 0.1
k^2_{obs} ($mM^{-1}h^{-1}$)	0.21 ± 0.05	0.34 ± 0.03

As a further independent validation of the derived theoretical rate law, the two sets of calculated values for k^1_{obs} and k^2_{obs} were used to predict the slope of the plot of v_i against [Fe(III)PPIX] (eqn. 13). These values were then compared to the experimentally determined slope (Table 5.3). It was found there was no statistically significant difference between the experimentally observed slope (3.1 ± 0.1 h^{-1}) and the predicted slopes ($p = 0.7743$; calculated using a one-way ANOVA with multiple comparisons).

Table 5.3: Predicted slope of Fig. 5.4b using experimentally determined values for k^1_{obs} and k^2_{obs}.

k^1_{obs} **and** k^2_{obs}	**Predicted slope (h^{-1})**
v_i vs. $[H_2O_2]$	2.9 ± 0.3
v_i vs.[ABTS]	3.1 ± 0.2

When considering the postulated rate law (eqn. 8), it is clear that each branch of the competing reactions presented in Scheme 5.4 can be described by two separate terms. The first term, k^1_{obs}, corresponds to processes in the upper pathway and only depends on the reaction between Fe(III)PPIX and H_2O_2 and not the subsequent reduction of ABTS to $ABTS^{\bullet+}$. This implies that formation of the high-valent $[Fe(IV)=O(porph)^{\bullet+}]$ species is the rate determining step and that this species reacts very rapidly with the available ABTS. Evidently, the large excess of ABTS compared to both H_2O_2 and Fe(III)PPIX results in it being available to reduce this highly reactive intermediate. This finding is in agreement with previous studies of the peroxidatic activity of Fe(III) porphyrins in solution.[29,37] Determining separate values for k_1, k_{-1} and k_2 in a heterogeneous system is not possible using UV-visible spectroscopy because spectra of the Fe(III)PPIX centre cannot be readily obtained. Consequently, the precise nature of the intermediate remains unknown and it is not possible to conclusively establish whether the reactive intermediate is formed via heterolytic or homolytic bond cleavage.

The second term, k^2_{obs}, describes the alternative lower pathway in Scheme 5.4 where ABTS coordinates to Fe(III)PPIX and is approximately 6 times slower than the competing upper reaction in Scheme 5.4. Here, the rate determining step is the coordination of ABTS to Fe(III)PPIX (k_4). Once formed, this evidently readily reacts with the available H_2O_2 in the pores of the MOF. In the studies conducted by Ribeiro *et al*.[38] and Adams[29] involving homogeneous catalysis of ABTS oxidation catalysed by Fe(III)PPIX or MP-8, a similar competing pathway was also proposed in order to account for the observed kinetics. In both of these studies it was also found to be a minor contributor compared to the main pathway.

One of the few kinetic studies of the peroxidatic reactivity of a Fe porphyrin@MOF catalyst was carried by Qin *et al*. on a haemin@MIL–101(Al)–NH_2 MOF system with 3,3,5,5-tetramethylbenzidine (TMB) as substrate, although these authors used the Michaelis–Menten model to analyse the kinetics.[103] With a similar catalyst loading of about 1 % Fe, the maximal velocity of TMB oxidation by H_2O_2 was found to be 0.32 mM.h^{-1} at a fixed concentration of 0.8 mM TMB. Direct comparison is difficult owing to higher catalyst concentration in their study (≈20-fold) together with use of a different substrate (ABTS) at higher concentration (5 mM) in the present system. Nonetheless, a rate of 0.3 mM.h^{-1} was readily attained at 2 mM H_2O_2 without any evidence of saturation occurring in this system (Fig. 5.4a). A concern with going to high H_2O_2 concentrations is that catalase-like activity of Fe(III) porphyrins can be induced where the [Fe(IV)=O(porph)$^{\bullet+}$] species can react with excess H_2O_2 according to equation 15, with the result that no further increase in the rate of peroxidation occurs.[19]

$$[Fe(IV) = O(porph)^{\bullet+}] + H_2O_2 + H_2O \rightarrow [Fe(III) - H_2O] + H_2O + O_2 \qquad (\mathbf{15})$$

An advantage of the use of low H_2O_2 concentrations in the present study of the kinetics was that the upper branch in Scheme 5.4 did not completely dominate the rate of ABTS oxidation. It is interesting to note that the resulting rate law describing this system is very similar to those obtained for the oxidation of ABTS by H_2O_2 catalysed by both Fe(III)PPIX and MP-8 in solution.[38,29] This indicates that the catalytic cycle for the oxidation of ABTS by H_2O_2 using these Fe(III)PPIX species is likely conserved when Fe(III)PPIX is encapsulated in **1** (Scheme 5.4).

5.4 Summary and Conclusion

Despite much investigation of metalloporphyrin@MOF as heterogeneous catalysts, there have been very few studies which have investigated the details of the kinetics of these systems and those that have been done, have been conducted under saturating conditions. The oxidation of ABTS is commonly used to study the peroxidatic activity of systems, particularly with respect to homogeneous Fe(III)PPIX and synthetic Fe(III)TPP derivatives. It has also been further applied to heterogeneous catalysis with the assumption that there is little, if any difference between the two systems. In this Chapter, a detailed study of the kinetics of ABTS oxidation by H_2O_2 catalysed by heterogeneous Fe(III)PPIX-**1** was undertaken. To limit the effects of the ABTS radical disproportionation reaction, which were significant at longer reaction times, initial rates were used in this study. Systematic variation of each component of the reaction system yielded initial rates that were used to determine an empirical rate law.

A mechanism for this reaction was proposed, from which a theoretical rate law was derived which agreed with the empirical rate law. It was necessary to include a secondary competing pathway which described the coordination of ABTS to Fe(III)PPIX. Importantly, the reaction mechanism proposed in this study is the same as reported for homogeneous Fe(III)PPIX catalysis of the ABTS oxidation reaction. This therefore indicates the process of ABTS oxidation by H_2O_2 catalysed by Fe(III)PPIX is not markedly influenced by incorporation of Fe(III)PPIX into **1**. There are, however, two notable differences when comparing the heterogeneous and homogeneous systems. In the case of the latter it is necessary to include terms for the degradation and dimerization of Fe(III)PPIX,[29,38] whereas in the case of the former the MOF environment prevents such processes from occurring. Interestingly, solid state effects such as particle size do not seem to dominate the system as might be expected in heterogeneous catalysis, at least under the conditions used in this study.

Finally, derivation of the empirical rate for Fe(III)PPIX-**1**, and the determination of rate constants for k_{obs}^1 and k_{obs}^2, enables calculation of an initial rate (v_i) under any conditions provided they are non-saturating. This provides a convenient method to facilitate direct comparison of activities of different Fe(III)porphyrin@MOF systems which is currently difficult since there is a high degree of variability in the experimental conditions employed. Unfortunately, such comparisons with the available literature could not be made because studies which have made use of the ABTS oxidation reaction have not reported the concentration of catalyst used.

Chapter Six: Fe(III)PPIX-1 as an oxidation catalyst

6.1 Introduction

Catalysis of oxidation of organic substrates is a well-known role of Fe(III)PPIX in nature.[8] Fe(III)PPIX acts as a cofactor in enzymes such as cytochromes *P450* and peroxidases where it uses hydrogen peroxide to oxidise organic substrates *in vivo*.[176,177] Oxidation of organic substrates, especially alcohols, is an important class of industrially relevant reactions[1] and therefore there has been much interest in developing heterogeneous catalysts for this purpose.[1–3] Due to Fe(III)PPIX's well-documented efficacy as a cofactor in enzymes oxidising organic substrates, its use as an oxidation catalyst outside of the enzyme environment has also been explored.[176]

As mentioned in Chapter 1, Fe(III)PPIX quickly loses its catalytic activity once removed from its enzyme environment, due to a variety of factors, including low solubility, aggregation and dimerization in aqueous solution.[20,24] It is for this reason that Fe(III)PPIX has been encapsulated into a MOF (see Chapter 3) forming Fe(III)PPIX-**1**. The MOF provides a relatively well-defined active site somewhat similar to an enzyme environment and, due to its tunable and porous nature,[92] results in the formation of an effective heterogeneous catalyst that can be designed to catalyse a specific reaction. Fe(III)PPIX-**1** shows far superior catalytic activity to its solid Cl-Fe(III)PPIX counterpart and produces greater yields of product than Fe(III)PPIX in solution (Chapter 3). Furthermore, the ability of Fe(III)PPIX-**1** to be reused through multiple catalytic cycles as well as its stability in both aqueous and organic solvents, points to its potential use as a heterogeneous oxidation catalyst. Due to the observed catalytic efficacy of Fe(III)PPIX-**1** for ABTS and MO, the ability of Fe(III)PPIX-**1** to catalyse the

oxidation of primary and secondary alcohols was investigated to determine how effective this catalyst is with other substrates.

6.2 Experimental methods and characterisation of products

6.2.1 Oxidation of Organic substrates

Hydroquinone (HQ) (15 mg, 0.136 mmol), benzyl alcohol (BN) (15 µL, 0.144 mmol) thymol (TH) (15 mg, 0.0995 mmol) and phenyl ethanol (PE) (15 µL, 0.163 mmol) were dissolved in 1 mL of solvent (H_2O or MeCN) containing 5 mg of Fe(III)PPIX-**1**. The reaction was initiated by adding 50 µL of peroxide (either 30% (w/w) H_2O_2 or 70% (w/w) *tert*-butyl hydroperoxide [^{t}BuOOH]) and was conducted at room temperature. Reactions were monitored spectrophotometrically by removing 3.7 µL (HQ), 6.3 µL (PH and TH) or 8.66 µL (BN) of the reaction mixture and diluting with 2.5 mL of the appropriate solvent. Spectra were recorded from 800 - 200 nm at various time points during the reaction. The concentration of the product was obtained using the molar extinction coefficient (molar absorptivity coefficient) from Beer's law UV-visible spectroscopy plots of commercially available products/substrates in the absorption range tested.

Reactions were also monitored *in situ* by ^{1}H NMR spectroscopy, using deuterated solvents (D_2O or MeCN-d_3). NMR spectra were recorded at 0, 2, 24 and 48 h respectively. A pre-saturation pulse programme was used to minimize interference from the water peak in the ^{1}H NMR spectrum where necessary. In the case of experiments performed using ^{t}BuOOH, the combined integration of methyl peaks for ^{t}BuOOH and ^{t}BuOH (δ 1.18 and δ 1.17 respectively) was used as an internal standard to facilitate determination of the substrate (alcohol) and its carbonyl product concentration. Full ^{1}H and ^{13}C NMR spectra used for characterisation of starting material and products are provided in Appendix C.

6.3 Results and Discussion

6.3.1 Optimization of conditions for oxidation reactions

Oxidation of HQ was chosen as a model reaction to optimize the conditions for further oxidation reactions (Scheme 6.1). HQ and its oxidation product benzoquinone (BQ) have distinctly different UV-visible spectra in both aqueous and organic solutions which provide a convenient means to follow reaction progress. Consequently, the decrease in absorbance at 280 nm (HQ) and corresponding increase in absorbance at 250 nm (BQ) was used to monitor the oxidation process (Fig. 6.1a).

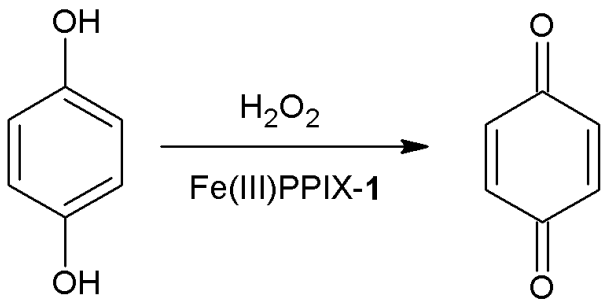

Scheme 6.1: *Oxidation of HQ to BQ by a peroxide (H_2O_2) catalysed by Fe(III)PPIX-**1**.*

The initial step in investigating Fe(III)PPIX-**1** as an oxidation catalyst was to select a suitable solvent in which to conduct reactions. Water was the first choice due to its use in the field of Green Chemistry as a non-toxic solvent. Green chemistry is defined as the design of chemical products and processes that reduce or eliminate the use and generation of hazardous substances. Heterogeneous catalysis is one of the fundamental aspects of green chemistry.[6,178] Due to its success in the oxidation of ABTS in aqueous solution (as shown in Chapters 3 and 5), H_2O_2 was used as the oxidant for the conversion of HQ to BQ in water using the experimental method outlined in 6.2.1.

The reaction was monitored by UV-visible spectroscopy at fixed time points (Fig. 6.1b). After 0.5 h there was an initial increase in the absorbance at 250 nm (*) indicating some BQ was being formed. After 1 h, however, the spectrum begun to change drastically. A very broad peak appeared, which caused an increase in absorbance below 500 nm and the decrease in the peak at 280 nm was not able to be further monitored due to overlap with this broad peak. This broad peak likely arises from the formation of side products during the course of the reaction and changes in concentrations of H_2O_2 and HQ in the reaction did not inhibit the appearance of this broad band.

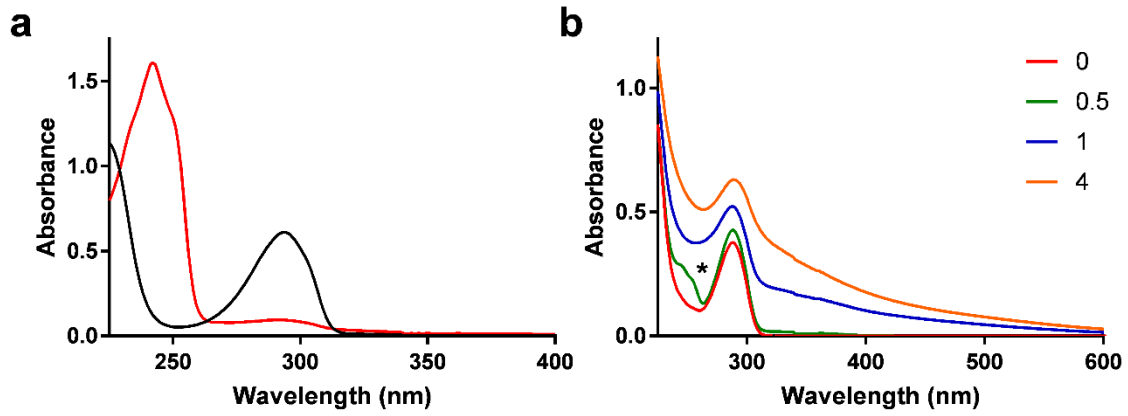

***Figure 6.1**: (a) UV-visible spectra of 100 µM HQ (black) and 100 µM BQ (red) showing λ_{max} at 280 nm and 250 nm of HQ and BQ respectively; (b) Fe(III)PPIX-**1** catalysed oxidation of HQ by H_2O_2 in aqueous solution monitored over time by taking aliquots of the reaction mixture and diluting them in H_2O. Initial formation of BQ indicated by (*).*

In an effort to circumvent this problem, the solvent was changed to an aprotic polar organic solvent, acetonitrile (MeCN). The stability of Fe(III)PPIX-**1** in MeCN was first confirmed by collecting the PXRD of the material after soaking in MeCN for 12 h. The PXRD showed no significant changes other than slight changes in intensity which can be attributed to changes in the solvent content in the crystal (Fig. 6.2a) and Pawley fitting confirmed that, other than a slight contraction along the *c* axis, there was very little change to the unit cell (Fig. 6.2b). Once the stability of Fe(III)PPIX-**1** in MeCN was confirmed, the oxidation was carried out using the same conditions previously used. While the UV-visible spectrum of the reaction mixture after 1 h showed an initial decrease in the peak at 280 nm (corresponding to HQ) and increase in the peak at 250 nm (corresponding to BQ) (Fig. 6.2c), after 17 hours significant peak broadening and changes in peak shape were observed. The lack of an isosbestic point also confirmed that there were more than two chromophoric species present in solution.

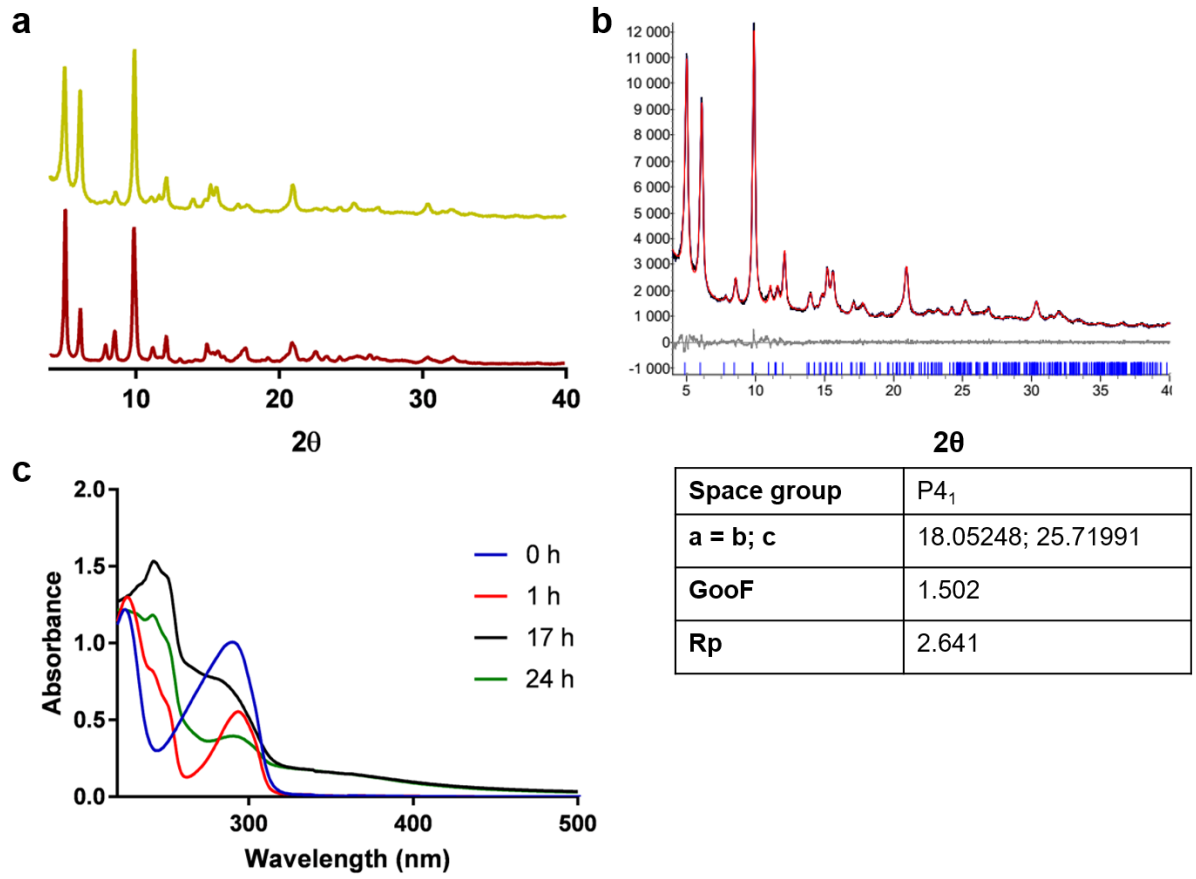

Space group	$P4_1$
a = b; c	18.05248; 25.71991
GooF	1.502
Rp	2.641

***Figure 6.2**: (a) PXRD of Fe(III)PPIX-**1** before (red) and after (green) soaking in MeCN; (b) Pawley fitting of Fe(III)PPIX-**1** after soaking in MeCN. Experimental pattern (blue), calculated pattern (red), difference pattern (expt-calc) (grey). Unit cell dimensions and agreement indices are shown in the table inset and are in good agreement with the unit cell of Fe(III)PPIX-**1**; (c) UV-visible spectra of the reaction mixture for the oxidation of HQ by H_2O_2 catalysed by Fe(III)PPIX-**1** in MeCN at various time points.*

To confirm the observed changes in the UV-visible spectra were indeed from the oxidation of HQ to BQ, the reaction was monitored *in situ* by recording ^{1}H NMR spectra at 0, 2 and 24 h respectively (Fig. 6.3). After 2 h there was a new signal from an aromatic -CH (δ 6.77) proton indicating the formation of BQ with approximately a 14% conversion with no evidence of any side products. After 24 h there was further conversion (to approximately 23%); however, there was also evidence of many side products for which structure could not be assigned. This, together with the UV-visible spectra, confirm that H_2O_2 is not a suitable oxidant in this system due to the presence of side reactions.

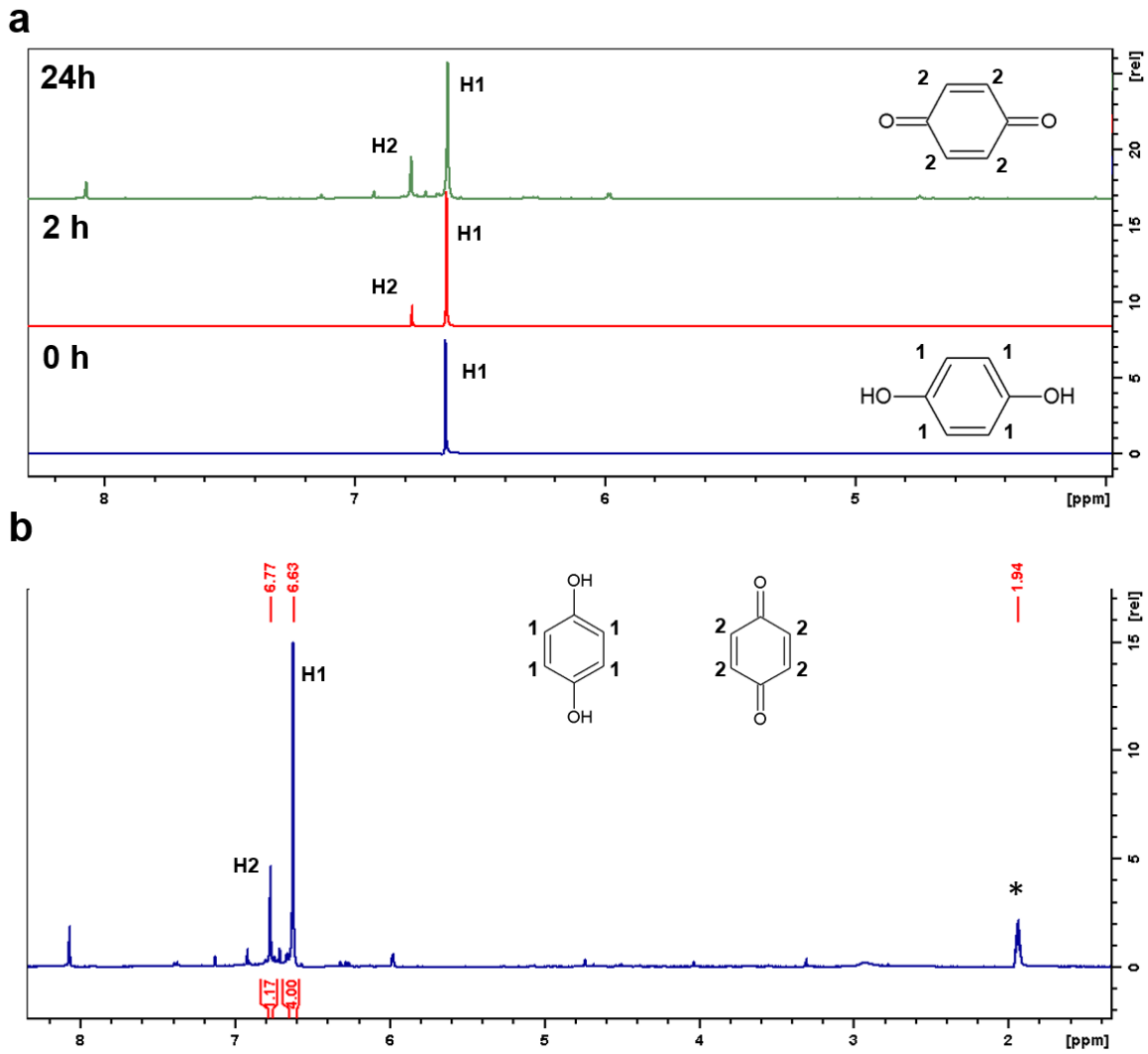

***Figure 6.3**: (a) ^{1}H NMR spectra of aromatic region of the reaction of the oxidation of HQ by H_2O_2 in the presence of Fe(III)PPIX-**1** at 0, 2 and 24 h showing the appearance of the signal from the -CH proton of benzoquinone (δ 6.77) as well as the appearance of additional peaks due to side products after 24 h; (b) Full ^{1}H NMR spectrum of the products of the oxidation of HQ after 24 h. Asterisk (*) corresponds to residual solvent peaks. A pre-saturation pulse programme was used to minimise the water peak.*

One option to an obtain a better yield for this reaction was to change the oxidant from H_2O_2 to an organic hydroperoxide. H_2O_2 decomposes to H_2O during the course or a reaction, whereas organic radicals such as ^{t}BuOOH will decompose to an alcohol, in this case *tert*-butanol. During the reaction, ^{t}BuOOH forms a less reactive intermediate than H_2O_2. It has been shown to have good reactivity with Fe(III) porphyrins with a similar mechanism to that of H_2O_2.[179–181]

The oxidation of HQ by ^{t}BuOOH was monitored as before using UV-visible spectroscopy. There was a decrease in the peak at 280 nm corresponding to HQ and an increase in the peak at 250 nm corresponding to BQ (Fig. 6.4a). Contrary to the previous conditions, there was no broadening of peaks or changes to the peak shape. Furthermore, the presence of an isobestic point confirms there were only two chromophoric species present in the solution. Using the calculated (determined from their respective Beers law plots) molar extinction coefficients for HQ ($\varepsilon_{280\ nm}$ 2853 L.mol^{-1}.cm^{-1}) and BQ ($\varepsilon_{250\ nm}$ 2660 L.mol^{-1}.cm^{-1}), the concentrations of each species could be calculated at each time point (Fig. 6.4b). The reaction fitted a pseudo-first order reaction model from which the rate constant and half-life were determined (0.336 µmol BQ.h^{-1} and 2.07 h respectively). The UV-visible experiments indicated that complete conversion of HQ to BQ had occurred. This was further supported by monitoring the reaction using ^{1}H NMR spectroscopy for 0, 2 and 24 h (Fig. 6.4c). The appearance of the signal at δ 6.77 indicated that BQ had indeed been formed (peak corresponds to -CH proton of the quinone) and the disappearance of the signal at δ 6.63 confirmed that complete conversion of HQ to BQ occurred after 24 h.

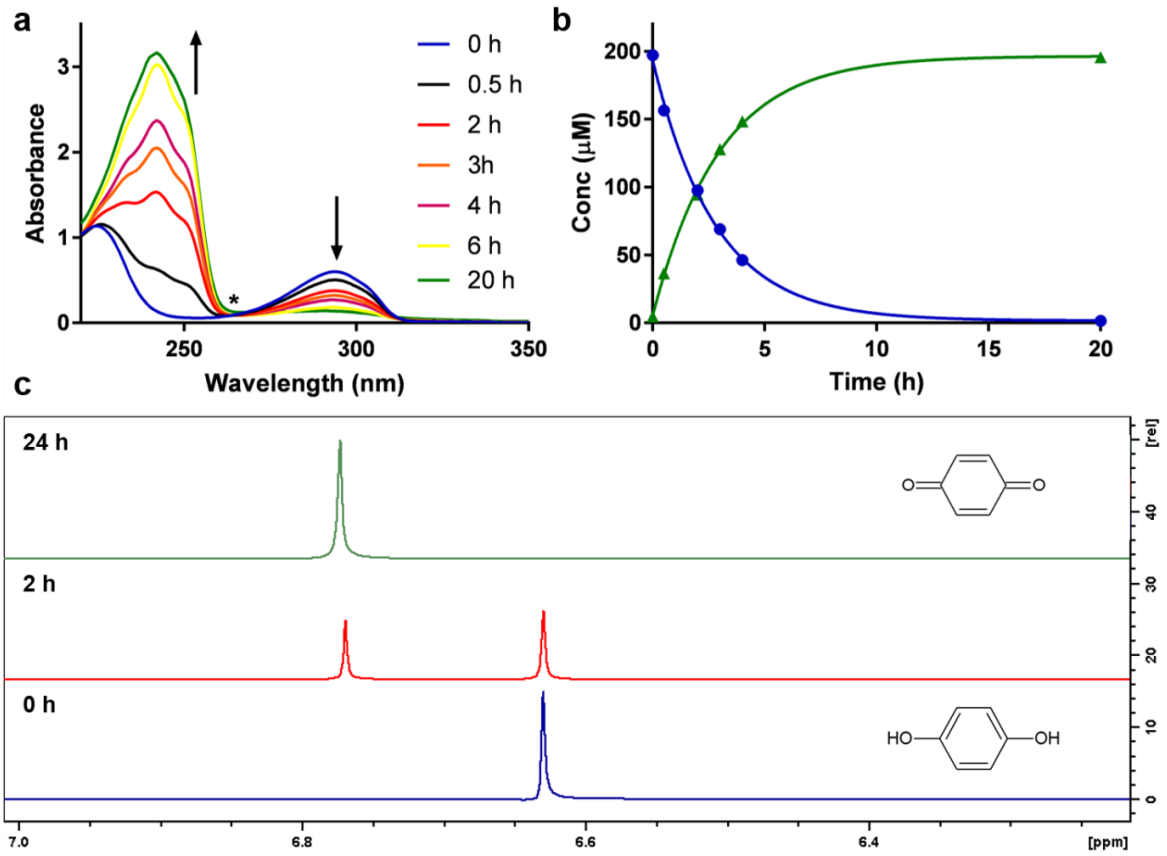

***Figure 6.4**: Oxidation of HQ by ^{t}BuOOH catalysed by Fe(III)PPIX-**1**. (a) UV-visible spectra of an aliquot of the reaction mixture at various time points. The asterisk (*) marks the isosbestic point; (b) increasing concentration of BQ (green) and decreasing concentration of HQ (blue) with respect to time showing pseudo-first order kinetics; and (c) ^{1}H NMR spectra of the reaction mixture at 0, 2 and 24 h showing the appearance of the signal at δ 6.77 corresponding to the -CH proton of BQ and the disappearance of the signal at δ 6.63 corresponding to the -CH proton of HQ.*

The successful oxidation of HQ to BQ by ^{t}BuOOH catalysed by Fe(III)PPIX-**1** in MeCN indicated that these conditions were suitable for further investigation into the versatility of Fe(III)PPIX-**1** as an oxidation catalyst.

6.3.2 Investigation of oxidation of additional substrates

The success of the oxidation of HQ to BQ justified an investigation into the oxidation of additional substrates, namely benzyl alcohol (BN), phenyl ethanol (PH) and thymol (TH) (Scheme 6.2). Since access of the substrate to the catalytic site is an important consideration in MOF heterogeneous catalysis,[40,89] substrates with differing molar volumes were chosen. All oxidations were carried out under the same conditions as used for the oxidation at HQ, (outlined in 6.2.1) and monitored by UV-visible spectroscopy. In the cases of BN and PH, the spectra of the substrate and the product were first recorded from commercially available samples (Fig. 6.5). Oxidation of BN caused an increase in the peaks at 240 nm and 280 nm which correspond to the λ_{max} of benzaldehyde and therefore supported formation of the product. A similar observation was made in the case of the oxidation of phenyl ethanol (PE) and thymol (TH) with increases in the peaks at 260 nm and 280 nm respectively.

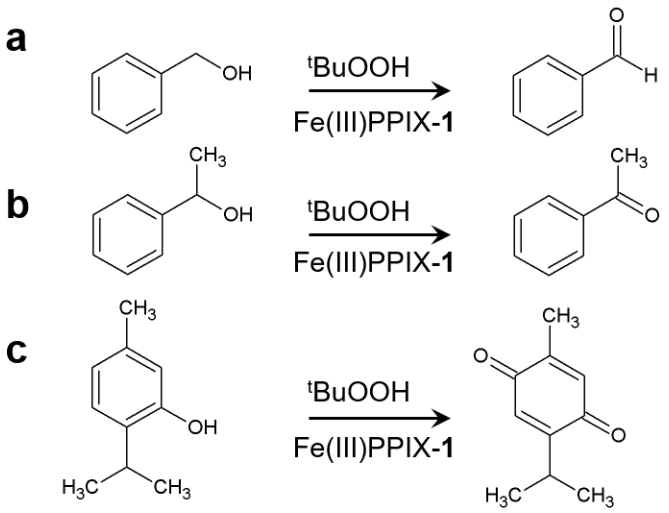

Scheme 6.2: *Oxidation of (a) benzyl alcohol (BN) to benzaldehyde; (b) phenyl ethanol to acetophenone and (c) thymol (TH).*

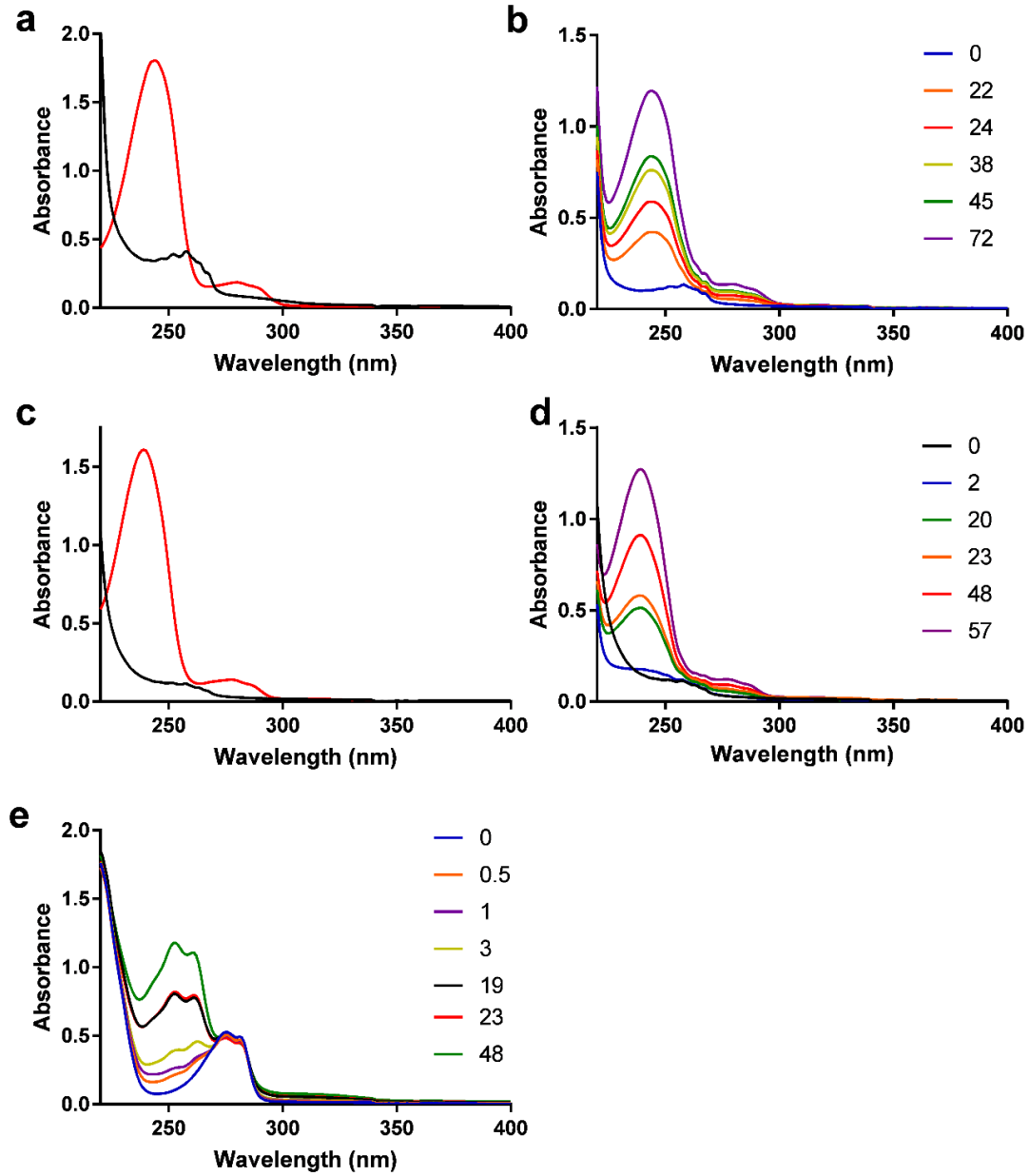

***Figure 6.5**: UV-visible spectrophotometric analysis of oxidation reactions. Spectra of commercially available starting materials and products (a and c) and time course of oxidation reactions (b, d, e). (a) 2.31 M benzyl alcohol (BN) (black) and 100 µM benzaldehyde (red); (b) BN oxidation reaction mixture at different time points (h); (c) 410 µM phenyl ethanol (PE) (black) and 100 µM acetophenone (red); (d) PE oxidation reaction mixture at different time points (h) and (e) Thymol (TH) oxidation reaction mixture at different time points (h).*

The progress of the oxidation of each substrate was monitored using UV-visible spectroscopy and complete conversion of each substrate was not achieved in the time frame studied. A plot of the increase of absorbance for each substrate indicated that the reactions still followed pseudo-first order kinetics (Fig. 6.6).

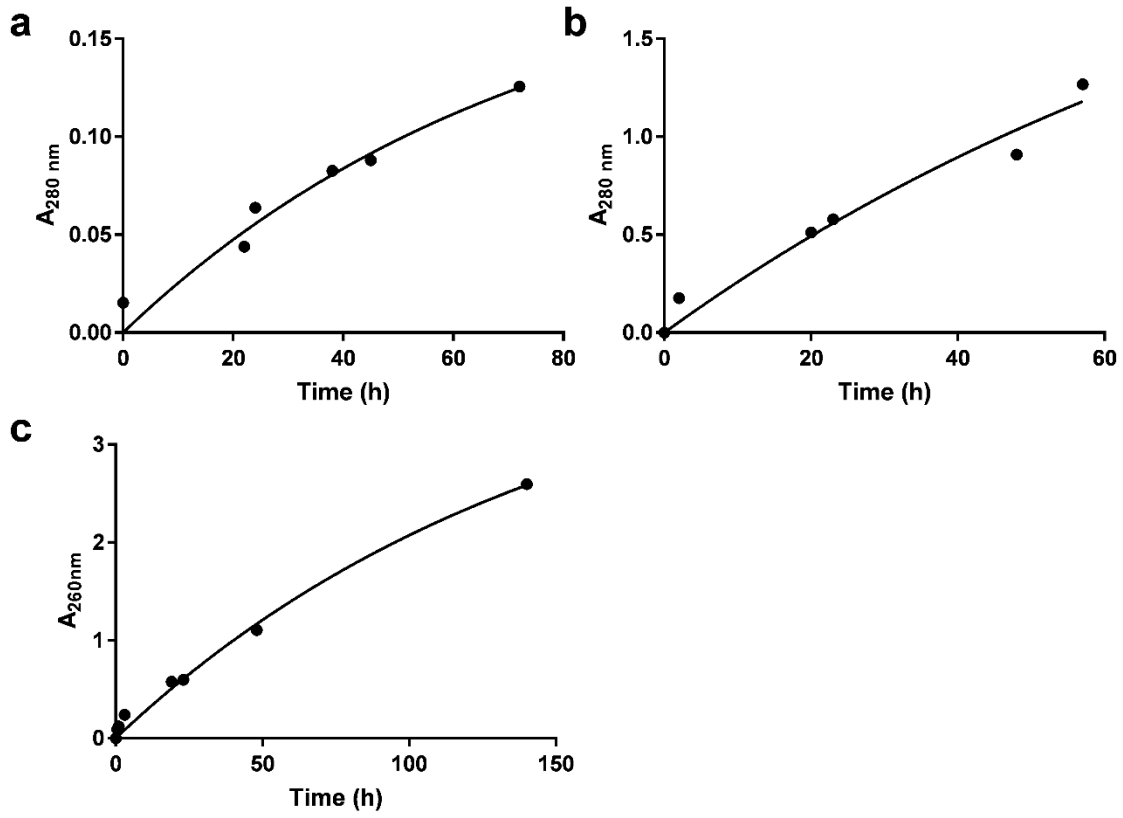

***Figure 6.6**: Increasing absorbance of (a) benzaldehyde, (b) acetophenone and (c) thymoquinone with respect to time showing pseudo-first order kinetics.*

An *in situ* NMR experiment for each substrate was conducted in the same manner as described for the oxidation of HQ in Section 6.3.1 with an extra time point added after 48 h due to the slower reaction rates. In the case of BN, the appearance of a singlet of the carbonyl proton at δ 10.00 as well as new aromatic signals between δ 7.5 and 8, was indicative of the formation of benzaldehyde (Fig. 6.7). Due to the complexity of the spectra, full assignment of specific aromatic protons was not determined. The NMR experiments allowed the conversion % to be calculated after 2, 24 and 48 h respectively for each substrate. The % conversion was calculated

by comparing the integration of the key signals identified and comparing them with the integration of the internal standard, ^{t}BuOOH. During the oxidation process, ^{t}BuOH is produced. The signal from this by product was close enough to the ^{t}BuOH signal to integrate them simultaneously, and ensures a constant contribution from these protons which are at a known fixed total concentration. All oxidation products were characterised by ^{1}H NMR and ^{13}C NMR spectroscopy after 48 h from the *in situ* NMR experiments (Appendix C). Full conversion of substrate to product was not achieved in any of these oxidation reactions within the time frame studied.

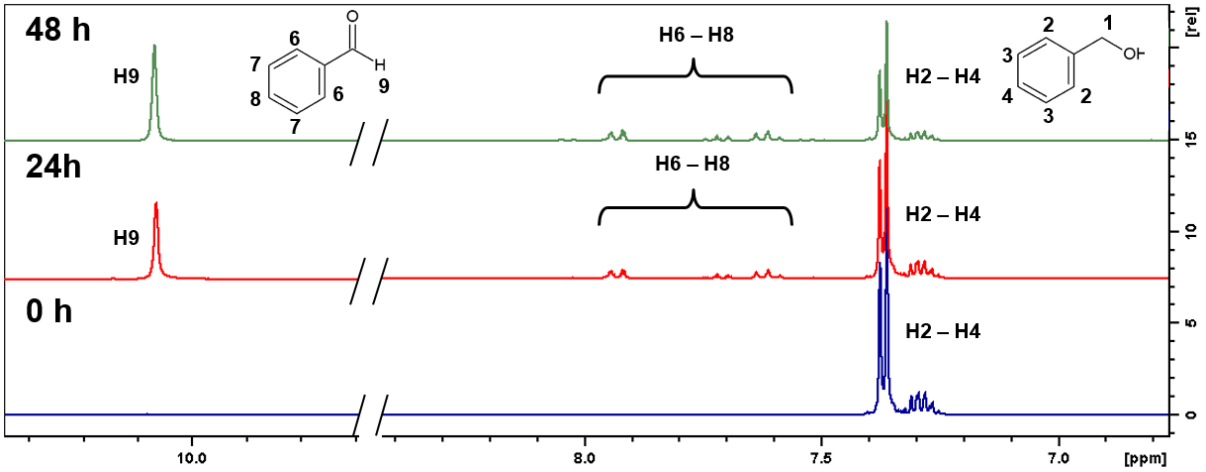

***Figure 6.7**: In situ ^{1}H NMR spectra for the oxidation of benzyl alcohol to benzaldehyde by ^{t}BuOOH catalysed by Fe(III)PPIX-**1**. Appearance of the carbonyl proton (δ 10.00) confirms formation of benzaldehyde.*

Comparison of the half-life of each reaction with the substrate volume shows a clear increase in the half-life of the reaction as the molar volume increases (Table 6.1). This suggests that the rate of diffusion into the channels of Fe(III)PPIX-**1** controls the reaction rate, a reasonable hypothesis, since the substrate will need to diffuse into the channels where the catalytic oxidation occurs. This hypothesis was supported by performing the same oxidation reactions but using homogeneous catalysis by dissolving Fe(III)PPIX in solution. Under these conditions, changes in molecular volume did not reproduce this trend (Table 6.2, Fig. 6.8). Rather, it was found that the half-lives for the oxidation of TH, BN and PH were approximately equal. This points towards the possible use of Fe(III)PPIX-**1** as a size-selective oxidation catalyst and emphasizes the importance of the catalytic sites in the interior of the MOF.

Table 6.1: Conversion, half-lives and molar volumes of substrates oxidised by ^{t}BuOOH catalysed by Fe(III)PPIX-**1**.

Substrate	Product	Catalyst loading	Conversion[a]	Half-life (h)[b]	Molecular volume (Å^3)[c]
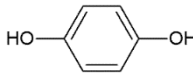		0.63 mol %	100% (24 h)	2.07	99.04
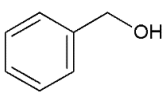	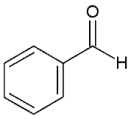	0.62 mol %	28% (48 h)	51.85	107.43
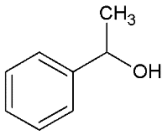	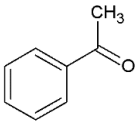	0.73 mol %	23% (48 h)	70.58	124.53
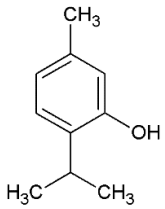	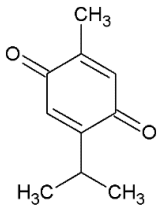	0.89 mol %	22% (48 h)	103.8	158.45

[a] Relative concentrations of substrate and product were determined by NMR at each time point by integrating each peak relative to an internal standard (^{t}BuOOH + *in situ* formed *tert*-butanol [^{t}BuOH]). All reactions were carried out with 15 mg of substrate in 1 mL of d_3-MeCN and initiated by addition of 50 µL of 70% (w/w) ^{t}BuOOH in water at 25 °C. Characterization of products is presented in Appendix C; [b] Half-lives were determined from UV-visible spectroscopy data obtained at 37.00 °C, fitted with a non-linear regression model in GraphPad Prism (Fig. 6.6)[117]; [c] molecular volume was calculated using Chemicalize.[182]

Table 6.2: Conversion, half-lives and molar volumes of substrates oxidized by ^{t}BuOOH in the presence of Fe(III)PPIX dissolved in solution.

Substrate	Product	Catalyst loading	Conversion (Solution)[a]	Half-life (solution) (h)[b]	Molecular volume (Å^3)[c]
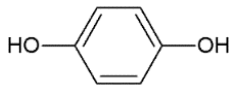	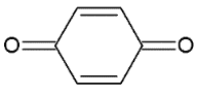	0.63 mol %	100% (0.13 h)	0.0208	99.04
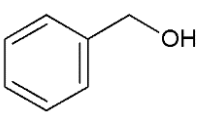	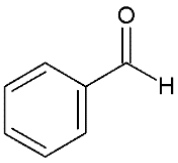	0.62 mol %	8% (0.5 h)	0.0888	107.43
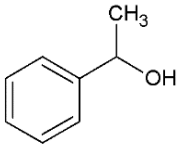	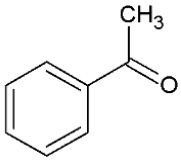	0.73 mol %	20% (0.5 h)	0.0796	124.53
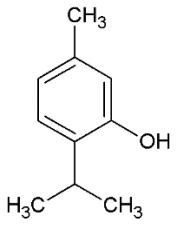	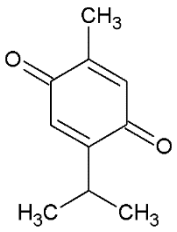	0.89 mol %	-	0.0989	158.45

[a] Relative concentrations of substrate and product were determined from UV-visible spectra of each reaction after the specified time. Calculation was not possible for TH due to overlapping product and reactant UV-visible spectra and lack of extinction coefficient for oxidised product. All reactions were performed using 15 mg of substrate in 1 mL of MeCN and initiated by addition of 50 µL of 7 % (w/w) ^{t}BuOOH in water at 25 °C. All reactions were followed by UV-visible spectroscopy ; [b] Half-lives were determined from UV-visible spectroscopy data obtained at 25.00 °C, fitted with a one phase-exponential function in GraphPad Prism (Fig. 6.8)[117]; [c] molecular volume was calculated using Chemicalize.[182]

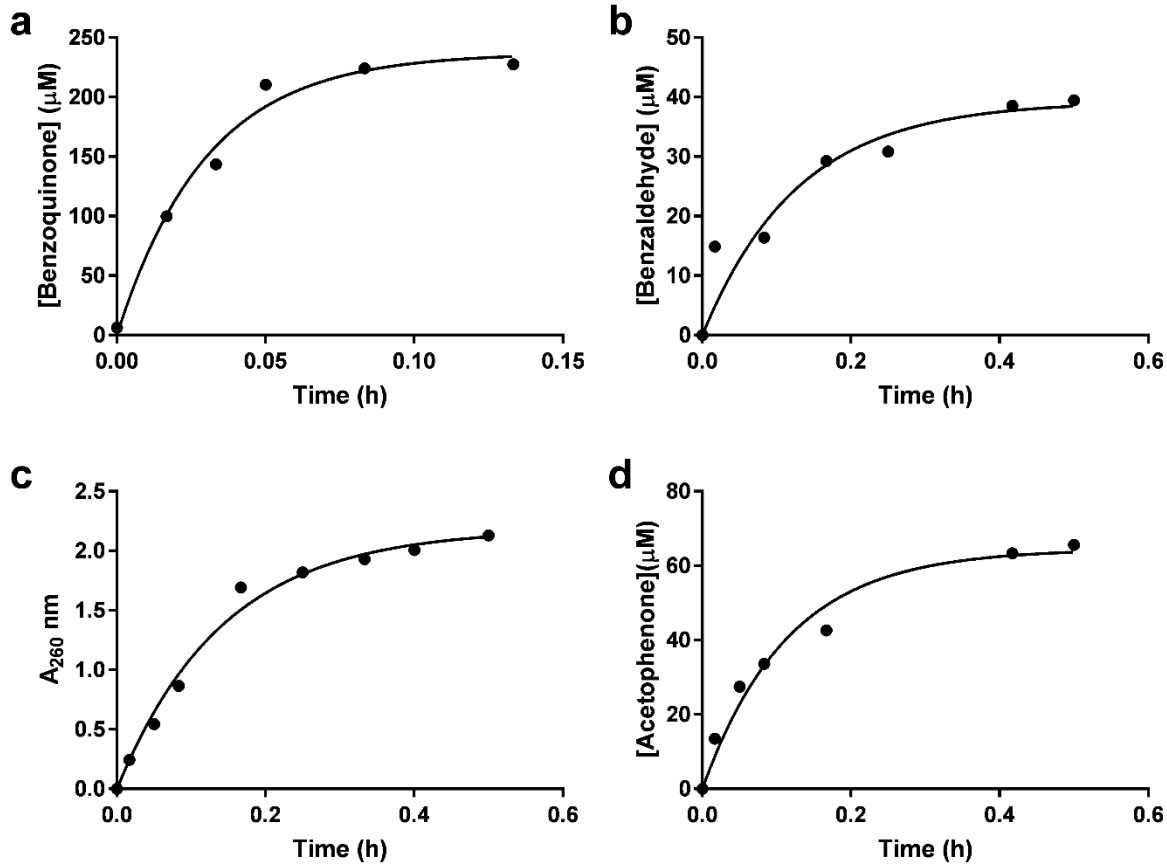

***Figure 6.8**: Increase in absorption of the product obtained in the catalytic oxidation of substrate by ^{t}BuOOH in MeCN catalysed by Fe(III)PPIX dissolved in solution. (a) hydroquinone; (b) benzyl alcohol; (c) thymol; and (d) phenyl ethanol. Data were fitted with a one-phase exponential function in Graph Pad Prism to determine the half-life of each reaction.*

6.4 Summary and Conclusions

The findings reported in this Chapter highlight the versatility of Fe(III)PPIX-**1** as a heterogeneous oxidation catalyst. Not only is Fe(III)PPIX-**1** able to catalyse the oxidation of ABTS (see Chapters 3 and 5), it is able to catalyse the oxidation of primary and secondary aromatic alcohols to their corresponding aldehydes and ketones. While the reaction can occur in aqueous solution using H_2O_2 as an oxidant, extensive side products are obtained. Findings show that side product formation can be effectively minimised, however, by performing the reactions in MeCN with ^{t}BuOOH as the oxidant. The reaction conditions established for this reaction are well suited for *in situ* measurement using NMR spectrometry. Although full conversion was not achieved for all substrates, it is important to note that Fe(III)PPIX-**1** is present as approximately 5 mol % in the reaction mixture. Consequently, these reactions are catalytic and further optimization of experimental conditions could lead to increased catalytic efficiency. Nevertheless, these preliminary results provide strong support for the use of Fe(III)PPIX-**1** as a heterogeneous oxidation catalyst.

An additional finding found in this work is the dependence of reaction half-lives on the molar volumes of the substrate. This dependence is proposed to arise from the rate of substrate diffusion into the channels of Fe(III)PPIX-**1**. The same trend is not observed for homogeneous catalysis by Fe(III)PPIX dissolved in solution and suggests that Fe(III)PPIX-**1** could possibly be used as a size selective catalyst. These results highlight the importance of considering substrate and MOF channel/pore size when designing metalloporphyrin@MOF heterogeneous catalysts.

Chapter Seven: Conclusions and Future work

7.1 Overall Conclusions

Using Fe(III) porphyrins as heterogeneous oxidation catalysts is an attractive goal owing to the catalytic versatility of the Fe(III)PPIX co-factor observed in haemoproteins.[13,14] The encapsulation of both native Fe(III)PPIX and synthetic derivatives such as Fe(III)tetraphenyl porphyrin, Fe(III)TPP, in a solid support is an effective means to achieve this aim.[40] MOFs have been identified as a solid support which can potentially encapsulate the porphyrin in well-defined active sites that a substrate can access.[1,91–93] Indeed, encapsulation of both Fe(III)PPIX[103,107,111] and Fe(III) tetraphenyl porphyrins[41,99,154,162] into MOFs for use as heterogeneous oxidation catalysts has been the focus of many studies in recent years. The majority of these studies, however, have used redox active metals for the construction of the framework which complicates interpretation of the observed catalytic activity. For example, Cu-HKUST-1 used by Luo *et* al.[107] to encapsulate Fe(III)PPIX has been shown to have inherent peroxidatic activity.[110,135] Thus the contribution of Fe(III)PPIX (or other Fe(III) porphyrins) in such systems is unclear.

Consequently, this study aimed to encapsulate catalytically-active porphyrins Fe(III)PPIX and Fe(III)TPP in redox inactive MOFs to properly establish the potential of each iron porphyrin as heterogeneous oxidation catalysts. Two frameworks, namely $[H_2N(CH_3)_2][Zn_3(TATB)_2(HCOO)]\cdot HN(CH_3)_2\cdot DMF\cdot 6H_2O$ (**1**) and Zn-HKUST-1 (**2**), were used to achieve this goal. In the case of **2**, both Fe(III)PPIX and Fe(III)TPP could be successfully encapsulated and the crystal structure could be determined for the latter. Upon further investigation, however, this framework proved to be unsuitable for heterogeneous catalysis in aqueous solution for two primary reasons: (i) the framework itself exhibited poor

substrate uptake, as measured using methyl orange (MO) as a model substrate, despite the presence of large cages in its structure; (ii) crystals of Fe(III)TPP-**2** were unstable when exposed to moisture in air and consequently Fe(III)PPIX-**2** displayed poor activity as a peroxidation catalyst. Both Fe(III)PPIX-**2** and Fe(III)TPP-**2** may well be better suited towards catalytic activity in non-aqueous media in an inert environment, but this was not investigated.

By contrast, framework **1** was found to be more suitable as a potential solid support for encapsulating porphyrins. Substrate adsorption into **1** was much greater than **2** and was likely facilitated through diffusion into the former's infinite 4_3 helical channels. Importantly, the framework was stable in aqueous solution. On the other hand, encapsulation of Fe(III)TPP into **1** was unsuccessful despite the larger size of the channels in **1** compared to the cages in **2**. This finding highlights the importance of considering framework topology when designing metalloporphyrin encapsulating MOFs since the ability of the phenyl rings of Fe(III)TPP to extend into the adjacent cavities in **2** is crucial for successful encapsulation. On the other hand, crystals of Fe(III)PPIX-**1** were obtained under the same synthetic conditions and were of sufficient quality for single crystal X-ray diffraction using synchrotron radiation. This allowed the distribution and accessibility of catalytic sites in Fe(III)PPIX-**1** to be confirmed. While the full porphyrin could not be modelled due to extensive disorder and twinning of the crystal, locating the iron centre and the first coordination shell allowed the position of Fe(III)PPIX in the channels to be determined. This presents the first reported crystal structure of Fe(III)PPIX encapsulated in a MOF. Characterisation of Fe(III)PPIX-**1** by a variety of analytical techniques revealed two important points. Firstly, both PXRD and single crystal X-ray diffraction confirmed that encapsulation of Fe(III)PPIX did not alter the structure of the framework thereby maintaining the channels important for substrate diffusion. Secondly, solid-state UV-visible spectroscopy confirmed Fe(III)PPIX was encapsulated in a monomeric form and did not degrade during the synthesis process. This is crucial since loss of Fe(III)PPIX catalytic

activity outside of a protein environment in an aqueous solution can occur through formation of μ-oxo dimers.[20,24]

Fe(III)PPIX-**1** was found to be an effective heterogeneous catalyst for peroxidation reactions. The catalytic activity of Fe(III)PPIX-**1** was substantially higher than solid state Fe(III)PPIX-Cl, with regards to both the initial rate and yield of the reaction. This heterogeneous system produced an initial rate only an order of magnitude lower than the corresponding homogeneous Fe(III)PPIX reaction, but with a much improved yield. Importantly, Fe(III)PPIX-**1** could be readily recovered and reused through multiple cycles without loss in catalytic activity. Interestingly, the kinetics of the peroxidation reaction catalysed by Fe(III)PPIX-**1** produced a proposed rate law that is very similar to those obtained for the same reaction catalysed by both Fe(III)PPIX and MP-8 in aqueous solution.[38,29] This indicates that the catalytic cycle for the oxidation of ABTS by H_2O_2 using these Fe(III)PPIX species is likely conserved when Fe(III)PPIX is encapsulated in **1**. The key difference between this rate law and those derived in previous studies in solution is the lack of terms describing dimerization and degradation of the porphyrin in the MOF system. Thus, incorporating Fe(III)PPIX in the MOF maintains solution-like behaviour, while keeping the metalloporphyrin in a monomeric state, protected from degradation. Solid state effects such as particle size do not seem to dominate the system, at least under the conditions used in this study. This work is, seemingly, the first to describe the kinetics of a heterogeneous Fe(III) porphyrin containing MOF catalyst under non-saturating conditions of oxidant.

Finally, an interesting feature of Fe(III)PPIX-**1** is its ability to not only catalyse peroxidation reactions in aqueous solution, but to also catalyse the oxidation of aromatic alcohols to the corresponding aldehydes and ketones in non-aqueous media. The dependence of the half-life on the size of the substrate points to the potential use of Fe(III)PPIX-**1** as a size selective oxidation catalyst. These findings and those presented above highlight Fe(III)PPIX-**1** as an effective and versatile heterogeneous oxidation catalyst which demonstrates the efficacy of MOFs for use as solid-state supports for harnessing the catalytic power of Fe(III)PPIX.

7.2 Future Work

A number of findings from this study prompt further investigation. For clarity, these have been divided into two sections, namely: (i) Further investigations of Fe(III)PPIX-**1** and (ii) Development of other porphyrin containing MOF catalysts.

7.2.1 Investigations of Fe(III)PPIX-1

Fe(III)PPIX-**1** shows great potential as a heterogeneous oxidation catalyst, and has been thoroughly characterised, but further investigation into its application as a catalyst is warranted to gain a better understanding of how to effectively utilise its catalytic activity. During the course of this investigation much emphasis has been placed on the performance of Fe(III)PPIX-**1** in an aqueous environment. In Chapter 6, it was observed that Fe(III)PPIX-**1** performed better in MeCN when oxidising alcohols by minimising the production of side products when oxidising HQ to BQ. A further study is warranted on effects of solvent choice that will be crucial to determine the efficacy of Fe(III)PPIX-**1** under varying conditions. A study with GC-MS could identify any possible side products and therefore increase understanding of the mechanism of action of the catalyst. It is important to note that solvents such as MeOH cannot be used, as MeOH can be oxidised to formaldehyde or formic acid.

The oxidation of alcohols catalysed by Fe(III)PPIX-**1** showed low yields for the larger alcohols. An investigation to optimise the reaction conditions could help to increase the yield as well as decrease the half-life of the reaction. It would be interesting to probe the potential of Fe(III)PPIX-**1** as a size selective oxidation catalyst by introducing a mixture of different sized substrates and analysing the composition of the products obtained using NMR spectroscopy and GC-MS spectrometry.

While Fe(III)PPIX-**1** has been shown to be effective at catalysing the oxidation of alcohols, an investigation into a wider range of substrates is needed. Porphyrin containing MOF catalysts

have also been shown to be very effective at catalysing epoxidation reactions.[154,162] Investigating the ability of Fe(III)PPIX-**1** to catalyse the epoxidation of substrates such as styrene would be of great interest as it will give an indication of the potential versatility of the catalyst. Furthermore, epoxidations are very important industrial reactions and it is of great import to develop better heterogeneous oxidation catalysts for various applications.

A further interesting study would be to investigate the role of each feature of Fe(III)PPIX in the catalytic activity of Fe(III)PPIX-**1**. This could be done by systematically encapsulating derivatives of Fe(III)PPIX into **1** and measuring the resultant peroxidatic activity. Suggested modifications are as follows: (i) encapsulation of Fe(III) protoporphyrin IX dimethyl ester, a Fe(III)PPIX analogue where both of the propionates have undergone dimethyl esterification, would allow the role of the propionates to be determined, and to determine whether the carboxylates are displacing the formate groups in the framework of **1**; (ii) encapsulation of Mn(II) and Co(II) PPIX to determine the role of the metal centre; (iii) encapsulation of Fe(III) deuteroporphyrin IX and mesoporphyrin IX to determine the role of the vinyl groups and finally (iv) Fe(III)porphine to determine the role of all the substituents. This could also help gain insight into the differences in reactivity observed in synthetic and natural porphyrins.

7.2.2 Development of other porphyrin containing MOF catalysts

As mentioned in the Conclusions, Fe(III)PPIX-**2** did possess some catalytic activity while Fe(III)TPP-**2** was completely unstable. The instability of **2** in an aqueous environment rendered a full investigation of their potential as heterogeneous oxidation catalysts in an aqueous environment futile. They may, however, possess much greater activity under different reaction conditions. A further investigation into the potential of Fe(III)PPIX-**2** and Fe(III)TPP-**2** under dry and inert conditions should be conducted to determine whether these catalysts could be efficient oxidation catalysts. If successful, this could also allow direct comparison of the catalytic activities of Fe(III)TPP and Fe(III)PPIX.

Finally, the encapsulation of other naturally occurring tetrapyrroles which act as co-factors, such as cobalamin (vitamin B_{12}) and chlorophyll, into framework **1**, and other MOFs, could increase the versatility of porphyrin MOF systems by increasing the types of reactions that they can support. For example, cobalamin can catalyse trans methylation, halide coupling and dehalogenation reactions.[183]

These proposed experiments would provide further insights both into the versatility and mechanism of action of Fe(III)PPIX-**1** as a heterogeneous oxidation catalyst and could result in the development of further heterogeneous catalysts synthesized by encapsulating porphyrins and other tetrapyrroles in MOFs.

Chapter Eight: References

(1) Dhakshinamoorthy, A.; Alvaro, M.; Garcia, H. *Catal. Sci. Technol.* **2011**, *1*, 856–867.

(2) Ojeda, M.; Grau-Atienza, A.; Campos, R.; Romero, A. A.; Serrano, E.; Maria Marinas, J.; García Martínez, J.; Luque, R. *ChemSusChem* **2015**, *8*, 1328–1333.

(3) Pereira, C.; Simoes, M.; Tome, J.; Almeida Paz, F. *Molecules* **2016**, *21*, 1348–1366.

(4) Chughtai, A. H.; Ahmad, A. N.; Younus, H. A.; Laypkov, A.; Verpoort, F. *Chem. Soc. Rev* **2015**, *44*, 6804–6849.

(5) Tundo, P.; Anastas, P.; Black, D. S.; Breen, J.; Collins, T. J.; Memoli, S.; Miyamoto, J.; Polyakoff, M.; Tumas, W. *Pure Appl. Chem.* **2000**, *72*, 1207–1228.

(6) Anastas, P. T.; Kirchhoff, M. M.; Williamson, T. C. *Appl. Catal. A Gen.* **2001**, *221*, 3–13.

(7) Poulos, T. L. *Chem. Rev.* **2014**, *114*, 3919–3962.

(8) Groves, J. T. In *Cytochrome P450*; Springer US: Boston, MA, 2007; pp 1–43.

(9) Fanelli, A. R.; Antonini, E.; Caputo, A. *Hemoglobin and Myoglobin*; Anfinsen, C. B., Anson, M. L., Edsall, J. T., Richards, F. M., Eds.; Academic Press, 1964; Vol. 19.

(10) Gray, H. B.; Winkler, J. R. *Annu. Rev. Biochem.* **1996**, *65*, 537–561.

(11) Rodgers, K. R. *Curr. Opin. Chem. Biol.* **1999**, *3*, 158–167.

(12) Bernard Meunier; Samuël P. de Visser; Sason Shaik; Meunier, B.; Visser, S. P. de; Shaik, S. *Chem. Rev.* **2004**, *104*, 3947–3980.

(13) Schmid, A.; Dordick, J. S.; Hauer, B.; Kiener, A.; Wubbolts, M.; Witholt, B. *Nature* **2001**, *409*, 258–268.

(14) Reedy, C. J.; Gibney, B. R. *Chem. Rev.* **2004**, *104*, 617–649.

(15) RCSB Protein Data Bank https://www.rcsb.org/pdb/home/home.do (accessed Jun 1, 2017).

(16) Roat-Malone, R. M. In *Bioinorganic Chemistry*; John Wiley & Sons, Inc.: Hoboken, NJ, USA; pp 343–476.

(17) Mansuy, D.; Battioni, P. *Bioinorganic catalysis*, Second Edi.; Reedijk, J., Bouwman, E., Eds.; Marcel Dekker Inc: New York, 1999.

(18) Poulos, T. L.; Kraut, J. *J. Biol. Chem.* **1980**, *255*, 8199–8205.

(19) Brausam, A.; Eigler, S.; Jux, N.; van Eldik, R. *Inorg. Chem.* **2009**, *48*, 7667–7678.

(20) Bruice, T. C. *Acc. Chem. Res.* **1991**, *24*, 243–249.

(21) Lee, W. A.; Bruice, T. C. *J. Am. Chem. Soc.* **1985**, *107*, 514–516.

(22) Soper, J. D.; Kryatov, S. V.; Rybak-Akimova, E. V.; Nocera, D. G. *J. Am. Chem. Soc.* **2007**, *129*, 5069–5075.

(23) Zipplies, M. F.; Lee, W. A.; Bruice, T. C. *J. Am. Chem. Soc.* **1986**, *108*, 4433–4445.

(24) Guo, C.-C.; Song, J.-X.; Chen, X.-B.; Jiang, G.-F. *J. Mol. Catal. A Chem.* **2000**, *157*, 31–40.

(25) Meunier, B. *Chem. Rev.* **1992**, *92*, 1411–1456.

(26) Roger A. Sheldon. *Metalloporphyrins in Catalytic Oxidations*; Dekker: New York, 1994.

(27) Hessenauer-Ilicheva, N.; Franke, A.; Meyer, D.; Woggon, W.-D.; van Eldik, R. *J. Am. Chem. Soc.* **2007**, *129*, 12473–12479.

(28) Nam, W.; Park, S.-E.; Lim, I. K.; Lim, M. H.; Hong, J.; Kim, J. *J. Am. Chem. Soc.* **2003**, *125*, 14674–14675.

(29) Adams, P. A. *J. Chem. Soc. Perkin Trans.* **1990**, *2*, 1407–1414.

(30) Meunier, B.; Visser, S. P. de; Shaik, S. *Chem. Rev.* **2004**, *104*, 3947–3980.

(31) Adler, A. D.; Longo, F. R.; Finarelli, J. D.; Goldmacher, J.; Assour, J.; Korsakoff, L. *J. Org. Chem.* **1967**, *32*, 476–476.

(32) Rose, E.; Kossanyi, A.; Quelquejeu, M.; Soleilhavoup, M.; Duwavran, F.; Bernard, N.; Lecas, A. *J. Am. Chem. Soc.* **1996**, *118*, 1567–1568.

(33) Collman, J. P.; Gagne, R. T.; Reed, C. A. *J. Am. Chem. Soc.* **1974**, *96*, 2629–2631.

(34) Collman, J. P.; Brauman, J. I.; Doxsee, K. M.; Halbert, T. R.; Bunnenberg, E.; Linder, R. E.; LaMar, G. N.; Del Gaudio, J.; Lang, G.; Spartalian, K. *J. Am. Chem. Soc.* **1980**, *102*, 4182–4192.

(35) Collman, J. P.; Gagne, R. R.; Reed, C.; Halbert, T. R.; Lang, G.; Robinson, W. T. *J. Am. Chem. Soc.* **1975**, *97*, 1427–1439.

(36) Almog, J.; Baldwin, J. E.; Dyer, R. L.; Peters, M. *J. Am. Chem. Soc.* **1974**, *97*, 227–228.

(37) Cunningham, I. D.; Danks, T. N.; O 'Connell, K. T. A.; Scott, P. W. *J. Chem. Soc. Perkin Trans. 2* **1999**, *2*, 2133–2139.

(38) de Almeida Ribeiro, M. C.; Augusto, O.; da Costa Ferreira, A. M. *J. Chem. Soc. Dalt. Trans.* **1995**, *23*, 3759–3766.

(39) Nagababu, E.; Rifkind, J. M. *Antioxidants Redox Signal.* **2004**, *6*, 967–978.

(40) Chakraborty, J.; Nath, I.; Verpoort, F. *Coord. Chem. Rev.* **2016**, *326*, 135–163.

(41) Larsen, R. W.; Wojtas, L.; Perman, J.; Musselman, R. L.; Zaworotko, M. J.; Vetromile, C. M. *J. Am. Chem. Soc.* **2011**, *133*, 10356–10359.

(42) Barloy, L.; Battioni, P.; Mansuy, D. *J. Chem. Soc. Chem. Commun.* **1990**, 1365–1367.

(43) Nakagaki, S.; Halma, M.; Bail, A.; Arízaga, G. G. C.; Wypych, F. *J. Colloid Interface Sci.* **2005**, *281*, 417–423.

(44) Nakagaki, S.; Benedito, F. L.; Wypych, F. *J. Mol. Catal. A Chem.* **2004**, *217*, 121–131.

(45) Nakagaki, S.; Machado, G. S.; Halma, M.; dos Santos Marangon, A. A.; de Freitas Castro, K. A. D.; Mattoso, N.; Wypych, F. *J. Catal.* **2006**, *242*, 110–117.

(46) Zhou, W.-Y.; Tian, P.; Sun, F.; He, M.-Y.; Chen, Q. *J. Catal.* **2016**, *335*, 105–116.

(47) Itoh, T.; Yamada, T.; Kodera, Y.; Matsushima, A.; Hiroto, M.; Sakurai, K.; Nishimura, H.; Inada, Y. *Bioconjug. Chem.* **2001**, *12*, 3–6.

(48) Zhang, L.; Gu, C.; Xiong, J.; Yang, M.; Guo, Y. *Sci. China Chem.* **2015**, *58*, 731–737.

(49) Beck, J. S.; Vartuli, J. C.; Roth, W. . J.; Leonowicz, M. E.; Kresge, C. T.; Schmitt, K. D.; Chu, C. T.; Olson, D. H.; Sheppard, E. W.; McCullen, S. B.; Higgins, J. B.; Schlenkert, J. L. *J. Am. Chem. Soc.* **1992**, *114*, 10834–10843.

(50) Kresge, C. T.; Leonowicz, M. E.; Roth, W. J.; Vartuli, J. C.; Beck, J. S. *Nature* **1992**, *359*, 710–712.

(51) Holland, B. T.; Walkup, C.; Stein, A. *J. Phys. Chem. B* **1998**, *102*, 4301–4309.

(52) Nur, H.; Hamid, H.; Endud, S.; Hamdan, H.; Ramli, Z. *Mater. Chem. Phys.* **2006**, *96*, 337–342.

(53) Kalilur Rahiman, A.; Shanmuga Bharathi, K.; Sreedaran, S.; Rajesh, K.; Narayanan, V. *Inorganica Chim. Acta* **2009**, *362*, 1810–1818.

(54) Rahiman, A. K.; Rajesh, K.; Bharathi, K. S.; Sreedaran, S.; Narayanan, V. *Inorganica Chim. Acta* **2009**, *362*, 1491–1500.

(55) Costa, A. A.; Ghesti, G. F.; de Macedo, J. L.; Braga, V. S.; Santos, M. M.; Dias, J. A.; Dias, S. C. L. *J. Mol. Catal. A Chem.* **2008**, *282*, 149–157.

(56) Li, Z.; Xia, C.-G.; Zhang, X.-M. *J. Mol. Catal. A Chem.* **2002**, *185*, 47–56.

(57) Zhang, J.; Zhao, G.-F.; Popović, Z.; Lu, Y.; Liu, Y. *Mater. Res. Bull.* **2010**, *45*, 1648–1653.

(58) Zanatta, L. D.; Barbosa, I. A.; Zanardi, F. B.; de Sousa Filho, P. C.; Bolzon, L. B.; Ramos, A. P.; Serra, O. A.; Iamamoto, Y. *RSC Adv.* **2016**, *6*, 104886–104896.

(59) Zhao, D.; Sun, J.; Li, Q.; Stucky, G. D. *Chem. Mater.* **2000**, *12*, 275–279.

(60) Zhang, J.-L.; Liu, Y.-L.; Che, C.-M. *Chem. Commun.* **2002**, 2906–2907.

(61) Che, C.-M.; Huang, J.-S.; Lee, F.-W.; Li, Y.; Lai, T.-S.; Kwong, H.-L.; Teng, P.-F.; Lee, W.-S.; Lo, W.-C.; Peng, S.-M.; Zhou, Z.-Y. *J. Am. Chem. Soc.* **2001**, *123*, 4119–4129.

(62) Nazari, K.; Shokrollahzadeh, S.; Mahmoudi, A.; Mesbahi, B.; Seyed Matin, N.; Moosavi-Movahedi, A. A. *J. Mol. Catal. A Chem.* **2005**, *239*, 1–9.

(63) Weitkamp, J. *Solid State Ionics* **2000**, *131*, 175–188.

(64) Balkus, K. J.; Gabrielov, A. G.; Bell, S. L.; Bedioui, F.; Roue, L.; Devynck, J. *Inorg. Chem* **1994**, *33*, 67–72.

(65) Viana Rosa, I. L.; Manso, C. M. C. P.; Serra, O. A.; Iamamoto, Y. *J. Mol. Catal. A Chem.* **2000**, *160*, 199–208.

(66) Moghadam, M.; Tangestaninejad, S.; Mirkhani, V.; Mohammadpoor-Baltork, I.; Moosavifar, M. *J. Mol. Catal. A Chem.* **2009**, *302*, 68–75.

(67) Karimipour, G.; Rezaei, M.; Ashouri, D. *J. Mex. Chem. Soc.* **2013**, *57*, 276–282.

(68) Steed, J. W. *Chem. Commun.* **2011**, *47*, 1379–1383.

(69) Buerkle, L. E.; Rowan, S. J. *Chem. Soc. Rev.* **2012**, *41*, 6089.

(70) Iamamoto, Y.; Ciuffi, K. J.; Sacco, H. C.; Prado, C. M. C.; de Moraes, M.; Nascimento, O. R. *J. Mol. Catal.* **1994**, *88*, 167–176.

(71) Battioni, P.; Cardin, E.; Louloudi, M.; Schollhorn, B.; Spyroulias, G. a.; Mansuy, D.; Traylor, T. G. *Chem. Commun.* **1996**, 2037–2038.

(72) Iamamoto, Y.; Ciuffi, K. J.; Sacco, H. C.; Iwamoto, L. S.; Nascimento, O. R.; Prado, C. M. . *J. Mol. Catal. A Chem.* **1997**, *116*, 405–420.

(73) De Paula, R.; Santos, I. C. M. S.; Simões, M. M. Q.; Neves, M. G. P. M. S.; Cavaleiro, J. A. S. *J. Mol. Catal. A Chem.* **2015**, *404–405*, 156–166.

(74) Rahimi, R.; Ghoreishi, S. Z.; Dekamin, M. G. *Monatshefte für Chemie - Chem. Mon.* **2012**, *143*, 1031–1038.

(75) Gilmartin, C.; Lindsay Smith, J. R. *J. Chem. Soc. Perkin Trans. 2* **1995**, 243–251.

(76) Benedito, F. L.; Nakagaki, S.; Saczk, A. A.; Peralta-Zamora, P. G.; Costa, C. M. M. *Appl. Catal. A Gen.* **2003**, *250*, 1–11.

(77) Sharghi, H.; Beyzavi, M. H.; Doroodmand, M. M. *European J. Org. Chem.* **2008**, *2008*, 4126–4138.

(78) Chen, Z.; Hua, Z.; Wang, J.; Guan, Y.; Zhao, M.; Li, Y. *Appl. Catal. A Gen.* **2007**, *328*, 252–258.

(79) Wang, Q.; Yang, Z.; Ma, M.; Chang, C. K.; Xu, B. *Chem. - A Eur. J.* **2008**, *14*, 5073–

5078.

(80) Wang, Q.; Yang, Z.; Zhang, X.; Xiao, X.; Chang, C. K.; Xu, B. *Angew. Chemie Int. Ed.* **2007**, *46*, 4285–4289.

(81) Chen, Z.; Xu, L.; Liang, Y.; Zhao, M. *Adv. Mater.* **2009**, *22*, 1488–1492.

(82) Wang, Z.; Chen, G.; Ding, K. *Chem. Rev.* **2009**, *109*, 322–359.

(83) Perry IV, J. J.; Perman, J. A.; Zaworotko, M. J. *Chem. Soc. Rev.* **2009**, *38*, 1400–1417.

(84) Zhang, Q.; Zhang, J.; Yu, Q.-Y.; Pan, M.; Su, C.-Y. *Cryst. Growth Des.* **2010**, *10*, 4076–4084.

(85) Qiu, S.; Zhu, G. *Coord. Chem. Rev.* **2009**, *253*, 2891–2911.

(86) Janiak, C.; Vieth, J. K. *New J. Chem.* **2010**, *34*, 2366–2388.

(87) Zhou, H.-C.; Long, J. R.; Yaghi, O. M. *Chem. Rev.* **2012**, *112*, 673–674.

(88) Zhou, H.-C.; Kitagawa, S. *Chem. Soc. Rev.* **2014**, *43*, 5415–5418.

(89) Chen, Y.; Ma, S. *Dalt. Trans.* **2016**, *45*, 9744–9753.

(90) Rowsell, J. L. C.; Yaghi, O. M. *Microporous Mesoporous Mater.* **2004**, *73*, 3–14.

(91) García-García, P.; Müller, M.; Corma, A. *Chem. Sci.* **2014**, *5*, 2979–3007.

(92) Corma, A.; García, H.; Llabrés i Xamena, F. X. *Chem. Rev.* **2010**, *110*, 4606–4655.

(93) Furukawa, H.; Cordova, K. E.; O'Keeffe, M.; Yaghi, O. M. *Science.* **2013**, *341*.

(94) Bélanger, S.; Hupp, J. T. *Angew. Chemie Int. Ed.* **1999**, *38*, 2222–2224.

(95) Alkordi, M. H.; Liu, Y.; Larsen, R. W.; Eubank, J. F.; Eddaoudi, M. *J. Am. Chem. Soc.* **2008**, *130*, 12639–12641.

(96) Larsen, R. W.; Miksovska, J.; Musselman, R. L.; Wojtas, L. *J. Phys. Chem. A* **2011**, *115*, 11519–11524.

(97) Zhang, Z.; Zhang, L.; Wojtas, L.; Eddaoudi, M.; Zaworotko, M. J. *J. Am. Chem. Soc.* **2012**, *134*, 928–933.

(98) Zhang, Z.; Zhang, L.; Wojtas, L.; Nugent, P.; Eddaoudi, M.; Zaworotko, M. J. *J. Am. Chem. Soc.* **2012**, *134*, 924–927.

(99) Zhang, Z.; Wojtas, L.; Zaworotko, M. J. *Cryst. Growth Des.* **2014**, *14*, 1526–1530.

(100) Li, C.; Qiu, W.; Long, W.; Deng, F.; Bai, G.; Zhang, G.; Zi, X.; He, H. *J. Mol. Catal. A Chem.* **2014**, *393*, 166–170.

(101) Ling, P.; Lei, J.; Zhang, L.; Ju, H. *Anal. Chem.* **2015**, *87*, 3957–3963.

(102) Mayer, G. *Angew. Chemie Int. Ed.* **2009**, *48*, 2672–2689.

(103) Qin, F.-X.; Jia, S.-Y.; Wang, F.-F.; Wu, S.-H.; Song, J.; Liu, Y. *Catal. Sci. Technol.* **2013**, *3*, 2761–2768.

(104) Stavitski, E.; Goesten, M.; Juan-Alcañiz, J.; Martinez-Joaristi, A.; Serra-Crespo, P.; Petukhov, A. V.; Gascon, J.; Kapteijn, F. *Angew. Chemie Int. Ed.* **2011**, *50*, 9624–9628.

(105) Josephy, P. D.; Eling, T.; Mason1 Ronald P. *J. Biol. Chem.* **1982**, *257*, 3669–3675.

(106) Marquez, L. A.; Dunford, B. H. *Biochemistry* **1997**, *36*, 9349–9355.

(107) Luo, F.; Lin, Y.; Zheng, L.; Lin, X.; Chi, Y. *ACS Appl. Mater. Interfaces* **2015**, *7*, 11322–11329.

(108) Motsenbocker, M. A. *J. Biolumin. Chemilumin.* **1988**, *2*, 9–16.

(109) Easton, P. M.; Simmonds, A. C.; Rakishev, A.; Egorov, A. M.; Candeias, L. P. *J. Am. Chem. Soc.* **1996**, *118*, 6619–6624.

(110) Zhu, Q.; Chen, Y.; Wang, W.; Zhang, H.; Ren, C.; Chen, H.; Chen, X. *Sensors Actuators B Chem.* **2015**, *210*, 500–507.

(111) Cheng, H.; Zhang, L.; He, J.; Guo, W.; Zhou, Z.; Zhang, X.; Nie, S.; Wei, H. *Anal. Chem.* **2016**, *88*, 5489–5497.

(112) Xie, S.; Ye, J.; Yuan, Y.; Chai, Y.; Yuan, R. *Nanoscale* **2015**, *7*, 18232–18238.

(113) Wang, L.; Yang, H.; He, J.; Zhang, Y.; Yu, J.; song, Y. *Electrochim. Acta* **2016**, *213*, 691–697.

(114) Yuan, G.; Wang, L.; Mao, D.; Wang, F.; Zhang, J. *Microchim. Acta* **2017**, *184*, 3121–3130.

(115) Chen, J.; Yu, C.; Zhao, Y.; Niu, Y.; Zhang, L.; Yu, Y.; Wu, J.; He, J. *Biosens. Bioelectron.* **2017**, *91*, 892–899.

(116) de Villiers, K. A.; Kaschula, C. H.; Egan, T. J.; Marques, H. M. *J. Biol. Inorg. Chem.* **2007**, *12*, 101–117.

(117) *GraphPad Prism v6.05*; GraphPad Software: San Diego, CA, 2014.

(118) TA Instruments. *Universal Analysis 2000 (Version 4.5A)*; 2007.

(119) Pawley, G. S. *J. Appl. Crystallogr.* **1981**, *14*, 357–361.

(120) Bruker AXS. *DiffracPlus Topas (Version 4.)2*; 2009.

(121) Bruker AXS Inc. *SAINT (Version 7.60a)*; Madison, WI, USA, 2006.

(122) Sheldrick, G. M. *SADABS (Version 2.05)*; 2007.

(123) Bruker Analytical X-ray Systems. *XPREP, Data Preparation and Reciprocal Space Exploration (Version 5.1)*; 1997.

(124) Wilson, K. S.; Dodson, E. J.; Di Marco, S.; Priestle, J. P.; Grüttler, M. G.; Mittl, P. R. E.; De La Rose, M. A.; Sheldrick, G. M. *Acta Crystallogr. Sect. A Found. Crystallogr.* **2008**, *64*, 112–122.

(125) Dolomanov, O. V.; Bourhis, L. J.; Gildea, R. J.; Howard, J. A. K.; Puschmann, H. *J. Appl. Crystallogr.* **2009**, *42*, 339–341.

(126) Gu, Z.-Y.; Park, J.; Raiff, A.; Wei, Z.; Zhou, H.-C. *ChemCatChem* **2014**, *6*, 67–75.

(127) Lee, J.; Farha, O. K.; Roberts, J.; Scheidt, K. A.; Nguyen, S. T.; Hupp, J. T.; Margiolaki, I.; Buntkowsky, G.; Limbach, H.-H.; Chaudret, B.; Fischer, R. A. *Chem. Soc. Rev.* **2009**, *38*, 1450–1459.

(128) Chen, Y.; Hoang, T.; Ma, S. *Inorg. Chem.* **2012**, *51*, 12600–12602.

(129) Feng, D.; Gu, Z.-Y.; Li, J.-R.; Jiang, H.-L.; Wei, Z.; Zhou, H.-C. *Angew. Chemie* **2012**, *124*, 10453–10456.

(130) Meng, L.; Cheng, Q.; Kim, C.; Gao, W.-Y.; Wojtas, L.; Chen, Y.-S.; Zaworotko, M. J.; Zhang, X. P.; Ma, S. *Angew. Chemie Int. Ed.* **2012**, *51*, 10082–10085.

(131) Smithenry, D. W.; Wilson, S. R.; Suslick, K. S. *Inorg. Chem.* **2003**, *42*, 7719–7721.

(132) Zhang, Z.; Wojtas, L.; Zaworotko, M. J. *Cryst. Growth Des.* **2014**, *14*, 1526–1530.

(133) He, J.; Yang, H.; Zhang, Y.; Yu, J.; Miao, L.; Song, Y.; Wang, L. *Sci. Rep.* **2016**, *6*, 36637.

(134) Zhou, X.; Guo, S.; Gao, J.; Zhao, J.; Xue, S.; Xu, W. *Biosens. Bioelectron.* **2017**, *98*, 83–90.

(135) Tan, H.; Li, Q.; Zhou, Z.; Ma, C.; Song, Y.; Xu, L.; Wang, L. *Anal. Chim. Acta* **2015**, *856*, 90–95.

(136) Sun, D.; Ke, Y.; Collins, D. J.; Lorigan, G. A.; Zhou, H.-C. *Inorg. Chem.* **2007**, *46*, 2725–2734.

(137) García, E.; Medina, R.; Lozano, M.; Hernández Pérez, I.; Valero, M.; Franco, A. *Materials (Basel).* **2014**, *7*, 8037–8057.

(138) Nowell, H.; Barnett, S. A.; Christensen, K. E.; Teat, S. J.; Allan, D. R. *J. Synchrotron Radiat.* **2012**, *19*, 435–441.

(139) Oxford Diffraction. *CrysAlis Pro*; Rigaku Corporation: Oxford, UK, 2017.

(140) Yang, S.; Sun, J.; Ramirez-Cuesta, A. J.; Callear, S. K.; David, W. I. F.; Anderson, D. P.; Newby, R.; Blake, A. J.; Parker, J. E.; Tang, C. C.; Schröder, M. *Nat. Chem.* **2012**, *4*, 887–894.

(141) Feldblyum, J. I.; Liu, M.; Gidley, D. W.; Matzger, A. J. *J. Am. Chem. Soc.* **2011**, *133*, 18257–18263.

(142) Macrae, C. F.; Edgington, P. R.; McCabe, P.; Pidcock, E.; Shields, G. P.; Taylor, R.; Towler, M.; Van De Streek, J. *J. Appl. Crystallogr.* **2006**, *39*, 453–457.

(143) Macrae, C. F.; Bruno, I. J.; Chisholm, J. A.; Edgington, P. R.; McCabe, P.; Pidcock, E.; Rodriguez-Monge, L.; Taylor, R.; van de Streek, J.; Wood, P. A. *J. Appl. Crystallogr.* **2008**, *41*, 466–470.

(144) Song, X.; Jeong, S.; Kim, D.; Lah, M. S. *CrystEngComm* **2012**, *14*, 5753–5756.

(145) Inokuma, Y.; Yoshioka, S.; Ariyoshi, J.; Arai, T.; Hitora, Y.; Takada, K.; Matsunaga, S.; Rissanen, K.; Fujita, M. *Nature* **2013**, *495*, 461–466.

(146) Asher, C.; de Villiers, K. A.; Egan, T. J. *Inorg. Chem.* **2009**, *48*, 7994–8003.

(147) Kuter, D.; Venter, G. A.; Naidoo, K. J.; Egan, T. J. *Inorg. Chem.* **2012**, *51*, 10233–10250.

(148) Jessiman, A. S.; MacNicol, D. D.; Mallinson, P. R.; Vallance, I. *J. Chem. Soc. Chem. Commun.* **1990**, *18*, 1619–1621.

(149) Lee, S.; Kapustin, E. A.; Yaghi, O. M. *Science.* **2016**, *353*, 808–811.

(150) Serra, A. C.; Docal, C.; Rocha Gonsalves, A. M. d'A. *J. Mol. Catal. A Chem.* **2005**, *238*, 192–198.

(151) Childs, R. E.; Bardsley, W. G. *Biochem. J.* **1975**, *145*, 93–103.

(152) Bruice, T. C.; Zipplies, M. F.; Lee, W. A. *Proc. Natl. Acad. Sci. U. S. A.* **1986**, *83*, 4646–4649.

(153) Ortiz de Montellano, P. R.; De Voss, J. J. In *Cytochrome P450*; Springer US: Boston, MA, 2005; pp 183–245.

(154) Zhang, Z.; Zhang, L.; Wojtas, L.; Eddaoudi, M.; Zaworotko, M. J. *J. Am. Chem. Soc.* **2012**, *134*, 928–933.

(155) Zhang, Z.; Wojtas, L.; Eddaoudi, M.; Zaworotko, M. J. *J. Am. Chem. Soc.* **2013**, *135*, 5982–5985.

(156) Chen, Y.; Wojtas, L.; Ma, S.; Zaworotko, M. J.; Zhang, Z. *Chem. Commun.* **2017**, *53*, 8866–8869.

(157) Larsen, R. W.; Miksovska, J.; Musselman, R. L.; Wojtas, L. *J. Phys. Chem. A* **2011**, *115*, 11519–11524.

(158) Larsen, R. W.; Wojtas, L.; Sagun, E.; Shugla, A.; Bachilo, S.; Vetromile, C. M.; Yaghi, O. M.; Ess, D. H.; McCafferty, D. G.; Meyer, T. J. *Dalt. Trans.* **2015**, *44*, 2959–2963.

(159) Chen, Y.; Wojtas, L.; Ma, S.; Zaworotko, M. J.; Zhang, Z. *Chem. Commun.* **2017**, *53*, 8866–8869.

(160) Chui, S. S.-Y.; Lo, S. M.-F.; Charmant, J. P. H.; Orpen, A. G.; Williams, I. D. *Science* **1999**, *283*, 1148–1150.

(161) Groom, C. R.; Bruno, I. J.; Lightfoot, M. P.; Ward, S. C. *Acta Crystallogr. Sect. B Struct. Sci. Cryst. Eng. Mater.* **2016**, *72*, 171–179.

(162) Zhang, Z.; Zhang, L.; Wojtas, L.; Nugent, P.; Eddaoudi, M.; Zaworotko, M. J. *J. Am. Chem. Soc.* **2012**, *134*, 924–927.

(163) Hoffman, A. B.; Collins, D. M.; Day, V. W.; Fleischer, E. B.; Srivastava, T. S.; Hoard, J. L. *J. Am. Chem. Soc.* **1972**, *94*, 3620–3626.

(164) Jones, P.; Mantle, D.; Wilson, I. *J. Chem. Soc. Dalt. Trans.* **1983**, 161–164.

(165) Panicucci, R.; Bruice, T. C. *J . Am. Chem. Soc* **1990**, *112*, 6063–6607.

(166) Li, D.; Wu, S.; Wang, F.; Jia, S.; Yong, L.; Han, X.; Zhang, L.; Zhang, S.; Wu, Y. *Mater. Lett.* **2016**, *178*, 48–51.

(167) Davies, M. J.; Hawkins, C. L.; Pattison, D. I.; Rees, M. D. *Antioxid. Redox Signal.* **2008**, *10*, 1199–1234.

(168) Banci, L. *J. Biotechnol.* **1997**, *53*, 253–263.

(169) Battistuzzi, G.; Bellei, M.; Bortolotti, C. A.; Sola, M. *Arch. Biochem. Biophys.* **2010**, *500*, 21–36.

(170) Groves, J. T. *J. Inorg. Biochem.* **2006**, *100*, 434–447.

(171) Labrinea, E. P.; Georgiou, C. A. *Anal. Chim. Acta* **2004**, *526*, 63–68.

(172) Cano, A.; Hernández-Ruíz, J.; García-Cánovas, F.; Acosta, M.; Arnao, M. B. *Phytochem. Anal.* **1998**, *9*, 196–202.

(173) McCoy-Messer, J. M.; Bateman, R. C. *Biotechniques* **1993**, *15*, 270–273.

(174) Leofantia, G.; Padovanb, M.; Tozzolac, G.; Venturellic, B. *Catal. Today* **1998**, *41*, 207–219.

(175) Boudart, M.; Djega-Mariadassou, G. *Kinetics of Heterogeneous Catalytic Reactions*; Princeton University Press, 1984.

(176) Mansuy, D. *Comptes Rendus Chim.* **2007**, *10*, 392–413.

(177) Bernard Meunier; Samuël P. de Visser; Sason Shaik. *Chem. Rev.* **2004**, *104*, 3974–3980.

(178) Anastas, P. T.; Kirchhoff, M. M. *Acc. Chem. Res.* **2002**, *35*, 686–694.

(179) Koubek, E.; Haggett, M. L.; Battaglia, C. J.; Ibne-Rasa, K. M.; Pyun, H. Y.; Edwards,

J. O. *J. Am. Chem. Soc.* **1963**, *85*, 2263–2268.

(180) Traylor, T. G.; Xu, F. *J. Am. Chem. Soc.* **1990**, *112*, 178–186.

(181) Traylor, T. G.; Ciccone, J. P. *J. Am. Chem. Soc.* **1989**, *111*, 8413–8420.

(182) ChemAxon. *Chemicalize*; 2017.

(183) Giedyk, M.; Goliszewska, K.; Gryko, D. *Chem. Soc. Rev.* **2015**, *44*, 3391–3404.

Appendix A: Further crystallographic details

A.1 Thermal Gravimetric Analysis of synthesized materials

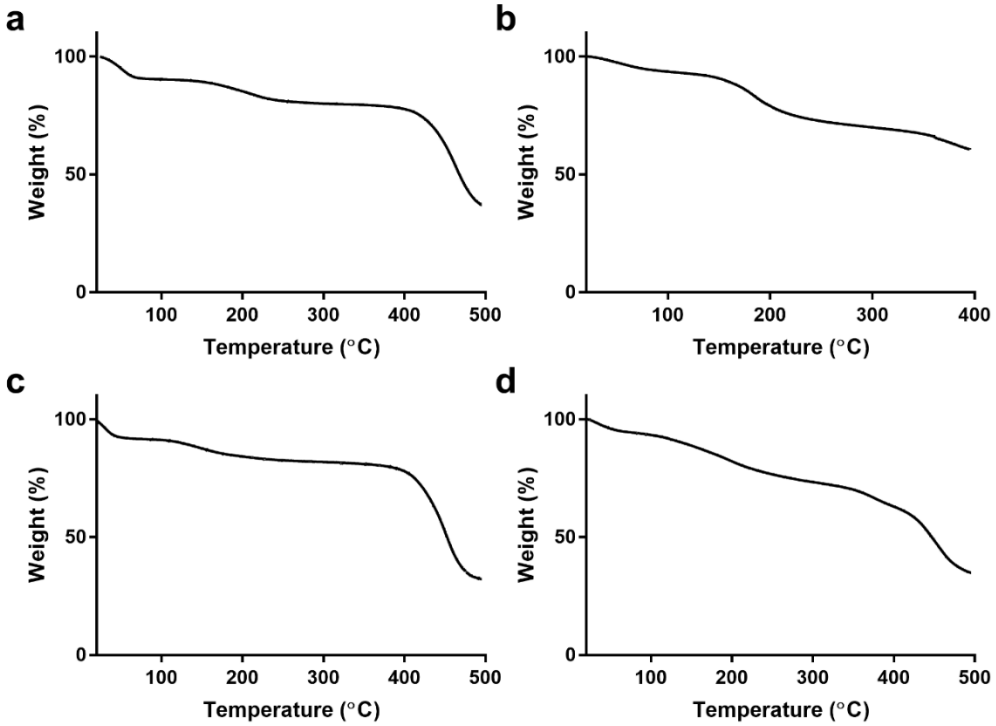

***Figure A1**: TGA of (a) **1**, (b) **2**, (c) Fe(III)PPIX-**1** and (d) Fe(III)PPIX-**2**.*

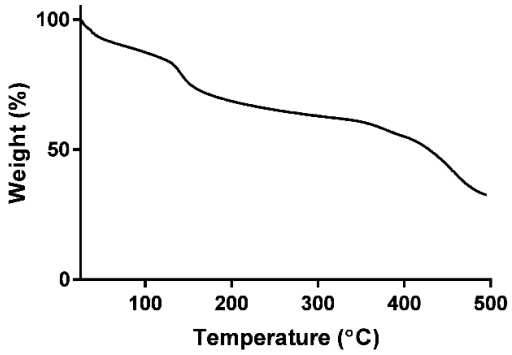

Figure A2:** TGA of Fe(III)TPP-**2

A.2 Crystallographic tables for all crystal structures

Table A1: Crystallographic data for the single crystal X-ray structure of **1**.

	1
Chemical Formula	$Zn_3C_{56}N_9O_{21}H_{59}$
Molar mass (g mol^{-1})	1390.23
Crystal System	Tetragonal
Space Group	$P4_322$
a (Å)	17.9300(9)
c (Å)	26.0524(13)
V (Å^3)	8375.5(9)
Z	4
$\rho_{calcd.}$ (g cm^{-3})	0.886
μ (mm^{-1})	0.895
λ (Å)	0.71073
F(000)	2248
Temperature (K)	173(2)
Crystal size (mm)	0.38 × 0.14 × 0.13
Range scanned θ (°)	1.379 – 28.429
Total number of reflections	153876
Number of independent reflections	10487
Number of reflections with $I > 2\sigma(I)$	8899
R_{int}	0.0604
$R_1(F)$ [a] $[I > 2\sigma(I)]$	0.0552
$wR_2(F^2)$ [a]	0.1968
$S(F^2)$ [a]	1.162
Number of parameters (p)	323
Number of restraints (r)	2
Number of reflections omitted	2
$(\delta/\sigma)_{mean}$	<0.001
Max./min $\Delta\rho$ excursions (e Å^{-3})	-0.602; 1.909

[a] $R1(F) = \Sigma(|F_o| - |F_c|)/\Sigma|F_o|$; $wR_2(F^2) = [\Sigma w(F_o^2 - F_c^2)^2/\Sigma wF_o^4]^{½}$; $S(F^2) = [\Sigma w(F_o^2 - F_c^2)^2/(n + r - p)]^{½}$

Table A2: Crystallographic data for the single crystal X-ray structure of Fe(III)PPIX-**1**.

	Fe(III)PPIX-**1**
Chemical Formula	$Zn_3H_{30}C_{54.12}N_{6.72}O_{13.72}Fe_{0.18}$
Molar mass (g mol^{-1})	1119.81
Crystal System	Tetragonal
Space Group	$P4_1$
a (Å)	18.0063(4)
c (Å)	26.5714(10)
V (Å^3)	8615.2(4)
Z	4
$\rho_{calcd.}$ (g cm^{-3})	0.852
μ (mm^{-1})	0.831
λ (Å)	0.6889(3)
F(000)	2221
Temperature (K)	100(2)
Crystal size (mm)	0.64 × 0.52 × 0.512
Range scanned θ (°)	1.719 – 24.919
Total number of reflections	50940
Number of independent reflections	50940
Number of reflections with $I > 2\sigma(I)$	38880
R_{int}	0.1286
$R_1(F)$ [a] $[I > 2\sigma(I)]$	0.1495
$wR_2(F^2)$ [a]	0.3255
$S(F^2)$ [a]	1.187
Number of parameters (p)	653
Number of restraints (r)	10
Number of reflections omitted	55
$(\delta/\sigma)_{mean}$	<0.001
Max./min $\Delta\rho$ excursions (e Å^{-3})	-0.807; 1.935

[a] $R1(F) = \Sigma(|F_o| - |F_c|)/\Sigma|F_o|$; $wR_2(F^2) = [\Sigma w(F_o^2 - F_c^2)^2/\Sigma wF_o^4]^{½}$; $S(F^2) = [\Sigma w(F_o^2 - F_c^2)^2/(n + r - p)]^{½}$

Table A3: Crystallographic data for the single crystal X-ray structure of Fe(III)TPP-**2**.

	Fe(III)TPP-**2**
Chemical Formula	$ZnO_5H_2C_6 \cdot 0.067[FeN_4C_{44}H_{28}]$
Molar mass (g mol^{-1})	264.6
Crystal System	Cubic
Space Group	*F*m-3m
a (Å)	26.4566(15)
b (Å)	
c (Å)	
V (Å^3)	18708(3)
Z	48
$\rho_{calcd.}$ (g cm^{-3})	1.041
μ (mm^{-1})	1.589
λ (Å)	0.71073
F(000)	5777
Temperature (K)	173(2)
Crystal size (mm)	0.18 × 0.14 × 0.14
Range scanned θ (°)	1.379 – 28.429
Total number of reflections	37033
Number of independent reflections	1014
Number of reflections with $I > 2\sigma(I)$	842
R_{int}	0.0561
$R_1(F)$ [a] [$I > 2\sigma(I)$]	0.0965
$wR_2(F^2)$ [a]	0.3237
$S(F^2)$ [a]	1.656
Number of parameters (*p*)	59
Number of restraints (*r*)	16
Number of reflections omitted	3
$(\delta/\sigma)_{mean}$	<0.001
Max./min Δρ excursions (e Å^{-3})	-0.620; 2.359

[a] $R_1(F) = \Sigma(|F_o| - |F_c|)/\Sigma|F_o|$; $wR_2(F^2) = [\Sigma w(F_o^2 - F_c^2)^2/\Sigma wF_o^4]^{½}$; $S(F^2) = [\Sigma w(F_o^2 - F_c^2)^2/(n + r - p)]^{½}$

Table A4: Crystallographic data for the single crystal X-ray structure of $(Fe(III)TPP)_2O$.

	$(Fe(III)TPP)_2O$
Chemical Formula	$Fe_2C_{88}N_8H_{56}O$
Molar mass (g mol^{-1})	1353.10
Crystal System	Orthorhombic
Space Group	*Aea*2
a (Å)	17.8575(9)
b (Å)	24.9479(13)
c (Å)	15.1042(8)
V (Å^3)	6729.0(6)
Z	4
$\rho_{calcd.}$ (g cm^{-3})	1.336
μ (mm^{-1})	0.488
λ (Å)	0.71073
F(000)	2800
Temperature (K)	173(2)
Crystal size (mm)	0.33 × 0.18 × 0.17
Range scanned θ (°)	5.546 – 70.39
Total number of reflections	58503
Number of independent reflections	18193
Number of reflections with $I > 2\sigma(I)$	14011
R_{int}	0.0547
$R_1(F)$ [a] $[I > 2\sigma(I)]$	0.0452
$wR_2(F^2)$ [a]	0.0976
$S(F^2)$ [a]	1.008
Number of parameters (*p*)	448
Number of restraints (*r*)	1
Number of reflections omitted	0
$(\delta/\sigma)_{mean}$	<0.001
Max./min Δρ excursions (e Å^{-3})	-0.440; 0.473

[a] $R_1(F) = \Sigma(|F_o| - |F_c|)/\Sigma|F_o|$; $wR_2(F^2) = [\Sigma w(F_o^2 - F_c^2)^2/\Sigma wF_o^4]^{½}$; $S(F^2) = [\Sigma w(F_o^2 - F_c^2)^2/(n + r - p)]^{½}$

Appendix B: Full derivation of rate laws

B.1 Derivation of theoretical rate law (Scheme 5.1)

The theoretical rate law can be derived using the following equations describing each step of the simplified catalytic cycle in Scheme 5.1;

$$\frac{d[FeOOH]}{dt} = k_1[Fe(III)H_2O][H_2O_2] - k_{-1}[FeOOH] - k_2[FeOOH] = 0 \quad (\boldsymbol{B1})$$

$$\frac{d[Fe(IV) = O(porph^{\bullet+})]}{dt} = k_2[FeOOH] - k_3[Fe(IV) = O(porph^{\bullet+})][ABTS]^2 \quad (\boldsymbol{B2})$$

$$= 0$$

$$\frac{d[ABTS^{\bullet+}]}{dt} = k_3[Fe(IV) = O(porph^{\bullet+})][ABTS]^2 \quad (\boldsymbol{B3})$$

Steady state approximations were made for equations B**1** and B**2** since after an initial stage of formation of the intermediates, they will likely react as fast as they are formed. Therefore, the change in concentration of the intermediate is negligible. Using the steady state approximations the following expressions for [FeOOH] and [Fe(IV)=O(porph)] can be obtained.

$$[FeOOH] = \frac{k_1[Fe(III)H_2O][H_2O_2]}{k_{-1} + k_2} \quad (\boldsymbol{B4})$$

$$[Fe(IV) = O(porph^{\bullet+})] = \frac{k_2k_1[Fe(III)H_2O][H_2O_2]}{k_3k_{-1}[ABTS]^2 + k_3k_2[ABTS]^2} \quad (\boldsymbol{B5})$$

From these expressions, a theoretical rate law for the observed change in [$ABTS^{\bullet+}$] can be obtained.

$$\frac{d[ABTS^{\bullet+}]}{dt} = \frac{k_2 k_1 [Fe(III)H_2O][H_2O_2]}{k_{-1} + k_2} \qquad (\boldsymbol{B6})$$

This can be simplified to the following expression;

$$\frac{d[ABTS^{\bullet+}]}{dt} = k_{obs}[Fe(III)H_2O][H_2O_2] \qquad (\boldsymbol{B7})$$

where k_{obs} is the experimentally observed rate constant. According to the theoretical rate law, the rate of the reaction should be dependent on both the concentration of catalyst (Fe(III)PPIX-**1**) and H_2O_2.

B.2 Derivation of full theoretical rate law (Scheme 5.4)

The reaction between Fe(III)PPIX-**1** and H_2O_2 and subsequent oxidation of ABTS to $ABTS^{\bullet+}$ including the secondary pathway where ABTS can coordinate as an axial ligand to the Fe centre is described in Scheme 5.4.

A theoretical rate law was derived using the following equations which describe each intermediate in the reaction:

$$\frac{d[ABTS^{\bullet+}]}{dt} = k_3[Fe(IV)=O(porph^{\bullet+})][ABTS]^2 + k_7[ABTS\cdots Fe(IV)=O(porph^{\bullet+})][ABTS] \quad (\boldsymbol{B8})$$

$$\frac{d[Fe(IV)=O(porph^{\bullet+})]}{dt} = k_2[FeOOH] - k_3[Fe(IV)=O(porph^{\bullet+})][ABTS]^2 = 0 \quad (\boldsymbol{B9})$$

$$\frac{d[FeOOH]}{dt} = k_1[Fe(III)H_2O][H_2O_2] - k_{-1}[FeOOH] - k_2[FeOOH] = 0 \quad (\boldsymbol{B10})$$

$$\frac{d[ABTS\cdots Fe(IV)=O(porph^{\bullet+})]}{dt} = k_6[ABTS\cdots Fe(III)OOH] - k_7[ABTS\cdots Fe(IV)=O(porph^{\bullet+})][ABTS] = 0 \quad (\boldsymbol{B11})$$

$$\frac{d[ABTS\cdots FeOOH]}{dt} = k_5[ABTS\cdots Fe(III)H_2O][H_2O_2] - k_{-5}[ABTS\cdots Fe(III)OOH] - k_6[ABTS\cdots Fe(III)OOH] = 0 \quad (\boldsymbol{B12})$$

$$\frac{d[ABTS \cdots Fe(III)H_2O]}{dt} = k_4[Fe(III)H_2O][ABTS] - k_{-4}[ABTS \cdots Fe(III)H_2O] - k_5[ABTS \cdots Fe(III)H_2O][H_2O_2] + k_{-5}[ABTS \cdots Fe(III)OOH] = 0 \quad (\boldsymbol{B13})$$

Using steady state approximations for each intermediate the following expressions can be derived to describe the concentration of each species:

$$[FeOOH] = \frac{k_1[Fe(III)H_2O][H_2O_2]}{k_{-1} + k_2} \quad (\boldsymbol{B14})$$

$$[Fe(IV) = O(porph^{\bullet+})] = \frac{k_2 k_1[Fe(III)H_2O][H_2O_2]}{k_3 k_{-1}[ABTS]^2 + k_3 k_2[ABTS]^2} \quad (\boldsymbol{B15})$$

$$[ABTS \cdots Fe(III)H_2O] = \frac{k_4[Fe(III)H_2O][ABTS] + k_{-5}[ABTS \cdots FeOOH]}{k_{-4} + k_5[H_2O_2]} \quad (\boldsymbol{B16})$$

$$[ABTS \cdots FeOOH] = \frac{k_4 k_5[Fe(III)H_2O][H_2O_2][ABTS]}{(k_{-4} + k_5[H_2O_2])(k_{-5} + k_6) - k_5 k_{-5}[H_2O_2]} \quad (\boldsymbol{B17})$$

$$[ABTS \cdots Fe(IV) = O(porph^{\bullet+})] = \frac{k_4 k_5 k_6[Fe(III)H_2O][H_2O_2]}{k_7(k_{-4} + k_5[H_2O_2])(k_{-5} + k_6) - k_5 k_{-5} k_7[H_2O_2]} \quad (\boldsymbol{B18})$$

Using these expressions, a theoretical rate law for the observed rate of formation of [ABTS$^{\bullet+}$] was obtained.

$$\frac{d[ABTS^{\bullet+}]}{dt} = \frac{k_1 k_2[Fe(III)H_2O][H_2O_2]}{k_{-1} + k_2} + \frac{k_4 k_5 k_6[Fe(III)H_2O][H_2O_2][ABTS]}{(k_{-4} + k_5[H_2O_2])(k_{-5} + k_6) - k_5 k_{-5}[H_2O_2]} \quad (\boldsymbol{B19})$$

By making the assumption that $k_5[H_2O_2] \gg k_{-4}$ this expression can be simplified to the following:

$$\frac{d[ABTS^{\bullet+}]}{dt} = \frac{k_1 k_2 [Fe(III)H_2O][H_2O_2]}{k_{-1} + k_2} + k_4[Fe(III)H_2O][ABTS] \qquad (\boldsymbol{B20})$$

This assumption is supported by the experimentally observed data which conforms to this equation. The simplified rate law can be represented as;

$$\frac{d[ABTS^{\bullet+}]}{dt} = k^1_{obs}[Fe(III)H_2O][H_2O_2] + k^2_{obs}[Fe(III)H_2O][ABTS] \qquad (\boldsymbol{B21})$$

where;

$$k^1_{obs} = \frac{k_1 k_2}{k_{-1} + k_2} \; and \; k^2_{obs} = k_4$$

Appendix C: Characterisation of oxidation substrates and products by NMR spectroscopy

C.1 Characterization of starting materials: ^{1}H NMR spectra

All starting materials (HQ, BN, PH and TH) were analysed by ^{1}H NMR spectroscopy (Fig C.1- C.4) in acetonitrile-d_3. Signals that underwent significant changes during the oxidation process were identified and were later used to monitor the progress of the reaction. These signals are highlighted in green in all the figures.

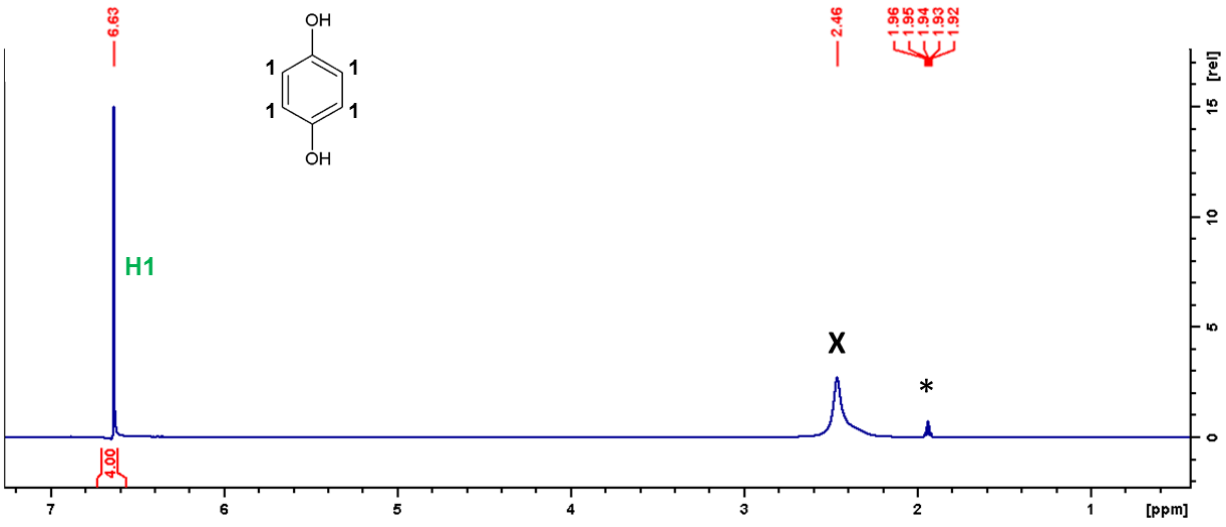

***Figure C.1**: ^{1}H NMR spectrum of hydroquinone in acetonitrile-d_3. Peaks denoted with an asterisk (*) and (**X**) indicate the presence of residual MeCN and water respectively. Signal labelled signal in green (δ 6.63, ArCH) was used to monitor the reaction and calculate % conversion.*

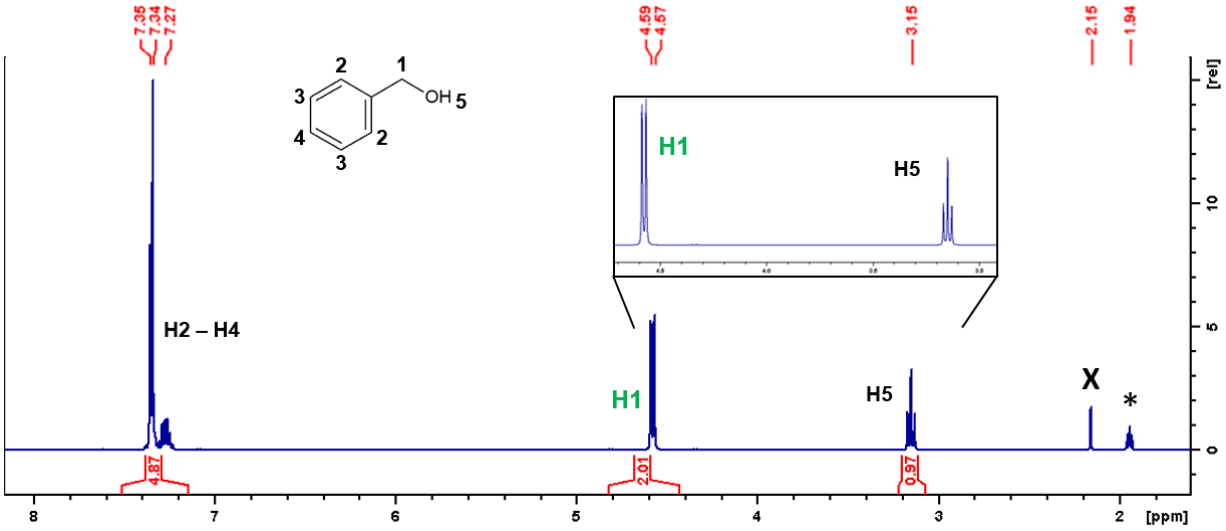

***Figure C.2**: [1]H NMR spectrum of benzyl alcohol in acetonitrile-d_3. Peaks denoted with an asterisk (*) and (**X**) indicate residual MeCN and water respectively. Signal labelled in green (δ 4.57, -CH_2) was used to monitor the reaction and calculate % conversion.*

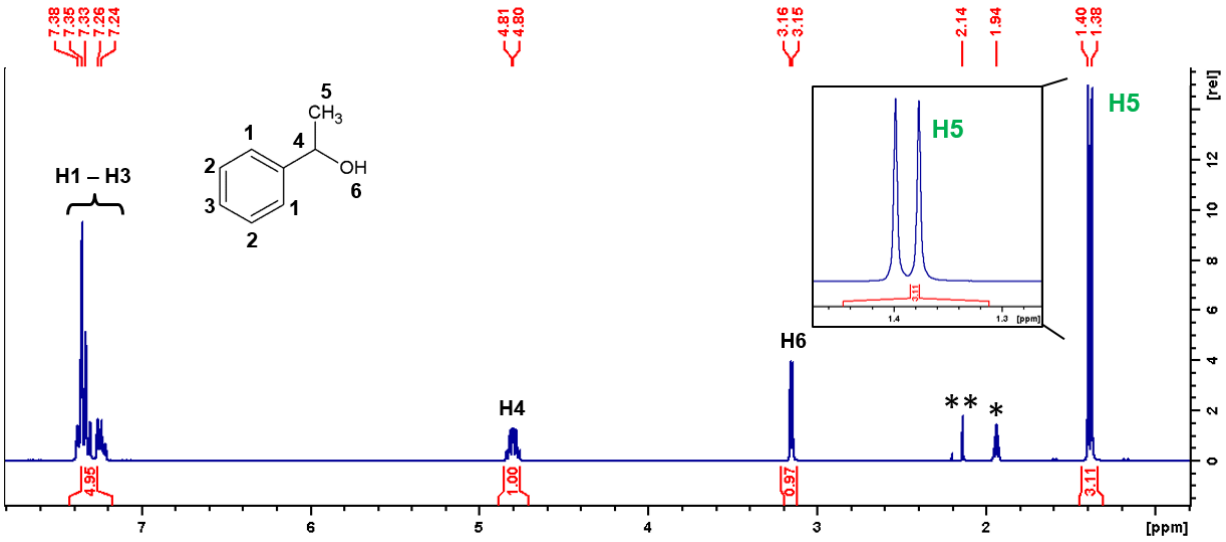

***Figure C.3**: [1]H NMR spectrum of phenyl ethanol in acetonitrile-d_3. Peaks denoted with asterisks (* and **) indicate residual MeCN and acetone respectively. Signal labelled in green (δ 1.38, -CH_3) was used to monitor the reaction and calculate % conversion.*

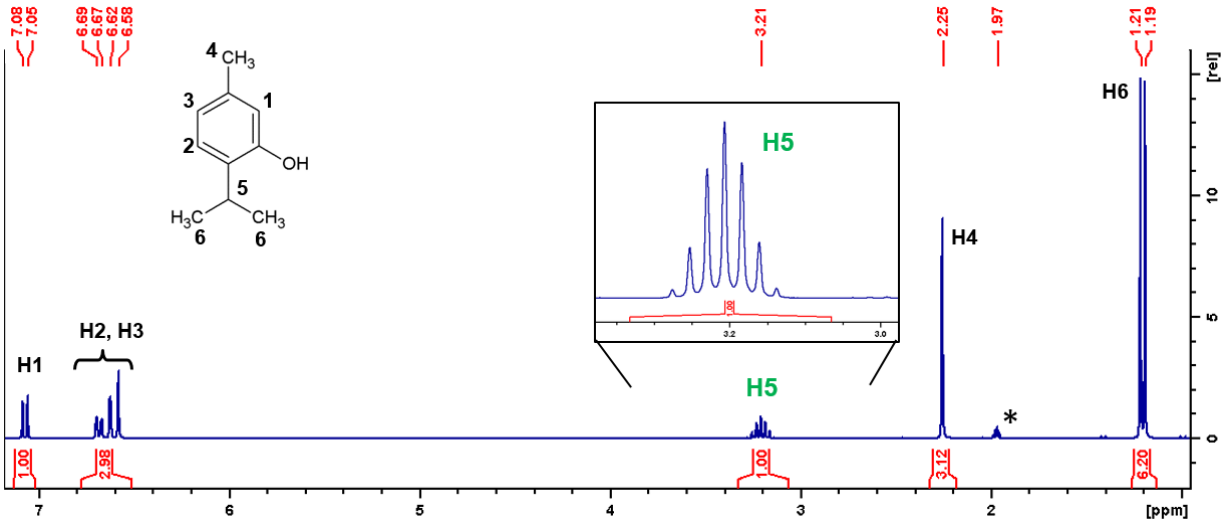

***Figure C.4**: [1]H NMR spectrum of thymol in acetonitrile-d_3. Asterisk (*) indicates residual MeCN. Signal labelled signal in green (δ 3.21, -CH [isopropyl]) was used to monitor the reaction and calculate % conversion.*

C.2 Characterization of products: ^{1}H NMR and ^{13}C NMR spectra

The products of all oxidations (HQ, BN, PH and TH) were analysed by ^{1}H NMR spectroscopy and, where necessary, ^{13}C NMR spectroscopy in acetonitrile-d_3 (Fig C.5- C.10). Signals that underwent significant changes during the oxidation process were identified and were used to monitor the progress of the reaction. These signals are highlighted in green in all figures. Spectra were recorded after 24 h (HQ) or 48 h (BN, PH and TH) and, where, appropriate, a presaturation pulse programme was used to minimise the peak arising from water in the ^{1}H NMR spectrum.

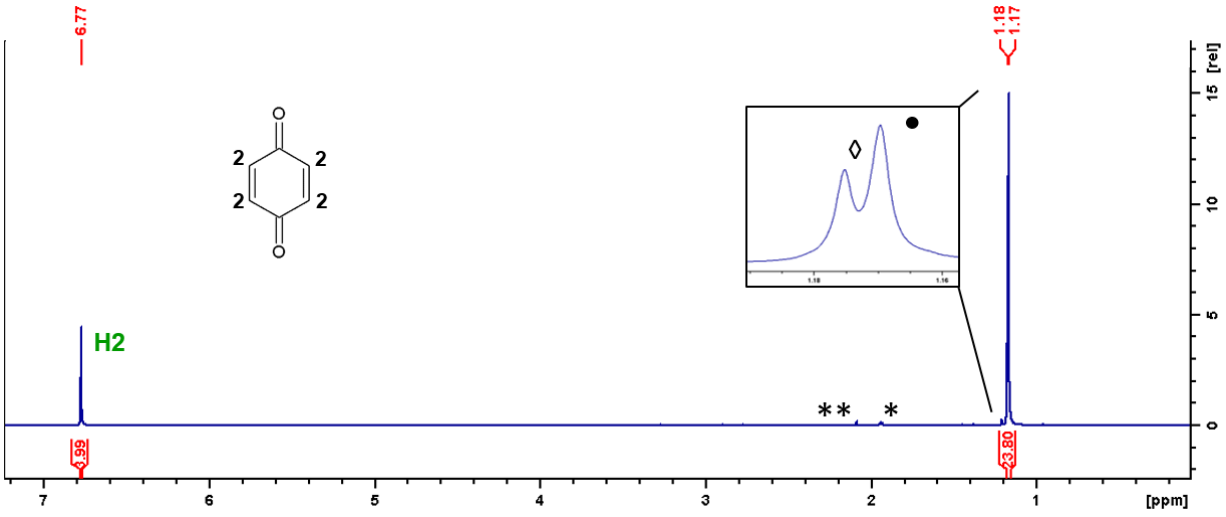

***Figure C.5**: ^{1}H NMR spectrum of benzoquinone product in acetonitrile-d_3. Spectrum was recorded after in situ reaction of hydroquinone with ^{t}BuOOH for 24 h and following filtration of Fe(III)PPIX-**1**. Pre-saturation was used to minimize the peak due to water. Asterisks indicate the presence of residual MeCN (*) and acetone (**); (●) indicates peak due to ^{t}BuOH and (◊) indicates peak due to ^{t}BuOOH. Labelled signal in green (δ 6.77) indicates signal from –CH protons of benzoquinone used for monitoring of reaction and % conversion calculation. No signal from –CH protons of hydroquinone (δ 6.63) can be seen in this spectrum.*

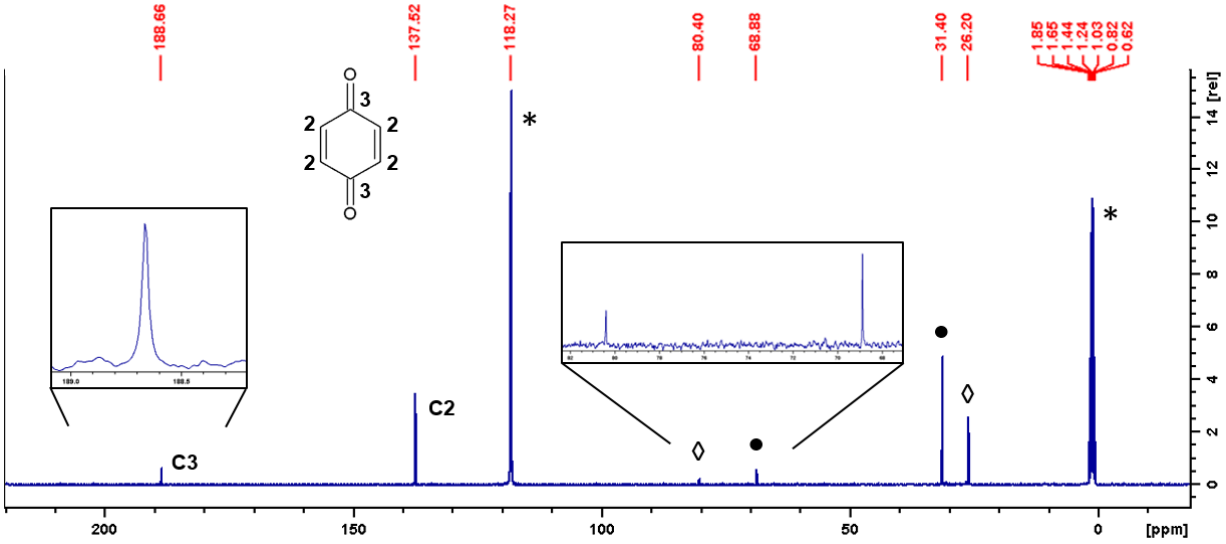

***Figure C.6**: [13]C NMR spectrum of benzoquinone product in acetonitrile-d_3. Spectrum was recorded after in situ reaction of hydroquinone with [t]BuOOH for 24 h and following filtration of Fe(III)PPIX-**1**. Asterisks indicate the presence of residual MeCN (*); (●) indicates peaks due to [t]BuOH and (◊) indicates peaks due to [t]BuOOH. The presence of the carbonyl carbon (C3) at δ 183.66 as well as the signal arising from C2 (137.52) is indicative of the formation of the benzoquinone product. There is no evidence of any signals arising from HQ.*

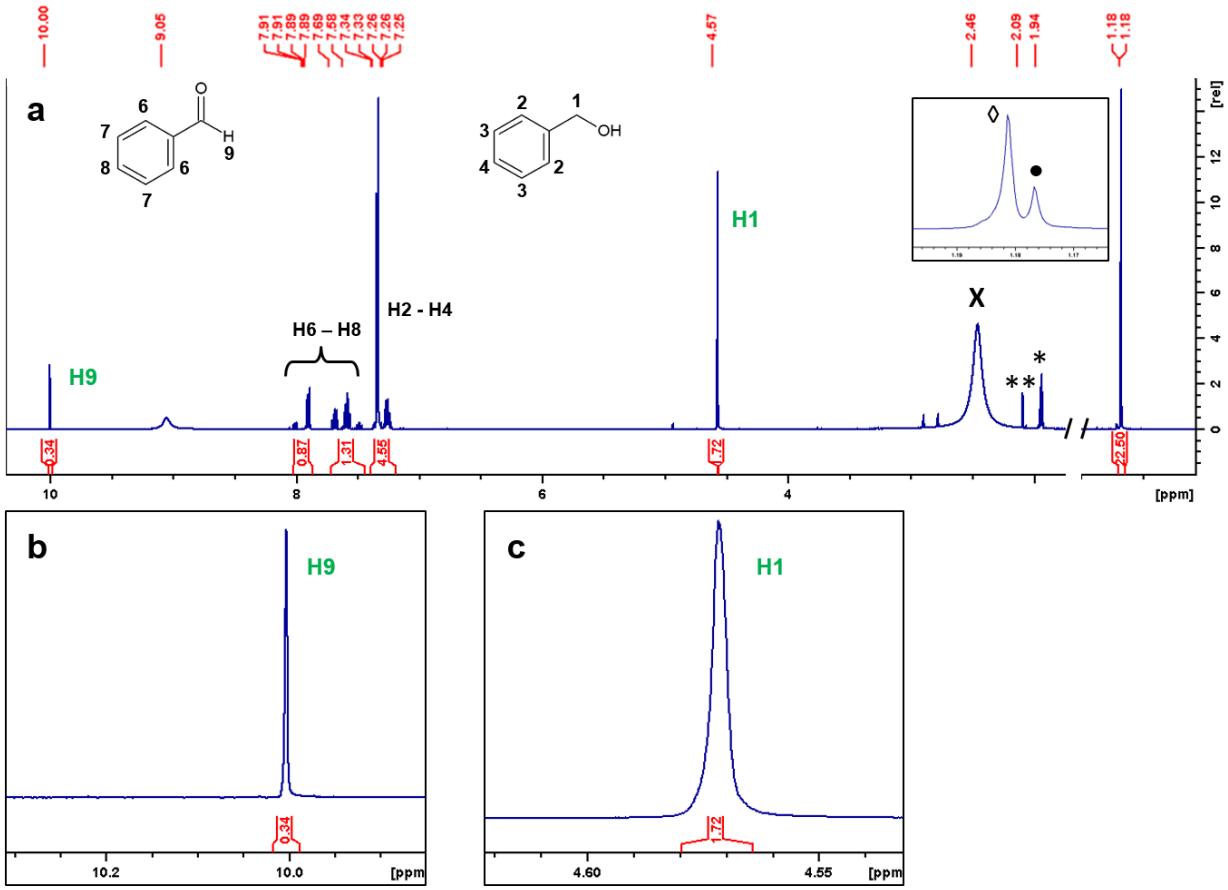

***Figure C.7**: (a) ^{1}H NMR spectrum in acetonitrile-d_3 obtained after the oxidation of benzyl alcohol by ^{t}BuOOH (catalysed by Fe(III)PPIX-**1**) after 48 h. Presence of both starting material CH_2 (δ 4.57) and product benzaldehyde CH peaks (δ 10.00) indicated only partial conversion occurred. Asterisks (* and **) indicate residual MeCN and acetone peaks; (**X**) denotes a water peak; (●) indicates peak due to ^{t}BuOH and (◊) indicates peak due to ^{t}BuOOH. Protons labelled in green indicate were used to monitor the reaction and calculate % conversion. Expansions of (b) the aldehyde proton (δ 10.00) from the product benzaldehyde and (c) CH_2 protons (δ 4.57) of the starting material benzyl alcohol. The ^{1}H NMR spectrum of the reaction mixture after 48 h indicates that there is a mixture of starting material (benzyl alcohol) and product (benzaldehyde present). The persistent signal of H1 (-CH_2 of benzyl alcohol) at δ 4.57 confirms complete conversion has not occurred while the signal of H9 (aldehyde proton of benzaldehyde) at δ 10.00 confirms there has been some conversion.*

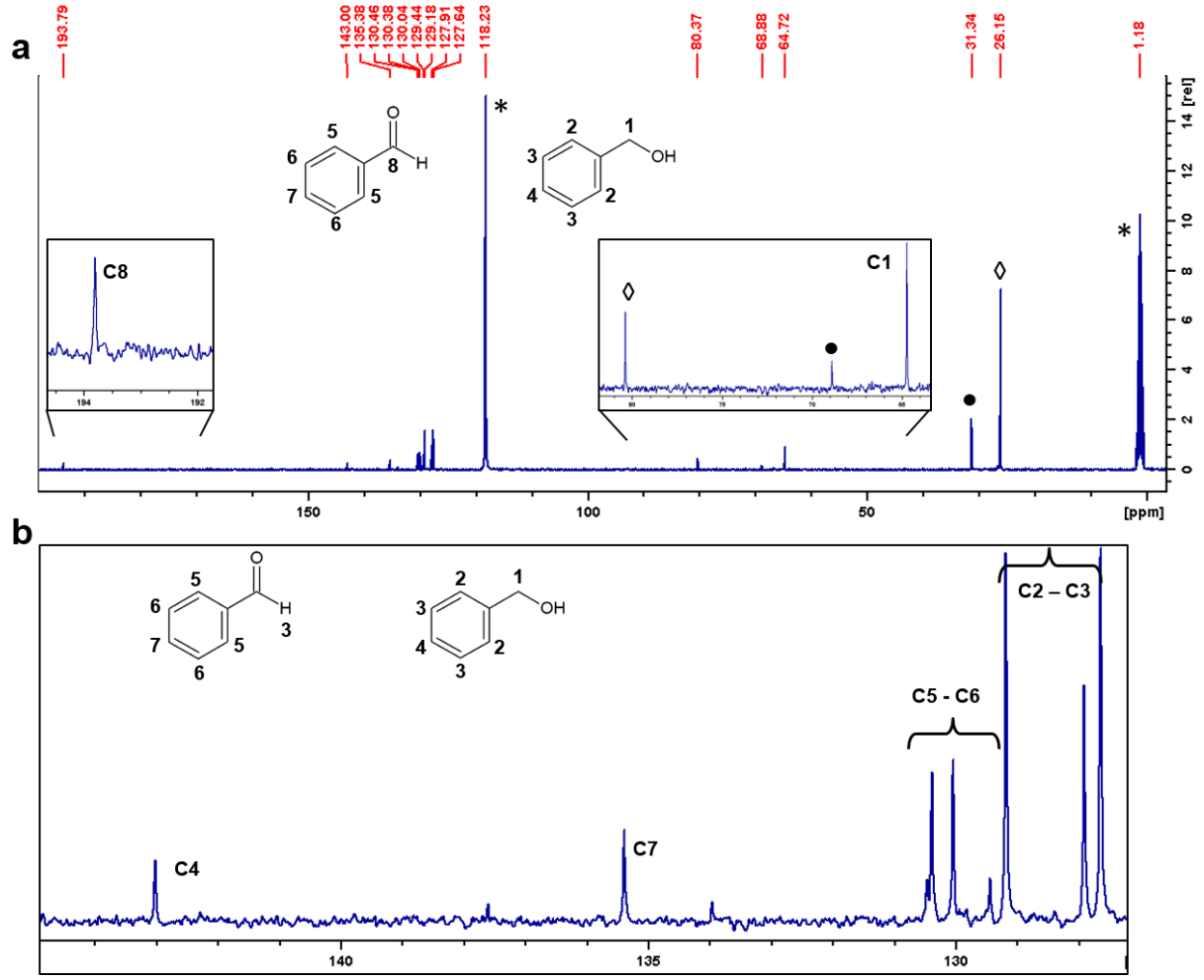

***Figure C.8**: (a) ^{13}C NMR spectrum in acetonitrile-d_3 obtained after the oxidation of benzyl alcohol by ^{t}BuOOH (catalysed by Fe(III)PPIX-**1**) after 48 h. Presence of both starting material C1 (δ 4.57) and product benzaldehyde quaternary C peaks (δ 10.00) indicated only partial conversion occurred. Asterisks (*) indicate residual MeCN peaks; (●) indicates peak due to ^{t}BuOH and (◊) indicates peak due to ^{t}BuOOH. The appearance of the signal at δ 193.79 corresponding to the carbonyl carbon of the product confirms some conversion has occurred while the persistence of the signal at δ 64.72 corresponding to the -CH_2 on benzyl alcohol confirms complete conversion has not taken place; (b) expansion of aromatic region of the same spectrum. The aromatic region shows two distinct sets of aromatic protons, confirming a mixture of starting material and product in the mixture.*

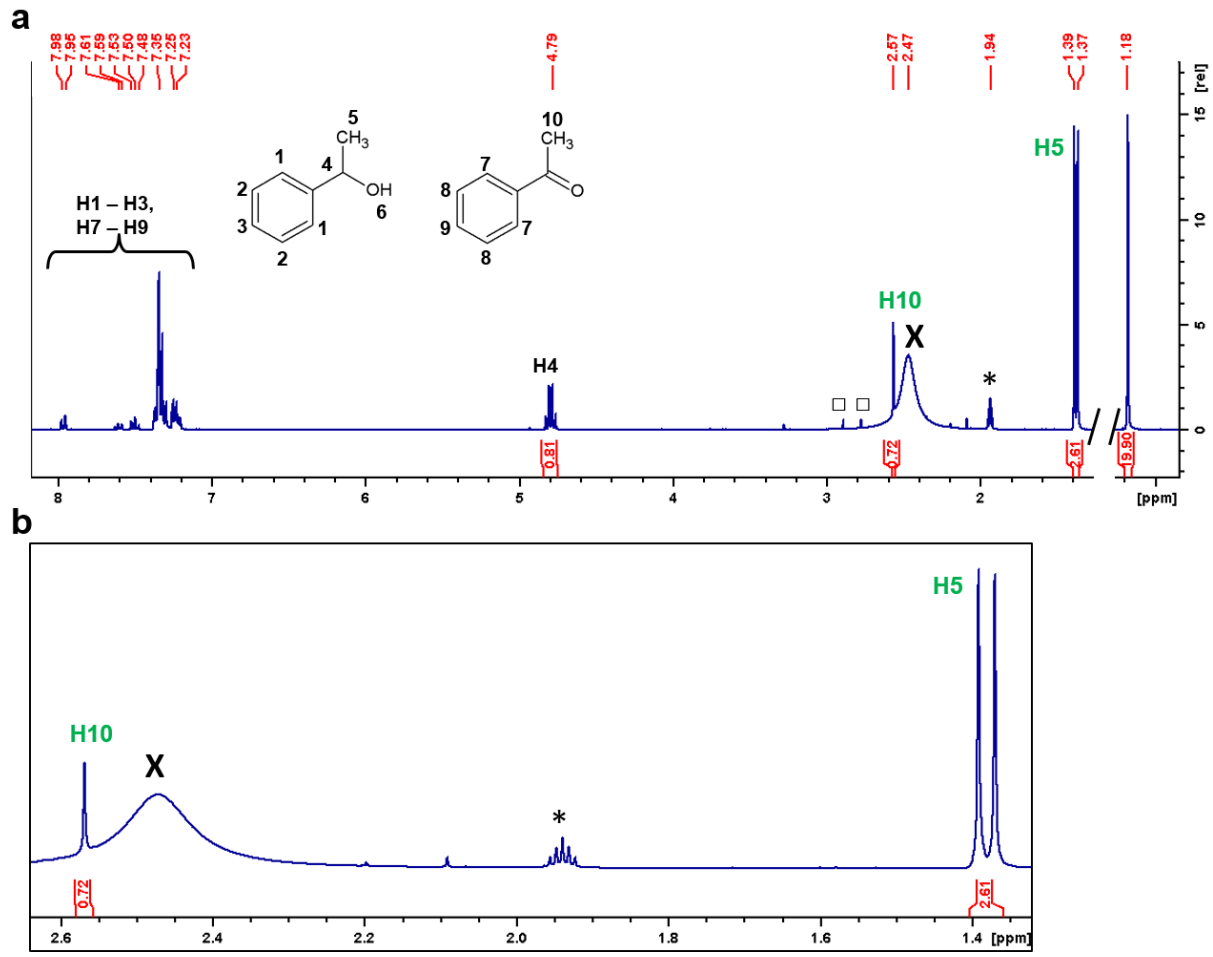

***Figure C.9**: (a) ^{1}H NMR spectrum in acetonitrile-d_3 obtained after the oxidation of phenyl ethanol to acetophenone by ^{t}BuOOH (catalysed by Fe(III)PPIX-**1**) after 48 h. Presence of both starting material CH_3 (δ 1.39) and product CH_3 (δ 2.57) indicate only partial conversion occurred. Asterisk (*) indicates the presence of residual MeCN; (X) corresponds to signal from acetone and (□) indicates peaks due to DMF from the catalyst. Protons labelled in green were used to monitor the reaction and calculate % conversion. (b) Expansion of signal from –CH_3 protons from phenyl ethanol (δ 1.39) and acetophenone (δ 2.57) respectively used for conversion calculation and reaction monitoring.*

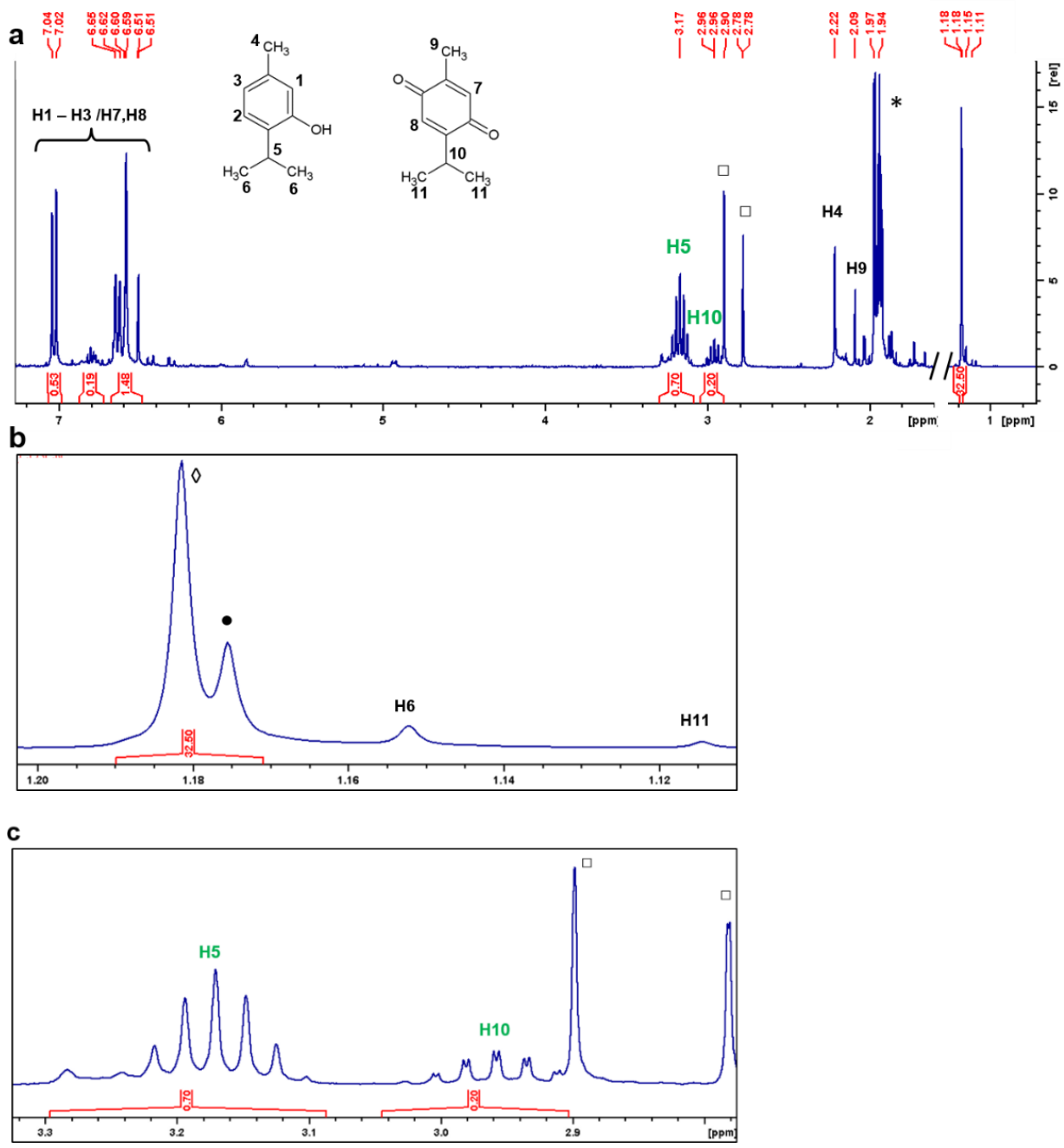
a
H1 – H3 /H7,H8
H5
H10
H4
H9
b
H6
H11
c
H5
H10

***Figure C.10**: (a) ^{1}H NMR spectrum in acetonitrile-d_3 obtained after the oxidation of THby ^{t}BuOOH (catalysed by Fe(III)PPIX-**1**) after 48 h. Presence of both starting material CH (δ 3.17) and product CH peaks (δ 2.96) indicate only partial conversion. Presaturation was used to minimize the water peak. Asterisk indicates the presence of residual MeCN (*); (●) and (◊) indicates peaks due to ^{t}BuOH and ^{t}BuOOH respectively; (□) indicates peaks due to DMF from the catalyst. Protons labelled in green were used for reaction monitoring and calculation of % conversion; (b) Expansion of isopropyl region where thymol (H6) and thymoquinone (H11) protons are observed; (c) Expansion of signal from -CH of thymol (δ 3.17) and thymoquinone (δ 2.96) respectively, used for % conversion calculation and reaction monitoring.*